EUROPEAN COMMISSION

European Research Area

Control of nitrogen oxide emission at the electric arc furnace — CONOX

Research Fund for Coal & Steel

Interested in European research?

RTD info is our quarterly magazine keeping you in touch with main developments (results, programmes, events, etc.). It is available in English, French and German. A free sample copy or free subscription can be obtained from:

Directorate-General for Research and Innovation
Information and Communication Unit
European Commission
1049 Bruxelles/Brussel
BELGIQUE/BELGIË
Fax +32 229-58220
E-mail: research@ec.europa.eu
Internet: http://ec.europa.eu/research/rtdinfo.html

EUROPEAN COMMISSION
Directorate-General for Research and Innovation
Research Fund for Coal and Steel Unit

Contact: RFCS publications
Address: European Commission, CDMA 0/178, 1049 Bruxelles/Brussel, BELGIQUE/BELGIË

Fax +32 229-65987; e-mail: rtd-steel-coal@ec.europa.eu

European Commission

Research Fund for Coal and Steel

Control of nitrogen oxide emission at the electric arc furnace — CONOX

H. Pfeifer, T. Echterhof, L. Voj, J. Gruber
RWTH Aachen University
Templergraben, 55, 52056 Aachen, GERMANY

H.-P. Jung, S. Lenz, C. Beiler
Deutsche Edelstahlwerke GmbH
Obere Kaiserstrasse, 57078 Siegen, GERMANY

F. Cirilli
Centro Sviluppo Materiali
Via di Castel Romano, 100/102, 00128 Rome, ITALY

U. De Miranda
ORI Martin
Corso Garibaldi, 49, 20100 Milan, ITALY

N. Veneri, E. Bressan
Riva Acciaio Spa
Lungadige A. Galtarossa, 21/c, 37133 Verona, ITALY

Contract No RFSR-CT-2006-00033
1 July 2006 to 30 June 2009

Final report

Directorate-General for Research and innovation

2012 EUR 25078 EN

Europe Direct is a service to help you find answers to your questions about the European Union

Freephone number (*)**:**
00 800 6 7 8 9 10 11

(*) Certain mobile telephone operators do not allow access to 00 800 numbers or these calls may be billed.

A great deal of additional information on the European Union is available on the Internet. It can be accessed through the Europa server (http://europa.eu).

Cataloguing data can be found at the end of this publication.

Luxembourg: Publications Office of the European Union, 2012

ISBN 978-92-79-22227-6

doi:10.2777/25616

ISSN 1831-9424

Printed in Luxembourg

PRINTED ON WHITE CHLORINE-FREE PAPER

Table of contents

1 Summary

The CONOX project has been carried out by two research institutes with working areas in steel research, the Department of Industrial Furnaces and Heat Engineering at RWTH Aachen University (RWTH) and the Centro Sviluppo Materiali (CSM) and three electric steel making plants, Deutsche Edelstahlwerke GmbH Siegen (DEWG), ORI Martin Acciaieria E Ferreira di Brescia (ORI) and RIVA Acciaio Spa Verona (RIVA) with a wide range of produced steel grades (low alloyed construction steels to high alloyed stainless steels) and EAF technologies (oxygen, dust, and coal injectors, gas burners, CoJets, scrap preheating, slag foaming). The project work was based on the combination of (a) experimental investigations of the NO_x formation in EAFs at industrial production plants and, additionally, at pilot plant EAFs at well defined conditions and (b) modelling of the NO_x formation mechanisms in the EAF.

In the frame of the project activities of research institutes and industrial partners have been carried out in strong cooperation and integration. The general objective was to elaborate guidelines to reduce NO_x emissions from the Consteel process as well as standard EAFs employing various EAF technologies.

The Consteel is the process in which the charge is loaded directly from the scrap-yard to the charge conveyor, where it is automatically and continuously transferred to the EAF as it is preheated by off gases. This permits flat bath operation.

The work regarding the Consteel process has been based on the individuation of the main mechanisms controlling NO_x formation and emission, the development of a *semi empirical* model, and on industrial plant measurements under different working conditions.

The work at the standard EAFs has been based on the modelling of different process conditions and a deduction of predictions regarding NO_x formation. These predictions have been further investigated and validated by industrial plant measurement. Eventually best practices to reduce NO_x emissions have been derived from the combined results of modelling and industrial measurements.

The work packages (WP) that were covered by the project programme are:

WP 1: Initial Measurements of NO_x emissions at DEWG, ORI Martin, RIVA

The objective of this first WP was to define a reference situation of NO_x emission for standard EAFs and the Consteel process. In this work package initial measurements of NO_x emissions have been performed. The industrial measurements at the three electric steel making plants were conducted in close cooperation and with the support of the research institutes. The measurements have been carried out to establish a data set of reference values of NO_x emissions under current standard operating parameters for the Consteel process and at standard EAFs.

WP 2: Study of NO_x generation from combustion reactions in EAF

In this work package a semi empirical model of NO_x emissions has been developed. This model has been developed on the basis of literature data and industrial measurements. The developed model was able to take into account the effect of the main EAF Consteel operational parameters in determining nitrogen oxide formation.

The model has been calibrated through experimental tests carried out on EAF pilot furnace and refined by means of plant measurements. These activities permitted to calculate the kinetic constants.

The model has been then applied to individuate the relative weight of the operating parameters.

WP 3: Study of NO_x generation from EAF plasma reactions

After modifications of a pilot plant EAF within this work package the influence of electric arc parameters and furnace atmosphere on the emission of NO_x gas species has been experimentally determined. The trials were conducted in an airtight pilot plant EAF under controlled atmospheres.

Additionally the influence of the EAF furnace atmosphere has been modelled based on thermodynamic calculations taking temperature and gas composition into account. The results of the modelling have been compared to the trials and to operational results of industrial partners.

Main conclusions in view of the control of NO_x emissions are:

- For the trials conducted the amount of NO_x produced by the electric arc is to be seen as constant and not influenced by electric parameters of the arc (arc current, arc length) within the range of parameter variations technical available and tested.
- The NO_x emission of the pilot plant EAF as well as industrial EAFs is strongly correlated with the composition of the furnace atmosphere the arc is ignited and burning in. The highest amounts of NO_x are produced in O_2 rich atmospheres. Atmospheres like this occur in the EAF e. g. after the scrap charging. To lower NO_x generation in the furnace therefore the amount of leak air increasing the O_2 content of the furnace off-gas has to be as low as possible.
- EAF off-gas is usually not in equilibrium. The kinetics of the gas reactions in the furnace and the post combustion zone are determining the NO_x content of the off-gas. Differences between real off-gas data and equilibrium calculations would be smaller with a longer residence time of the off-gas in the hot zones and higher temperatures respectively. To achieve this objective the off-gas flow rate has to be controlled as low as possible still ensuring sufficient exhaust of any furnace emissions.
- Reducing agents like CO and H_2 are significantly lowering the NO_x concentration in the off-gas and reduce NO_x formed by the electric arc. Because of this, operational practices like slag foaming with the increased generation of CO, which are already in use to lower energy losses in the EAF, have an additional positive effect on the NO_x emissions of EAFs.

WP 4: Impact of oxygen injectors and CoJets on NO_x emission

The objective of this work package was to determine the impacts of current EAF burner and injector technologies and EAF gas atmospheres on the NO_x emissions under industrial operating conditions. The important factors influencing the NO_x emission at EAFs equipped with gas burners or CoJets have been identified:

- There is no correlation between the amount of carbon blown and the total NO_x emissions when carbon is blown at all.
- The correlation between the CO and NO_x content in the furnace off-gas predicted in the modelling stage of WP 3 could be confirmed.
- Trials regarding the ratio of injected oxygen to methane in the CoJet burners led to a reduction of NO_x emissions of up to 30 % by reducing the oxygen amount available inside the furnace. This is also in agreement with the predictions derived from the modelling in WP 3.

Deduced from these results the following best practices could be formulated:

- Continuation of the carbon blowing (slag foaming) standard practice because of the positive influence of the resulting CO-rich atmosphere on the NO_x emissions for carbon steel grades.
- Evaluation of new developments in foamy slags for stainless steel grades and application when available for standard operational use.
- Reduction of the CoJet ratio to reduce the oxygen supply to the furnace and to prevent an oxygen rich atmosphere in the EAF.

WP 5: Impact of scrap preheating (Consteel) on NO_x emission

The objective of this work package was to individuate the effect of the different Consteel and EAF operations on the emission of NO_x. The activities have been focused on the individuation of the effect of the main operational parameters on NO_x emission through plant measurements, on the definition of guidelines to reduce NO_x emission and on final plant testing of the developed guidelines.

Industrial tests with different oxygen to coal ratios, as well as post combustion oxygen lancing inside the EAF have been carried out. Plant measurements carried out simultaneously both at the EAF and downstream in the tunnel permitted to quantify the amount of NO_x generated in these two different points. The model developed in WP 2 has been applied to support the definition of improved guidelines to manage EAF Consteel in order to decrease NO_x emissions.

Main issues to be pointed out on the basis of the investigation activities are listed as follows:

- Peaks of NO_x emission (concentration) appear generally during the transient operation into the furnace, difficult to avoid but that do not affect strongly the average emission; during main period of the heats NO_x formation decreases strongly, due to the CO/CO_2 formation that 'fills' the furnace freeboard and decreases the air in-leakage.
- Post Combustion inside EAF (by dedicate lancing) contributes to lower the NO_x emission decreasing the air in-leakage even if a suitable amount of coal is required to generate enough (and as longer as possible) CO_x (related to the slag foaming management); the net effect of coal addition is therefore 'positive' being the nitrogen content of this material not playing a significant role in oxides formation.
- The amount (in terms mass flow rate, derived by off gas mass flow rates determination at the furnace exit and downstream) generated in the pre-heater tunnel is about five times higher than the furnace, due to the air dilution and reactions to complete combustion of residual CO and H_2 coming out from EAF.
- Available data show that an optimal balancing of the effective depression throughout the running is required to avoid excess of air leakage at the connecting car stage (i.e. the air that mixes with EAF off gases) by proper setting of the de-dusting system.

WP 6: Impact of adapted dedusting on NO_x emission

In this work package off-gas measurements examining the influence of oxygen injection by door lance, of the use of different carrier gases for carbon and dust injection and of airtightness and the dedusting system operation have been performed. Within this WP also predictions from modelling have been verified and validated with results from the industrial EAF.

Main results of the investigations conducted are:

- Delayed oxygen injection during/after arc ignition is lowering the NO_x emissions due to a reduced oxygen supply in the EAF vessel.
- The use of an inert carrier gas instead of air for the injection of carbon and dust is only for the dust injection beneficial in regard to NO_x emissions. When used for the carbon injection it leads to even higher NO_x concentrations in the off-gas.

According to the results found in this WP the following best practices have been established to reduce the oxygen supply in the EAF:

- Delay of the oxygen injection after arc ignition.
- Use of inert carrier gas for the dust injection into the furnace.
- Keeping the slag door closed if possible to maximise the airtightness of the EAF.
- Variable control of the off-gas volume flow rate to minimise the amount of leak air in the furnace.

WP 7: CFD simulation of NO_x formation

In this work package CFD simulations of the investigated industrial EAF at DEWG were performed. The simulations were carried out to model the gas flow and air intake inside the EAF vessel and in the post combustion zone of the primary dedusting system. The interaction between gas chemistry, gas flow patterns and NO_x formation due to the electric arc and in post combustion zones has been investigated as well. Various EAF operating conditions like dedusting system operation, origin of leak air, furnace temperatures etc. have been varied and simulated.

Main issues to be pointed out on the basis of the CFD simulations are:

- CFD simulations visualized the flow pattern and mass fraction distribution in the EAF and post combustion zone and gave new information regarding the position of off-gas measurement probes.
- As a result of the simulations the off-gas measured at point A is not in thermo-chemical equilibrium but is composed of unburned CO and O_2 simultaneously.
- The amounts of CO and O_2, respectively, available in the furnace have a great influence on NO_x emissions.

2 Scientific and technical description of the results

2.1 Introduction

On the background of competing steel production technologies with different impact on the environment on one hand and world-wide competing production sites with different legislative framework on the other hand, sustainable development, especially minimum emission to the environment is substantial for the EAF process. Besides CO_2, NO_x (x = 0.5, 1, 2) gas species are the second most abundant air polluting gas species from industrial production sites.

The research project focuses on the special topic of NO_x emission and control of the EAF process, for which the parameters influencing the NO_x emission were not well known. The physical background of NO_x formation and emission of the EAF is quite different from the mechanisms of combustion of fuels, e.g., natural gas in reheating furnaces, due to very high temperatures in the electric arc and distinct process periods with and without oxygen in the furnace atmosphere. Off-gas measurements at four EAFs, that were performed prior to this project showed considerable variance in measured NO_x emission at the EAF from 0.015 kg/t to 0.78 kg/t (**Figure 1**). Furthermore, adaptation of legal restrictions for continuous combustion processes is difficult for batch processes as the EAF smelting process. Measurements showed that especially the emission peaks of very non-continuous mass flow rate of NO_x will exceed legislative limits. To define the appropriate emission factor in legislative (i.e. $g/m^3_{off\text{-}gas}$ or g/t_{Steel}), specific R & D related to the EAF process was necessary.

The industrial goal of the project has been the control and minimisation of NO_x emission. To obtain this purpose, the interrelation of process parameters with NO_x emission at the EAF is investigated

(1) in the furnace itself under special process conditions (e.g. plasma, furnace atmosphere) and

(2) in the high temperature part of the exhaust off gas system where the CO/H_2 post combustion occurs with high air ratio.

With this knowledge, the influence of EAF process parameters (e.g. arc length, arc current, oxygen lancing, foamy slag, carbon and dust injectors, burners, oxygen injectors, furnace atmosphere, airtight furnace) has been quantified. Conditions for minimising the NO_x emissions at the EAF have been predicted.

In order to enlighten the NO_x emission processes in the EAF, three main technical objectives have been defined:

- Measurements of NO_x emissions and other off-gas components (CO, CO_2, H_2, O_2) of industrial EAFs at the EAF elbow and simultaneously in the dedusting system.
- Additional investigation of NO_x formation due to combustion reactions and due to the plasma of the electric arc under well defined atmosphere conditions in laboratory and pilot EAFs.
- Modelling of NO_x emission in the EAF vessel and the post combustion unit of the exhaust gas system by means of thermo-chemistry of plasma gas species and CFD simulation of post-combustion.

From these investigations the following benefits were expected:

- Better understanding of NO_x formation in the EAF and in the dedusting system.
- Reduced NO_x emission from the EAF vessel.
- Reduced NO_x formation in the CO post combustion flame in the exhaust gas system.
- Control and protection of the environment in and around the workplace.

The project has been carried out by two research institutes with working areas in steel research (RWTH, CSM) and three electric steel making plants (DEWG at Siegen, ORI Martin at Brescia, Riva Acciaio Verona) with a wide range of produced steel grades (stainless, special and carbon steel) and EAF

technologies (injectors for oxygen, dust, and coal, gas burners, scarp preheating, slag foaming). The project work is based on the combination of

(1) experimental investigations of the NO_x formation in EAFs at industrial production plants (EWS, ORI Martin, Riva) and, additionally, at pilot plant EAFs (RWTH, CSM) at well defined conditions (furnace atmosphere and arc length) and

(2) modelling of the NO_x formation mechanisms in the EAF.

2.1.1 Background and State of the Art

The International Iron and Steel Institute (IISI) has carried out a study to describe the state of the art of Electric Arc Furnace (EAF) technology and its future trends, the IISI Delphi Survey [2]. From the Delphi study an increasing use of EAF was forecast, with a prevision of 40% of liquid steel production in 2010 compared to 33 % 2005. Beside reduction of total and electrical energy consumption reduction of dust and polluting gas species, i.e. CO_2, NO_x is of major importance. In order to successfully compete with integrated steel making in the production of steel strip, EAF steel making has to reduce emission of possible air pollutants, i.e. CO, CO_2 and NO_x gas species (x = 0.5, 1, 2). Various studies depict the estimation of overall NO_x emission for different process technologies (**Figure 1**). EAF: 0.24 kg/t [8], 0.23 kg/t to 0.27 kg/t [4], 0.12 kg/t [14], 0.325 kg/t [10], Basic Oxygen Furnace (BOF): 0.10 kg/t [8], 0.01 kg/t to 0.06 kg/t [4], 0.05 kg/t [14], Blast Furnace 0.001 kg/t to 0.033 kg/t [4], Sinter plant 0.04 kg/t to 0.32 kg/t [4], 0.57 kg/t [14] Preheating furnace 0.15 kg/t [8], Bell type furnace 0.05 kg/t).

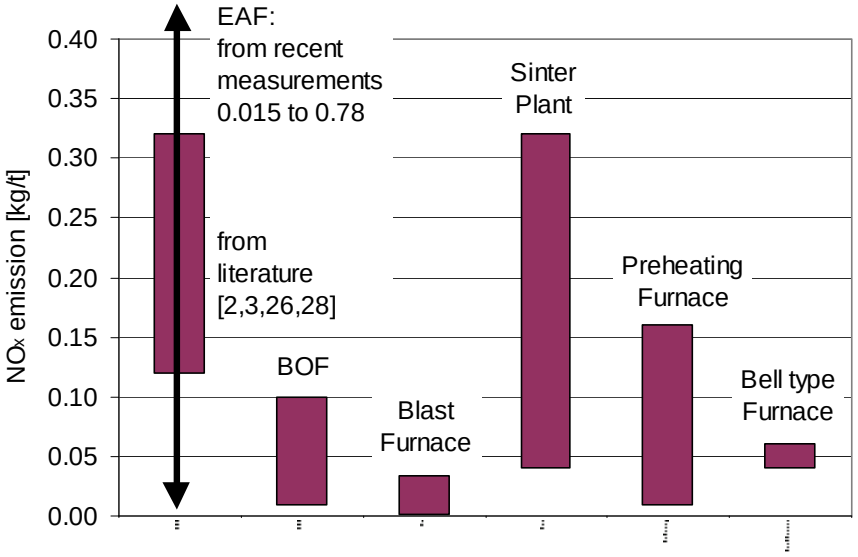

Figure 1: NO_x emissions of various furnace types in steel production, estimations and measurements

Relatively high NO_x emissions of the EAF, as shown in **Figure 1**, are not surprising due to combined occurrence of high temperature plasma and combustion reactions with air. However, preliminary measurements at four EAFs showed very high variance in NO_x emissions from EAF to EAF (from 0.015 kg/t to 0.78 kg/t [15], **Figure 1** and **Figure 2**). From **Figure 2** it is evident that the NO_x emission does not only depend on combustion processes (e.g. carbon content in off-gas) but from various other EAF process parameters (e.g. electric arc length, air-tight EAF, slag layer thickness etc.).

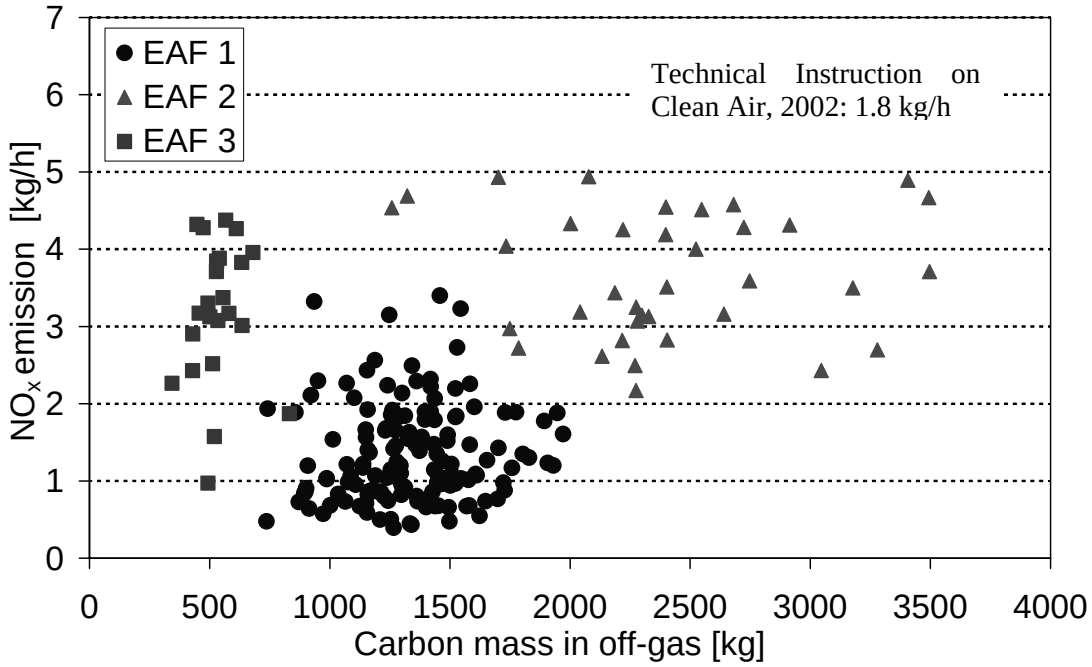

Figure 2: Measured mean NOx emission rates in kg/h at three EAFs [15]

EAF steel making provides very special conditions for NO_x formation as the electric arcs operate occasionally in oxidising gas atmosphere. Plasma temperatures in the range between 3000 K and 10000 K force ionisation of infiltrated air and formation of NO_x gas species in the arc, if oxygen is in excess (see also eq. (1) to (3)).

$$N_2 + O \rightleftarrows N + NO \quad (1)$$

$$N_2 + O \rightleftarrows N^* + NO \quad (2)$$

$$N_2 + N + O \rightleftarrows N_2^* + NO \quad (3)$$

with: N atomic nitrogen

N^* atomic electrical excited nitrogen

N_2^* molecular electrical excited nitrogen

Oxy-fuel gas burners provide NO_x formation at high temperature (thermal and prompt NO_x formation). The mechanism for the formation of thermal NO_x, also known as extended Zeldovich mechanism, is given by the equations (4) to (6).

$$O + N_2 \rightleftarrows NO + O \quad (4)$$

$$N + O_2 \rightleftarrows NO + O \quad (5)$$

$$N + OH \rightleftarrows NO + H \quad (6)$$

The formation of prompt NO_x is more complex and controlled by the formation of CH radicals. The CH radicals react with nitrogen to HCN and the HCN is then reacting in several subsequent steps to NO_x according to equation (7). The prompt NO_x formation is because of the CH dependency strongly controlled by local fuel concentration. In the EAF it is usually less relevant than thermal NO_x.

$$CH + N_2 \rightarrow HCN + N \ldots \begin{matrix} \nearrow NO \\ \searrow N_2 \end{matrix} \quad (7)$$

Combustion of nitrogen from coal leads to formation of fuel-NO_x (cf. eq. (8)). The external post combustion of CO gas emitted by the oxygen deficient furnace may cause once more formation of thermal NO_x in the first unit of the dedusting system (**Figure 3**). With respect to increasing EAF productivity, it is desirable to avoid primary formation of NO_x by controlled operation of the EAF.

$$2[N]_{coal} + O_2 \rightarrow 2\,NO \tag{8}$$

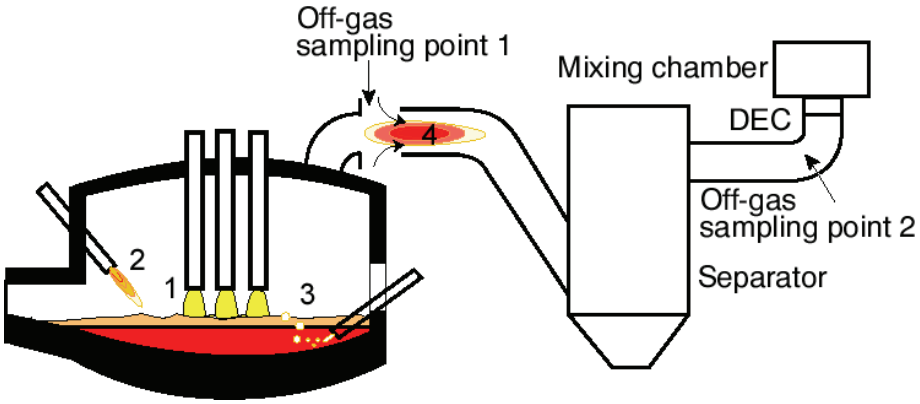

Figure 3: NO_x sources at the EAF: 1: electric arc, 2: oxy-fuel burner, 3 & 4: CO post-combustion

Increasingly strict environmental regulations in countries of the European Community are a challenge for energy intensive steel making at highly competitive worldwide markets. It is expected that environmental restrictions will further increase in future as, e.g., in Germany the Technical Instruction on Clean Air (2002: 1.8 kg/h for NO_x for emission of industrial furnaces), see also estimated emission factors in **Table 1**. Important emerging technologies to increase chemical energy yield and process efficiency affect significantly NO_x emission of the EAF:

- scrap pre-heating systems and techniques
- new injection systems of O_2 blowing into bath and for internal post-combustion
- foaming slag technology for carbon (and stainless) steel production
- air-tight EAF
- air quenching of off-gas after the post-combustion chamber in the fume collecting system
- direct exhaust control and dust recycling systems.

On the other hand, operating conditions of the off-gas extraction and dedusting system affects the volume flow of infiltrated air into the furnace vessel and, thus, the EAF energy efficiency. As a consequence, increasing importance of reduced dust and air polluting emissions will compete with minimum total EAF energy input and maximum energy efficiency.

Table 1: Prediction of process conditioned NO_x emission in Germany [14]

Activity	Emission factor NO_x [kg/t_{Steel}]					Emissions NO_x [t]				
	2000*	2005	2010	2015	2020	2000	2005	2010	2015	2020
Sinter	0.57	0.5	0.43	0.43	0.42	15.937	14.235	12.461	12.561	12.177
Pig iron steel	0.04	0.04	0.04	0.04	0.03	1.168	1.150	1.132	1.107	1.072
EAF steel	0.12	0.12	0.12	0.12	0.12	1.599	1.541	1.484	1.518	1.553
BOF steel	0.005	0.005	0.004	0.003	0.003	165	151	136	102	85

*: verified

2.2 Objectives of the project

The industrial goal of the project was to develop knowledge to control and minimise NO_x emission. To obtain this purpose, the impact of process parameters on NO_x emission mechanisms at the EAF have been investigated in the furnace itself under various process conditions (e.g. plasma, furnace atmosphere) and in the high temperature part of the exhaust off gas system where the CO/H_2 post combustion occurs with high air ratio. With this knowledge, the influence of EAF process parameters (e.g. arc length, arc current, oxygen lancing, foamy slag, carbon and dust injectors, burners, oxygen injectors, furnace atmosphere, airtight furnace) have been quantified. Conditions for minimising the NO_x emissions have been predicted. In order to enlighten the NO_x emission processes in the EAF, three main technical objectives had been defined:

- Measurements of NO_x emissions and other off-gas components (CO, CO_2, H_2, O_2) of industrial EAFs at the EAF elbow and in the dedusting system
- Additional investigation of NO_x formation under well defined atmosphere conditions in laboratory and pilot EAFs.
- Modelling of NO_x emission in the EAF vessel and the post combustion unit of the exhaust gas system by means of thermochemistry of plasma gas species and CFD simulation of post-combustion.

The objective of CSM and ORI Martin contribution to the project has been the evaluation of the effect of operating conditions and post combustion on NO_x emission from EAF Consteel. These results have been achieved through the development of a model able to simulate NO_x emission from EAF Consteel plant and from industrial measurements in standard and modified conditions.

The project has been carried out according to the following steps:

- Definition of a model able to reproduce NO_x emission from ORI Martin EAF Consteel (CSM). Due to the complexity of the EAF environment a semi empirical formulation of the model has been chosen. The model has been calibrated with experiments on EAF pilot plant and EAF industrial plant.
- First industrial measurements have been carried out (ORI Martin) to define the reference situation of NO_x emission
- Pilot plant experimentation at CSM facility to calibrate the model
- Application of the model to industrial cases for validation (CSM and ORI Martin)
- Industrial experimentation to identify the effect of the different operating operations on the NO_x emissions (ORI Martin)
- Application of the model and results of industrial tests to define guidelines for reduction of NO_x emission (CSM and ORI Martin)

The following scheme (**Figure 4**) describes the general logic of the work. As indicated in the scheme, the industrial tests were carried out at ORI Martin steel plant.

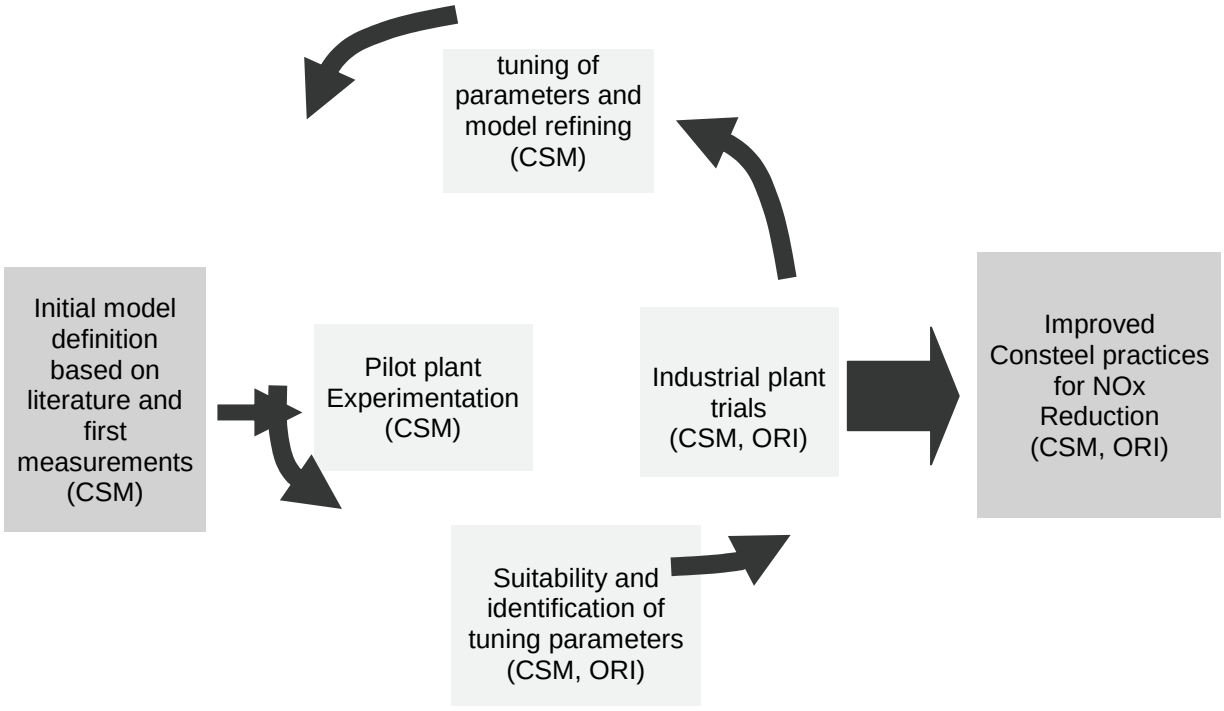

Figure 4: General logic of the activities of CSM and ORI

2.3 Description of activities and discussion

2.3.1 Initial measurements of NO_x emission

An overview on the production characteristics of all industrial partners is given in **Table 2**.

Table 2: Production characteristics of industrial partners

	DEWG (stainless)	DEWG	ORI	RIVA
Tapping weight [t]	120	140	75	2 × 80
Transformer power	105 MVA	105 MVA	31 MVA	43 MVA
Stainless steel	X	-	-	-
Special steel	-	X	-	-
Construction steel	-	-	X	X
Gas burner	-	-	-	X
Oxygen injection	Lance	Lance	Lance	CoJets
Coal injection	X	X	-	X
Dust injection	X	X	-	-
Consteel technology	-	-	X	-

2.3.1.1 Initial off-gas measurements at DEWG and determination of NO_x emission with current operation parameters

Off-gas analysis was performed at the primary dedusting system at the EAF at DEWG (**Figure 5**). The AC EAF with tapping capacity 140 ton (carbon steel) and 120 ton (stainless steel) has a water-cooled top cover, water-cooled wall panels and a lance manipulator (**Table 2**). While production of carbon-steel there is dust injected into the slag layer. Therefore compressed air is used as carrier gas.

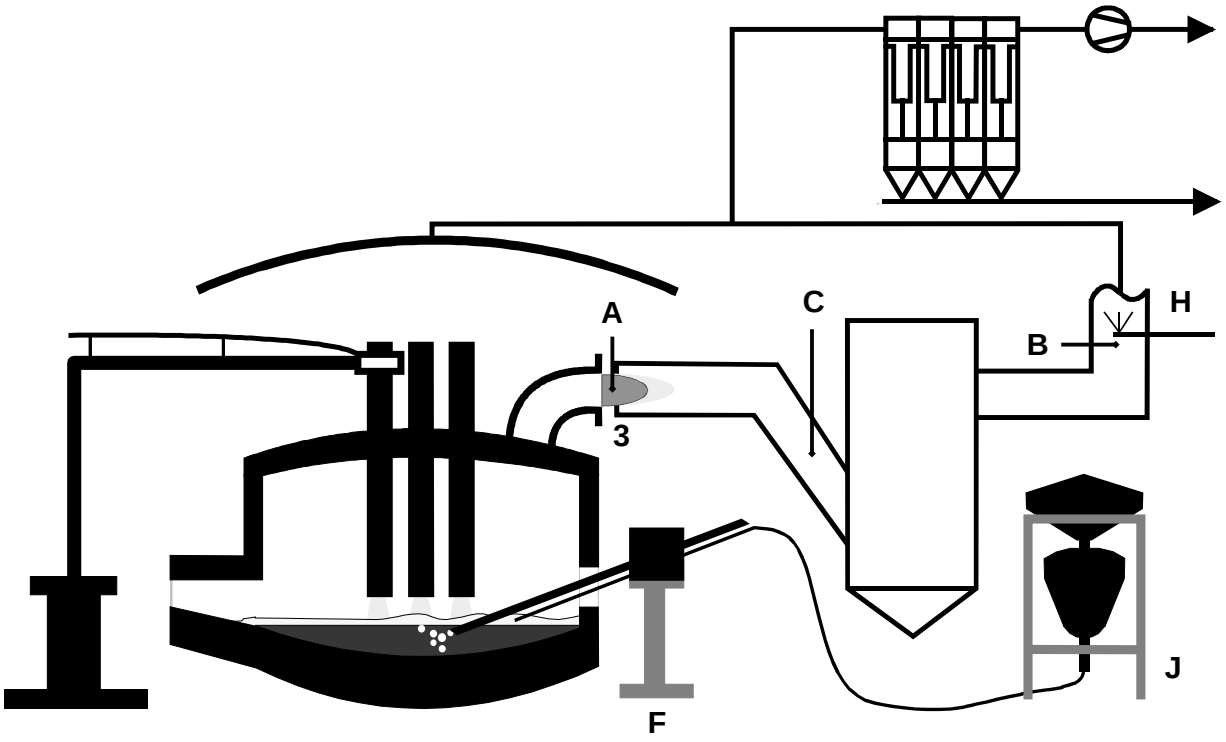

Figure 5: EAF layout at the DEWG Siegen plant
A: measurement point A, B: measurement point B, C: temperature measurement, F: oxygen/dust injector, H: water injector, J: dust silo; 3: gap between EAF vessel and primary dedusting system

Off-gas measurements have been conducted simultaneously at measurement point A and point B. The off-gas temperature has been measured near point A and additionally at point B. Measurement point A was located at the gap between EAF elbow and primary dedusting system. Measurement point B was

located at the end of the water-cooled hot gas line after the complete post combustion. The amount of off-gas ejected at the gap during melting is not well known. Measured volume flow rates in the dedusting system assume off-gas volume flow coming out of the EAF vessel and total amount of air intake at the EAF vessel and downstream. Off-gas composition, off-gas temperature, and off-gas volume flow rate was measured at measurement point B. The simultaneously measurement at point A and point B allowed the calculation of the volume flow rate at point A by carbon mass balances. This is possible by assuming the leak air to be free of carbon. Using two off-gas analysis spots the amount of NO_x formatted inside the EAF vessel, the post combustion zone at the gap and downstream point A could be distinguished. At measurement point A there is an ABB analysis system installed (**Figure 6**). An additional CLD NO_x analyser (RWTH) was integrated in the shown ABB analysis system. Additionally to the ABB off-gas analysis system a portable analysis system (RWTH) was installed. At measurement point B the second portable off-gas analysis system (RWTH) has been set up (**Figure 7**). The setup of the two portable off-gas analysis systems is described in **Table 3** together with technical data of the analysers like measurement range, measurement principle and accuracy. The off-gas analysis systems have been calibrated with test gases before each measurement campaign and in between if necessary.

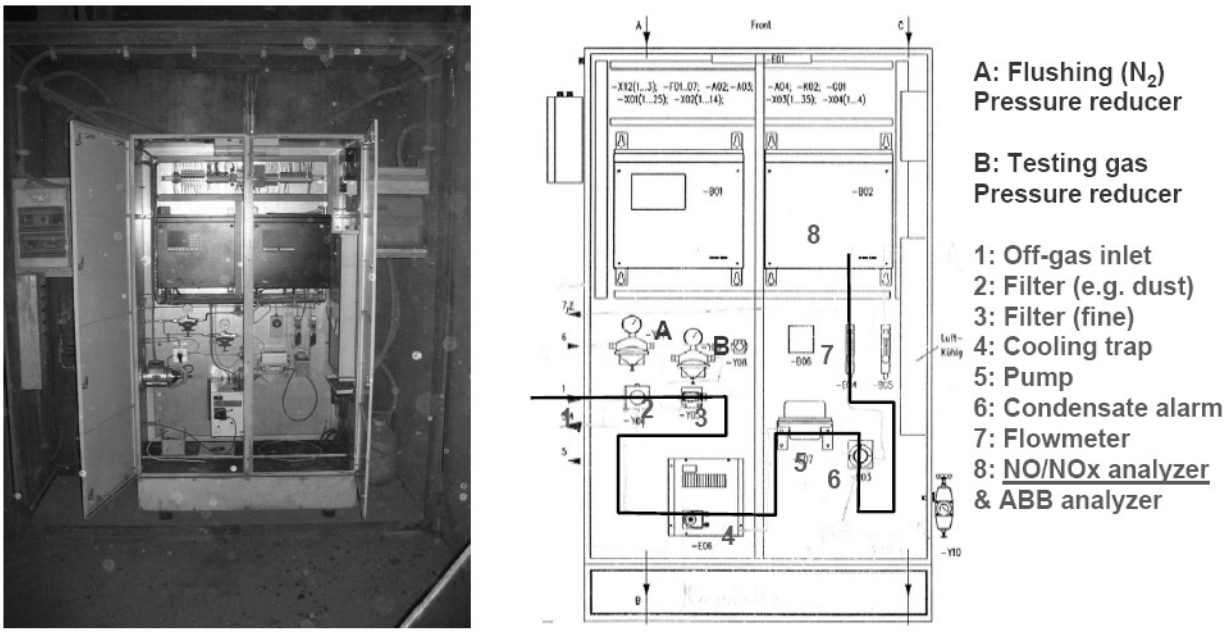

Figure 6: View of ABB analysis system installed (left), layout of analysis system and adapted NO/NO_x analyser (RWTH) at point A

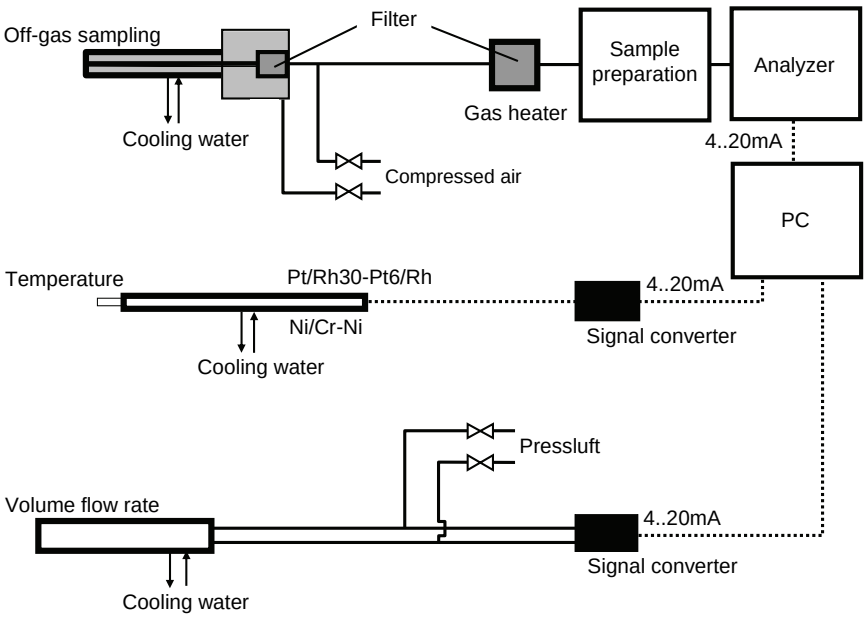

Figure 7: Layout of the off-gas analysis system: water-cooled probes and gas pre-treatment

Table 3: Setup of the portable off-gas analysis systems and technical data

System	Off-gas species	Measurement principle	Range	Accuracy*
Point A	CO	IR radiation absorption	0 % - 100 %	± 1 %
	CO_2	IR radiation absorption	0 % - 100 %	± 1 %
	O_2	O_2 paramagnetism	0 % - 25 %	± 1 %
	H_2	Thermal conductivity	0 % - 100 %	± 1 %
	CH_4	IR radiation absorption	0 % - 10 %	± 1 %
	NO_x / NO	Chemiluminescence	0 - 10000 ppm	± 1 %
Point B	CO_2	IR radiation absorption	0 % - 20 %	± 1 %
	O_2	O_2 paramagnetism	0 % - 25 %	± 1 %
	CO	IR radiation absorption	0 - 2500 ppm	± 1 %
	SO_2	IR radiation absorption	0 - 1300 ppm	± 1 %
	NO_2	UV radiation absorption	0 - 1500 ppm	± 1 %
	NO_x / NO	Chemiluminescence	0 - 10000 ppm	± 0.5 %

* in regard to the upper range value

The analysis system equipment consists of water-cooled probes, filters, detectors, and signal converters for measuring the off-gas composition (O_2, CO_2, CO, NO_x). At point B there was also the off-gas temperature and off-gas flow velocity measured. The off-gas compositions were determined using infrared absorption spectroscopy (CO, CO_2), paramagnetism (O_2), and chemiluminescence (NO_x) of sample gas. Off-gas temperature was measured by shielded thermocouples. The measured data for differential pressure, off-gas temperature, and off-gas composition were recorded continuously.

Figure 8 shows the measured off-gas composition (H_2, O_2, CO_2), off-gas temperature, and power-on signal at point A. There are significant O_2 peaks during the second power-on period. This O_2 peaks are due to flushing the analysis piping and filters with compressed air. **Figure 9** presents the NO_x concentration measured at point A. There are NO_x peaks correlated to the power-on signal. Every time power-on starting is correlated to a NO_x peak. While melting there is also NO_x measured. The amount of NO_x while melting is significant lower then while starting power-on. **Figure 10** shows the measured off-gas composition (CO, CO_2, NO_x), off-gas temperature, and power-on signal at point B. The amount of CO is clearly lower as at point A. There are post combustion zones downstream point A. The measured CO_2 and NO_x concentration is lower than at point A because of infiltrated air (e.g. at the gap). The measured off-gas temperature reaches 500 °C at point B. **Figure 11** presents the NO_x mass flow rate at point A and point B. Additionally there is the carbon mass flow rate shown. This carbon mass flow rate has been used calculating the volume flow rate at point A. The given carbon mass flow rate is correlated to the CO_2 mass flow rate at point B. This strategy allows calculating the NO_x mass flow rate at point A. The NO_x mass flow rate at point A is lower than at point B. This is due to a NO_x source downstream of point A. It clarifies that NO_x reduction measures will have different potential due to the location in the primary dedusting system.

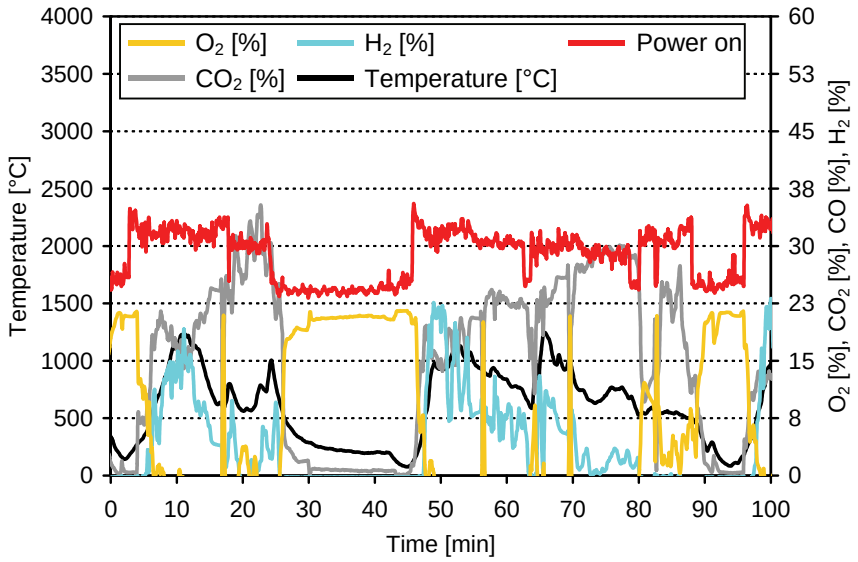

Figure 8: Measured off-gas composition (O_2, CO_2, H_2) and off-gas temperature at point A

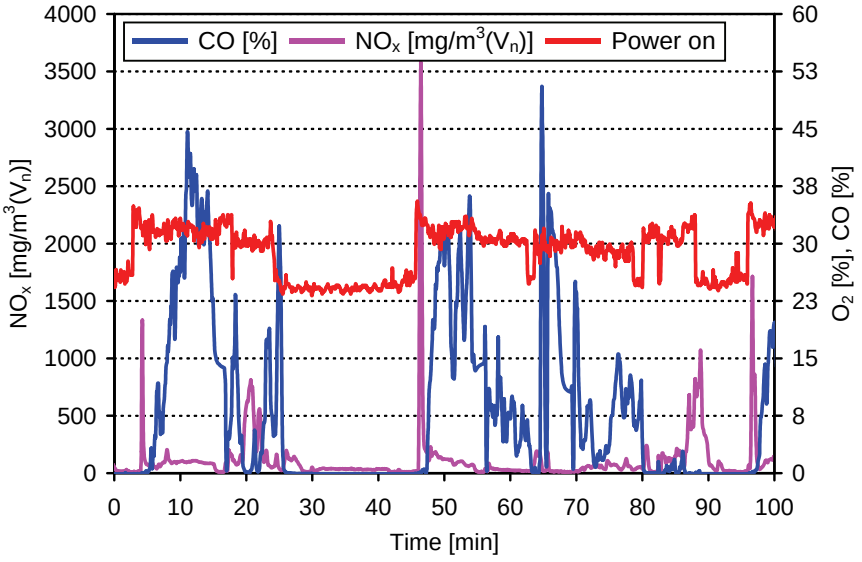

Figure 9: Measured off-gas composition (CO, NO_x) at point A

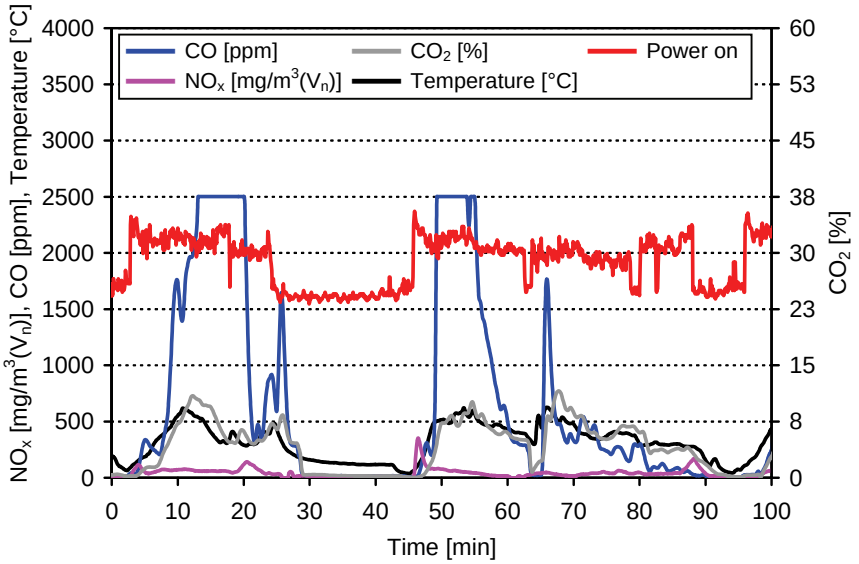

Figure 10: Measured off-gas composition (CO, CO_2, NO_x) and off-gas temperature at point B

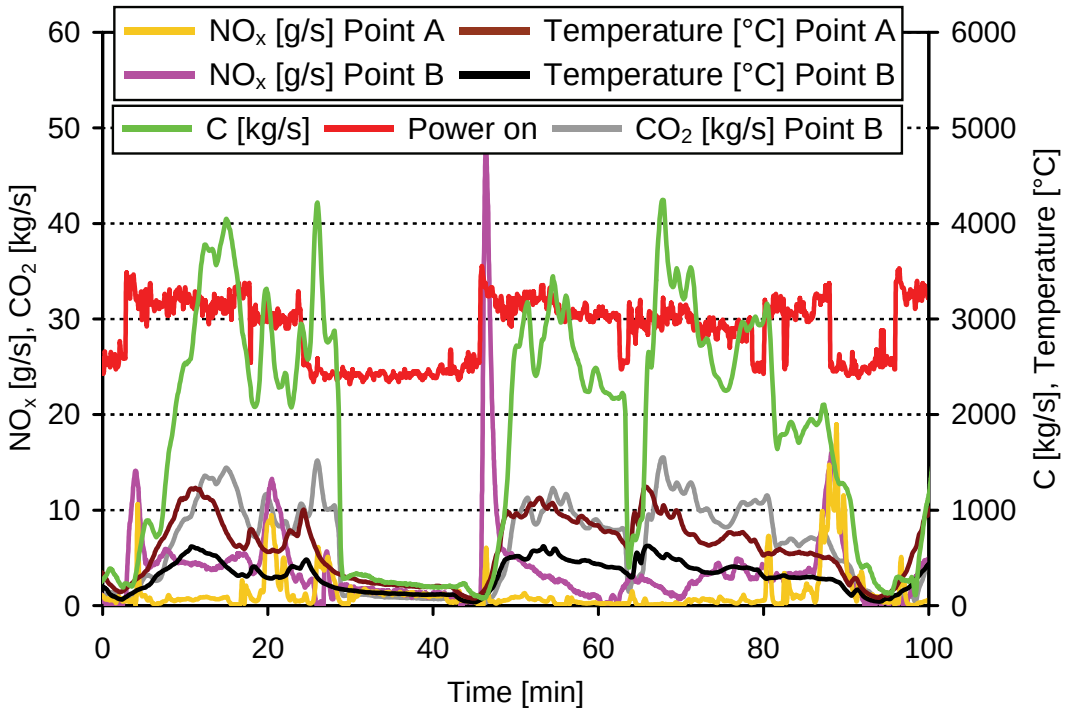

Figure 11: Measured NO_x mass flow rate at point A and point B, carbon mass flow rate, CO_2 mass flow rates, and off-gas temperature at point A and point B

Table 4 gives the average NO_x and CO_x emission rates at point A and at point B. The average NO_x mass flow rate at point A is 0.49 g/s and 0.78 g/s (point B). This average value provides the actual NO_x emission at EAF at DEWG.

Table 4: Average NO_x and CO_x emission at point A and point B at DEWG

	POINT A	POINT B
NO_x	0.49 [g/s]	0.78 [g/s]
CO	131 [g/(m^3(STP))]	900 [mg/m^3(STP)]
CO_2	856 [g/s]	1214 [g/s]

2.3.1.2 Initial off-gas measurements at ORI Martin and determination of NO_x emission with current operation parameters

The objective of this task has been to perform a first series of NO_x measurements at the ORI Martin Consteel plant. Such measurements have been performed during standard Consteel operations, in order to set a reference level of emissions. Before describing the obtained results, a short description of the Consteel plant is given here below.

Main characteristics of ORI Martin Consteel furnace

The plant is equipped with a melting unit composed by an AC electric furnace (Tagliaferri), with a Consteel® system for the continuous feeding and preheating of metallic charge.

Main plant characteristics:

Furnace type	AC/EBT
Shell diameter	5400 mm
Tapping capacity	75 ton
Liquid heel	40 ton
Total furnace capacity	115 ton
Operating power supply	35 MW
Minimum tap to tap time	52 min
Preheating tunnel length	8500 mm
Preheating tunnel width	2245 mm
Preheating tunnel height	3000 mm

The main Consteel operational features are the following:

a) Scrap addition is carried out by a conveyor system;

b) Oxygen injection by a supersonic wall mounted lance; the lance has a capacity of 2000-4700 m^3/h (STP);

c) Carbon addition is made by the Conveyor as pig iron and lump coal and by a wall mounted lance as pulverised coal. The Conveyor allows to feed the pig iron and coal (usually with size between 3 and 12 mm). Both these species are regularly distributed with the charge during the heat duration. The amount of pulverised coal injected by the wall mounted lance is of 1-1.5 kg/t (see **Figure 12** and **Figure 13**).

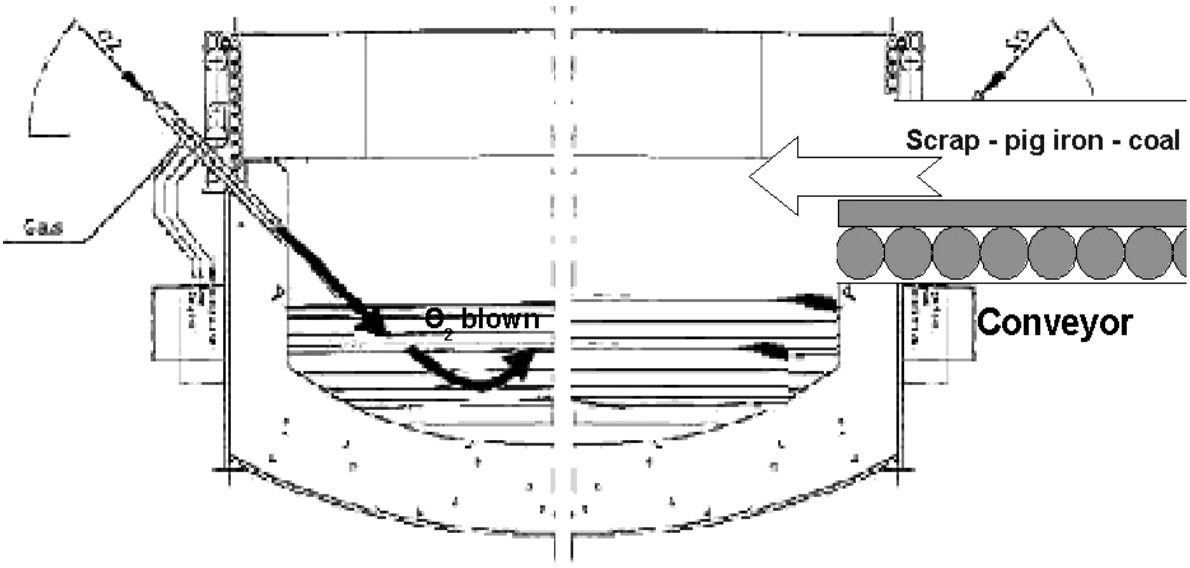

Figure 12: ORI Martin EAF - Schematic drawing of the arrangement for heats in airtight conditions (the additional lance for pulverised coal is not shown)

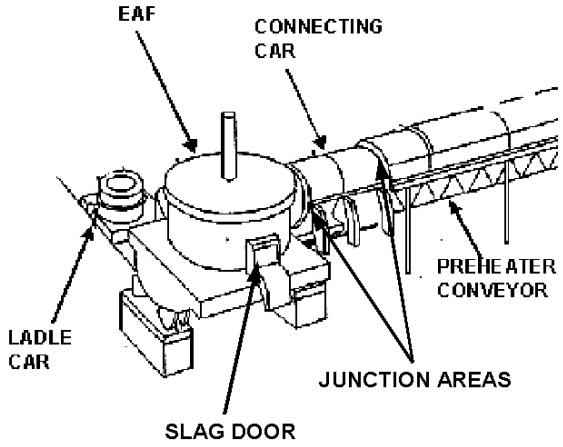

Figure 13: ORI Martin EAF, schematic drawing of the furnace plus a part of the tunnel of the Conveyor system

Definition of reference condition of NO_x emissions

The values of NO_x in the off-gas are a consequence of the plant configuration engineering solutions and of the process conditions applied during the heats. Improvements on plant configuration (reducing uncontrolled air entrance, more controlled electrode operations, reduction of time for charging and tapping operation, etc.) can reduce global NO_x emissions. Several improved conditions have been adopted in ORI Martin in the last years.

The first preliminary step in the present project has been to identify the best plant configuration, permitting to have the minimum of NO_x emission, on the basis of historical records of NO_x measurements. This situation is the adopted reference condition, starting from which to study process conditions permitting further NO_x emissions.

The average values of NO_x concentrations, in current operations, recorded during 2006 were compared with average values recorded in the year 2000 (**Figure 14**). The average distribution of NO_x concentrations shows a decrease of emission levels, and NO_x emissions above 100 mg/m^3 (STP) disappeared. This is due to improvement in the EAF-Consteel management practices.

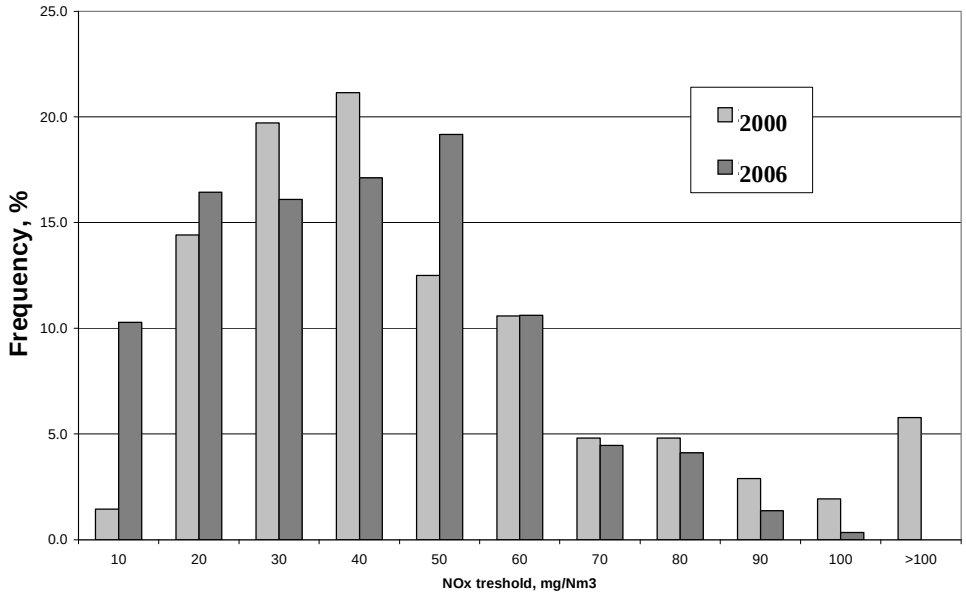

Figure 14: Comparison of NO_x emission of the year 2006 with the ones of year 2000

Preliminary measurements

NO_x composition from EAF Consteel® plant was measured at the tunnel, during standard operating conditions. **Figure 15** reports a scheme of the Consteel plant with the position of the measuring probe.

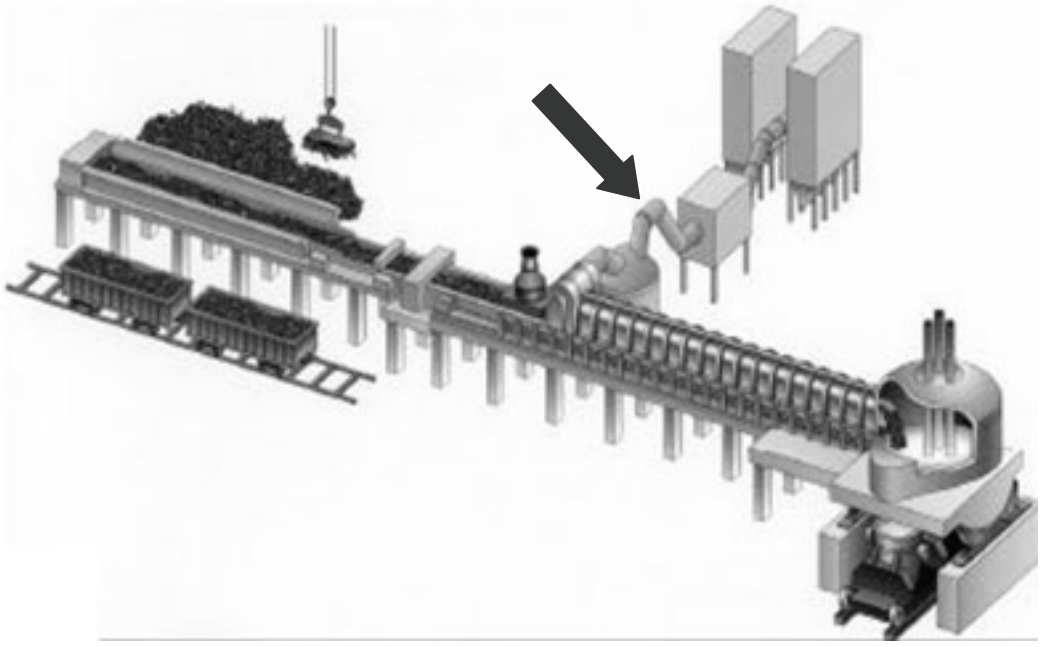

Figure 15: Scheme of the Consteel plant with the indication of the measuring point

In addition to NO_x the following parameters were also acquired:

a) CO, CO_2, O_2 concentrations

b) Gas flow rate

c) Gas temperature

Gas composition was measured by means of a dedicated gas sensor, gas flow rate was measured by single point pitot tube and temperature was measured by coated thermocouple. CO, NO_x and O_2 are detected by means of electrochemical sensors, while CO_2 is detected by IR sensor. The gas acquisition unit is equipped by a coarse filter, a cooling unit, a fine filter and then the gas analyser. **Figure 16** shows an example of measurement NO_x, CO and temperature in current operations.

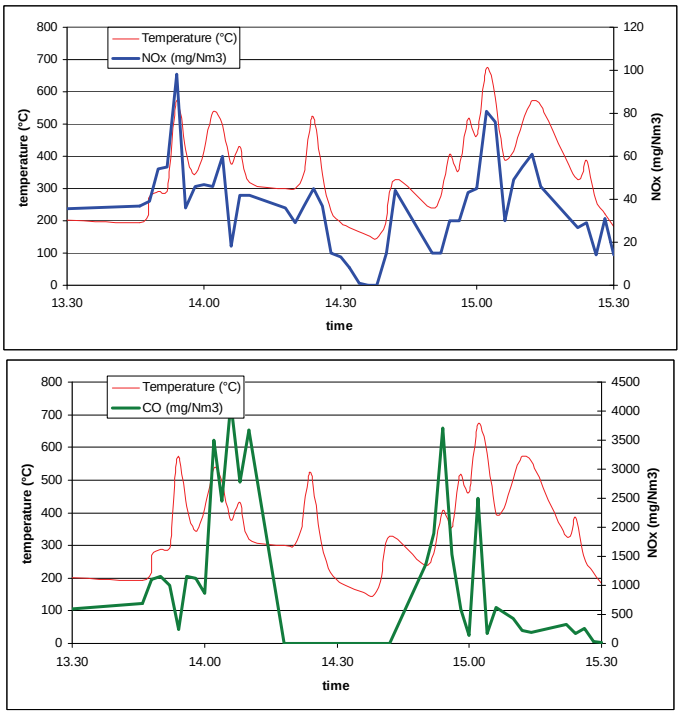

Figure 16: Example of measurements of NO_x, CO and gas temperature during standard Consteel operations

NO_x measurements in standard conditions revealed the following characteristics path of emission:

- Presence of large peak at the beginning of the heat
- Decreasing of NO_x emission during the heat
- Increasing of emission at the end of the heat

Measured peaks generally correspond to a sudden modification of operating conditions (electrode position, high level of post-combustion in the tunnel, etc.). The presence of these large peaks, especially at beginning and end of heat is also affected by the slag foaming behaviour. The average emission is about 30 mg/m^3 (STP), which corresponds to 0.01kg/t/h.

As expected CO vs. NO_x are inversely proportional, even if a large spreading of measured values occurs (cf. **Figure 17**).

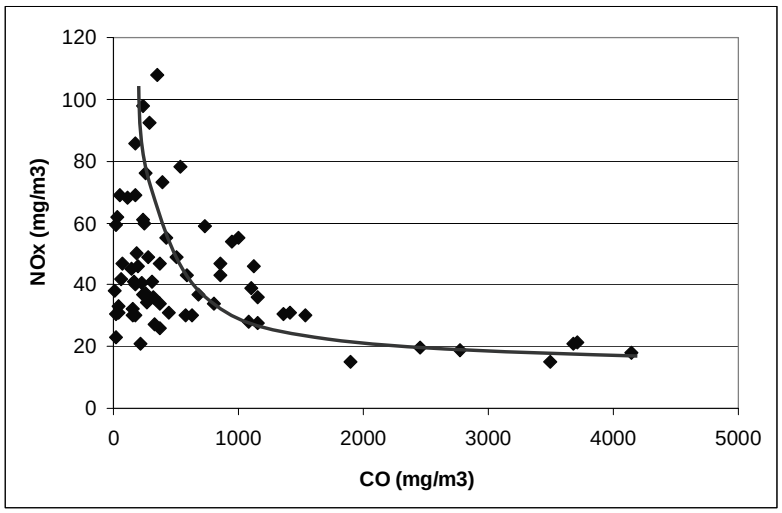

Figure 17: NO_x emission vs CO concentration. Both gases are measured at the tunnel downstream

2.3.1.3 Initial off-gas measurements at RIVA Verona and determination of NO_x emission with current operation parameters

Within the project off-gas measurements were performed at the primary dedusting system of the AC EAF at RIVA. **Figure 18** shows the layout of the EAF and the position of the measurement points. The EAF is equipped with CoJet burners mounted on the EAF sidewalls and an EBT Burner (**Table 2**). The slag door remains closed during production. The EAF vessel is housed and the doghouse dedusting will collect secondary off-gas and feed it to the filter house.

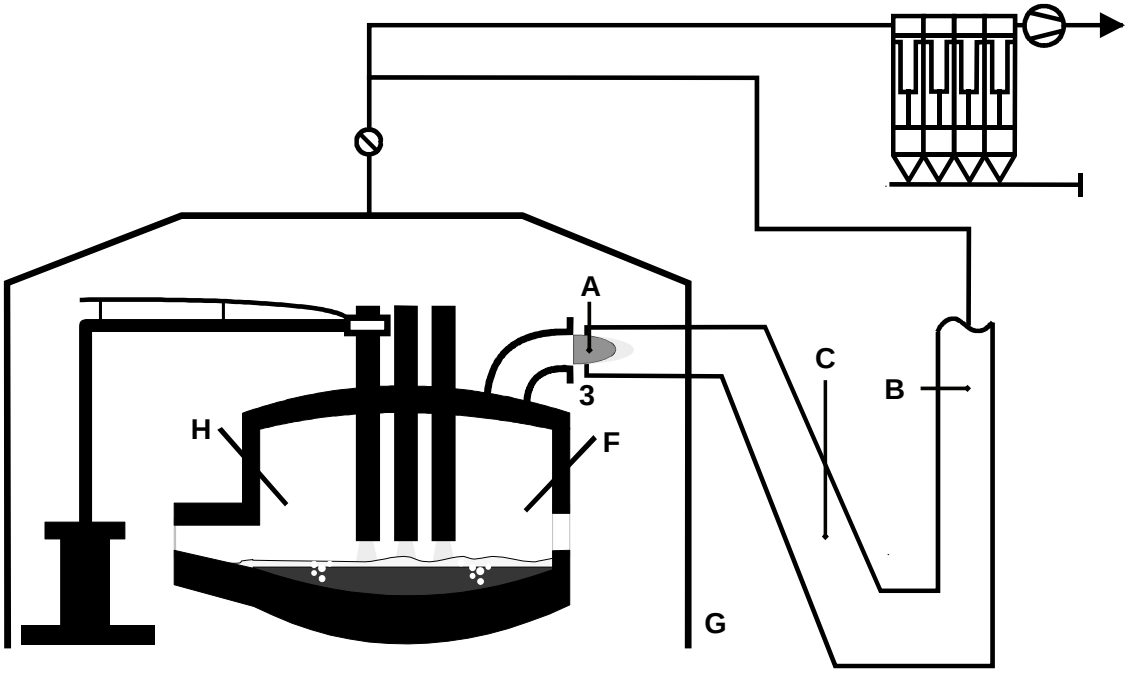

Figure 18: EAF layout at RIVA
A: Measuring point A, B: Measuring point B, C: Measuring point C, G: dog house, F: CoJet, H: EBT burner, 3: gap

Measurement point A is located at the gap between EAF vessel and primary dedusting system. Water-cooled probes for measuring the off-gas temperature and off-gas composition were installed at this measurement point. **Figure 19** shows the water-cooled probe installed directly behind the gap between the roof elbow and primary dedusting system at the midpoint of the movable elbow. This installation position has been chosen to minimize the clogging of the probe and maximize the protection against mechanical problems. It also becomes clear, that the off-gas sampling is carried out directly from the EAF off-gas stream.

At the measurement points B and C, respectively, also probes for measuring the off-gas temperature and off-gas composition were installed. At all measurement points the portable off-gas analysis systems of RWTH were installed (cf. **Table 3**). **Figure 20** shows the layout of the portable off-gas analysis system. The analysis system equipment consists of water-cooled and not cooled probes, filters, flushing box, detectors, and signal converters for measuring the off-gas composition and off-gas temperature. The gas sampling probes are flushed every 30 min with compressed air to prevent a clogging of the gas sampling line. Off-gas temperature is measured by shielded thermocouples. The measured data for off-gas temperature and off-gas composition are recorded continuously.

In the different measurement campaigns conducted the off-gas was measured at point A and B or point A and C simultaneously. Therefore the NO_x generated in the EAF vessel can be distinguished from the NO_x generated or reburned within the post combustion zone downstream.

In the course of the project the water-cooled off-gas sampling probe for measurement point A has also been slightly modified. From 2006 to 2008 the opening value of the probe has been enlarged from 12 mm to 15 mm. This led to an increased resistance of the probe against clogging.

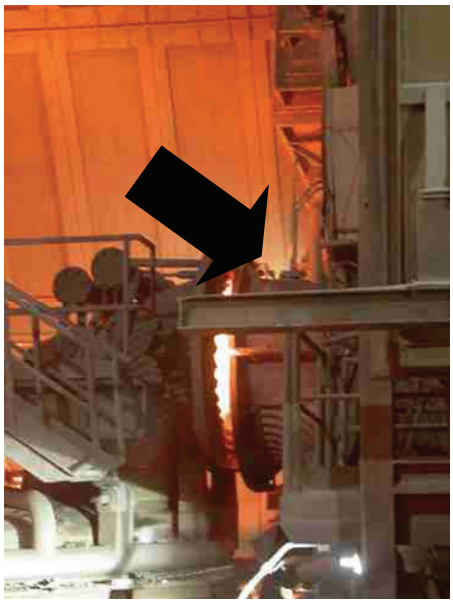

Figure 19: Location of the sampling probes at point A (composition and temperature) in the movable elbow near the EAF

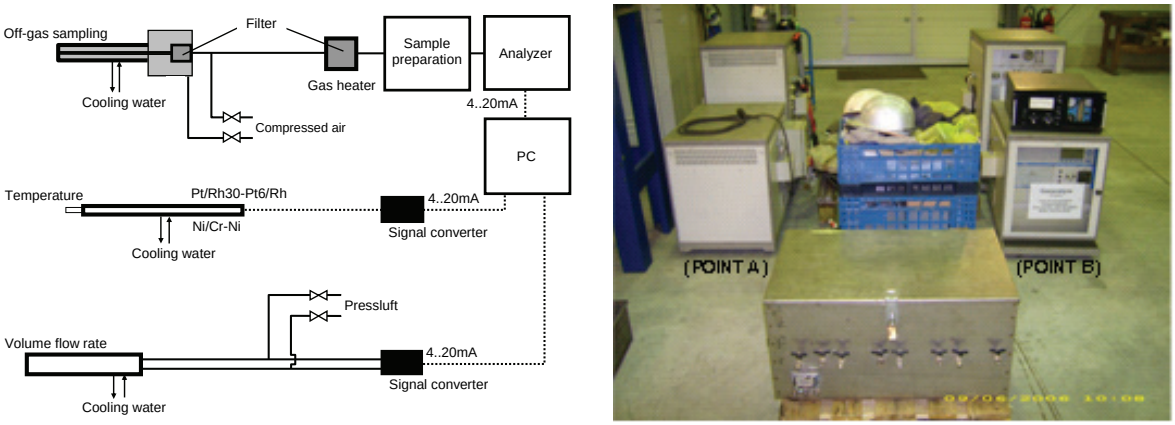

Figure 20: Layout of analysis system RWTH (left), RWTH off-gas measurement equipment (point A and point B) (right)

Figure 21 shows the measured off-gas composition and off-gas temperature at point A and **Figure 22** shows the off-gas composition, the off-gas temperature and power-on signal measured at point B. **Figure 23** shows the correspondent EAF operating data (oxygen injected by burners and CoJets and natural gas used). At the beginning of power-on times there are significant NO_x peaks. They are due to arc ignition in an O_2 and N_2 rich EAF atmosphere. Additionally there is a wide NO_x peak after shutting off the burner and CoJets. This is because the slag door is opened simultaneously and that causes a

change of the EAF atmosphere. It changes from reducing (CO rich) to an O_2 rich atmosphere. The correlation of this complex EAF operating practice and the measured NO_x emission have been investigated in WP 4. The average NO_x and CO_x emissions measured are given in **Table 5**. The average emissions measured are 0.54 g/s for NO_x and 396 g/s for CO_2. **Figure 24** shows the measured NO_x emission per charge at RIVA (right) and given values from literature. The NO_x emission measured is in the range of 0.005 kg/t up to 0.06 kg/t. The mean NO_x emission is clearly in the range of actual data given in literature.

Table 5: Average NO_x and CO_x emission at point B

	POINT B
NO_x	0.56 [g/s]
CO	323 [mg/m^3(STP)]
CO_2	396 [g/s]

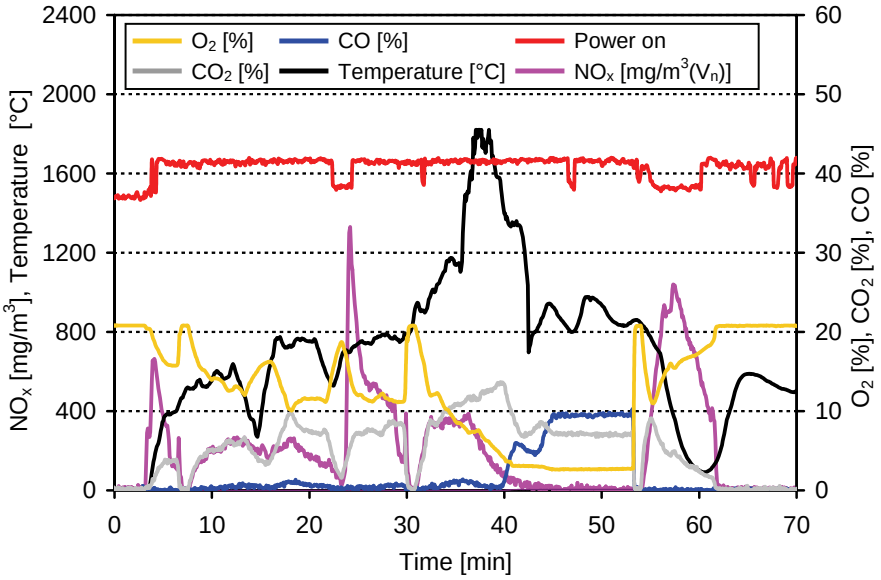

Figure 21: Measured off-gas composition and off-gas temperature at point A at RIVA

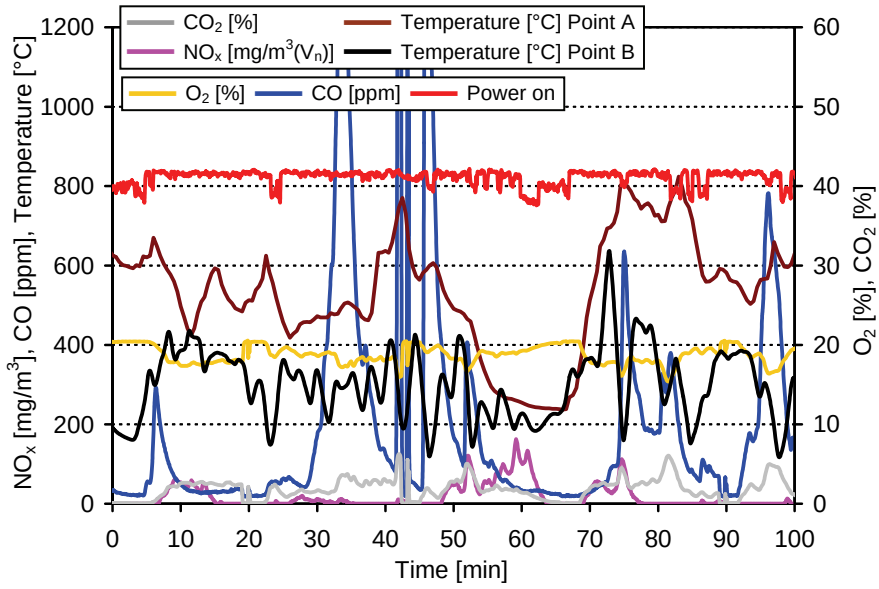

Figure 22: Measured off-gas composition at point B and temperatures at RIVA

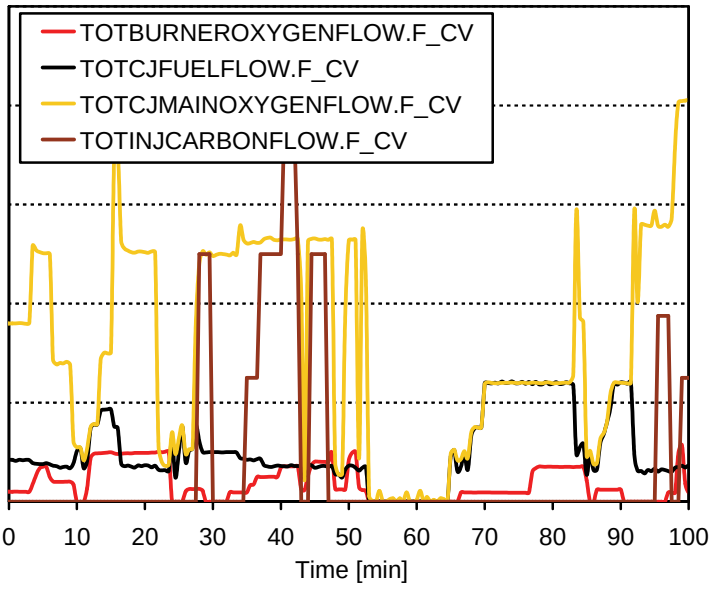

Figure 23: EAF operation data (gas burner, CoJet burner) at RIVA

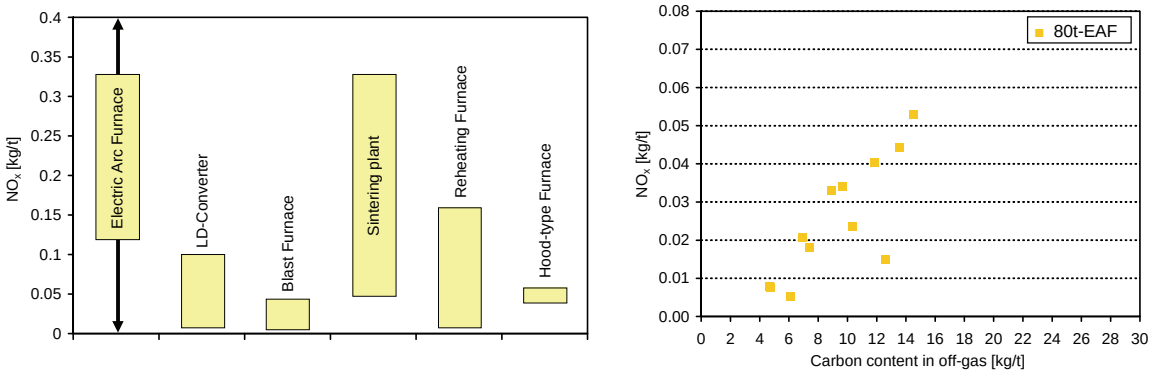

Figure 24: NO_x emission (left), measured NO_x emission (right)

2.3.2 Study of NO_x generation from combustion reactions in EAF

This part covers tasks 2.1 “definition of initial model and determination of model parameters”, task 2.3 “experiments with varying oxygen/methane/carbon ratios”, task 2.6 “Model tuning with result from pilot plant trials (CSM)” and task 2.7 “Adaptation of model parameters to results from initial measurements at industrial EAF (CSM)”. Tasks 2.4 and 2.5 have been re-defined with the coordinator. This part of experimental activity to be carried out on the pilot plant has been replaced by new tests to define the effect of gas temperature on the formation of NO_x.

The study of NO_x generation from combustion reaction inside the EAF has been carried out according to the following steps:

a) Model definition,

b) Experimentation at CSM EAF pilot plant to tune the model,

c) Model refining and validation through measurements at industrial plant.

Model definition

The objective of the model is to estimate and quantify the effect of EAF process parameters (i.e. oxygen flow rate, fuel gas, injected solid carbon, pig iron amount, air tightness of the furnace) on NO_x emission. Due to the complexity of the mechanisms of NO_x formation inside the electric arc furnace (simultaneous presence of electric arc, combustion reactions, variable amount of reducing agents as CO and H_2/H_2O and pulverised coal, presence of foamy slag which can shield the electric arc) a semi empirical formulation of the model has been identified as the most suitable.

According to the available literature [9],[16] about the formation of NO_x in combustion flames, three distinct mechanisms contribute to NO_x formation:

a) Thermal

b) Fuel

c) Prompt

The same formation mechanisms have been assumed to act inside the EAF.

The thermal mechanism of formation (also known as Zeldovich mechanism), is a direct consequence of the thermal reactions occurring inside the furnace: the radiation from electric arc, the carbon oxidation forming CO and the post combustion reaction oxidizing CO to CO_2.

According to this mechanism, NO_x (expressed for example as NO) is formed through the reaction:

$$N_2 + O_2 \leftrightarrow 2\,NO \tag{9}$$

Which can be considered as the summation of the following steps [16]:

$$O + N_2 \rightarrow NO + N \tag{10}$$

$$N + O_2 \rightarrow NO + O \tag{11}$$

In this simplified model, the global reaction of formation has been considered, to avoid the presence of too many parameters to be tuned.

The fuel mechanism is the oxidation reaction of nitrogen contained inside coal. The mechanism is not fully understood; in literature it is represented by the following scheme:

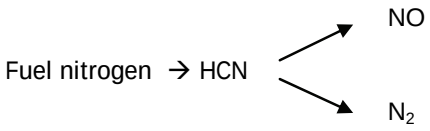

(12)

In literature different equation to express the rate of fuel NO_x formation are available; in any case the rate of formation is proportional to the nitrogen concentration in the fuel.

The prompt mechanism is related to the formation of radical species (CH), which quickly react with nitrogen in the combustion air to form transition substances which in turn oxidize to NO_x when they react with oxygen. The formation involves a complex series of reactions and many possible intermediate species. A typical reaction path is the following.

$$CH + N_2 \rightarrow HCN + N \tag{13}$$

$$N + O_2 \rightarrow NO + O \tag{14}$$

$$HCN + OH \rightarrow CN + H_2O \tag{15}$$

$$CN + O_2 \rightarrow NO + CO \tag{16}$$

The rate of NO_x formation is proportional to the concentration of radical species (CH) in the gaseous phase. As an approximation, in the model the rate of prompt NO_x formation has been considered proportional to the hydrogen content of coal.

Prompt and fuel mechanisms occur mainly in the electric arc, where coal degradation is promoted by arc energy and only partially in EAF atmosphere, due to reaction of oxygen with carbon before dissolution in the steel bath (**Figure 25**).

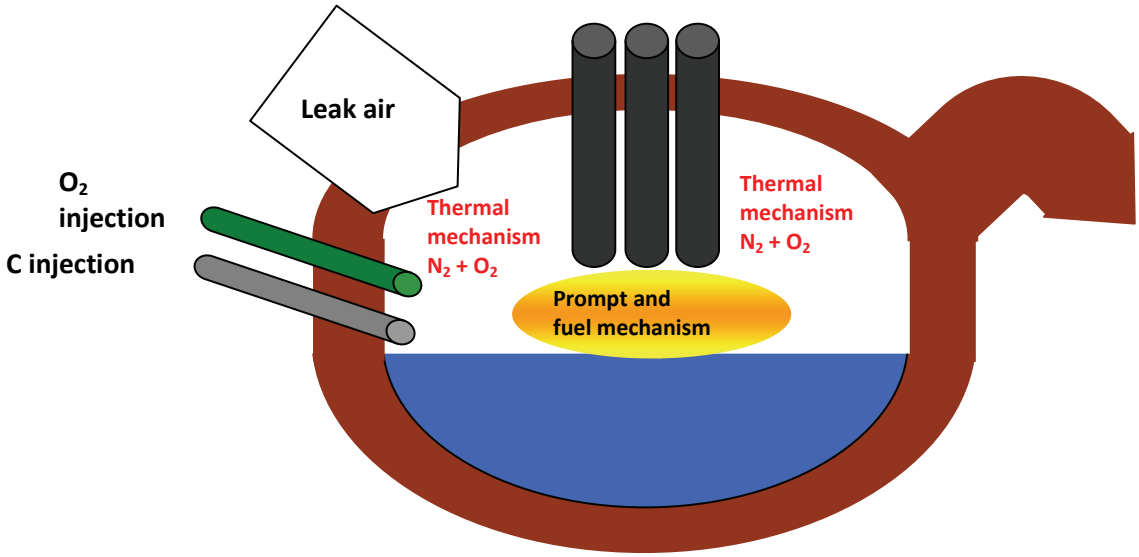

Figure 25: Scheme of formation of NO_x inside the electrical furnace used for the semi empirical model

On the basis of this hypothesis, NO_x formation can be expressed with the following relationship:

$$dNO_x/dt = \text{thermal}(C_{pulv} + O_2) + \text{fuel} + \text{prompt} + \text{electric arc} \quad (17)$$

The mathematical formulation of these processes is a simplified expression taken from the classical mechanisms available in literature for NO_x formation in combustion flames [9],[16], and is the following:

$$dNO_x/d\,t = k_1[N_2][O_2]_{EAF} + k_2[N]_{coal} + k_3[H]_{coal} + f(arc) \quad [mol/s] \quad (18)$$

where:

$k_{i,}$	[mol/s]	kinetic constants, calculated by model calibration with plant measurements
$[N_2]$	[%]	nitrogen concentration in the EAF atmosphere
$[O_2]_{EAF}$	[%]	oxygen concentration in the EAF atmosphere
$[N]_{coal}$	[%]	nitrogen content in the coal
$[H]_{coal}$	[%]	hydrogen content in the coal
f(arc)	[mol/s]	formation of NO_x due to the electric arc

f(arc) is a function describing the formation of NO_x due to the specific effect of the electric arc, which is able to promote the formation of NO_x, forming the radicals species N and O. This situation occurs especially at the beginning of the heat, or in case of Consteel operations, each time the furnace is opened, for example to charge an extra basket. An example of this emission pattern is visible in **Figure 16**. In case of Consteel regular operations, this large peak does not affect significantly the global NO_x emission, and for this reason the term f(arc) has been neglected in the model development.

The kinetic constants k_1, k_2 and k_3 have been experimentally determined with tests with a pilot EAF furnace, than a model refining was performed with industrial measurements.

Experimentation at pilot plant to tune the model

Experimental activity has been carried out at the experimental pilot EAF. The CSM pilot plant is an electric furnace having the following main characteristics:

maximum working temperature of post-combustor	1200 °C
maximum off gas flow rate of the post-combustor	7000 m^3 (STP)/h
maximum temperature of off gas of the post-combustor	130 °C
Transformer power	1.9 MVA

Maximum current intensity	6 kA
Maximum active power	1.5 MW
Inner shell diameter	900 mm
Electrode diameter	250 mm
Charged scarp	~600 kg

Figure 26 reports a general view of the furnace with a detail of the gas sampling point on the top of the furnace.

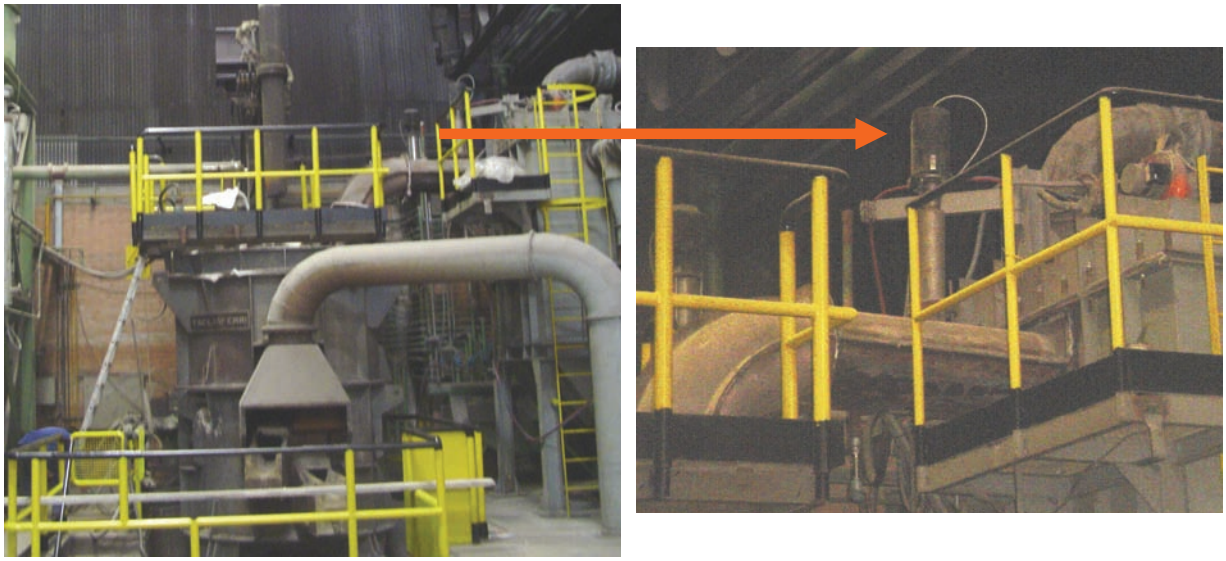

General view of the furnace *Gas sampling point of the top of furnace*

Figure 26: General view of the electric pilot furnace with a magnification of the gas sampling point

NO_x and other gaseous species (CO, CO_2, O_2) are sampled after the furnace. Gases are conditioned and analysed with standard IR sensors.

About 600 kg of scrap have been charged into the furnace and melted by electric arc. Coal and O_2 have been injected after complete scrap melting and bath temperature stabilization (1570°C).

Coal injection and electric power have been varied in order to see the effect on NO_x emission. Coal injection has been varied also to modify the temperature of the fumes to evaluate the variation of the kinetic constants of NO_x formation with temperature.

Two series of tests have been performed to calculate first the kinetic constants and then the dependency on temperature.

A first set of five tests have been carried out to calculate the values of kinetic constants at fumes temperature of 1500°C (±20°C). In these tests different amounts of chemical energy (provided as pulverised coal injection and oxygen) have been used.

To evaluate the effect of leak air, two different fumes aspiration have been used during tests: 5000 and 7000 m^3 (STP)/h. Chemical energy is provided by coal combustion forming CO and CO_2. From preliminary calculation performed in another RFCS project [17] it has been assumed that 40% of CO and 60% of CO_2 are formed in the EAF atmosphere and 15% of pulverised coal is lost in fumes and does not contribute to chemical energy supply.

In a second set of tests, electric power has been maintained constant and increasing amount of coal and oxygen have been injected, to increase fumes temperature. Fumes aspiration was maintained constant at 5000 m^3 (STP)/h. **Table 6** and **Table 7** report the experimental conditions of both sets of tests.

Table 6: Experimental conditions of the first set of tests at pilot plant

test	% chemical energy	coal kg/h	O_2 m^3 (STP)/h
CE00	0	0	0
CE10	10	12	21
CE20	20	23	41
CE30	30	35	62
CE40	40	47	82

Table 7: Experimental conditions of second set of tests at pilot plant

test code	scrap charged (kg)	C flow rate (kg/h)	O_2 flow rate (m^3 (STP)/h)	T gas (°C)	power (MW)
1A	600	15	28	1500	0.7
2A	600	20	37	1600	0.7
3A	600	22	40	1640	0.7
1B	600	15	28	1560	0.9
2B	600	20	37	1670	0.9
3B	600	22	40	1700	0.9

Results

Figure 27 and **Figure 28** report the results obtained for the first set of tests. **Figure 27** reports the NO_x emission before injection of coal and oxygen, which has been taken as reference level of emission; **Figure 28** shows the effect of chemical energy and fumes aspiration on NO_x gas concentration.

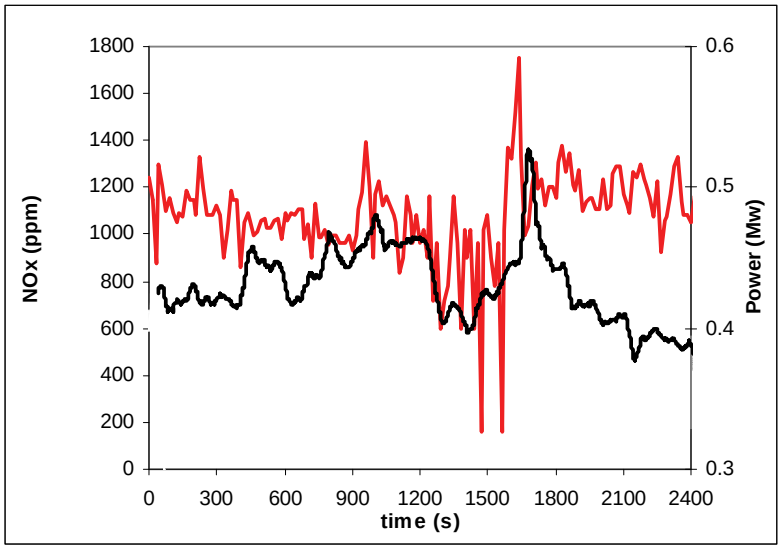

Figure 27: NO_x concentration in off gas of pilot plant tests before injecting coal and oxygen

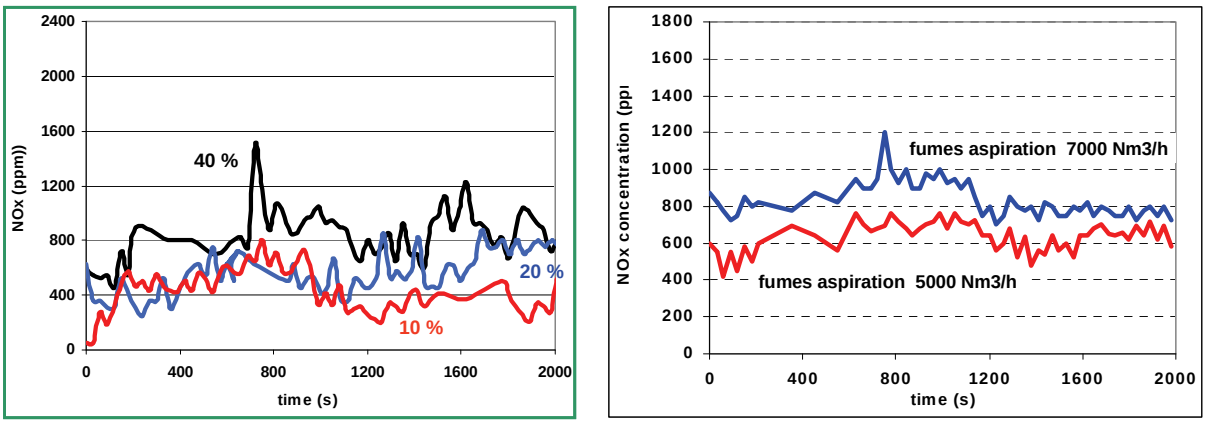

Figure 28: NO_x concentrations with different percentages of chemical energy (left) and with different values of fumes aspiration (right)

The following **Figure 29** reports two examples of NO_x measurements during the second set of tests: the continuous line is the measurements and the dots represent the model application to calculate the variation of the kinetic constants with temperature.

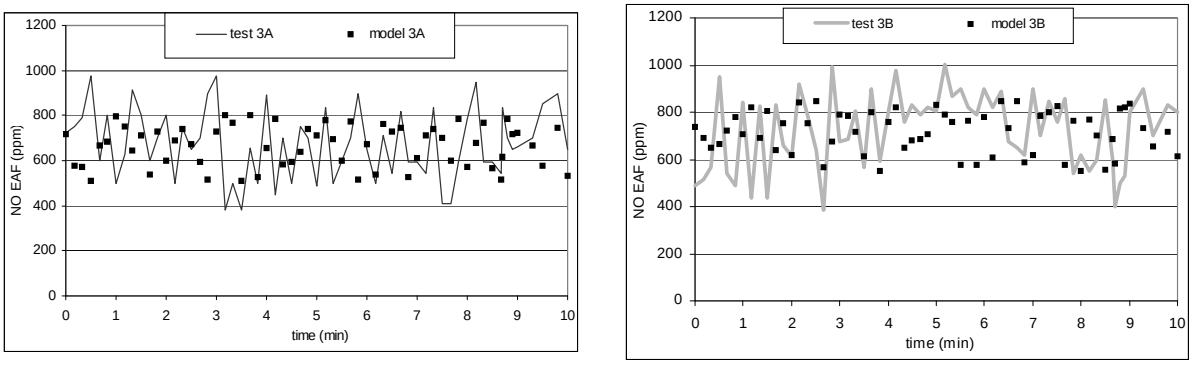

Figure 29: Measurement and model application in two experimental conditions (see table above) to calculate the variation of kinetic constants with temperature

The main results of the experimental tests can be summarised as follows:

- The average emission of NO_x, before injecting coal and oxygen is 800 ppm
- A sudden variation of arc current produces strong peaks in NO_x emission, similarly to what happens in the real furnace;
- Higher fumes aspiration increases significantly NO_x concentration in off gas, which confirms that the presence of leak air has a predominant effect on NO_x formation
- 10 and 20 % of chemical energy gives similar amounts of NO_x concentration

The concentrations of oxygen and nitrogen in the EAF atmosphere which are included in equation (17) are derived from mass balances calculated combining plant measurements and input data (scrap and pig iron charge, oxygen injected, lump and pulverised coal injected and off gas flow rate) of the monitored heats. From these calculations the values of the constant k_1 and k_2 have been determined. These tests permitted to calculate the value of the kinetic constants as a function of temperature.

Table 8 reports the values of the kinetic constants found in the gas temperature range 1500° - 1700°C. Being the contribution of the constants k_3 very small, its value has been assumed constant in this temperature range.

Table 8: Kinetic constants found in the temperature range 1500° - 1700°C. Values of the constant k_3 has been assumed constant in this temperature range

	1500 °C	**1560°C**	**1600°C**	**1640°C**	**1670°C**	**1700°C**
k_1 [mol/s]	0.0023	0.0035	0.0041	0.0052	0.0062	0.0072
k_2 [mol/s]	0.0006	0.0006	0.0006	0.0006	0.0006	0.0006
k_3 [mol/s]	0.0006	0.0006	0.0006	0.0006	0.0006	0.0006

Model refining and validation through measurements at industrial plant

After the calibration with pilot plant tests to determine the values of kinetic constants k_1 and k_2 (see equation (18) in previous paragraph) a model refining has been performed using plant measurements. The available industrial data of NO_x, CO, CO_2, N_2 and mass flow rate of off gas permitted to calculate from mass balances the amount of O_2 and N_2 in the furnace atmosphere and to calculate the constants k_1 and k_2. The values of the numerical constants k_2 and k_3, determining the reaction rate according to the mechanism of fuel and prompt NO_x (see previous paragraph for explanation of mechanisms) have assumed the same of the pilot furnace. According to literature, the contribution of these mechanisms to NO_x formation is smaller respect thermal mechanism.

Figure 30 and **Figure 31** report the result of model calibration with industrial data.

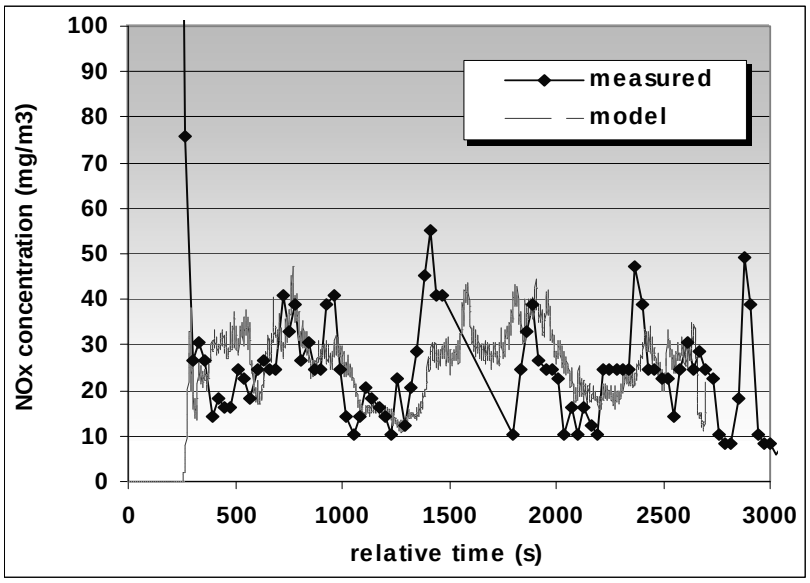

Figure 30: Example of model calibration with industrial measurement

Once the model has been calibrated, a comparison of model calculation with industrial measurements has been carried out.

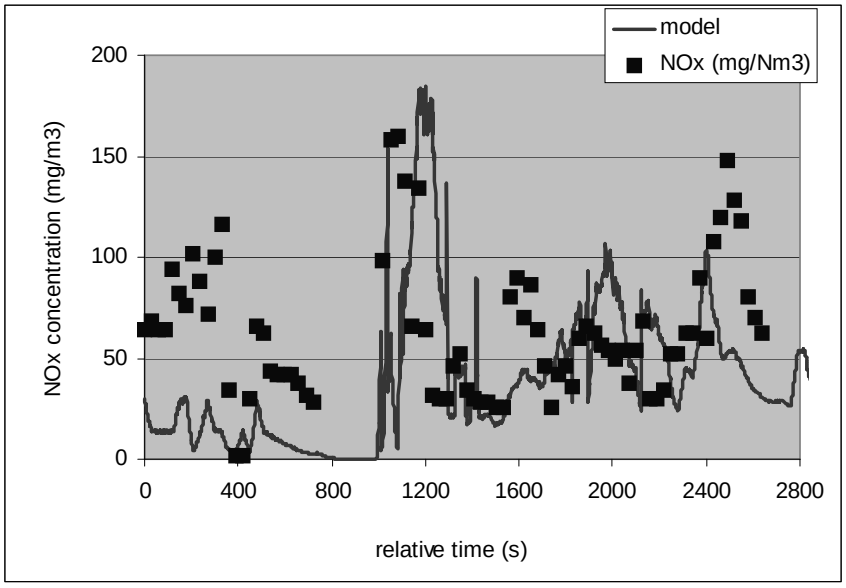

Figure 31: Comparison of measured and calculated values of NO_x concentration

The comparison between measured and calculated values shows that the model is able to simulate the NO_x emission. **Table 9** reports the comparison for three heats of measured and calculated values.

Table 9: Comparison of measured and calculated values of NO_x concentration

heat	measured NO_x (mg/m^3)	calculated NO_x (mg/m^3)	delta %
2081	27	26	4
2084	27	31	15
2085	35	40	13

According to the calculations, the model is able to reproduce the average value of NO_x emissions with a relative error respect measurement of maximum 15%. The model is not able to reproduce the strong peak which may be present at the beginning of the heat for furnace opening (as in case of **Figure 31**).

2.3.3 Study of NO_x formation from EAF plasma reactions

2.3.3.1 Preparation of pilot furnace

RWTH Aachen operates a closed 600 kW pilot arc furnace which can be operated in AC as well as in DC mode. The furnace is equipped with hollow-bored graphite electrodes (ø100 mm, hole ø15 mm) and for DC operation, which was used for this project, with a bottom electrode. The graphite electrode is connected to the water-cooled shaft by means of copper nipples. The furnace is sealed air-tight by an inflatable sealing between upper and lower shell of the furnace as well as an inflatable sealing in the lead-through of the electrodes. Arc current can be held constant up to 2000 A, arc length can be varied from 70 to 200 mm. The furnace operates at slight over pressure of about +10 mbar. The pilot tests are carried out with steel melts of 150 kg and, if desired, with additionally up to 20 kg of slag. **Figure 32** shows a schematic of the used pilot furnace.

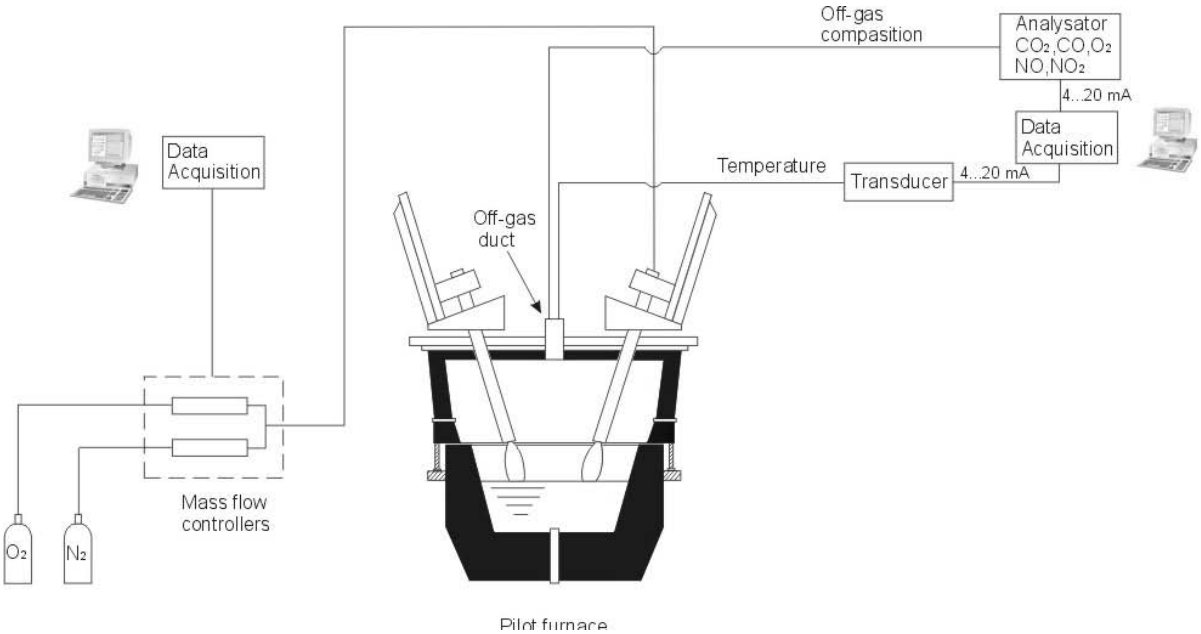

Figure 32: Pilot arc furnace with the gas-supply system and off-gas analyser

The special feature of the pilot furnace is the air-tight operation under very well controlled conditions of the furnace atmosphere by gas injection through the electrodes and/or from the sidewalls. In the course of this project some modifications to the gas-supply system have been made. These changes include the installation of additional mass flow controllers to precisely control the flow rate and composition of the gas injected into the furnace (**Figure 33**). The gas-supply system has been extended successfully up to 7 mass flow controllers which now in two groups control the gas injected through the electrodes and gas injected by a ring line in the sidewall of the furnace.

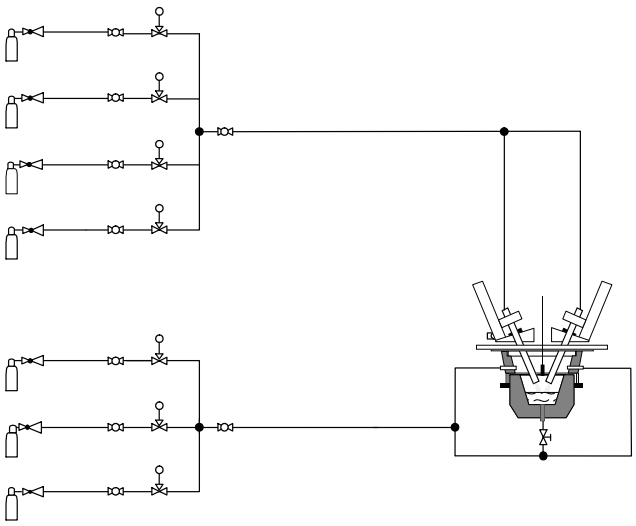

Figure 33: Pilot arc furnace with the gas-supply system (7 mass flow controllers)

The furnace also has been equipped with an off-gas analyser continuously measuring O_2, CO, CO_2 and NO_x. The furnace off-gas is analysed by means of infrared absorption spectrometry (CO, CO_2), paramagnetic method (O_2) and chemiluminescence method (NO_x). **Table 10** shows specific technical data for each of the analyser. The analysers have been calibrated with test gases in periods according to the specifications of the manufacturer. The off-gas is sampled at the off-gas duct of the furnace where also the off-gas temperature is measured by a thermocouple.

Table 10: Technical data of off-gas analysers used at the pilot plant

Off-gas species	Measurement principle	Range	Accuracy*
CO	IR radiation absorption	0 % - 100 %	± 1 %
CO_2	IR radiation absorption	0 % - 100 %	± 1 %
O_2	O_2 paramagnetism	0 % - 25 %	± 1 %
NO_x / NO	Chemiluminescence	0 - 10000 ppm	± 1 %

* in regard to the upper range value

The preparation of the pilot furnace enclose: (a) Variable gas injection through hollow-bored electrode and ring line in furnace sidewall; (b) Continuous off-gas analysis. Experimental trials about the influence of controlled variation of the pilot furnace atmosphere and simultaneous changes of parameters of the electric arc will lead to a deeper insight into the NO_x formation in the EAF.

2.3.3.2 Determination of NO_x contents in furnace off-gas by variation of process parameters

Within the scope of this task a number of trials have been conducted at the air-tight pilot furnace. The goal of these trials was to determine the NO_x content of the furnace off-gas in relation to varying process parameters. Therefore a number of process parameters like furnace atmosphere and gas flow rates, arc length and current have been varied during the trials.

In a first group of trials the arc was ignited only for short periods of time in an almost cold furnace in predefined furnace atmospheres. The furnace atmosphere has been adjusted by flushing the air-tight furnace for a sufficient time with a mixture and flow rate of gas set by the mass flow controllers. In this way a specific composition of the furnace atmosphere regarding N_2, O_2, CO content etc. could be reached prior to the ignition of the electric arc. After arc ignition the arc length and current have been varied.

In the second group of trials the furnace was operated for a given time till it reached a ‘hot’ steady thermal state. Only after this state was reached the trials were conducted by changing arc length and current and, most important, by changing the furnace atmosphere and flow rates.

For all changes in furnace atmosphere a scavenging time had to be maintained which was determined for this furnace to be about 15 minutes at a given flow rate in the pretests. The changes in furnace atmosphere conducted above all relate to the O_2 offer in the furnace atmosphere and to the offer of reducing agents like CO. Therefore a number of trials were conducted in which the N_2/O_2 ratio of the furnace atmosphere was changed and also some trials were performed where arc was ignited in a CO rich atmosphere. The flow rate of the gas mixture was also varied to influence the residence time of the gases within the furnace freeboard area.

During all trials the off-gas composition as well as the off-gas temperature was measured and recorded together with the flow rates of the mass flow controllers and the electrical data of the furnace.

The trials accomplished in the first group are shown in **Table 11**. As a result of these trials no significant influence of the electrical process parameters like power, arc current or length on the amount of NO_x produced could be established. Relating to the electrical parameters of the arc alone the amount of NO_x produced by the arc can be seen as constant as long as the arc is ignited. NO_x formation is much more depending on the atmosphere the arc is ignited or burning in. **Figure 34** and **Figure 35** show the results of arc ignition in oxygen depleted atmospheres. Reducing the oxygen content of the atmosphere from 17.8 % to 9.9 % resulted in the reduction of the NO formation from 2000 to about 1000 ppm.

Table 11: Short term trials conducted at pilot plant furnace

Trial	Test conducted	Power
Pretests	Determination of required flushing time subject to flow rate	-
Trial 01	Arc ignition in air	100 – 150 kW
Trial 02	Arc ignition in air	120 kW
Trial 03	Arc ignition in 17.8 % O_2 / 82.2 % N_2	120 kW
Trial 04	Arc ignition in 9.9 % O_2 / 90.1 % N_2	120 kW
Trial 05	Arc ignition in 1 % O_2 / 99 % N_2, Injection of 5 % CO_2	200 – 300 kW
Trial 06	Arc ignition in 1.5 % O_2 / 98.5 % N_2, Injection of 5 % CO_2	200 kW
Trial 07	Arc ignition in air, Injection of N_2	150 kW
Trial 08	Arc ignition in 4.5 % CO_2 / 95.5 % N_2, Increase of CO_2 injection from 5 % to 10 %	100 – 200 kW
Trial 09	Arc ignition in 2 % CO_2 / 98 % N_2	75 – 150 kW
Trial 10	Arc ignition in air, Injection through electrode (50 l/min) and by sidewall ring line (50/150 l/min)	100 – 200 kW

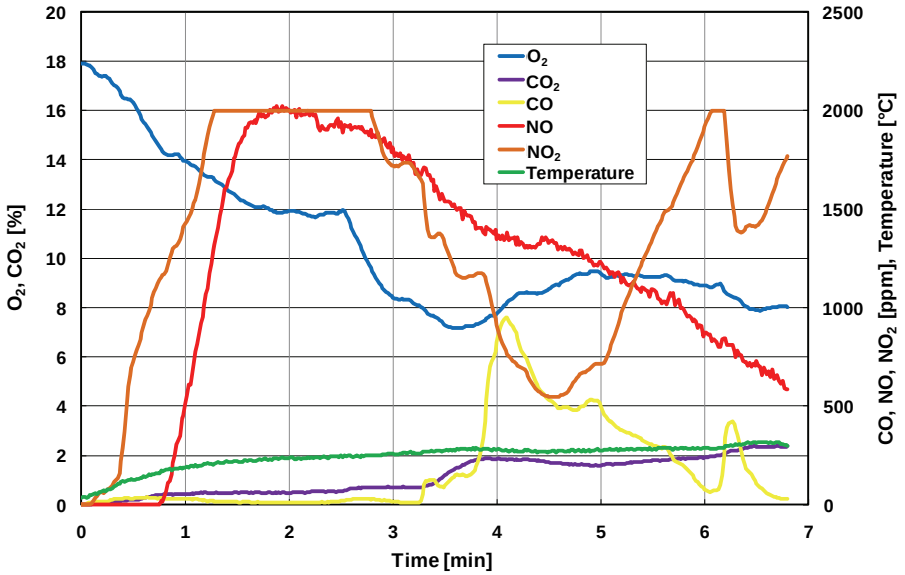

Figure 34: Trial with arc ignition on 17.8 % O_2 and 82.2 % N_2

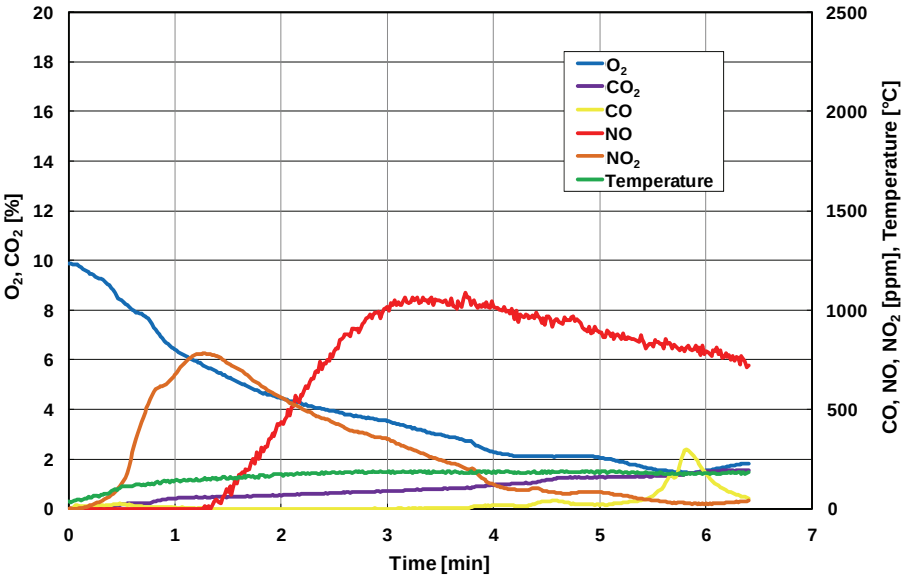

Figure 35: Trial with arc ignition on 9.9 % O_2 and 90.1 % N_2

Figure 36 exemplifies a long time trial during which the O_2 content as well as the total flow rate of the gas flushing the furnace was varied. The flow rate has been varied between 60 and 225 l/min and the O_2 content of the inflow has been varied between 0 and 19.7 %. It can be seen that the NO_x content in the off-gas is indirectly correlated with the flow rate and therefore the residence time within the furnace and also with the O_2 content of the gas. If the flow rate is considerably below 150 l/min the CO content in the off-gas is building up and the NO_x content is falling whereas at flow rates of 150 l/min and beyond there is no CO in the off-gas but NO_x. The existence of NO_x in the off-gas is always in combination with a measurable amount of oxygen which is only given at high flow rates with high oxygen content.

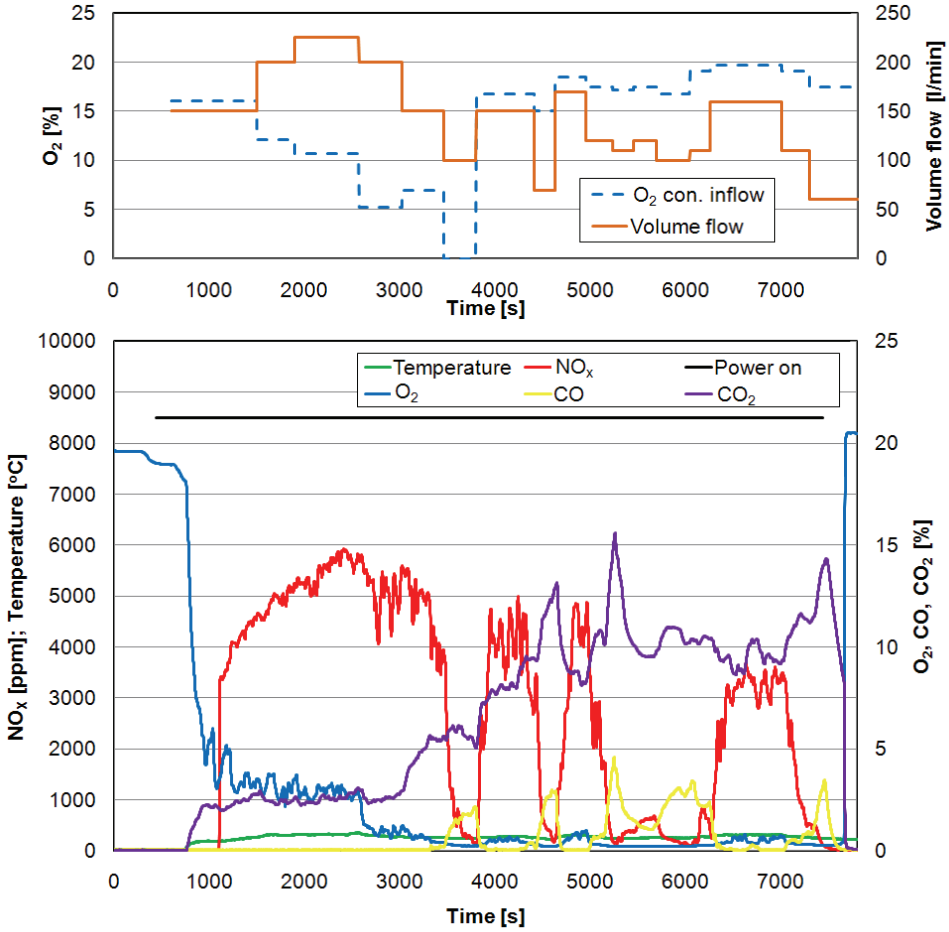

Figure 36: Trial with varying O_2/N_2 ratio and flow rate, volume flow rate and oxygen concentration of the inflow (top), off-gas composition and temperature (bottom)

The influence of reducing species like CO can also be seen in **Figure 37** where exemplary the arc ignition in a CO-rich and an oxygen containing atmosphere is shown. The typical NO_x peak known from measurements in industry can only be seen when igniting the electric arc in an oxygen containing atmosphere. The ignition of the arc in a CO-rich and O_2-free atmosphere shows no measurable NO_x in the off-gas.

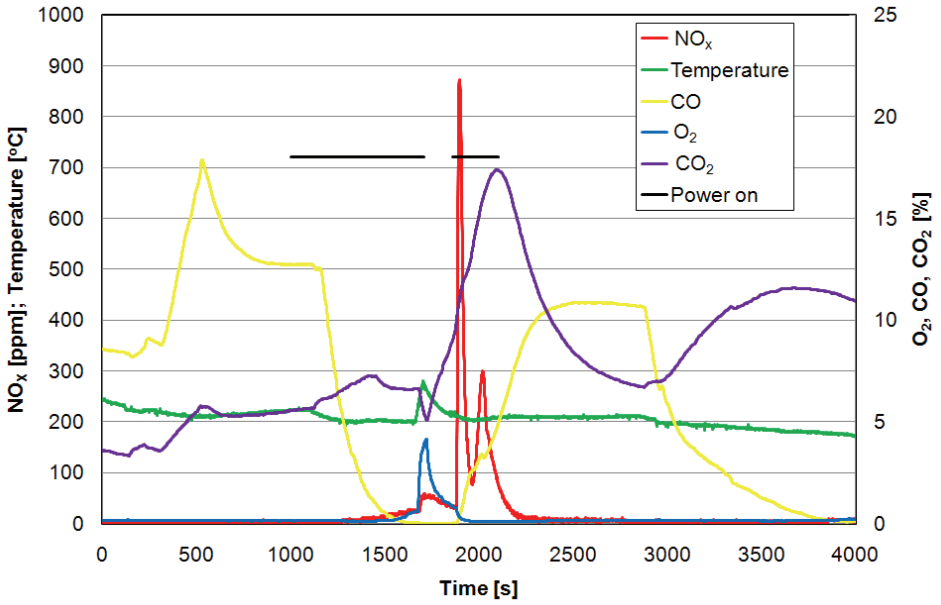

Figure 37: Arc ignition in CO-rich (12%) and O_2 containing atmosphere

In further trials there some more variations conducted on the O_2, the CO and the CO_2 content of the gas inflow as well as on the flow rate. **Table 12** gives an overview on the process parameters varied in the long time trials.

Table 12: Process parameters varied during long time trials

Trial	Inflow content [%]			Flow rate [l/min]
	O_2	CO	CO_2	
Trial 1	0 – 21	0 – 12	0	70
Trial 2	7.5	0	0	200
Trial 3	0 – 19.7	0	0	60 – 225
Trial 4	12.25 – 15.75	0	0 – 1.5	160 – 200
Trial 5	0 – 15	0	0	100
Trial 6	17 – 20	5 – 20	0	100

In the following figures for exemplary trials the measured NO_x concentration is plotted against the O2, CO and CO_2 concentration to show some correlations between NO_x and O_2, CO and CO_2 respectively. In **Figure 38** the NO_x content is shown against the O_2 content measured in the off-gas. It can be clearly seen that with the oxygen content nearing zero there is a steep slope of the NO_x content also going down to 0 ppm. The decline of NO_x content to higher oxygen contents is due to the fact that for example also the starting period of the trial is captured within this figure.

Figure 39 shows the correlation between NO_x and CO content of the off-gas. The reducing effect of CO on the NO_x content of the off-gas is distinguished by the strong decline of the NO_x content with increasing CO content in the off-gas.

The NO_x content against the CO_2 content in the off-gas is shown in **Figure 40**. Even though an influence of the CO_2 content on the NO_x amount in the off-gas was assumed (see section 2.3.3.3) there is no clear correlation visible.

Aggregating the measurement data of all long time measurements, in **Figure 41** the NO_x content is shown in a three-dimensional figure against the CO and the O_2 content of the off-gas. The highest values for the NO_x content were measured with no CO and O_2 in the range of 2 – 13 % present. The lowest NO_x contents were measured at 0 – 1 % O_2 and simultaneous presence of CO in the off-gas.

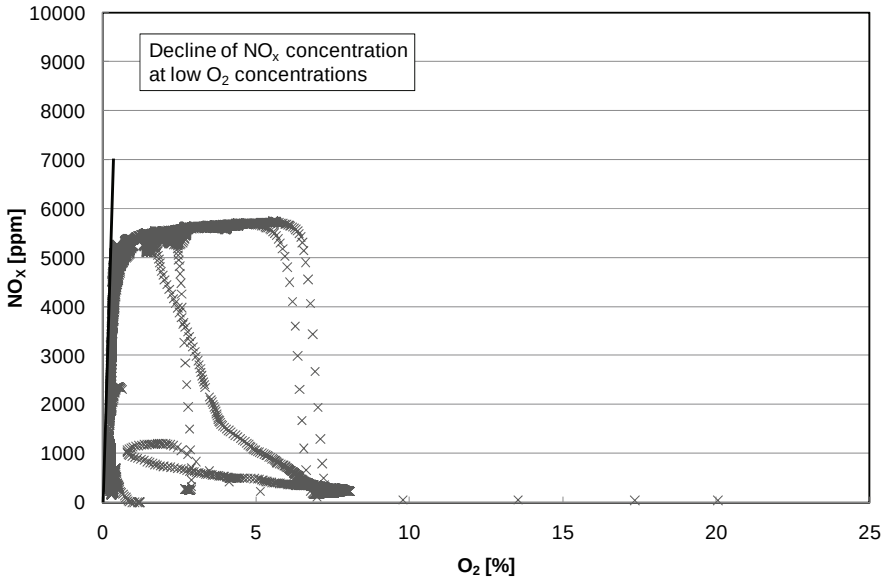

Figure 38: NO_x content against O_2 content in the off-gas for an exemplary trial

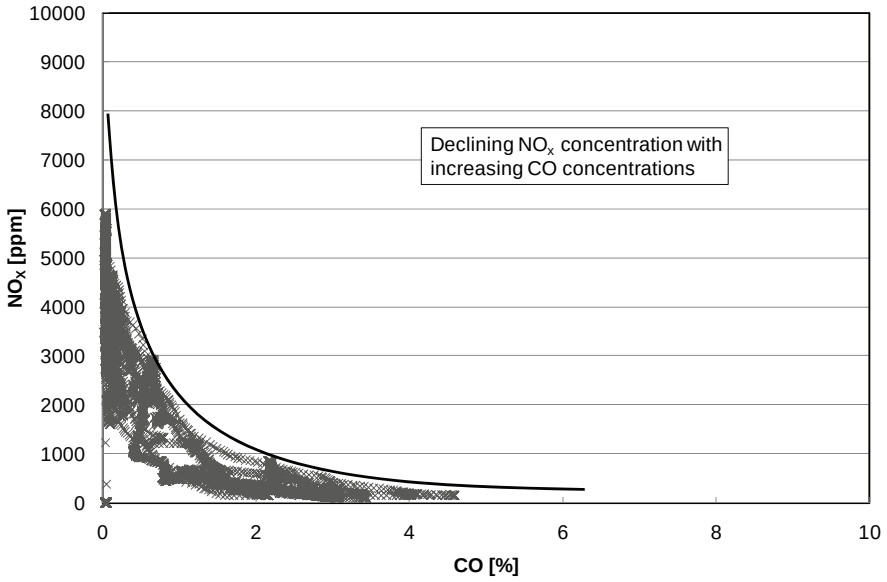

Figure 39: NO_x content against CO content in the off-gas for an exemplary trial

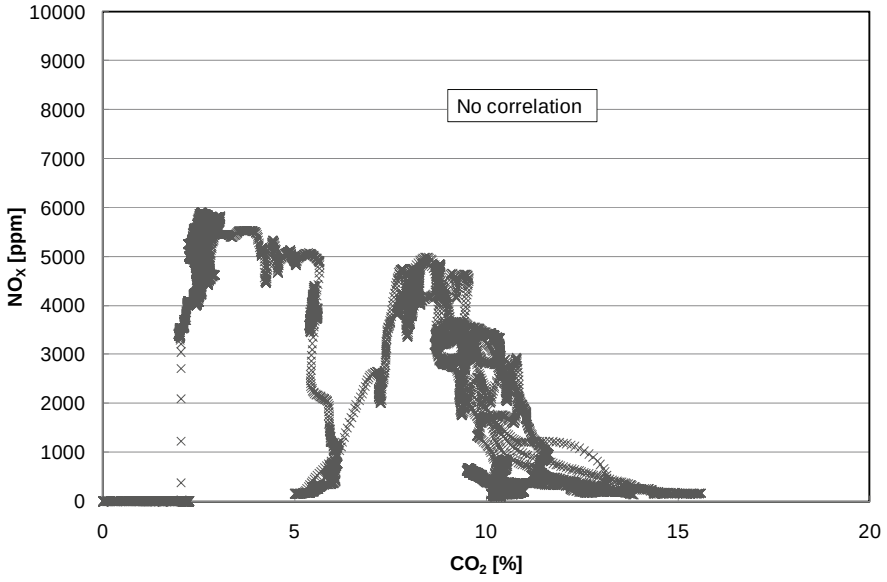

Figure 40: NO_x content against CO_2 content in the off-gas for an exemplary trial

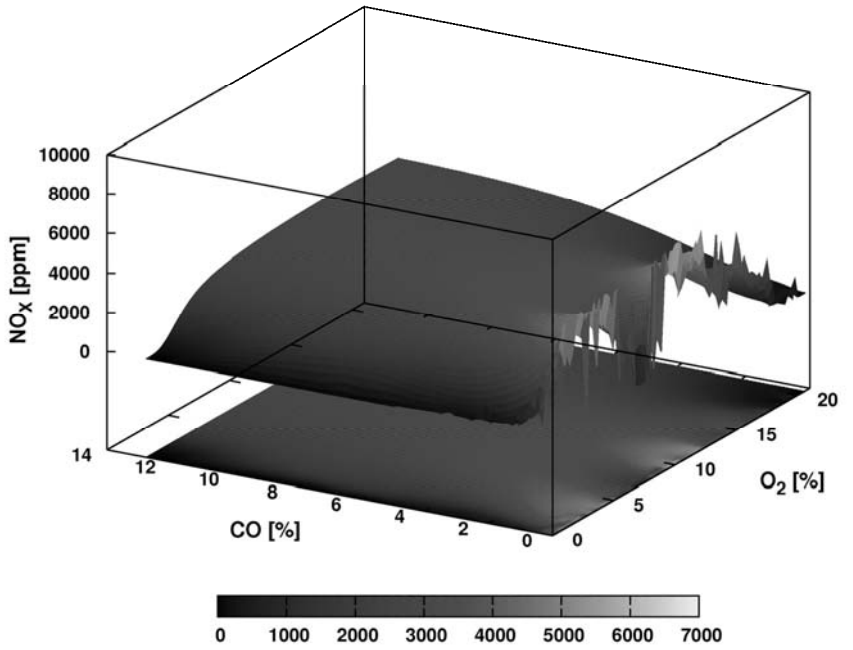

Figure 41: NO_x content against CO and O_2 content in the off-gas

2.3.3.3 Thermodynamic calculation of NO_x formation for different process conditions

The thermodynamic calculations performed within this task are based on the GRI-MECH 3.0 thermochemistry [21] and were conducted using the CANTERA software package [1],[11]. To begin with the thermodynamic equilibrium of O_2/N_2 mixtures has been calculated over a range of temperatures. The temperatures have been varied in a range of 700 to 3500 K and the equilibrium has been calculated for oxygen contents of 21, 10 and 5 %. **Figure 42** shows a diagram of the calculation results. Here you can already see that the NO content of the mixture in thermodynamic equilibrium even at an O_2 content of 21 % is very low (< 30 ppm) up to temperatures of 1700 K (1427°C). Temperatures measured at the exit of the furnace (point A) are usually lower than 1700 K.

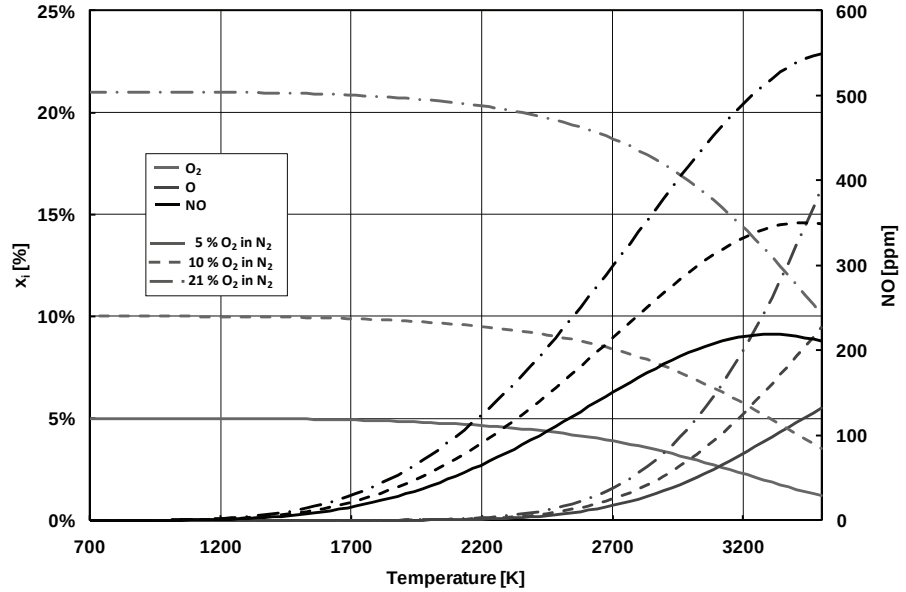

Figure 42: Thermodynamic equilibrium of an O_2/N_2 mixture subject to temperature and O_2 content (x_i: volume fraction of O_2, O)

In the following **Figure 43** to **Figure 45** the influence of reducing species like CO and H_2 (cf. eq. (19) and (20)) and, because of its dissociation at high temperatures, also CO_2 (cf. eq. (21)) on the NO content in equilibrium is shown for a base composition of 10 % O_2 and a N_2 balance. The figures show that in the presence of these reducing species even lower amounts of NO are stable in the mixture.

Figure 43 shows the thermodynamic equilibrium composition of a $CO/O_2/N_2$ mixture in the temperature range of 700 to 3500 K for a CO content of 5 %, 25 % and 50 %. For a temperature of 1700 K and a CO content of 5 % the NO content is reduced by 15 % from 20 to 17 ppm. Higher amounts of CO lead to NO contents < 0.01 ppm for this temperature.

$$2\ CO + 2\ NO \rightarrow 2\ CO_2 + N_2 \tag{19}$$

$$2\ H_2 + 2\ NO \rightarrow 2\,H_2O + N_2 \tag{20}$$

$$CO_2 + C \rightleftarrows 2\ CO \tag{21}$$

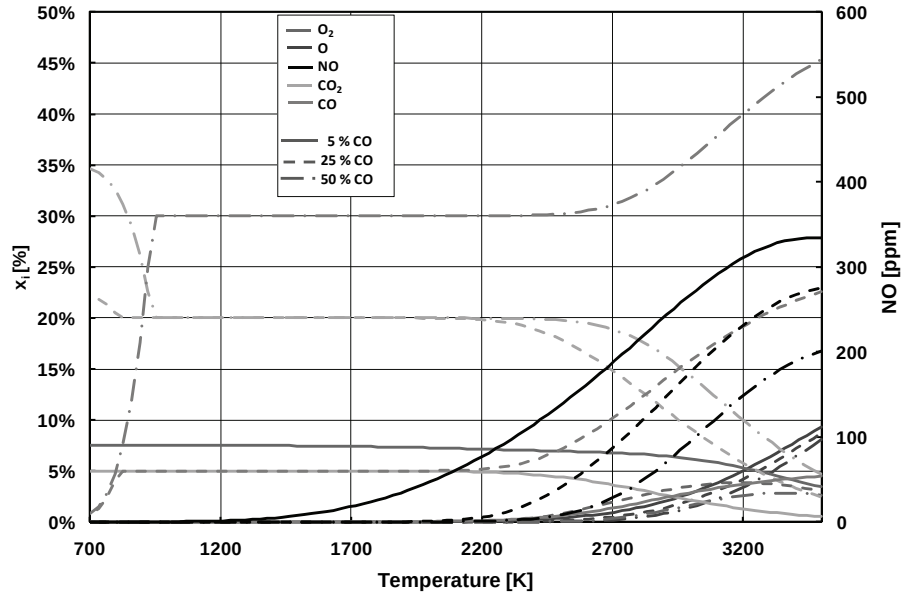

Figure 43: Thermodynamic equilibrium of a $CO/O_2/N_2$ mixture subject to temperature and CO content (Base composition 10 % O_2, balance N_2; x_i: volume fraction of O_2, O, CO_2, CO)

The thermodynamic equilibrium composition of a $H_2/O_2/N_2$ mixture is shown in **Figure 44**. The H_2 content is varied between 5 and 15 % and a hydrogen content of 5 % is reducing the NO content at 1700 K by 35 % from 20 to 13 ppm. The CO_2 content in the mixture as shown in **Figure 45** has only a negligible effect on the NO content at temperatures up to 1700 K.

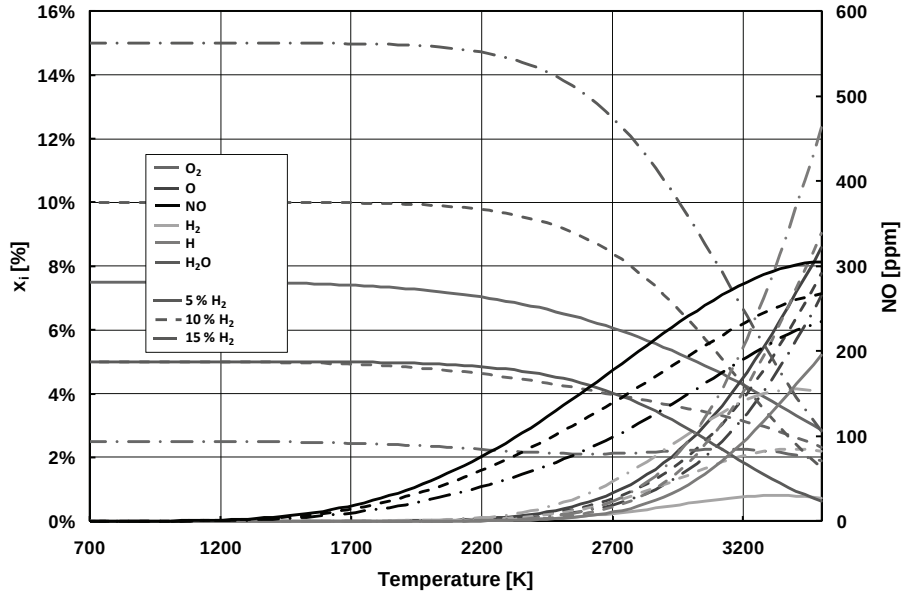

Figure 44: Thermodynamic equilibrium of a $H_2/O_2/N_2$ mixture subject to temperature and H_2 content (Base composition 10 % O_2, balance N_2; x_i: volume fraction of O_2, O, H_2, H, H_2O)

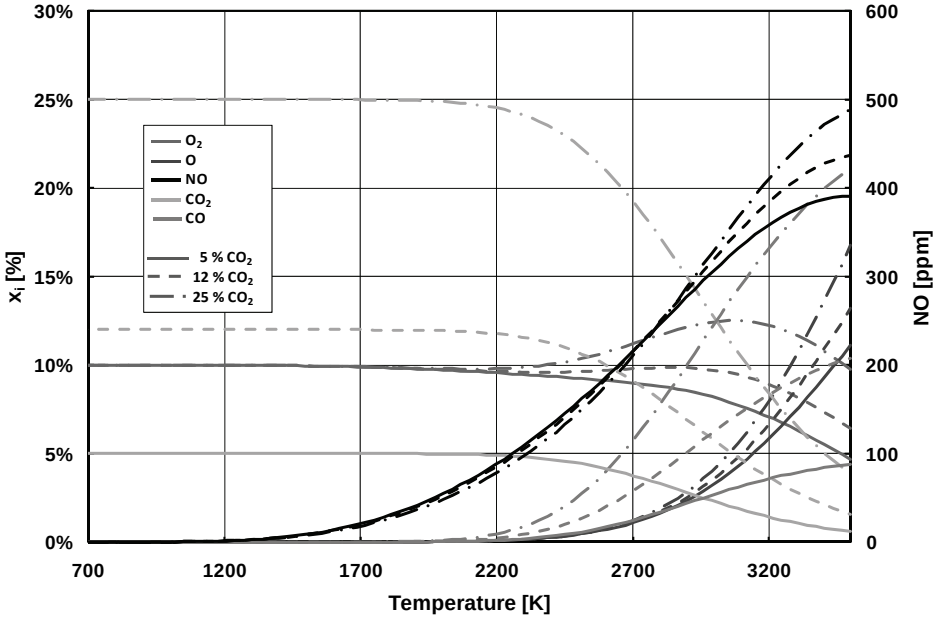

Figure 45: Thermodynamic equilibrium of a $CO_2/O_2/N_2$ mixture subject to temperature and CO_2 content (Base composition 10 % O_2, balance N_2; x_i: volume fraction of O_2, O, CO_2, CO)

To perform thermodynamic calculations for different process conditions an exemplary heat as well as three different cases within this heat were chosen. **Figure 46** shows the off-gas measurement data of point A for the chosen heat together with process data. The three cases which were furthermore calculated are marked within the figure.

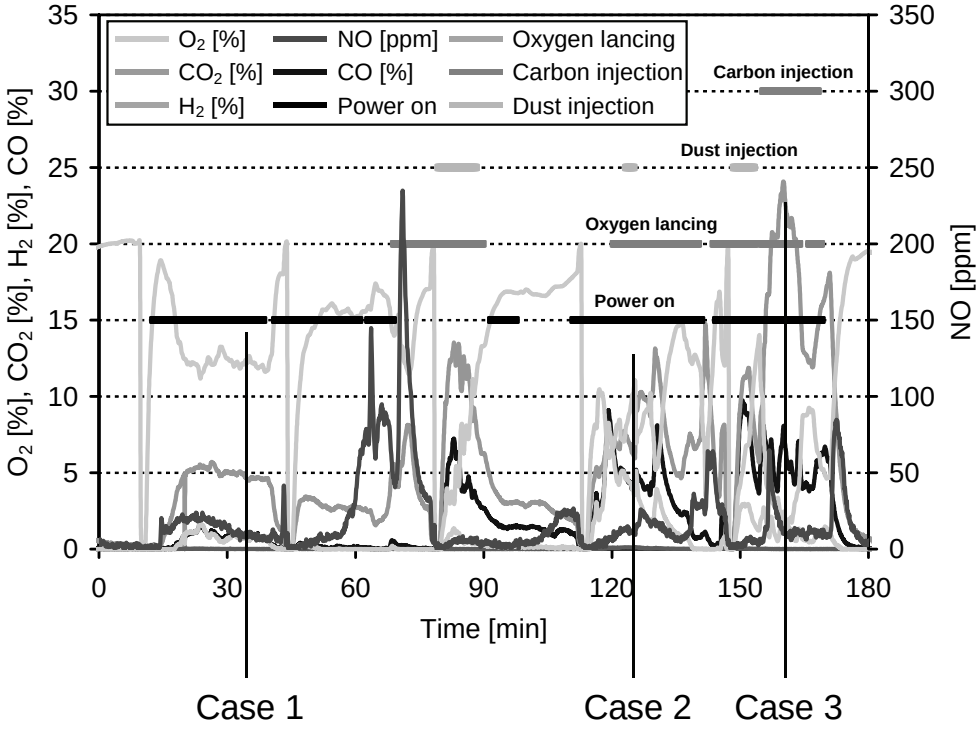

Figure 46: Off-gas composition measured at point A (CO,H_2,CO_2,O_2,NO_x) and process data of exemplary heat as well as cases chosen to be calculated

For each of the cases the off-gas composition has been extracted from measurement data and then was the starting point of thermodynamic equilibrium calculations. Additionally the NO content was set to 1000 ppm for each case. The composition of the gas mixture used in the thermodynamic calculation of each case can be taken from **Table 13**.

Table 13: Gas mixture composition of cases for thermodynamic calculations

	O_2 [%]	CO [%]	CO_2 [%]	H_2 [%]	NO [ppm]
Case 1	12	2	5	2	1000
Case 2	7	5	7	5	1000
Case 3	2	8	20	2	1000

In **Figure 47** to **Figure 49** for each case the thermodynamic equilibrium composition is plotted over the temperature. It can be seen that in all three cases at temperatures up to 1700 K the NO content in equilibrium would be reduced from a starting amount of 1000 ppm to less than 20 ppm.

The general thermodynamic calculations performed therefore show that in thermodynamic equilibrium at temperatures up to 1700 K only small amounts of NO (< 30 ppm) are stable. In the presence of reducing agents like CO or H_2 these amounts of NO are even lower.

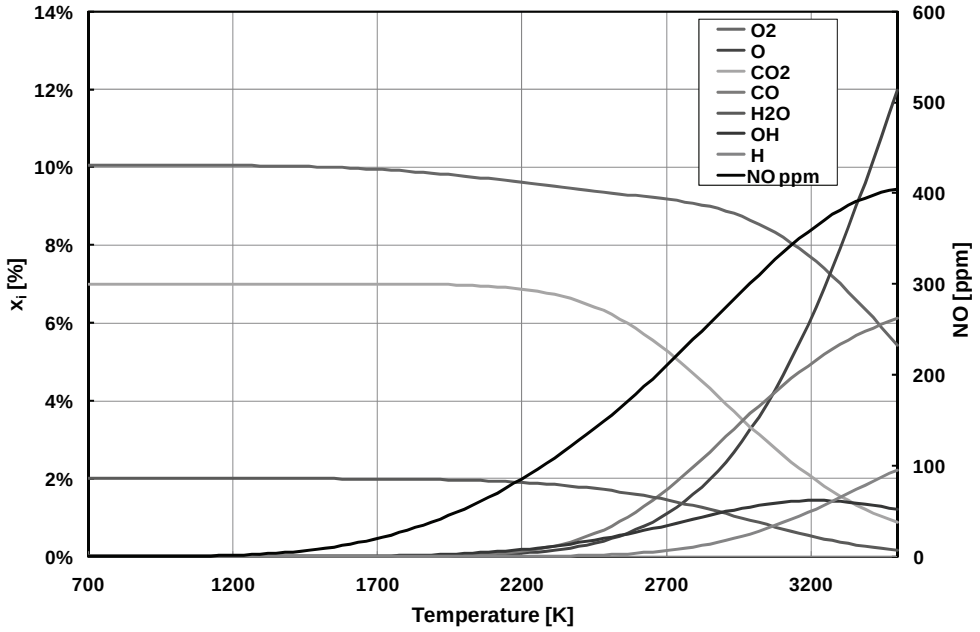

Figure 47: Thermodynamic equilibrium composition plotted over temperature, Case 1

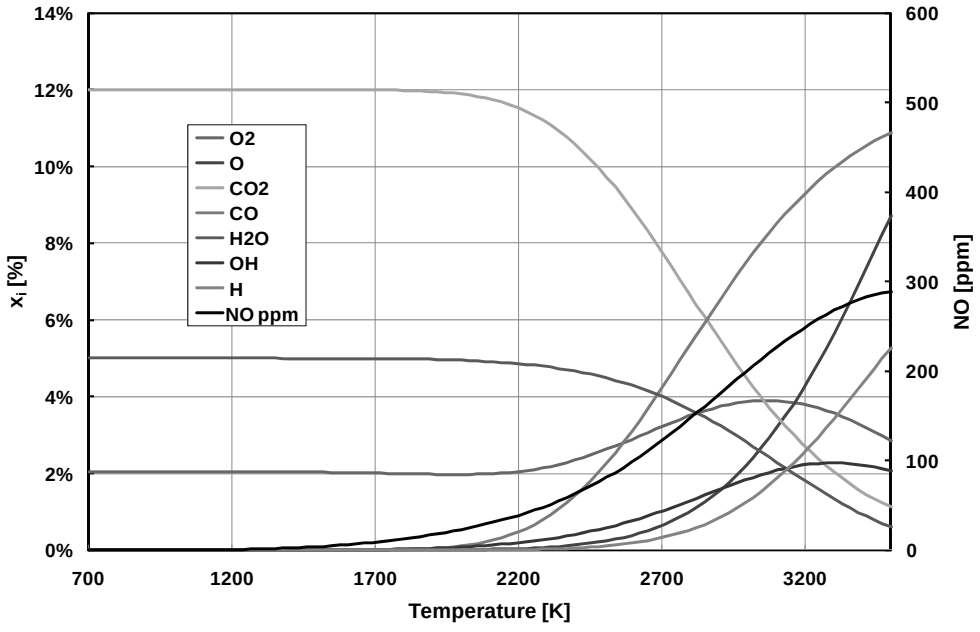

Figure 48: Thermodynamic equilibrium composition plotted over temperature, Case 2

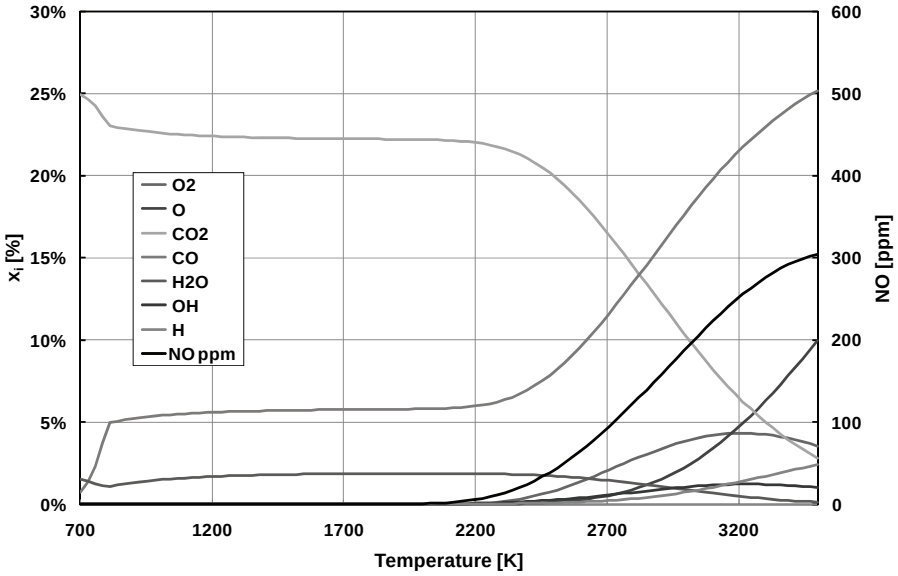

Figure 49: Thermodynamic equilibrium composition plotted over temperature, Case 3

The thermodynamic calculation of cases taken out of an exemplary heat show that at temperatures up to 1700 K the reducing agents present in the off-gas like CO and H_2 would cause a reduction of NO from 1000 ppm (e. g. from the electric arc) down to < 20 ppm. A CO concentration of only 5 % would reduce the NO content to below 10 ppm at 1700 K if in equilibrium.

2.3.3.4 Comparison of results from trials with equilibrium calculations and with partners operational results

The comparison of cases out of real off-gas measurements at industrial EAFs as well as the pilot plant with thermodynamic calculations show that there is more NO in the off-gas than predicted by equilibrium calculations. The EAF off-gas seems usually not to be in thermodynamic equilibrium which may be due to high off-gas flow rates and short residence times of the off-gas in the furnace freeboard.

Nevertheless the fundamental correlations between the O_2, CO and NO_x content in the off-gas are not only shown by the thermodynamic calculations (**Figure 42** and **Figure 43**) but could also be seen in the analysis of the pilot plant tests (**Figure 38** and **Figure 39**) as well as in industrial measurements. The more oxygen is available the more NO_x is generated by the electric arc and in hot areas of the furnace. On the other hand the NO_x amount in the off-gas is decreasing with increasing CO contents.

The NO_x peaks seen in off-gas measurement data like **Figure 50** correlate with low off-gas temperatures and therefore slow kinetics of any NO_x reduction reactions and high oxygen contents of the off-gas. These conditions are typical for the phases of arc ignition after opening and charging of the furnace, when great amounts of leak air are flushing the furnace freeboard.

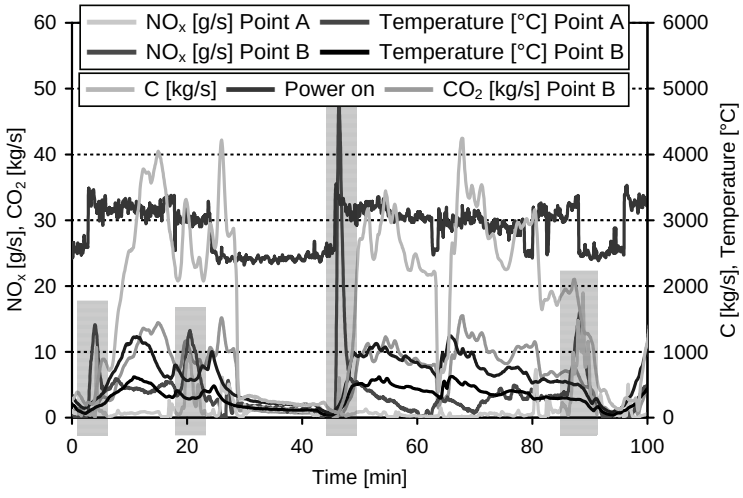

Figure 50: Measured NO_x peaks at arc ignition and off-gas temperatures for exemplary heat (point A and B)

2.3.3.5 Conclusions in view of control of NO_x emissions

The highest amounts of NO_x are produced in O_2-rich atmospheres. The higher the oxygen content of the gas in the furnace the more NO_x is generated. Atmospheres like this occur in the EAF e. g. after the scrap charging. To lower NO_x generation in the furnace therefore the amount of leak air increasing the O_2 content of the furnace off-gas has to be as low as possible. In the charging phase this could for example be realized by strongly decreasing the off-gas volume flow extracted by the primary off-gas system.

Furthermore the EAF off-gas is usually not in equilibrium. The kinetics of the gas reactions in the furnace and the post combustion zone are determining the NO_x content of the off-gas. Differences between real off-gas data and equilibrium calculations would be smaller with a longer residence time of the off-gas in the hot zones and higher temperatures respectively. To achieve this objective the off-gas flow rate has to be controlled as low as possible still ensuring sufficient exhaust of any furnace emissions.

And last but not least reducing agents like CO and H_2 are significantly lowering the NO_x concentration in the off-gas and can reduce NO_x formed by the electric arc. Because of this, operational practices like slag foaming with the increased generation of CO, which are already in use to lower energy losses in the EAF, have an additional positive effect on the NO_x emissions of EAFs.

2.3.4 Impact of oxygen injection and CoJets on NO_x emission

2.3.4.1 Lance utilisation at EAF with changing O_2/N_2 ratio

Off-gas measurements have been conducted simultaneously at point A and point B at the EAF of DEWG. The off-gas temperature and differential pressure (volume flow rate) have been measured at point B. Measurement point B is located at the end of the water-cooled hot gas line after complete post combustion. **Figure 51** and **Figure 52** present the off-gas profiles for stainless steel (0 min to 100 min) and for carbon steel (100 min to 180 min).

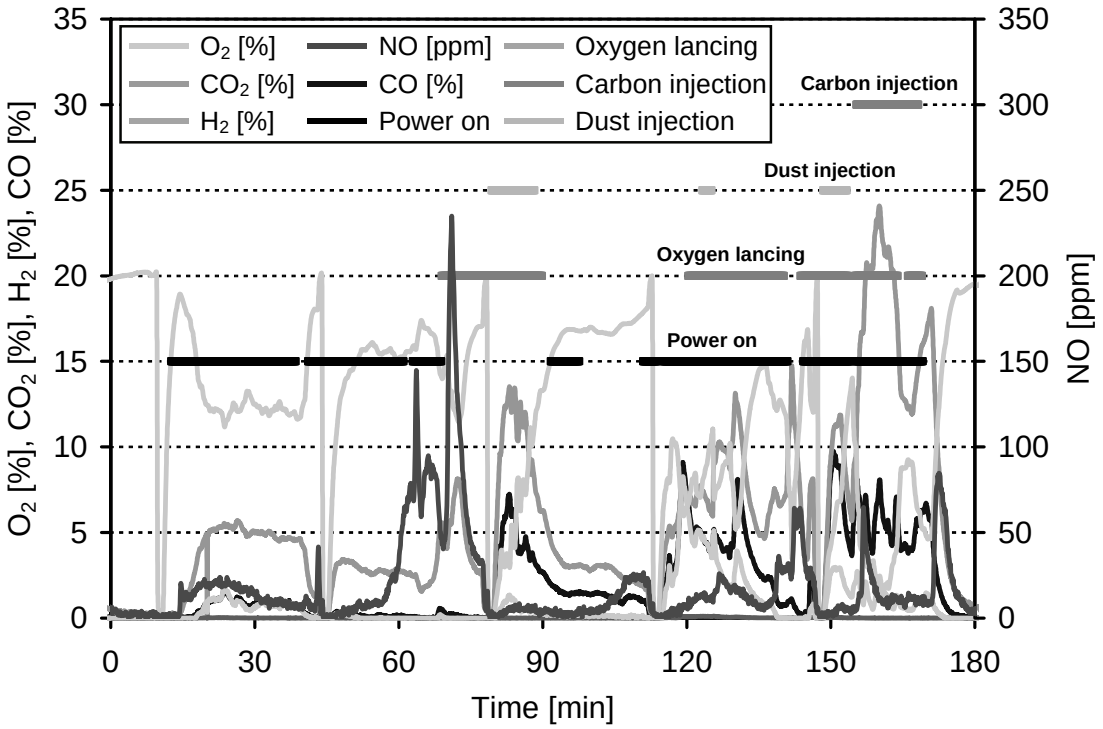

Figure 51: Measured off-gas composition (CO, H_2, CO_2, O_2, NO) and process periods at point A

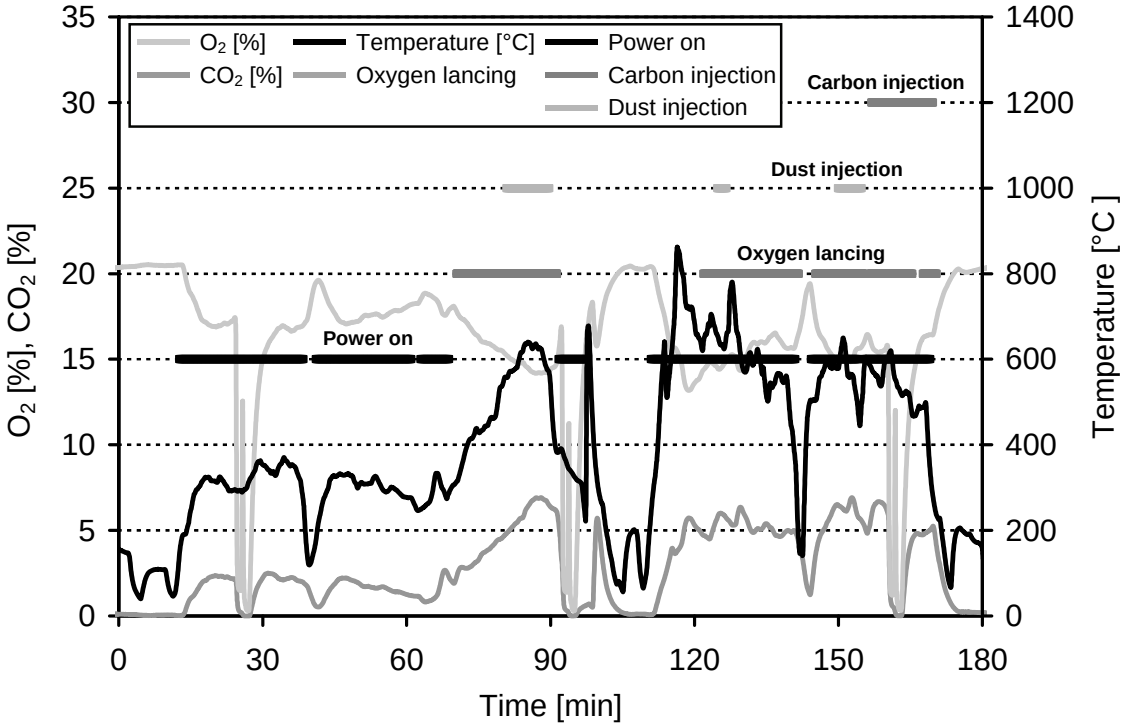

Figure 52: Measured off-gas composition (CO_2, O_2) and process periods at point B

During stainless steel production the power on period is clearly separated to the oxygen lancing. After oxygen lancing there is a short period of power on. While melting down the NO concentration is due to the electric arc based NO_x formation mechanism. At the end of melt down period and starting oxygen lancing there is a NO peak up to 250 ppm. While oxygen lancing there is CO in the off-gas in high amounts. High CO concentrations seem to decrease the total NO emission. The concentration profile for carbon steel is shown in minutes 100 – 180 in **Figure 51** and **Figure 52**. The power on/melting period and oxygen lancing/dust injection are not separated. The measured NO concentration profile is due to electric arc formation and the lancing/injecting process. **Table 14** gives production characteristics of stainless steel and carbon steel. During carbon steel production the off-gas flow rate is 100000 m^3 (STP) and 60000 m^3 (STP) for stainless steel production. Dust is injected by use of compressed air. When air is injected to the electric arc it may result in unnecessary NO formation and will increase the total NO_x emission. The average NO emission for stainless steel is 26 ppm and 15 ppm for carbon steel. **Figure 53** shows the NO emission vs. measured off-gas temperature at point B. There is a clear NO peak at 300 °C to 500 °C at stainless steel. At carbon steel there are smaller peaks at 200°C and round about 600 °C. It becomes clear that strategies for decreasing NO_x at EAF will be process depending. In case of carbon steel the average potential for decreasing NO is quite higher than that for stainless steel. In Task 6.1 strategies for decreasing the total NO_x emission at carbon steel at DEWG have been evaluated.

Table 14: Production characteristics and average NO_x emission

	Stainless steel	Carbon steel
DEC	60000 m^3(STP)	100000 m^3(STP)
Oxygen lancing	1100 m^3(STP)	2000 m^3(STP)
Dust injection	1100 kg	913 kg
Air (dust injection)	500 m^3(STP)	450 m^3(STP)
Carbon injection	-	456 kg
NO_x	26 ppm (53 mg/m^3 (STP)	15 ppm (30 mg/m^3 (STP)

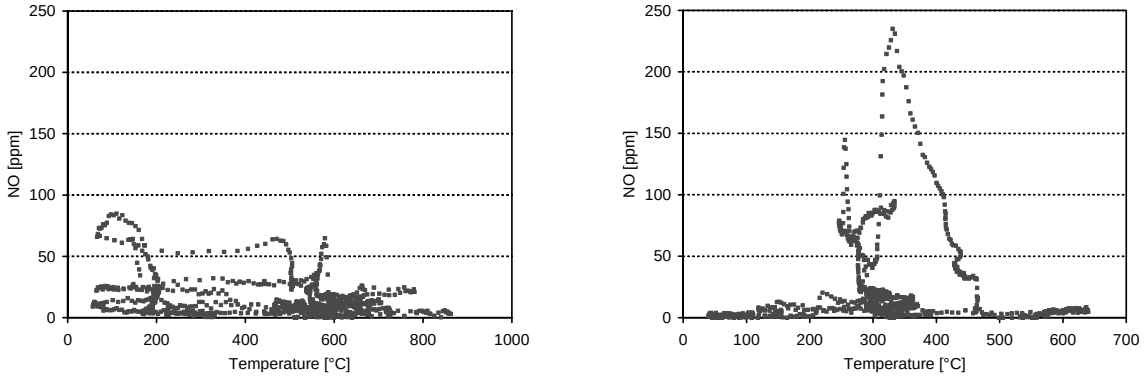

Figure 53: NO emission (point A) vs. off-gas temperature (point B) (left), NO emission (point B) vs. off-gas temperature (point B) (right)

2.3.4.2 CoJet utilization at EAF with changing O_2/CH_4 ratio

Based on the initial NO_x values measured at the RIVA EAF within WP1 the influence of EAF operation on NO_x emissions has been investigated. The EAF operations investigated within this task include (a) EBT Burner and (b) CoJet burner operation. **Figure 54** shows the layout of the EAF at RIVA. The EAF is equipped with 3 CoJet burners and 1 EBT burner. They are mounted on the EAF side walls. The CoJet burner injects oxygen and natural gas into the EAF. The EBT burner injects only oxygen.

The oxygen amount injected by EBT/CoJet is presented in **Table 15**. The CoJet ratio is calculated as (MAIN O_2 and SHOURD O_2) vs. (CoJet CH_4). **Figure 55** shows the EAF operating data as well as the CoJet ratio. It becomes clear that the CoJet ratio is in the range of 2.0 up to 2.5. **Figure 56** shows the measured concentration profile at point B and the corresponding operating data for two exemplary heats.

Table 15: Production characteristics (CoJet and EBT) at RIVA

	Average [m^3(STP)]	1st Ignition [m^3(STP)]
EBT O_2	147	66
Main O_2	1460	574
SHROUD O_2	500	582
Total O_2	2100	1224
CoJet CH_4	486	547
CoJet ratio	4.60	2.14

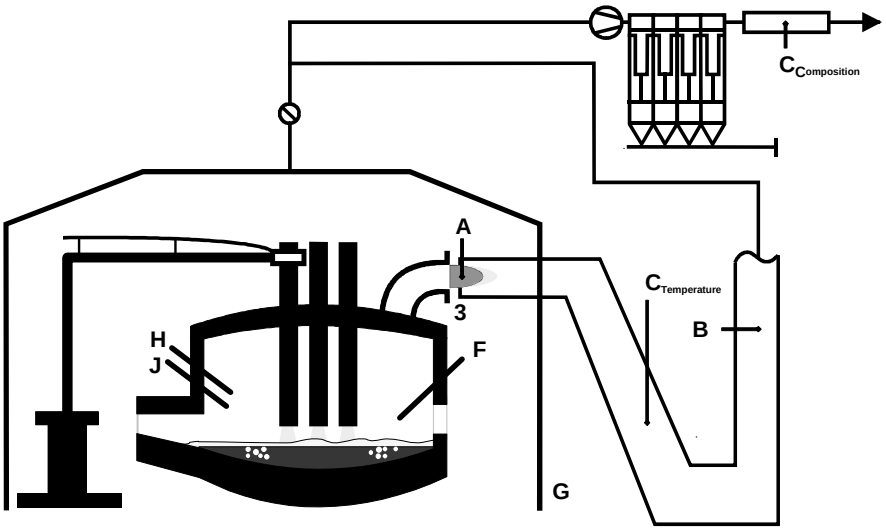

Figure 54: EAF layout at RIVA
A: Measuring point A, B: Measuring point B, C: Temperature, G: dog house, F: CoJet , H: EBT burner, J: injector, 3: gap

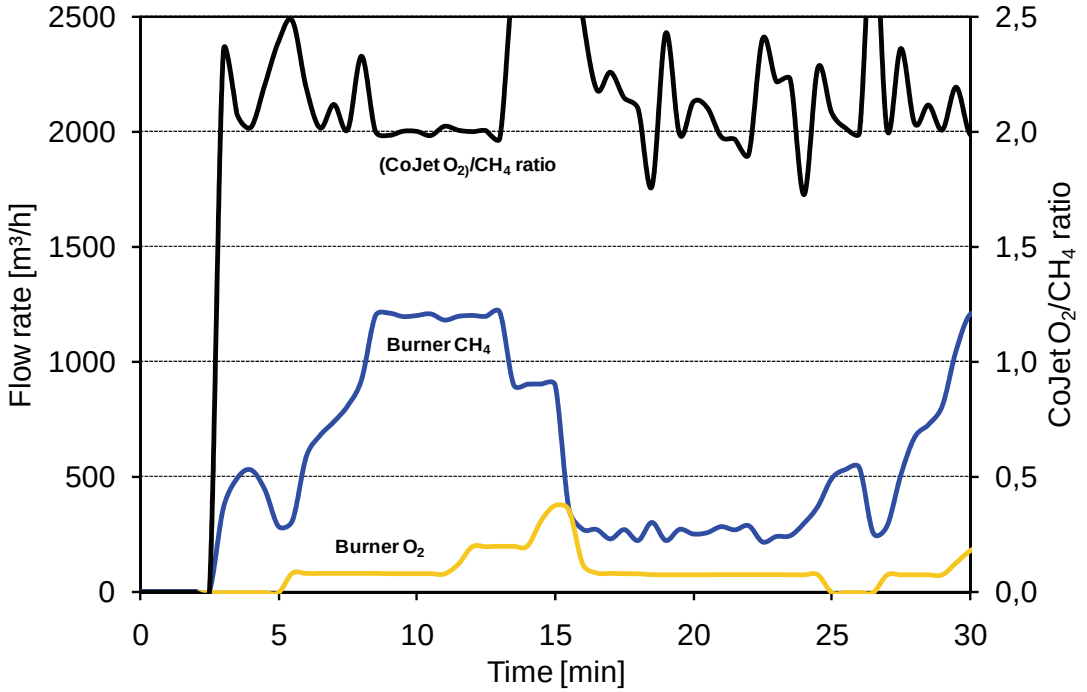

Figure 55: EAF operating data (EBT,CoJet) and CoJet ratio

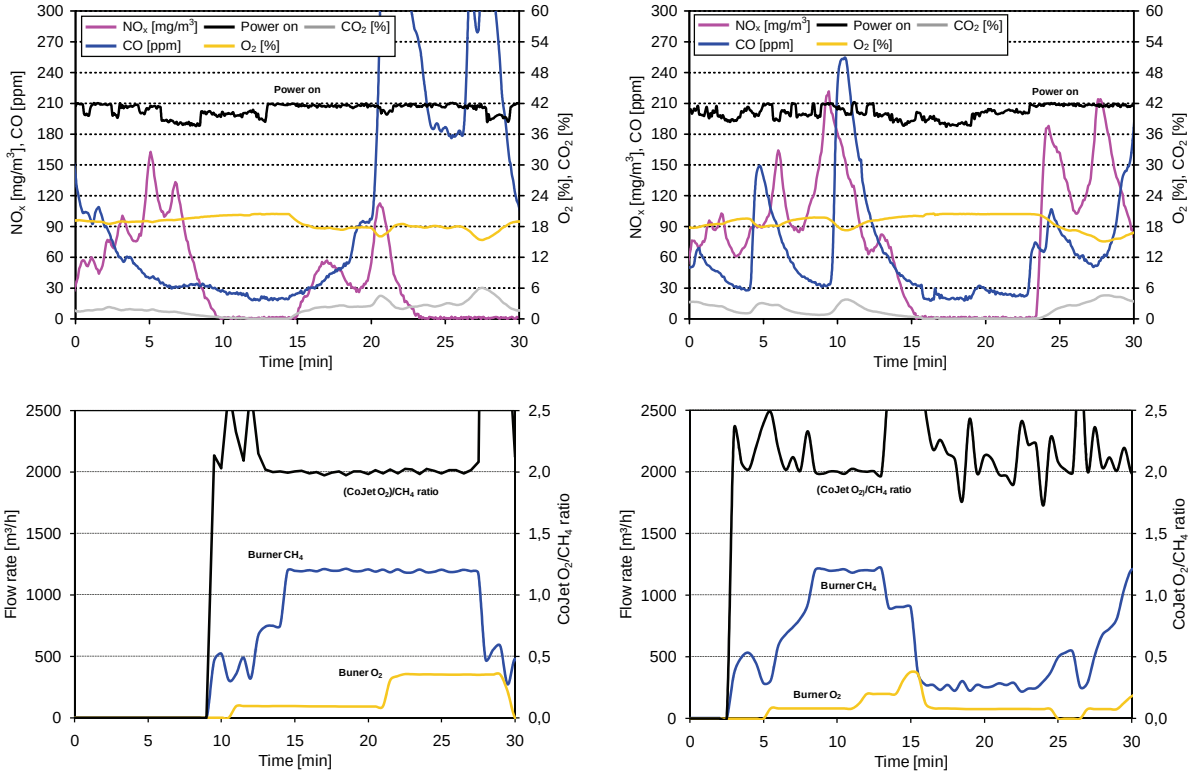

Figure 56: Measured off-gas composition (CO_2,O_2,CO,NO_x) at point B (top),EAF operating data (EBT,CoJet) and CoJet ratio (bottom)

There are clear NO_x peaks after ignition. The shown 2 heats differ in the CoJet ratio during ignition. CoJet ratio of 2.0 seems to decrease NO_x peaks during ignition. **Table 16** gives the corresponding operation data and maximal NO_x emission while 1st ignition. The CoJet ration seems to have a strong effect to the NO_x peak while ignition.

Additional off-gas measurements have been realized at point C at RIVA (**Figure 54**). Measurement point C is located at the bag house. The amount of air injected for cleaning the bag filters is not well known. High amount of air may influence the measured off-gas concentration profile. The off-gas

analysis system consisted of a mobile hand-held measuring instrument, a standard probe without water-cooling for off-gas sampling and filters.

Table 16: Production characteristics (EBT and CoJet) and average NO_x emission

	Left Diagram 1st Ignition [m³(STP)]	Right Diagram 1st Ignition [m³(STP)]
EBT O_2	147	66
Main O_2	1460	574
SHROUD O_2	500	582
Total O_2	2100	1224
CoJet CH_4	486	547
CoJet ratio	2.00	2.14
NO_x	246 mg/(m³(STP)	431 mg/(m³(STP)
NO_x	120 ppm	210 ppm

The hand-held instrument consists of a real time data logger and analyser modules for measuring the off-gas composition (O_2, CO, CO_2, H_2, and NO_x). At measuring point C the combustion of flammable gas species (CO, H_2) is completely finished. The aim of the work undertaken is to identify most important factors influencing the total amount of NO_x. Therefore the point C is useful.

Figure 57 shows the operating data at RIVA. When the 1st basket is charged and the arc ignited the burners are switched on. The CoJet burner started a short time before 1st ignition. This normal procedure is not to be correlated to any additional emission at point C. But it seems to be not necessary to start the CoJet burner before 1st ignition. The CoJet ratio is increasing during the 1st melt down period up to 6. During the 1st melt down period there is a short power off. There is a clear NO_x peaks after ignition again. During power off the burner are switched off. Simultaneously the O_2/CH_4 ratio decreases down to 2. During 2nd ignition there is CoJet oxygen injection and the ratio is 2. Injection of lime and coal is clearly separated to each other (**Figure 58**). While starting injection of lime the CoJet ratio increases up to 11. This operating procedure is typical at RIVA. After monitored the current state of EAF operation the influence of EAF burner operation to the NO_x emission have been investigated. Variations of the current EAF operation strategy: (a) CoJet ratio while 1st ignition; (b) CoJet ratio starting 2nd ignition period may suppress NO_x emission.

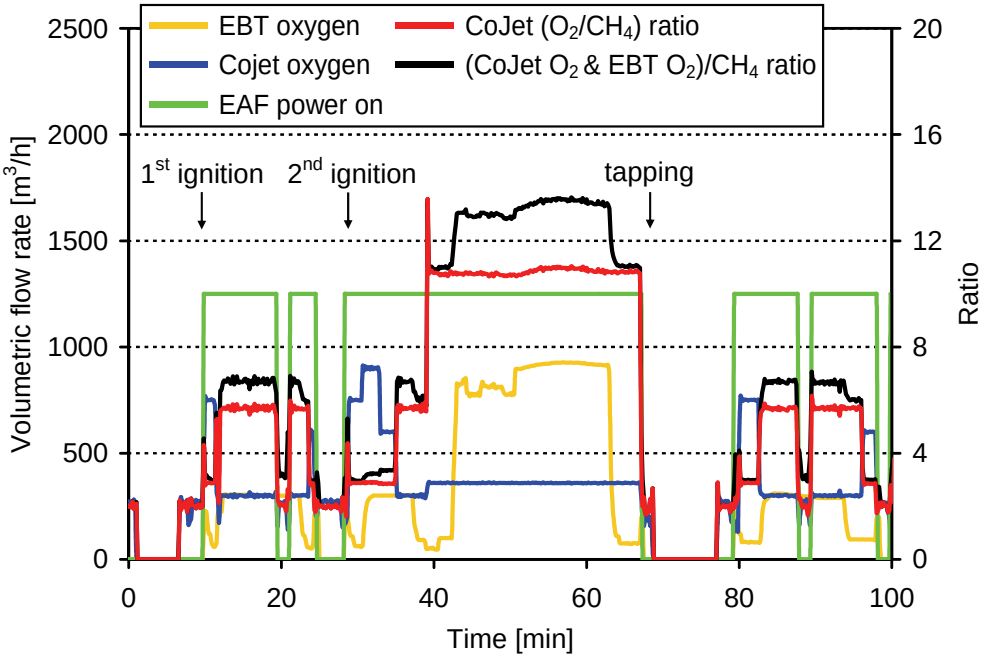

Figure 57: EAF operating data and CoJet ratio for an exemplary heat

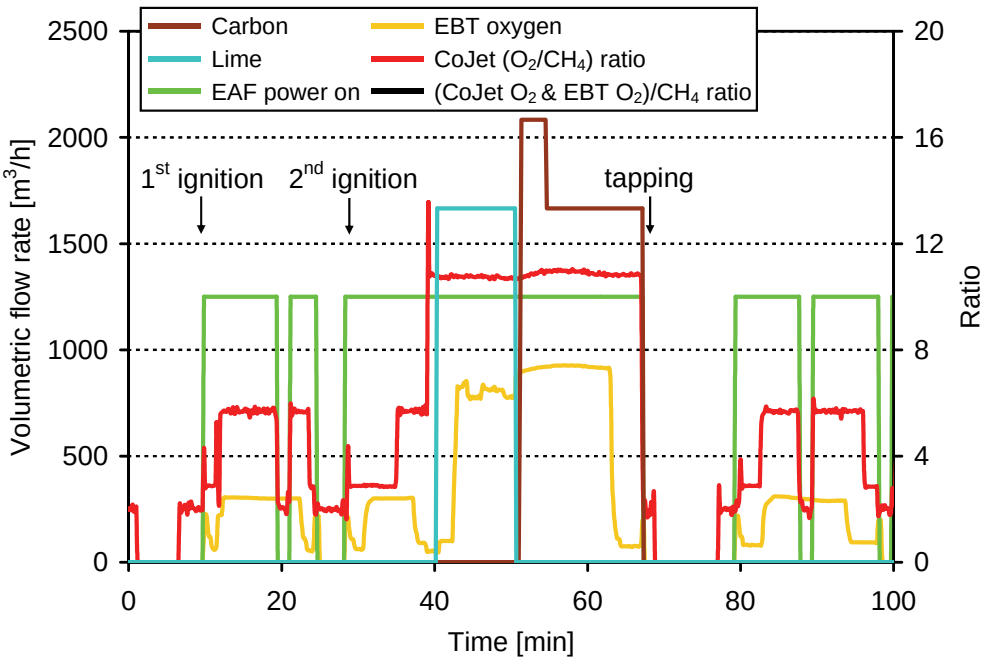

Figure 58: EAF operating data: Carbon injection and Lime injection for an exemplary heat

Figure 59 shows the measured off-gas profile (NO_x, O_2, CO, CO_2, H_2) at point C. During 1st ignition and first melt down period the NO_x profile is due to peaks. The range is 50 ppm to 100 ppm. The second NO_x peak is emitted because of an additional ignition. During 2nd ignition the NO_x profile goes off smoothly (up to 15 ppm). The injection of lime is due to EBT burner switched off and CoJet burner is switched off too. The CoJet ratio is between 10 and 12 while injection. The maximum NO_x emission reaches 60 ppm. The H_2 maximum is reached when carbon injection is started. Simultaneously the CO content is maximal too. The H_2 content seems to have no negative impact to the total NO_x emission at point C. The H_2 content seems to correlate to the CO content. This leads to the hypothesis that there is a common source of CO and H_2 when stopping lime injection and starting coal injection. The **Figure 60** shows the NO_x emission vs. the CoJet ratio. There are four operation periods to be distinguished: (a) ignition without EBT switched on; (b) ignition and melting down while EBT burner is switched off; (c) injection of carbon while EBT is switched on; (d) injection of lime while EBT is switched on. While ignition without EBT is switched on the CoJet ratio is 2 and the NO_x emission reaches 20 ppm. While ignition and melting down with EBT burner switched on the CoJet ratio is 3 (ignition) and 6 (melting down). The NO_x emission increases maximum up to 140 ppm (ignition) and 100 ppm (melting down). While ignition period the CoJet ratio is 11. The NO_x emission increases up to 140 ppm (coal injection) and 100 ppm (lime injection). The maximum NO_x emission while injection lime and coal is due to additional ignition procedures.

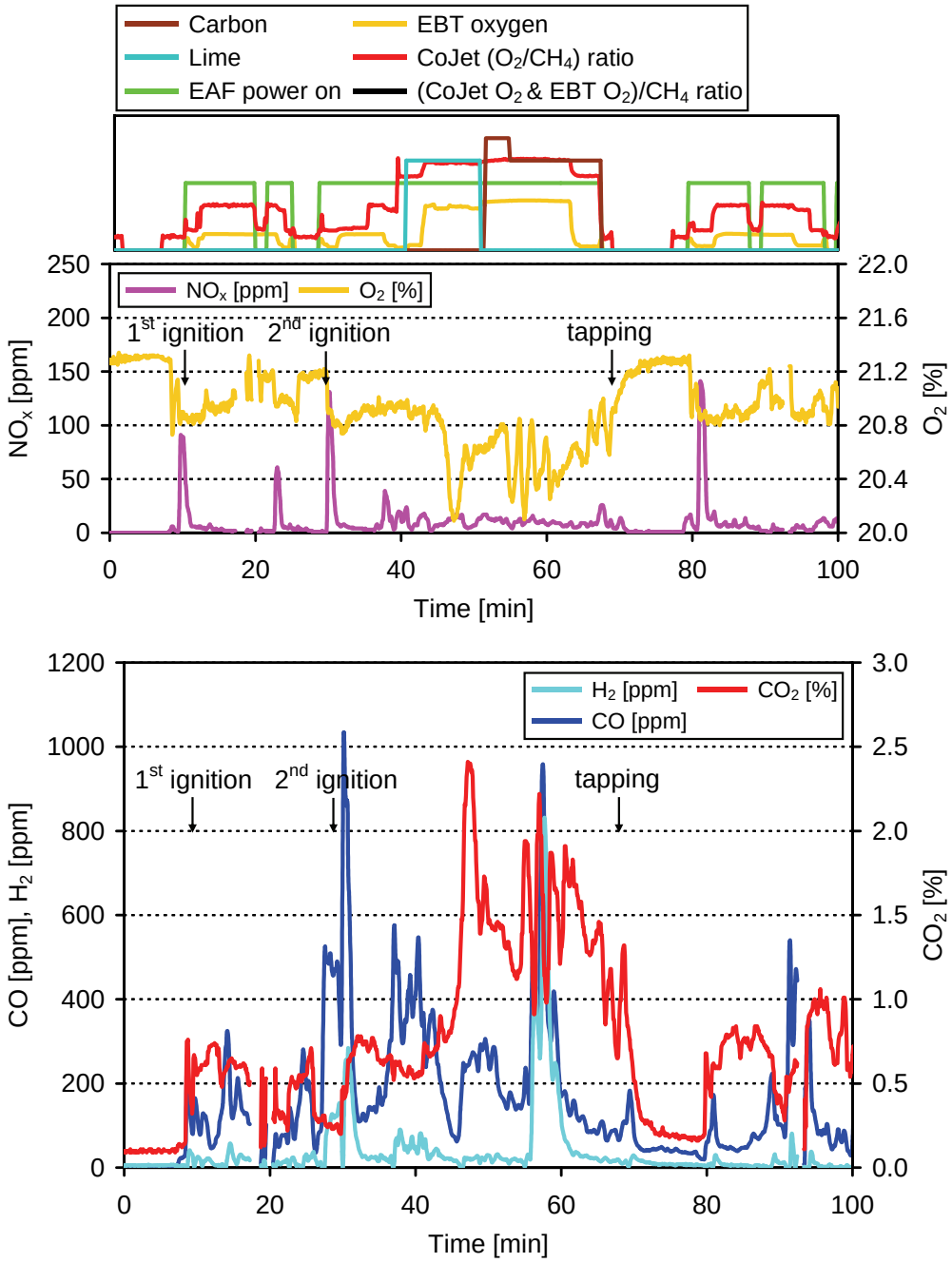

Figure 59: EAF operating data (top), measured off-gas concentrations (middle and bottom) for an exemplary heat

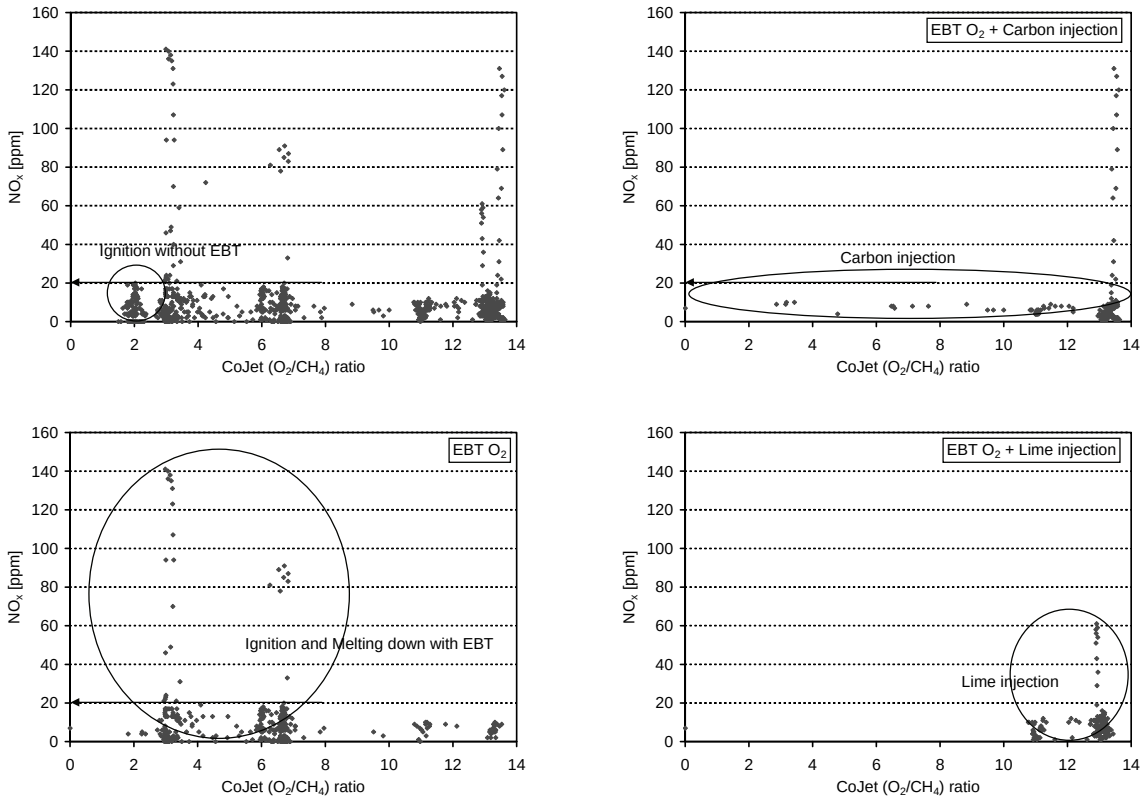

Figure 60: Measured NO_x concentration vs. CoJet ratio at point B

2.3.4.3 Carbon blowing tests by injection from lance

Based on the initial measurement of NO_x at the DEWG EAF (point A and point B) and the results of WP 4.1 further investigations due to impact on the NO_x have been carried out. In order to investigate the influence of different amounts of carbon lancing on the NO_x emission a plant trial campaign has been carried out, which included: (a) Installation of off-gas analysis system at point B (**Figure 61**); (b) Variation of the entire carbon lancing (2^{nd} basket); (c) Evaluation of data recorded and operational data provided by DEWG.

During production of carbon/tool quality steels carbon is injected in order to foam the slag after melt down of the 2^{nd} basket. The Carbon is lanced with air (carrier gas) in the layer between melt and slag. When the slag starts foaming there is a decrease of the loudness of the EAF and simultaneously the heat losses decrease too. While foaming slag there is less air intake through the slag door. The slag door remains open during the lancing period (**Figure 61**). This will lead to additional NO_x formation inside the EAF vessel. Because of high CO/H_2 content in the EAF off-gas there is higher post combustion at the PC camber. This can have a bad impact on total NO_x at point B. point B is located at the end of the water-cooled hot gas line after the complete post combustion. The amount of off-gas ejected at the gap during melting is not well known. Measured volume flow rates in the dedusting system assume off-gas volume flow coming out of the EAF vessel and total amount of air intake at the EAF vessel and downstream.

Off-gas composition, off-gas temperature, and off-gas volume flow rate was measured at measurement point B. At measurement point B the portable off-gas analysis system was installed. The analysis system equipment consists of water-cooled probes, filters, detectors, and signal converters for measuring the off-gas composition (O_2, CO_2, CO, NO_x). Off-gas temperature is measured by shielded thermocouples. The measured data for differential pressure, off-gas temperature, and off-gas composition are recorded continuously. **Figure 62** presents the NO_x mass flow measured at point B for a high alloyed steel heat.

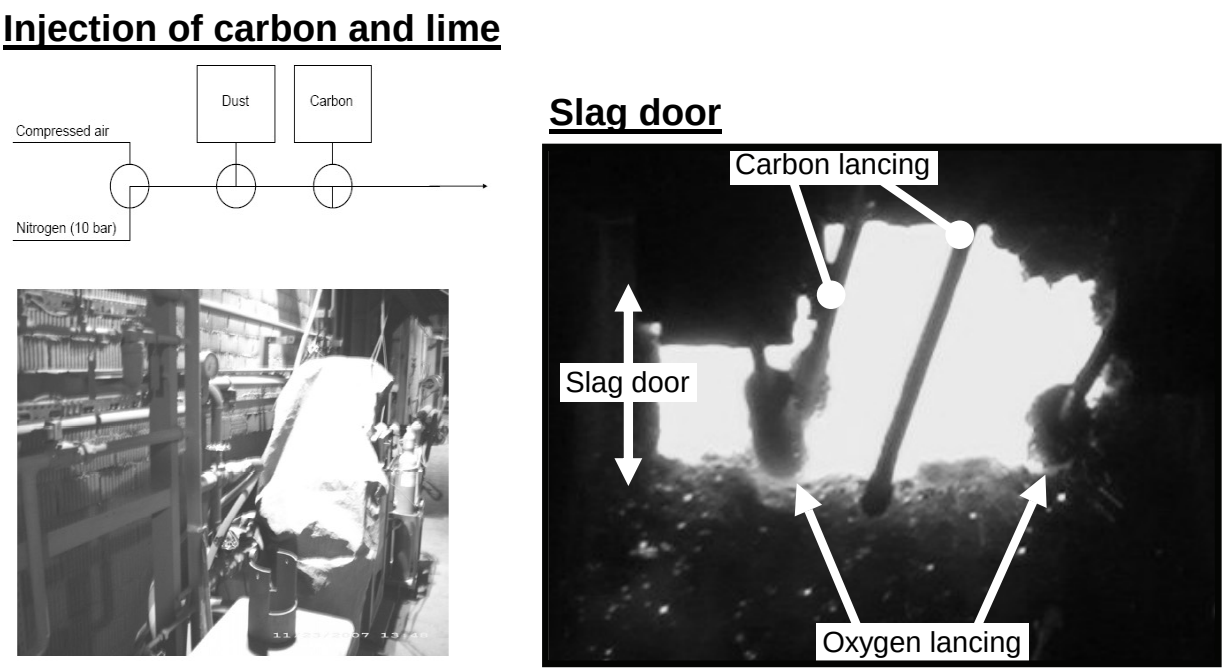

Figure 61: Off-gas analysis system (RWTH) and injection of carbon (left); layout EAF (right)

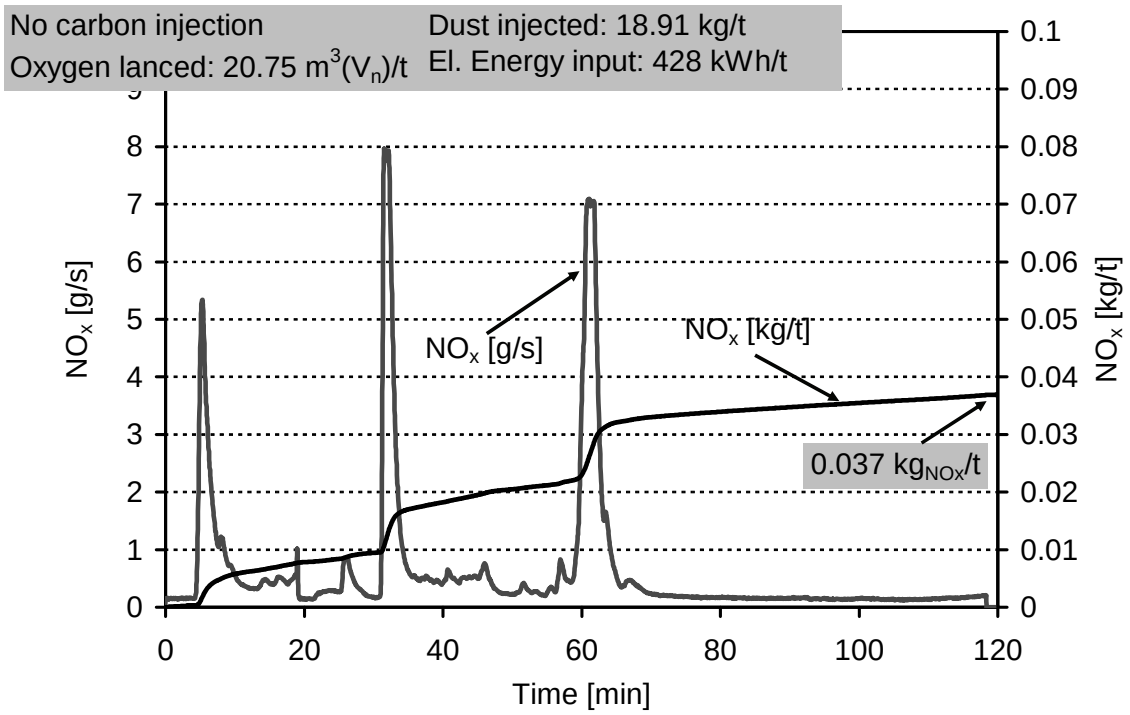

Figure 62: Total NO_x emission and total NO_x mass flow rate (CID 208651, high alloyed)

While melting down there is no oxygen injected. When the scrap is molten oxygen injection starts. As can be seen in **Figure 63** there also is dust injected. **Figure 64** shows the specific CO_2 output in the off-gas related to the process time. The NO_x emission measured while melt down is due to: (a) NO_x formation inside the electric arc in a N_2/O_2 atmosphere; (b) Post combustion reaction in a N_2/O_2 rich atmosphere. While oxygen injection there is power-off. The NO_x emission while oxygen injection is due to: (a) Post combustion reaction in a $CO/H_2/CO_2/N_2/O_2$ atmosphere; (b) Post combustion reaction with air intake.

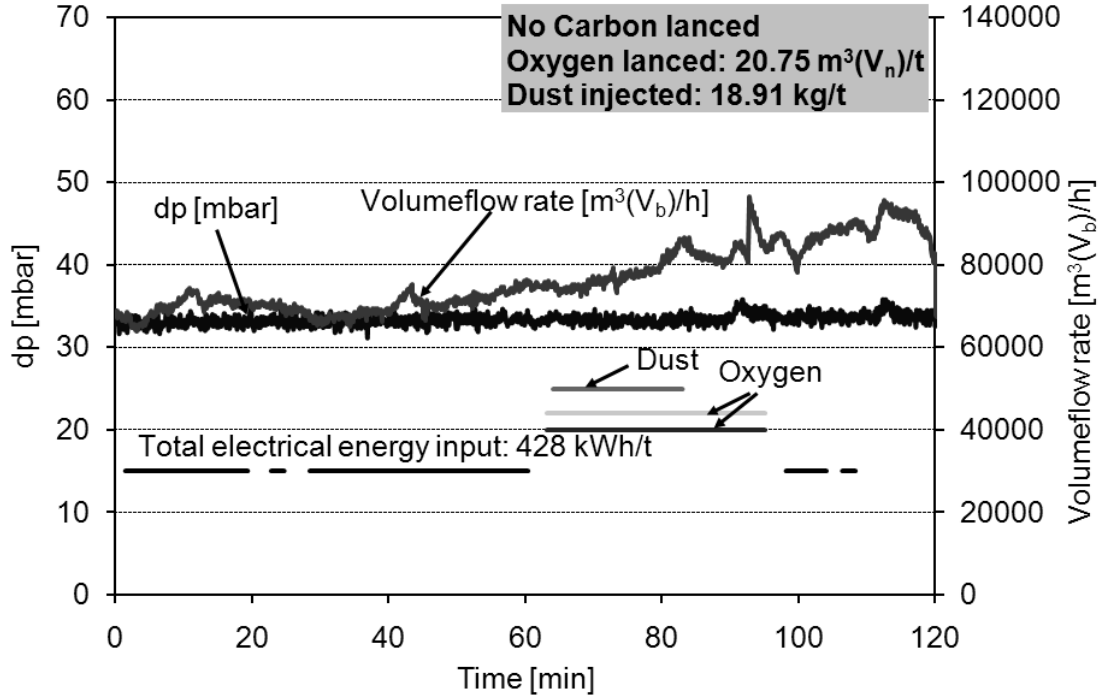

Figure 63: Carbon blowing tests by injection from lance (Cr-Ni) (CID 208649), operational data

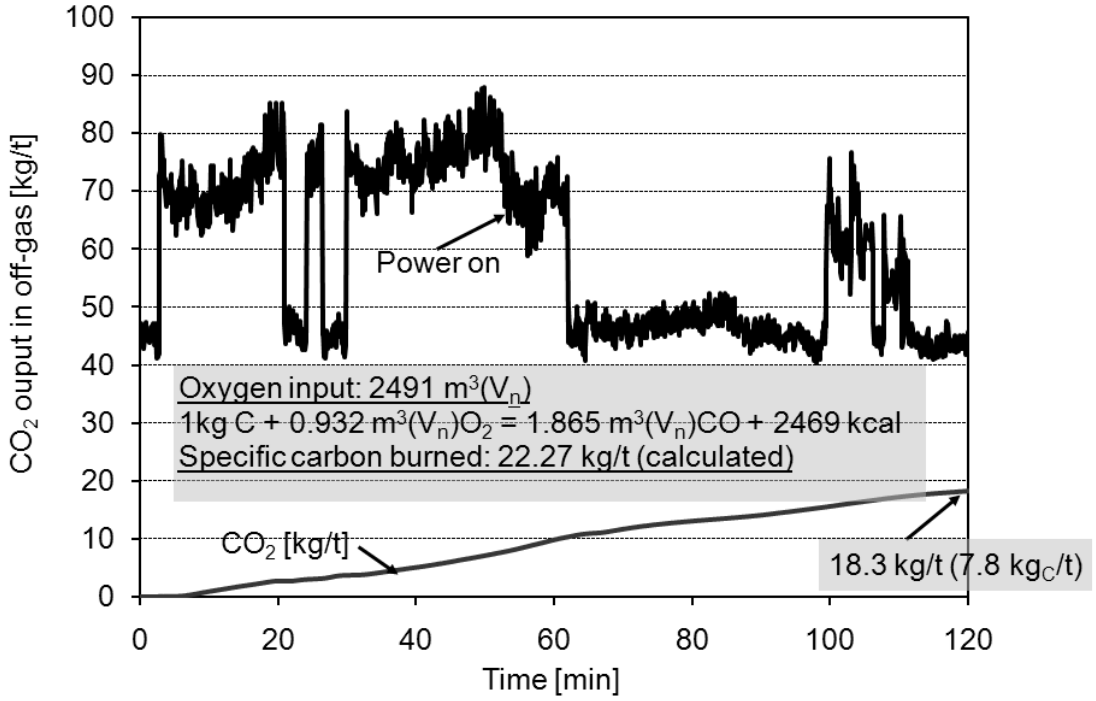

Figure 64: Carbon blowing tests by injection from lance (Cr-Ni) (CID 208649), CO_2 emissions

The total NO_x emission is 0.037 kg/t (86.4 mg/kWh). There are NO_x peaks (5 g/s up to 8 g/s, **Figure 65**) correlated to the power-on signal. While melting there is also NO_x measured (up to 1 g/s). It becomes clear that the amount of NO_x while melting down is significant lower then while starting power-on. This is due to the electric arc and no injection of oxygen. When power-off, oxygen is injected as well as dust. The NO_x is decreasing to very low values. Simultaneously the EAF atmosphere is CO/H_2 rich and there is no O_2 content. NO_x is reburned and there is less NO_x formed too. It clarifies that NO_x reduction measures will have different potential due to the steel produced.

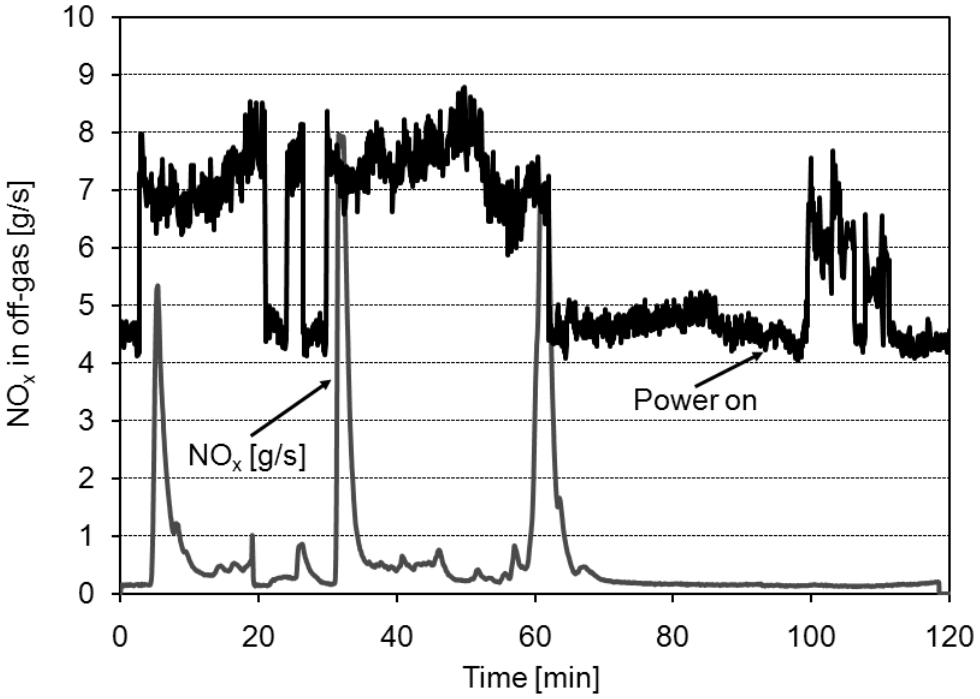

Figure 65: Carbon blowing tests by injection from lance (Cr-Ni) (CID 208649), NO_x emissions

Figure 66 to **Figure 71** show operating data, total CO_2 mass flow rate, and the NO_x mass flow rate. There was 2.12 kg/t and 0.43 kg/t carbon injected respectively. While melting down there is oxygen injection in order to: (a) Accelerate the melt down process; (b) Increase the chemical energy input. Carbon is injected in order to: (a) Foam the slag; (b) Increase the chemical energy input. Foaming slag will decrease the thermal stress of the cooling panels mounted at the EAF side walls. In case of 0.43 kg/t carbon injected there is clear less foaming slag.

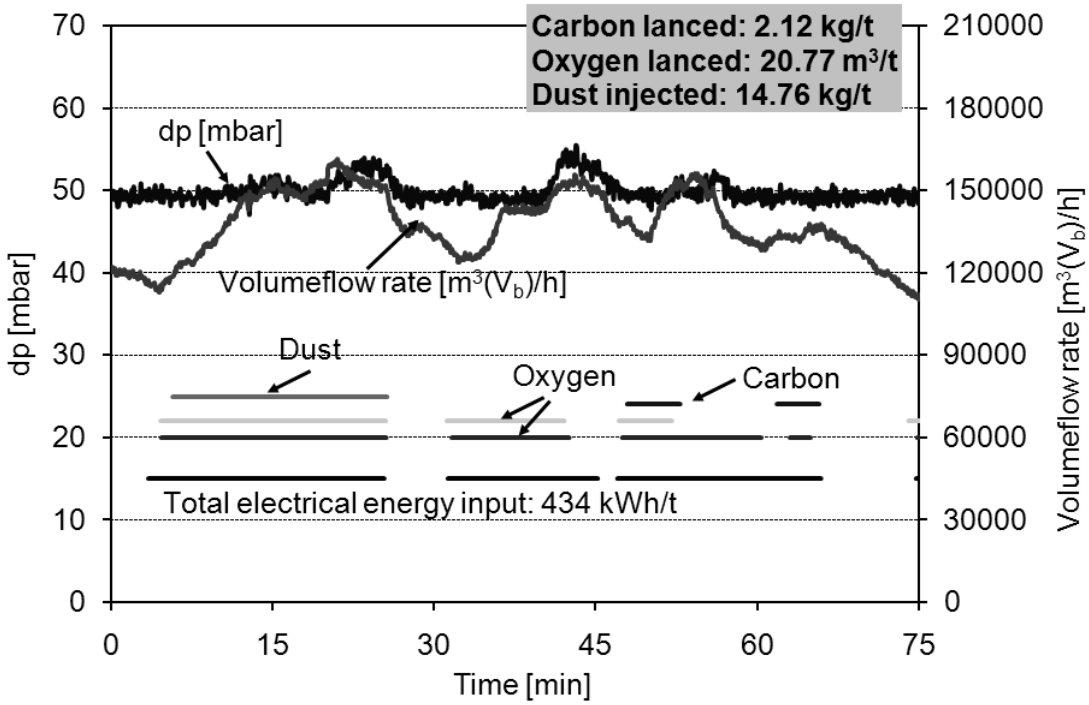

Figure 66: Carbon blowing tests by injection from lance (2.12 kg_C/t) (CID 208621), operational data

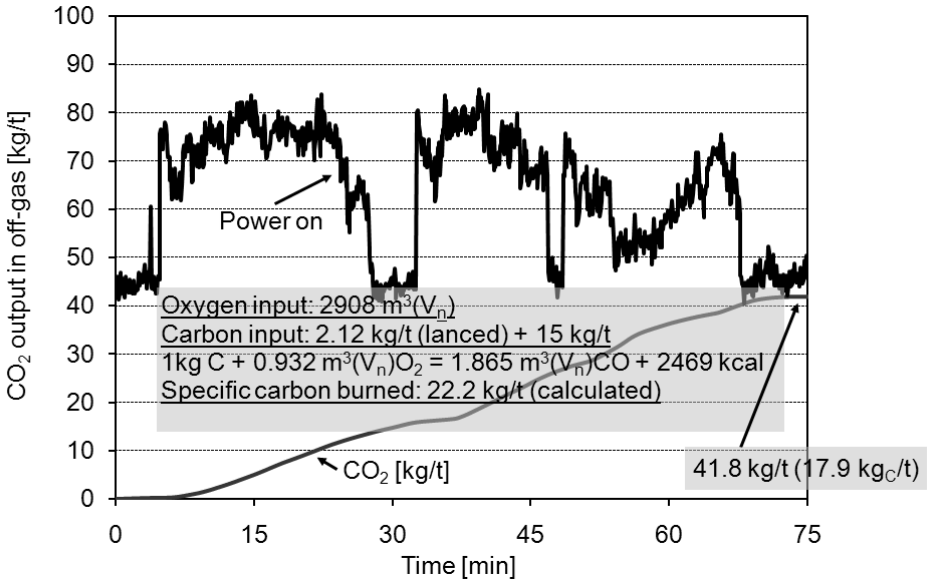

Figure 67: Carbon blowing tests by injection from lance (2.12 kg_C/t) (CID 208621), CO_2 emissions

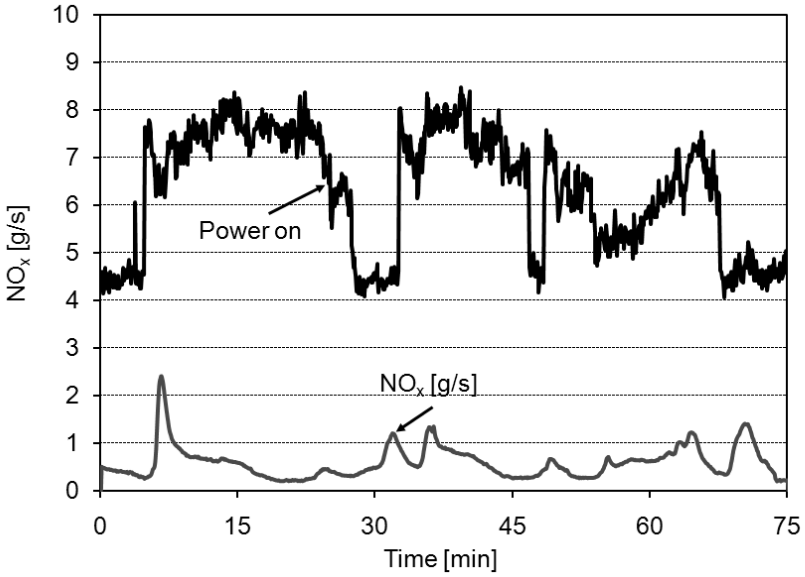

Figure 68: Carbon blowing tests by injection from lance (2.12 kg_C/t) (CID 208621), NO_x emissions

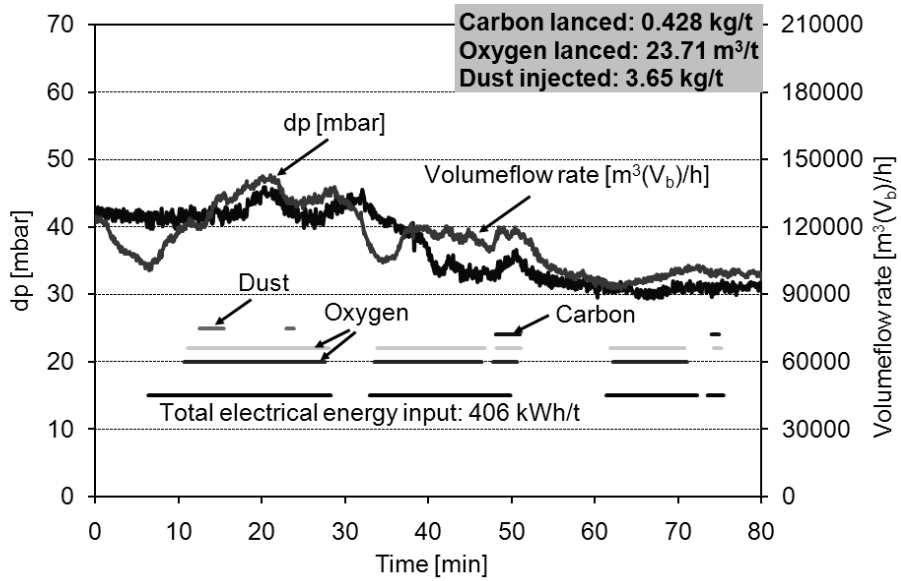

Figure 69: Carbon blowing tests by injection from lance (0.43 kg_C/t) (CID 208643), operational data

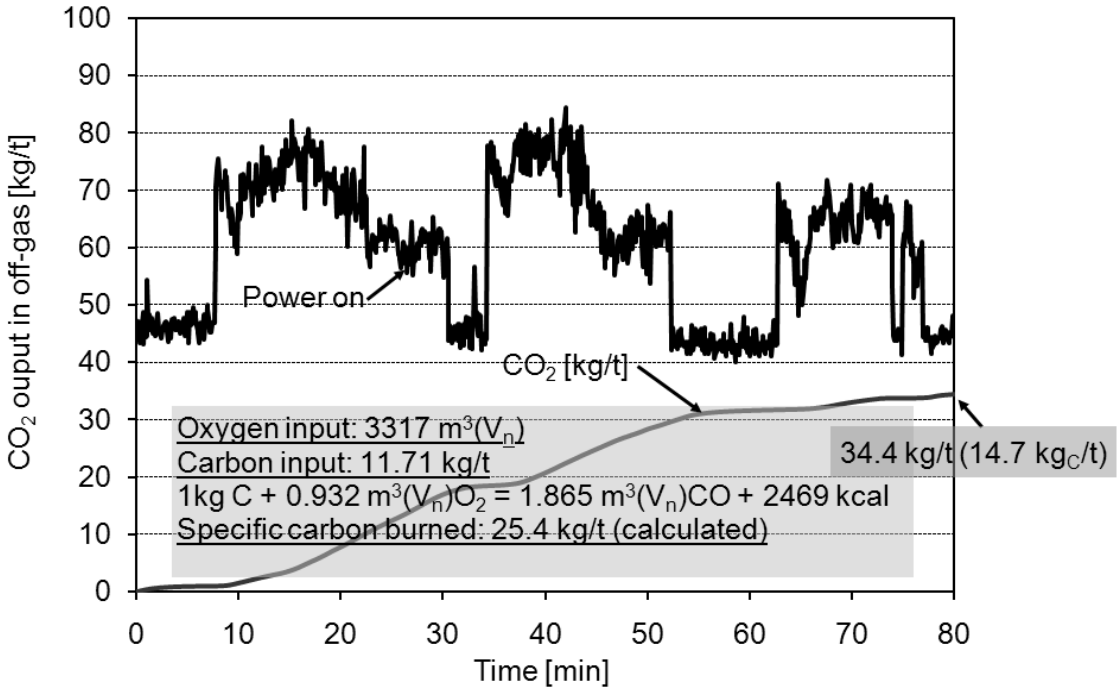

Figure 70: Carbon blowing tests by injection from lance (0.43 kg_C/t) (CID 208643), CO_2 emissions

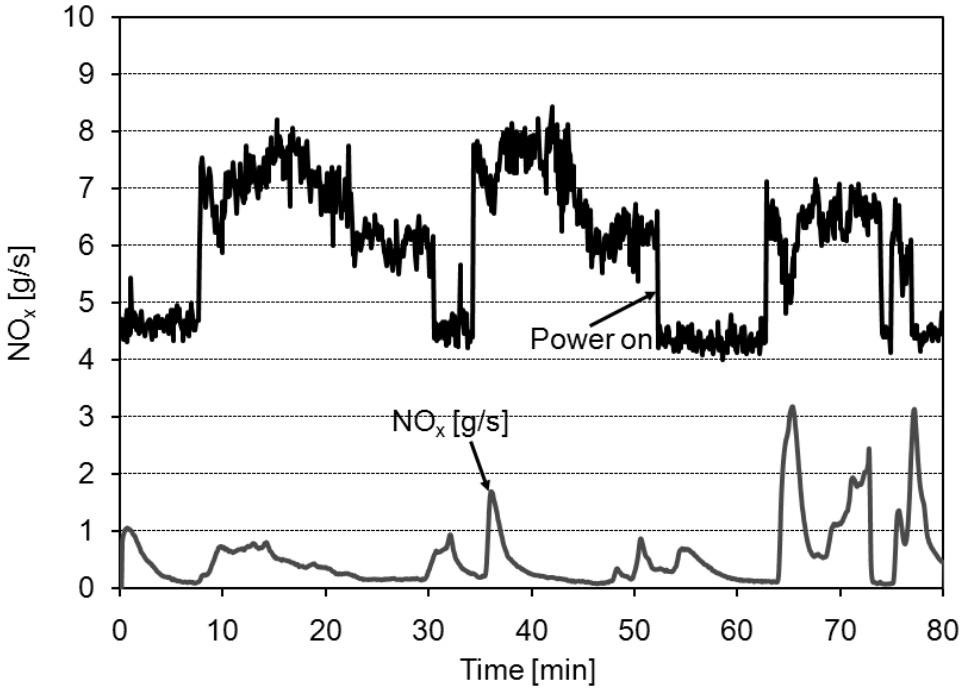

Figure 71: Carbon blowing tests by injection from lance (0.43 kg_C/t) (CID 208643), NO_x emissions

Figure 72 and **Figure 73** show the entire NO_x emission at point B: 0.018 kg/t (41.4 mg/kWh) in case of 2.12 kg/t carbon injected; 0.018 kg/t (44.3 mg/kWh) in case of 0.43 kg/t carbon injected. There is no correlation of NO_x and carbon injection rate.

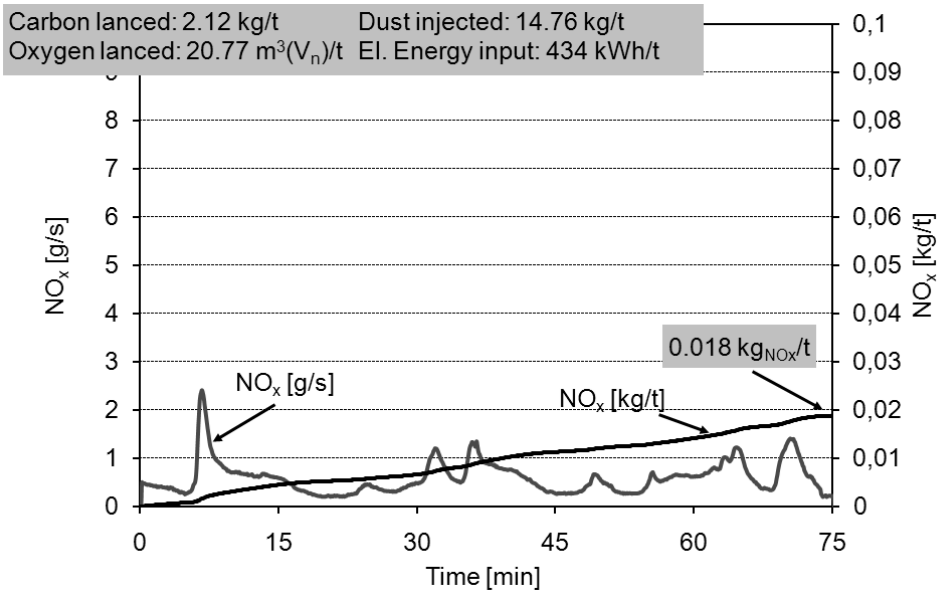

Figure 72: Carbon blowing tests by injection from lance: total NO_x emission and total NO_x mass flow rate (CID 208621)

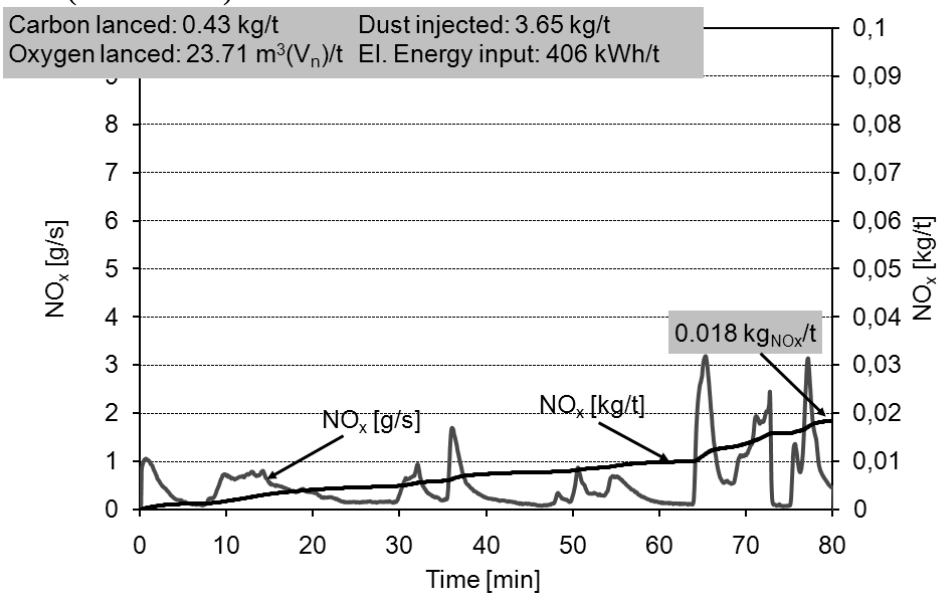

Figure 73: Carbon blowing tests by injection from lance: total NO_x emission and total NO_x mass flow rate (CID 208643)

2.3.4.4 Carbon blowing test by injection inside the burners flame

In 2008 a plant trial program has been conducted at the RIVA EAF to determine the impact of the CoJet ratio and carbon injection on the total NO_x emissions. The accompanying off-gas measurements have been realized simultaneously at point A and point C in the primary dedusting system. In total 35 heats have been evaluated regarding this task.

The data for an exemplary standard procedure heat is shown in **Figure 74** to **Figure 79**. **Figure 74** and **Figure 75** show operational data of the heat over time. When starting of injection of carbon and starting the CoJet burners the off-gas temperature increases up to 1000 °C. Simultaneously the NO_x concentration decreases. **Figure 76** depicts the measured off-gas composition at point A and **Figure 77** the off-gas composition at point C. With increasing air tightness of the EAF vessel, the CO concentration increases while the CO_2 concentration reaches 20 %. The scrap is been charges by two baskets. While starting the melt down of the first and second basket there is a NO_x peak of 1000 ppm. The carbon mass flow rates as well as the total carbon input both calculated based on the off-gas measurements can be seen in **Figure 78**. In **Figure 79** the NO_x measurements for point A and C have been overlaid. It can be seen that the NO_x peaks measured occur at the same time and that due to dilutions effects because of air intake and water injection the value differ by a factor of 10.

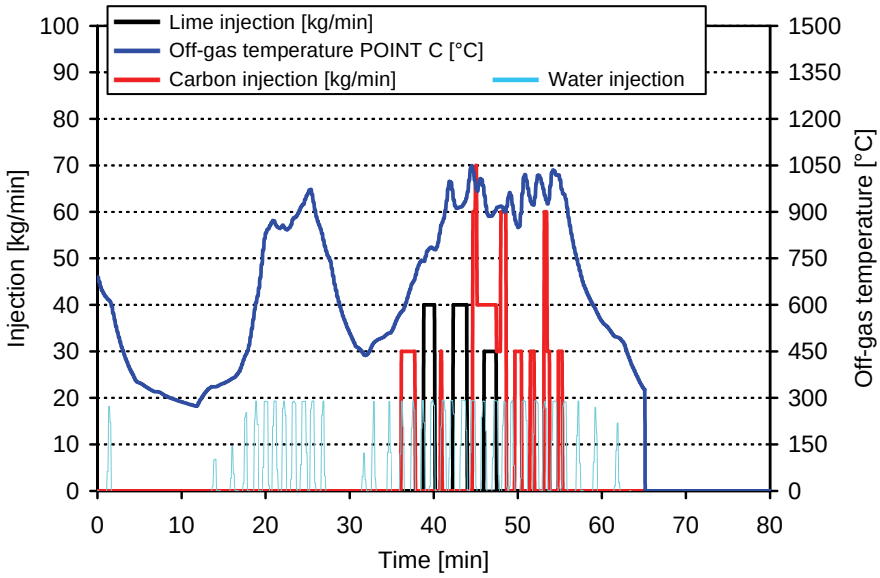

Figure 74: EAF operational data (lime, carbon and water injection, off-gas temperature at point C) for heat 22836

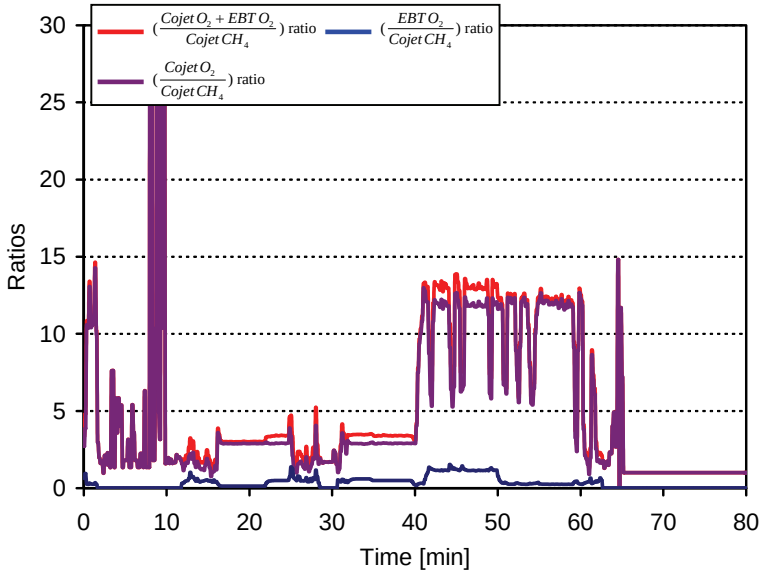

Figure 75: EAF burner ratios for heat 22836

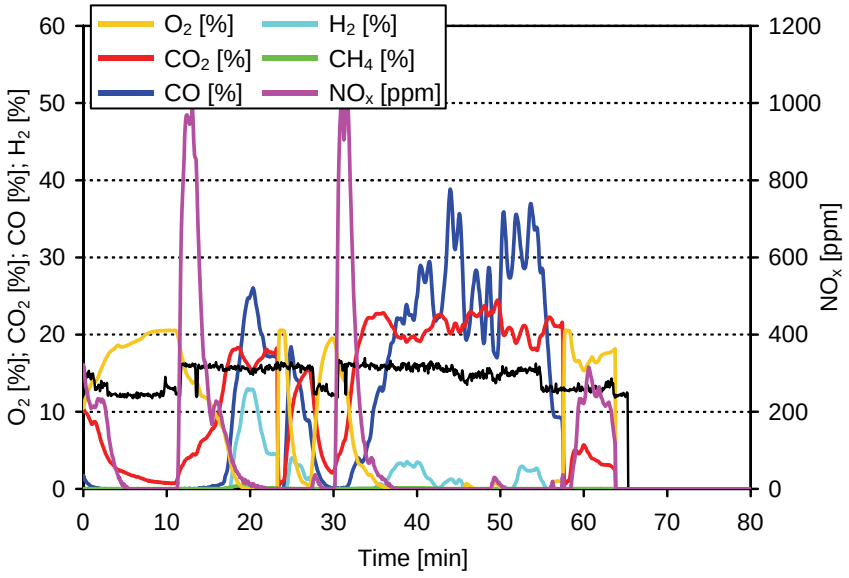

Figure 76: Measured off-gas composition (O_2, CO_2, CO, H_2, NO_x) at point A for heat 22836

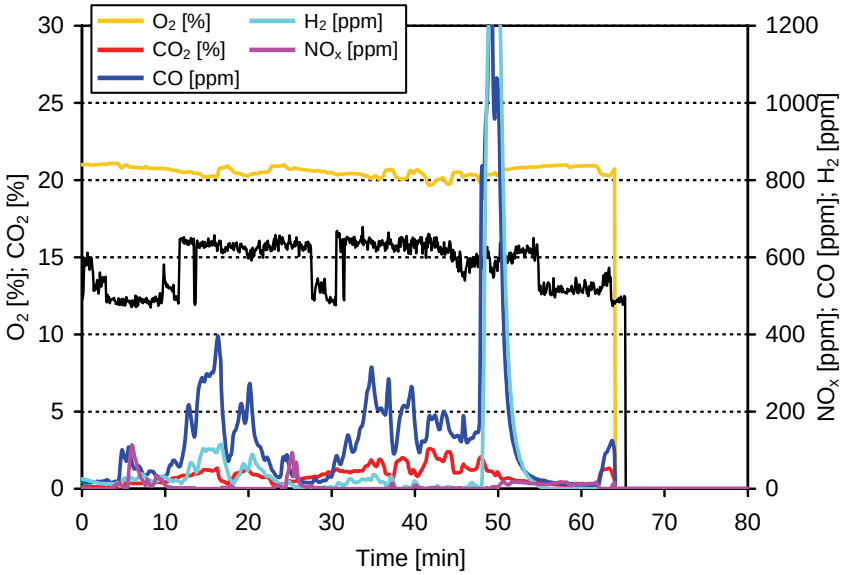

Figure 77: Measured off-gas composition (O_2, CO_2, CO, NO_x) at point C for heat 22836

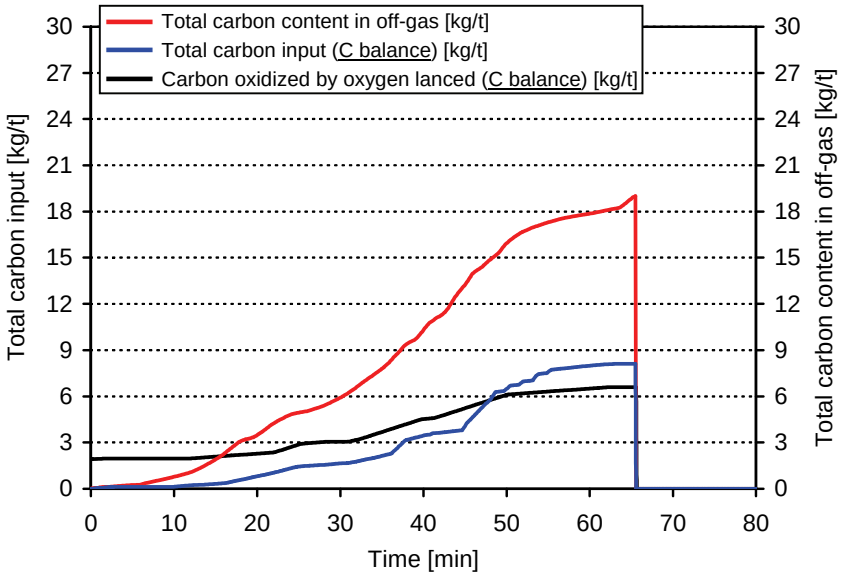

Figure 78: Carbon mass flow rates (C-balance) for heat 22836

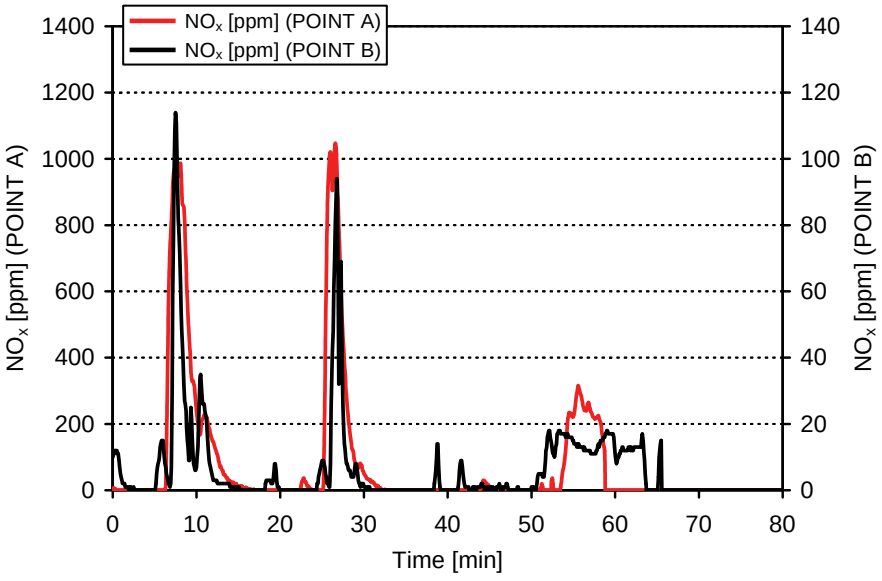

Figure 79: NO_x content in off-gas (point A vs. point C) for heat 22836

The heats have been evaluated regarding mean input and output values for carbon, oxygen and NO_x. These data are presented in Sankey diagrams. Equation (22) describes the carbon mass balance used to evaluate the heats and **Figure 80** shows the Sankey diagram for the carbon conversion within the process. Carbon is injected in order to: (a) Foam the slag; (b) Increase the energy efficiency. The average direct carbon input (11 kg/t) is composed of (a) CH_4 injection through CoJet (6 kg/t) and (b) carbon injection (5 kg/t). The total carbon output in the off-gas is in average 16 kg/t.

$$\sum_{\text{scrap i}} x_{C,i} m_i + \sum_{\text{alloy i}} x_{C,i} m_i + x_{C,\text{carbon}} m + x_{C,CH_4} \int \dot{m}\, dt + x_{C,HC} (x\, m) + \\ x_{C,\text{electrode}} m = x_{C,\text{steel}} m + \sum_{i=co,co_2} \int x_{C,i}\, \dot{m}\, dt \tag{22}$$

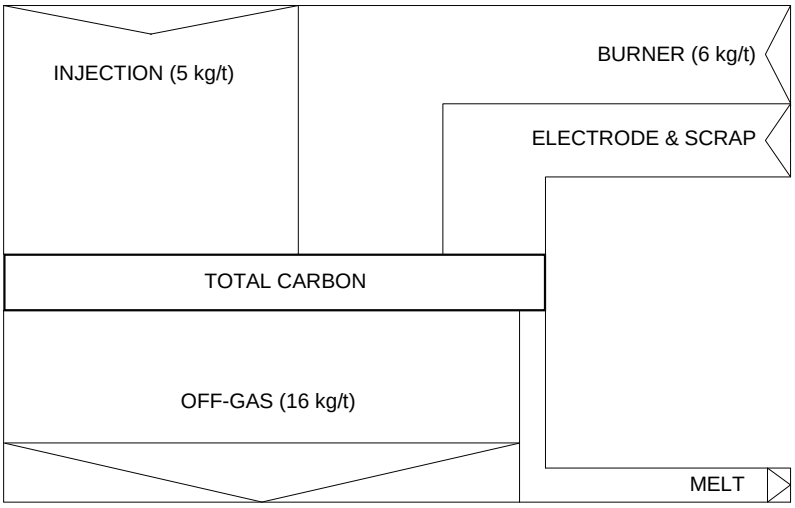

Figure 80: Sankey diagram carbon

$$m_{\text{injected } O_2} + \sum_{\text{alloy i}} x_{O,i} m_i + \sum_{\text{refractory i}} x_{O,i} m_i + \sum_{\text{scarp i}} x_{O,i} m_i + \int x_{O,\text{air intake}} \dot{m}\, dt = \\ \sum_{\text{slag i}} x_{O,i} m_i + \sum_{\text{dust i}} x_{O,i} m_i + M_O \dot{n}_{\text{off-gas}} \left(x_{CO} + 2\, x_{CO_2} + 2\, x_{O_2} + x_{H_2O} \right) \tag{23}$$

To calculate the oxygen mass balance equation (23) has been used. Oxygen is injected (a) throughout the CoJet burners in order to enhance the melting of scrap and to increase the chemical energy input and (b) for the post combustion of CO and H_2 inside the EAF vessel. The overall average oxygen input is 35 kg/t and the average oxygen output 34 kg/t. **Figure 81** shows the Sankey diagram for the oxygen conversion.

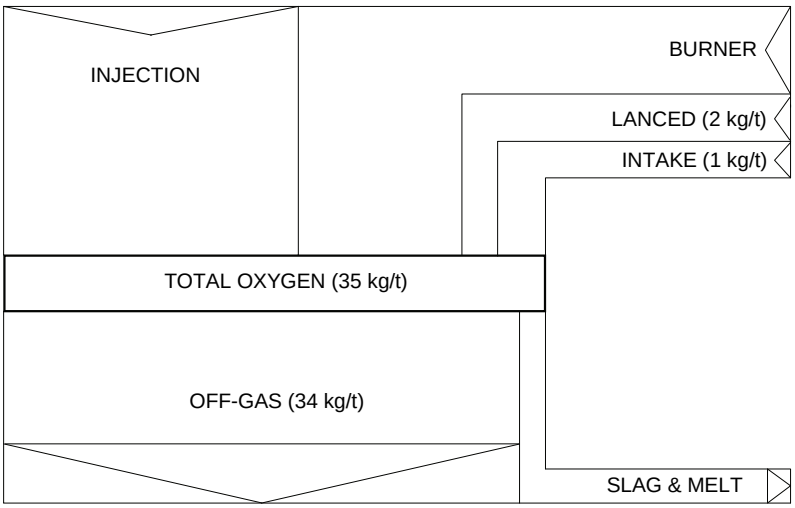

Figure 81: Sankey diagram Oxygen

The general Sankey diagram for the NO_x conversion in the EAF is shown in **Figure 82**. Sources for NO_x are (a) the electric arc, (b) burners and (c) post combustion inside the EAF and in the post combustion chamber. Sinks for NO_x within the Sankey diagram are (a) the off-gas leaving the primary dedusting system and (b) the reburning of NO_x in CO/H2 rich off-gas atmosphere.

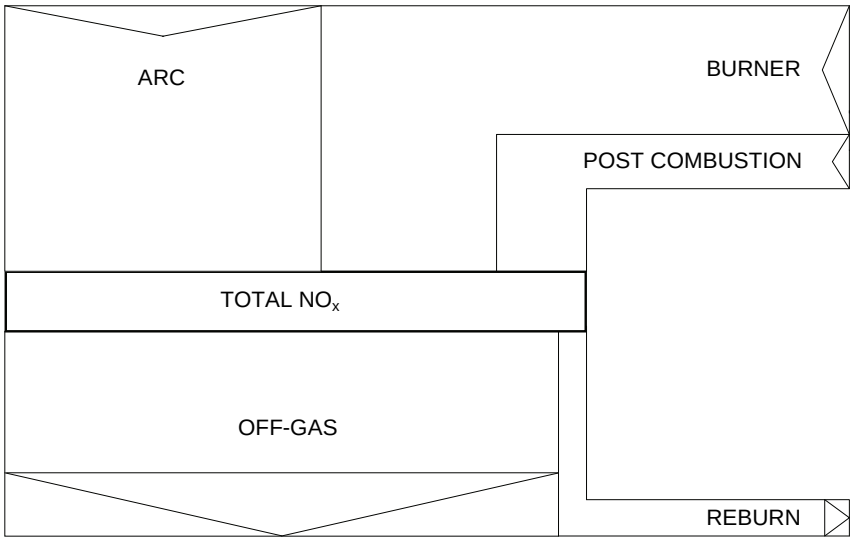

Figure 82: Sankey diagram NO_x

Regarding the influence of injected inside the burner flame **Figure 83** shows the measured total NO_x emission (point A) vs. the carbon injection. The carbon injection has been increased up to 12 kg/t (total carbon input increased up to 18 kg/t). There is no correlation of NO_x and carbon injection rate which could be deducted from this diagram. This is in agreement with the results obtained at DEWG EAF (WP 4.3).

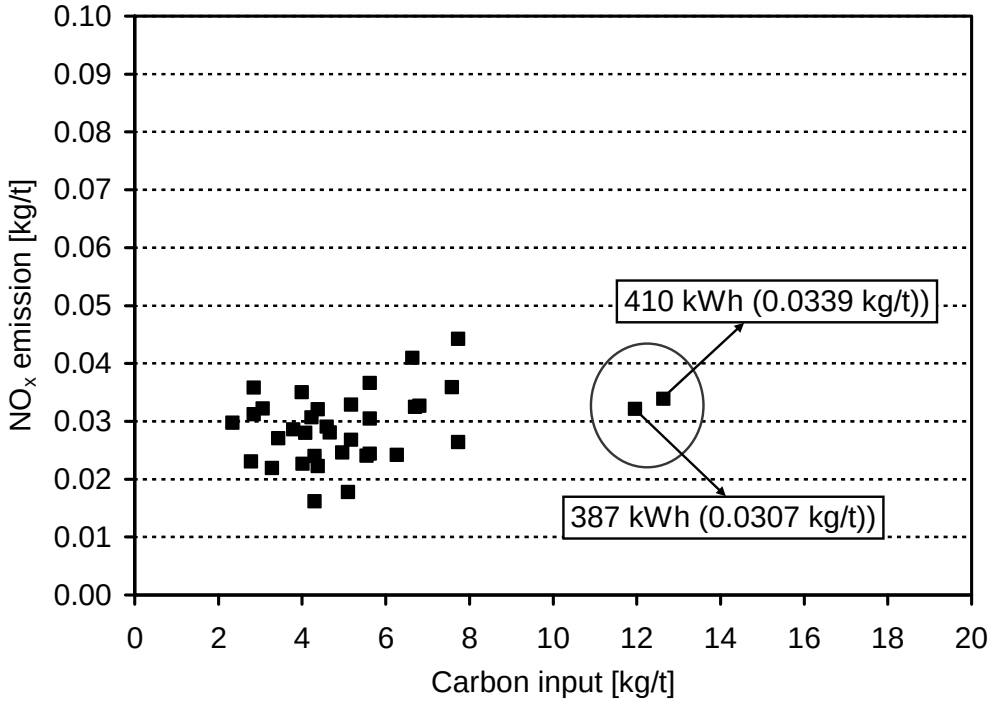

Figure 83: Carbon blowing test by injection inside the burners flame vs. total NO_x emission in off-gas at point A (plant trial: see circle)

Figure 84 shows the total NO_x emission (point A) vs. the total carbon content in off-gas. There is no correlation of the carbon content in off-gas (10 kg/t to 25 kg/t (additional carbon input: 6.9 kg/t (CH_4 and C injection)) and total NO_x emission (0.015 kg/t to 0.045 kg/t). The total NO_x emission (2008) is comparable to the data in 2006 (0.005 kg/t to 0.055 kg/t). In 2006 the total NO_x emission has been investigated at point B (2008 at point A).

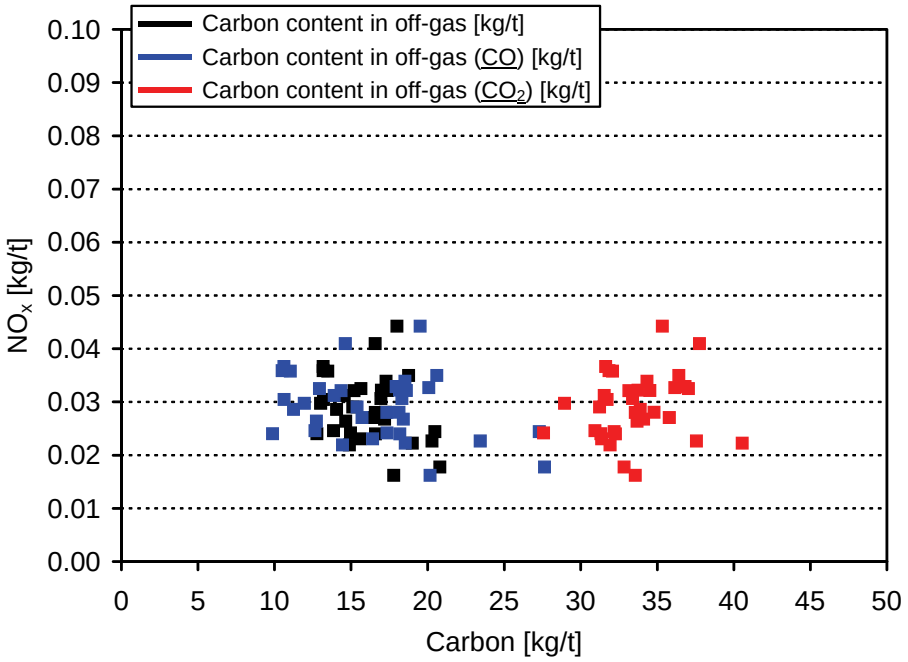

Figure 84: Carbon blowing test by injection inside the burners flame: specific carbon content in off-gas vs. total NO_x emission in off-gas at point A

Two additional trials with CoJet ratios of 15 and 20 have been conducted. **Figure 86** shows operational and measurement data for the trial with a CoJet ratio of 15. Depicted are the CoJet ratio and the measured off-gas composition at point A over time. **Figure 87** shows the same data for the trial with a CoJet ratio of 20. The amounts of CO and H_2 measured are noticeably smaller and the NO_x peaks measured are higher when working with a ratio of 20.

Figure 85 shows the correlation of the total NO_x (point A) vs. the carbon content in the off-gas. In case of a CoJet ratio of 15 the total NO_x emission decreases to 0.018 kg/t (0.029 kg/t average). In case of a CoJet ratio of 20 there the total NO_x emission increases to (0.025 kg/t) (0.029 kg/t average).

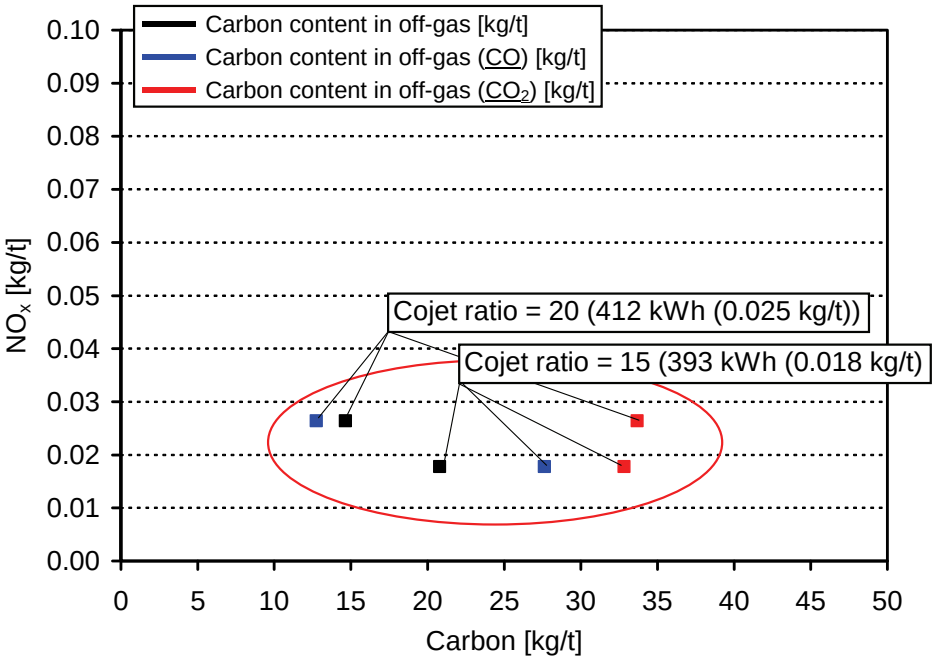

Figure 85: Specific carbon content vs. total NO_x emission in the off-gas at point A for two different CoJet ratios

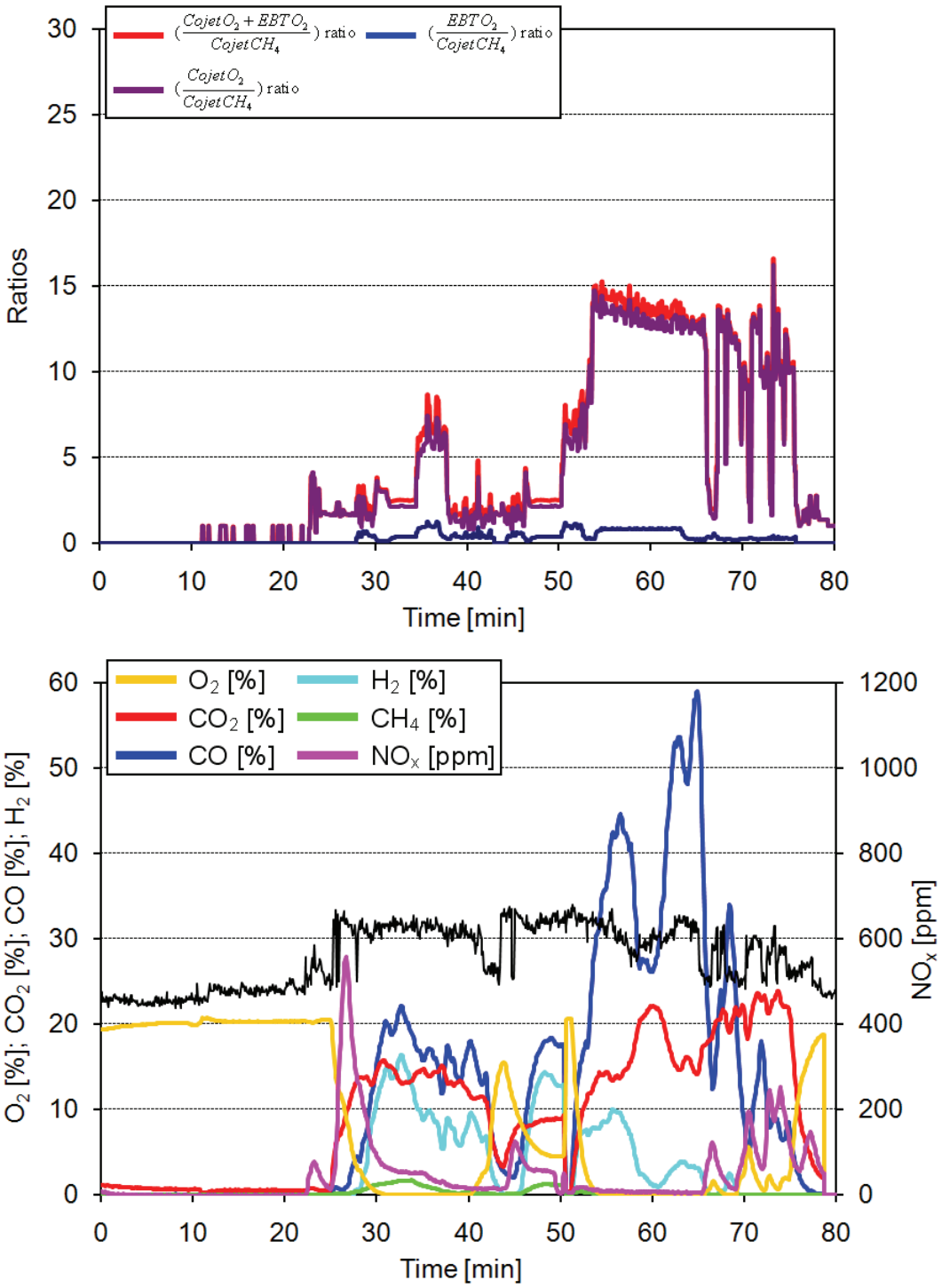

Figure 86: Measurement and operational data for plant trial with CoJet ratio 15 (heat 22773)

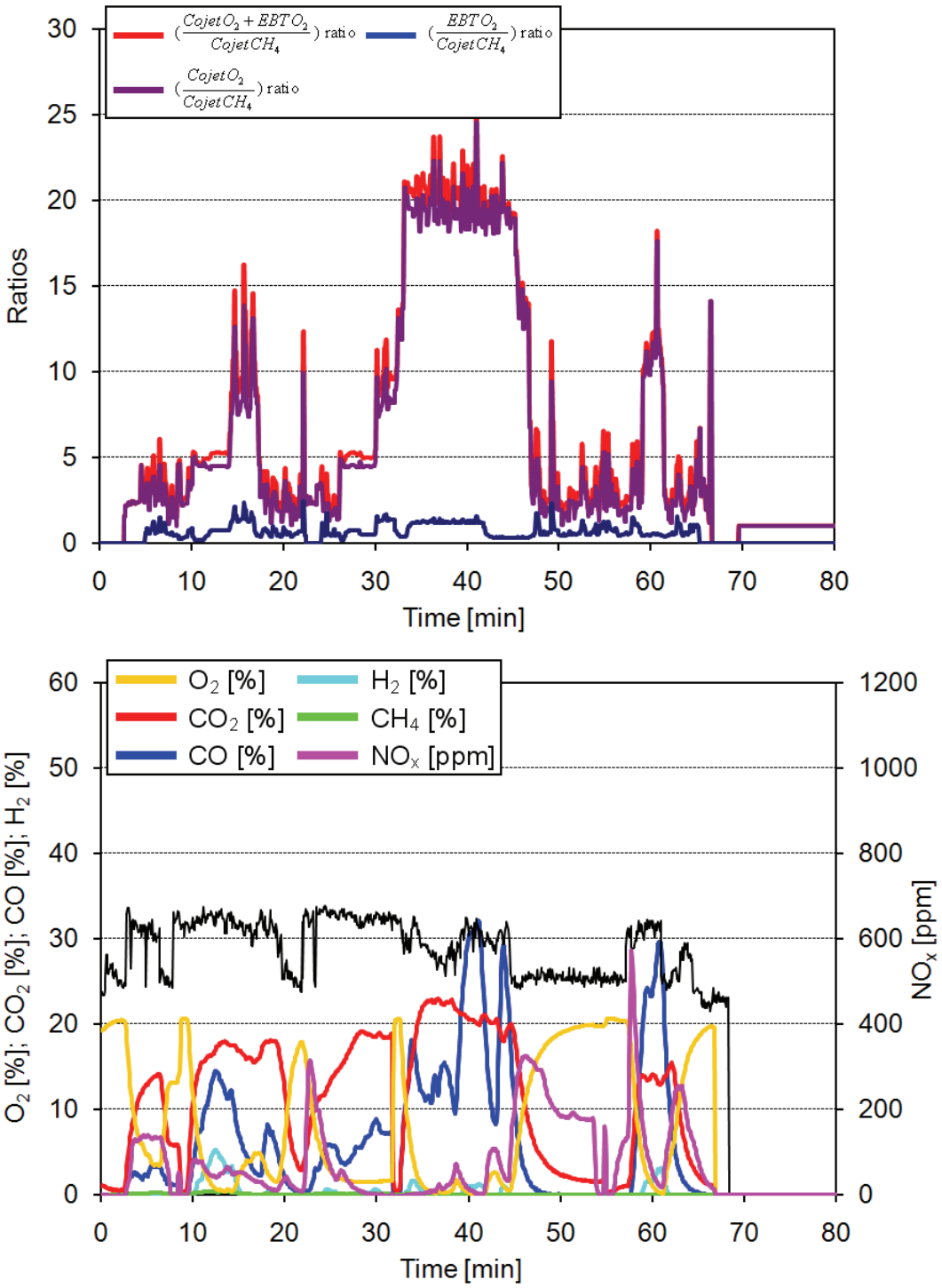

Figure 87: Measurement and operational data for plant trial with CoJet ratio 20 (heat 22772)

2.3.4.5 Exhaust gas analysis to control: burner parameters, oxygen/inert gas flow rate, post combustion level, estimation of partial pressure of O_2 in the furnace, NO_x generation

From the beginning of the project till the end of 2008 a number of off-gas measurement and plant trial campaigns have been conducted at the EAFs of RIVA and DEWG. An overview of the campaigns is given in **Table 17**.

Table 17: Off-gas measurement and plant trials campaigns at DEWG and RIVA

Campaign	Furnace	Point A	Point B/C
10/2006	RIVA	composition, temperature	composition
06/2007	DEWG	composition	composition, temperature, flow rate
11/2007	DEWG		composition, temperature, flow rate
12/2007	RIVA		composition
05/2008	RIVA	composition, temperature, flow rate	composition
11/2008	DEWG		composition, temperature, flow rate

At DEWG the campaigns were successfully performed in order to control important operational parameters like (a) dust injection, (b) oxygen lancing and (c) coal lancing (see section 2.3.4.1 and 2.3.4.3). Those parameters seem to influence the NO_x formation as well as reburn of formatted NO_x.

At RIVA burner parameter, injection of oxygen and carbon was controlled. The effect has been reported in section 2.3.4.2 and 2.3.4.4. There is a decreasing of NO_x emission due to control of the burners/EBT parameters and no effect within control of the carbon injection. When carbon is injected there has been no NO_x detected. So the effect decreasing the total amount of carbon injected is not to be correlated to total NO_x emission. The effect of variation of EBT parameters seems to decrease the total NO_x emission because of the entire duration of the period while the EBT/CoJet burners are on. The total oxygen input (average 35 kg/t) is been mainly injected by EBT and CoJet burners after feeding the 2nd basket. The injection of carbon and lime is been performed with oxygen too. This practice is not correlated with NO_x emission.

2.3.4.6 Collecting data and steel sampling

Over the course of the project off-gas measurement results together with operational data and steel samples have been collected. Additionally mass balances have been used extensively to calculate the amount of materials charged and discharged per element. **Table 18** to **Table 23** show exemplary data collected at DEWG. **Table 18** and **Table 19** comprise data of materials charged per heat. **Table 20**and **Table 21** present amounts of tapped steel as well as the composition of steel samples. **Table 22** and **Table 23** show the data of materials discharged per heat calculated from measurements and mass balances. **Table 24** and **Table 25** show similar data collected at RIVA.

Table 18: Data of materials charged per heat calculated by mass balances, DEWG

No.	C^{A}_{IN}	Si^{B}	Mn^{C}	Cr^{D}	Mo^{E}	Ni^{F}	$O_2{}^{G}$	$DUST^{H}$	C^{I}	C^{J}
	[kg]	[kg]	[kg]	[kg]	[kg]	[kg]	[m_3(STP)]	[kg]	[kg]	[kg]
201043	2428	410	810	543	78	235	2785	1691	460	1600
201045	2318	426	838	478	77	201	2910		320	1600
201047	2355	410	805	561	75	240	2940	2250	380	1600
201049	2592	409	805	491	76	242	3090	2240	800	1640
201053	2314	404	751	282	63	182	3063		440	1620
201055	2242	387	752	296	69	189	3443		420	1640
201057	2614	382	756	295	68	190	3053		820	1600
201059	2373	392	769	307	76	201	3220		480	1640
201061	2526	443	893	552	83	238	2520		350	1600
201063	2446	441	890	579	82	250	2850	613	300	1660
∅	2421	410	807	438	75	217	2987	1699	477	1620

A,I,J:

$$\left(\sum_{\text{Scrap i}} x_{C,i}\, m_i\right)^{A} + \left(\sum_{\text{Basket i}} x_{C,i}\, m_i\right)^{A,J} + \left(x_{C,\text{Carbon}}\, m\right)^{A,I} + \left(x_{C,CH_4} \int \dot{m}\, dt\right) + \left(x_{C,\text{Electrode}}\, m\right)$$

$$= \left(x_{C,\text{Melt}}\, m\right) + \left(\sum_{i=CO,CO_2,CH_4} \int x_{C,i}\, \dot{m}\, dt\right)$$

B,..,F:

$$\left(\sum_{\text{Scrap i}} x_{Me,i}\, m\right)^{B,..,F} + \left(\sum_{\text{Bucket i}} x_{Me,i}\, m\right)^{B,..,F} + \left(x_{Me,\text{Refractory}}\, m\right)$$

$$= \left(x_{Me,\text{Melt}}\, m\right) + \left(x_{Me,\text{Slag}}\, m\right) + \left(x_{Me,\text{Dust}}\, m\right)$$

$$\left(\sum_{\text{Dust i}} x_{O,i}\, m\right) = x_{O,FeO}\, m_{FeO,\text{Dust}} + x_{O,CaO}\, m_{CaO,\text{Dust}} + x_{O,MgO}\, m_{MgO,\text{Dust}} + x_{O,SiO_2}\, m_{SiO_2,\text{Dust}}$$

$$+ x_{O,Al_2O_3}\, m_{Al_2O_3,\text{Dust}} + x_{O,Cr_2O_3}\, m_{Cr_2O_3,\text{Dust}}$$

G,H:

$$\left(m_{\text{Lance } O_2}\right)^{G} + \left(\sum_{\text{Basket i}} x_{O,i}\, m\right) + \left(\sum_{\text{Refractory i}} x_{O,i}\, m\right) + \left(\sum_{\text{Scrap i}} x_{O,i}\, m\right)$$

$$+ \left(\int x_{O,\text{Air}}\, \dot{m} dt\right) + \left(\sum_{\text{Dust i}} x_{O,i}\, m\right)^{H} = \left(\sum_{\text{Slag i}} x_{O,i}\, m\right) + \left(M_O \dot{n}_{\text{off-gas}} \left(x_{CO} + 2\, x_{CO_2} + 2\, x_{O_2}\right)\right)$$

Table 19: Data of materials charged per heat calculated by mass balances, DEWG

No.	Group	C[A] [kg]	Si[B] [kg]	Mn[C] [kg]	Cr[D] [kg]	Mo[E] [kg]	Ni[F] [kg]	O_2[G] [m_3(STP)]	DUST[H] [kg]	FESI[I] [kg]	FESI[J] [kg]
200857	14404009	1562	2306	1355	20672	1409	12253	1500	1100	1200	291
200861	14305003	1087	2339	1643	23055	410	10412	969	1190	1298	291
200863	14305003	1087	2340	1627	22910	406	10299	974	1050	1300	295
200865	14305003	1087	2341	1629	22928	406	10541	965	1100	1300	297
200867	14435050	1144	2591	1559	21279	2282	14844	1006	1621	1600	290
200869	14404054	1183	2595	1507	20775	2197	13354	1033	1800	1600	297
200871	14404009	1021	1461	2069	18390	2299	12069	652		800	300
200873	14404009	1124	2599	1583	21511	2224	13217	1019	1621	1604	297
200875	14404009	1124	2254	1585	21479	1357	12287	1038	1781	1200	297
200877	14307050	1159	2374	2096	24245	447	9779	1328	2000	1300	296
200879	14307050	1151	2364	2060	24138	447	9733	1307	2040	1300	299
200881	14307050	1151	2371	2039	24176	447	9731	1334	1900	1300	297
200883	14546001	1709	2477	1093	22285	277	10991	2020	2300	1200	296
	∅	1268	2192	1621	20608	1058	10741	1165	1500	1308	296

A:

$$\left(\sum_{\text{Scrap i}} x_{C,i}\, m_i\right)^{A} + \left(\sum_{\text{Basket i}} x_{C,i}\, m_i\right)^{A} + \left(x_{C,\text{Carbon}}\, m\right)^{A} + \left(x_{C,CH_4} \int \dot{m}\, dt\right) + \left(x_{C,\text{Electrode}}\, m\right)$$

$$= \left(x_{C,\text{Melt}}\, m\right) + \left(\sum_{i=CO,CO_2,CH_4} \int x_{C,i}\, \dot{m}\, dt\right)$$

B,..,F,I,J:

$$\left(\sum_{\text{Scrap i}} x_{Me,i}\, m\right)^{B,..,F} + \left(\sum_{\text{Bucket i}} x_{Me,i}\, m\right)^{B,..,F,I} + \left(x_{Me,\text{Refractory}}\, m\right) + \left(x_{Me,\text{Lance}}\, m\right)^{J}$$

$$= \left(x_{Me,\text{Melt}}\, m\right) + \left(x_{Me,\text{Slag}}\, m\right) + \left(x_{Me,\text{Dust}}\, m\right)$$

G:

$$\left(m_{\text{Lance}\,O_2}\right)^{G} + \left(\sum_{\text{Basket i}} x_{O,i}\, m\right) + \left(\sum_{\text{Refractory i}} x_{O,i}\, m\right) + \left(\sum_{\text{Scrap i}} x_{O,i}\, m\right)$$

$$+ \left(\int x_{O,\text{Air}}\, \dot{m} dt\right) + \left(\sum_{\text{Dust i}} x_{O,i}\, m\right) = \left(\sum_{\text{Slag i}} x_{O,i}\, m\right) + \left(M_O \dot{n}_{\text{off-gas}} \left(x_{CO} + 2\, x_{CO_2} + 2\, x_{O_2}\right)\right)$$

$$\left(\sum_{\text{Dust i}} x_{O,i}\, m\right) = x_{O,FeO}\, m_{FeO,\text{Dust}} + x_{O,CaO}\, m_{CaO,\text{Dust}} + x_{O,MgO}\, m_{MgO,\text{Dust}}$$

$$+ x_{O,SiO_2}\, m_{SiO_2,\text{Dust}} + x_{O,Al_2O_3}\, m_{Al_2O_3,\text{Dust}} + x_{O,Cr_2O_3}\, m_{Cr_2O_3,\text{Dust}}$$

Table 20: Tapped steel and composition of steel sample, DEWG

No.	Tapped [kg]	C [%]	Si [%]	Mn [%]	P [%]	S [%]	Cr [%]	Mo [%]	Ni [%]	Al [%]	Fe [%]	N [%]
201043	131400	0.067	0	0.120	0.007	0.064	0.17	0.05	0.17	0.519	98.7	0.067
201045	125000	0.075	0	0.110	0.005	0.045	0.14	0.04	0.13	0.399	98.9	0.075
201047	138800	0.064	0	0.070	0.007	0.052	0.09	0.04	0.15	0.409	99.0	0.064
201049	131936	0.063	0	0.080	0.005	0.035	0.08	0.03	0.14	0.483	99.0	0.063
201053	134100	0.06	0	0.070	0.006	0.072	0.10	0.04	0.12	0.383	99.1	0.060
201055	133000	0.065	0	0.080	0.006	0.065	0.11	0.04	0.14	0.428	99.0	0.065
201057	133000	0.070	0	0.070	0.007	0.054	0.13	0.05	0.15	0.523	98.8	0.070
201059	140100	0.049	0	0.050	0.007	0.05	0.07	0.04	0.13	0.623	98.9	0.049
201061	136200	0.062	0	0.090	0.005	0.067	0.13	0.04	0.15	0.417	98.9	0.062
201063	135700	0.086	0	0.060	0.006	0.075	0.10	0.06	0.23	0.414	98.8	0.086
∅	133903	0.066	0	0.080	0.006	0.057	0.11	0.04	0.14	0.466	98.9	0.066

Table 21: Tapped steel and composition of steel sample, DEWG

No.	Tapped [kg]	C [%]	Si [%]	Mn [%]	P [%]	S [%]	Cr [%]	Mo [%]	Ni [%]	Al [%]	Fe [%]	N [%]
200857	110600	0.665	0.030	0.890	0.026	0.024	17.0	1.04	10.9	0	69.3	0.0239
200861	110000	0.520	0.020	0.670	0.029	0.316	17.6	0.35	7.6	0	72.7	0.0255
200863	116100	0.523	0.040	0.730	0.030	0.336	17.6	0.31	7.7	0	72.6	0.0241
200865	116900	0.602	0.150	0.820	0.029	0.326	18.3	0.34	7.8	0	71.5	0.0236
200867	118000	0.581	0.090	0.760	0.027	0.039	16.9	1.69	11.2	0	68.5	0.0257
200869	116000	0.556	0.060	0.690	0.026	0.043	17.1	1.70	10.5	0.007	69.1	0.0249
200871	115700	0.439	0.020	1.130	0.030	0.027	15.5	1.47	9.6	0	71.5	0.0407
200873	112600	0.495	0.070	0.640	0.027	0.032	16.5	1.67	10.2	0	70.1	0.0280
200875	116000	0.595	0.050	0.750	0.026	0.044	16.8	0.96	9.3	0	71.2	0.0308
200877	110000	0.520	0.020	1.280	0.030	0.026	18.0	0.29	7.6	0	72.0	0.0358
200879	116000	0.559	0.140	1.240	0.030	0.022	17.5	0.28	6.7	0	73.4	0.0291
200881	112000	0.742	0.180	1.050	0.029	0.026	18.0	0.26	7.3	0	72.2	0.0276
200883	105000	0.510	0.050	1.270	0.024	0.028	18.8	0.20	8.9	0	70.1	0.0346
∅	119485	0.524	0.075	0.859	0.0262	0.095	16.1	0.76	8.2	0.004	73.0	0.0277

Table 22: Data of materials discharged per heat calculated by mass balances, DEWG

No.	C^{A} [kg]	Si^{B} [kg]	Mn^{C} [kg]	P^{D} [kg]	S^{E} [kg]	Cr^{F} [kg]	Mo^{G} [kg]	Ni^{H} [kg]	Al^{I} [kg]	N^{J} [kg]	C^{K} [kg]	NO_x^{L} [g]	NO_x^{L} [kg/t]	NO_x^{N} [g]
201043	88	0	158	9	84	223	66	223	682	88	2100	1390	0.011	800
201045	94	0	138	6	56	175	50	163	499	94	3200	1385	0.011	1225
201047	89	0	97	10	72	125	56	208	568	89	2800	868	0.006	1000
201049	83	0	106	7	46	106	40	185	637	83	3300	1436	0.025	1298
201053	80	0	94	8	97	134	54	161	514	80	3000	1632	0.012	1332
201055	86	0	106	8	86	146	53	186	569	86	3200	2200	0.016	2600
201057	93	0	93	9	72	173	67	200	696	93	1700	1400	0.010	1800
201059	69	0	70	10	70	98	56	182	873	69	3323	1580	0.011	1350
201061	84	0	123	7	91	177	54	204	568	84	3200	1490	0.011	1520
201063	117	0	81	8	102	136	81	312	562	117	3000	1100	0.008	1650
∅	88	0	108	8	77	150	56	197	626	88	2882	1448	0.012	1458

A,K,L:

$$\left(\sum_{\text{Scrap i}} x_{C,i}\, m_i\right)+\left(\sum_{\text{Basket i}} x_{C,i}\, m_i\right)+\left(x_{C,\text{Carbon}}\, m\right)+\left(x_{C,CH_4}\int \dot{m}\, dt\right)+\left(x_{C,\text{Electrode}}\, m\right)$$

$$=\left(x_{C,\text{Melt}}\, m\right)^{A}+\left(\sum_{i=CO,CO_2,CH_4}\int x_{C,i}\,\dot{m}\, dt\right)^{K}+\left(\sum_{i=NO,NO_2}\int x_i\,\dot{m}\, dt\right)^{L}$$

B,..,J:

$$\left(\sum_{\text{Scrap i}} x_{Me,i}\, m\right)+\left(\sum_{\text{Basket i}} x_{Me,i}\, m\right)+\left(x_{Me,\text{Refractory}}\, m\right)$$

$$=\left(x_{Me,\text{Melt}}\, m\right)^{B,..,F}+\left(x_{Me,\text{Slag}}\, m\right)+\left(x_{Me,\text{Dust}}\, m\right)$$

N:

$$\left(NO_x{}^{ARC}+NO_x{}^{PC}+NO_x{}^{RB}\right)^{N}=\left(\int\left(x_{NO}+x_{NO_2}\right)\,\dot{m}_{\text{off-gas}}\, dt\right)^{N}$$

$$\dot{m}_{C,\text{off-gas}}\, dt=\frac{M_C}{M_{\text{off-gas}}}\int \dot{m}_{\text{off-gas}}\, dt$$

Table 23: Data of materials discharged per heat calculated by mass balances, DEWG

No.	C[A] [kg]	Si[B] [kg]	Mn[C] [kg]	P[D] [kg]	S[E] [kg]	Cr[F] [kg]	Mo[G] [kg]	Ni[H] [kg]	Al[I] [kg]	N[J] [kg]	C[K] [kg]	NO_x[L] [g]	NO_x[L] [kg/t]
200857	735	33	984	29	27	18758	1150	12000	0	26	880	1520	0.0137
200861	572	22	737	32	348	19404	385	8305	0	28	713	2790	0.0248
200863	607	46	848	35	390	20434	360	8916	0	28	766	5320	0.0458
200865	704	175	959	34	381	21404	397	9130	0	28	663	5000	0.0427
200867	686	106	897	32	46	19918	1994	13251	0	30	884	2290	0.0194
200869	645	70	800	30	50	19801	1972	12192	8	29	911	4060	0.0350
200871	508	23	1307	35	31	17957	1701	11072	0	47	818	7140	0.0617
200873	557	79	721	30	36	18602	1880	11440	0	32	1240	4160	0.0356
200875	690	58	870	30	51	19523	1114	10811	0	36	770	2590	0.0223
200877	572	22	1408	33	29	19789	319	8349	0	39	1219	1720	0.0156
200879	648	162	1438	35	26	20265	325	7726	0	34	736	3340	0.0287
200881	831	202	1176	32	29	20171	291	8198	0	31	765	3000	0.0267
200883	536	53	1334	25	29	19698	210	9293	0	36	1298	2840	0.0270
∅	598	93	978	30	111	18321	881	9418	9	32	897	3520	0.0310

A,K:

$$\left(\sum_{\text{Scrap i}} x_{C,i}\, m_i\right)+\left(\sum_{\text{Basket i}} x_{C,i}\, m_i\right)+\left(x_{C,\text{Carbon}}\, m\right)+\left(x_{C,CH_4}\int \dot{m}\, dt\right)+\left(x_{C,\text{Electrode}}\, m\right)$$

$$=\left(x_{C,\text{Melt}}\, m\right)^{A}+\left(\sum_{i=CO,CO_2,CH_4}\int x_{C,i}\, \dot{m}\, dt\right)^{K}+\left(\sum_{i=NO,NO_2}\int x_i\, \dot{m}\, dt\right)$$

B,..,J:

$$\left(\sum_{\text{Scrap i}} x_{Me,i}\, m\right)^{B,..,J}+\left(\sum_{\text{Basket i}} x_{Me,i}\, m\right)^{B,..,J}+\left(x_{Me,\text{Refractory}}\, m\right)$$

$$=\left(x_{Me,\text{Melt}}\, m\right)+\left(x_{Me,\text{Slag}}\, m\right)+\left(x_{Me,\text{Dust}}\, m\right)$$

L:

$$\left(NO_x^{\text{ARC}}+NO_x^{\text{PC}}+NO_x^{\text{RB}}\right)^{L}=\left(\int\left(x_{NO}+x_{NO_2}\right)\,\dot{m}_{\text{off-gas}}\, dt\right)^{L}$$

$$\dot{m}_{C,\text{off-gas}}\, dt=\frac{M_C}{M_{\text{off-gas}}}\int \dot{m}_{\text{off-gas}}\, dt$$

Table 24: Tapped steel and composition of steel sample, RIVA

No.	Tapped	C	Si	Mn	P	S	Cr	Mo	Ni	Al	Fe
	[kg]	[%]	[%]	[%]	[%]	[%]	[%]	[%]	[%]	[%]	[%]
22772	80090	0.058	0.008	0.092	0.003	0.038	0.08	0.02	0.10	0.47	99.1
22773	77490	0.184	0.060	0.189	0.006	0.063	0.24	0.02	0.14	0.57	98.5
22774	75750	0.173	0.024	0.146	0.008	0.051	0.15	0.02	0.08	0.54	98.8
22775	78120	0.035	0.007	0.119	0.006	0.039	0.06	0.02	0.07	1.42	98.2
22776	77080	0.051	0.008	0.099	0.003	0.033	0.05	0.02	0.06	0.47	99.2
22777	78120	0.072	0.006	0.127	0.003	0.033	0.06	0.02	0.08	0.52	99.1
22778	79570	0.075	0.006	0.102	0.003	0.040	0.07	0.02	0.08	0.56	99.1
22779	79220	0.086	0.007	0.112	0.001	0.033	0.07	0.01	0.06	0.25	99.4
22780	77080	0.054	0.009	0.094	0.003	0.038	0.06	0.02	0.06	0.53	99.1
22781	79110	0.042	0.016	0.071	0.002	0.039	0.06	0.01	0.07	0.55	99.1
22782	80780	0.074	0.011	0.104	0.005	0.042	0.08	0.01	0.08	0.67	98.9
22783	78640	0.157	0.025	0.177	0.009	0.046	0.15	0.01	0.07	1.10	98.3
22784	80600	0.312	0.034	0.207	0.006	0.038	0.16	0.02	0.11	0.37	98.7
22785	81070	0.143	0.033	0.220	0.007	0.039	0.16	0.02	0.10	0.49	98.8
22788	78990	0.114	0.029	0.199	0.005	0.037	0.17	0.01	0.08	0.97	98.4
22787	80700	0.098	0.026	0.228	0.006	0.032	0.14	0.01	0.07	0.69	98.7
22788	77490	0.063	0.026	0.199	0.002	0.038	0.12	0.02	0.07	0.65	98.8
22792	78530	0.069	0.011	0.067	0.001	0.036	0.07	0.02	0.10	0.63	99.0
22797	78120	0.036	0.012	0.059	0.003	0.043	0.07	0.02	0.11	0.68	99.0
22798	78120	0.049	0.008	0.073	0.002	0.040	0.08	0.02	0.08	0.39	99.3
22799	75630	0.070	0.007	0.085	0.003	0.041	0.10	0.02	0.12	0.55	99.0
22800	77950	0.061	0.011	0.117	0.005	0.044	0.12	0.02	0.09	1.03	98.5
22801	78120	0.115	0.008	0.145	0.002	0.036	0.13	0.02	0.08	0.54	98.9
22802	77830	0.085	0.005	0.114	0.001	0.037	0.09	0.01	0.07	0.80	98.8
22803	78470	0.104	0.005	0.107	0.003	0.042	0.09	0.02	0.08	0.58	99.0
22804	77600	0.045	0.007	0.078	0.001	0.038	0.07	0.01	0.07	0.89	98.8
22805	78760	0.109	0.004	0.131	0.002	0.037	0.09	0.01	0.07	0.35	99.2
22806	78200	0.068	0.008	0.092	0.005	0.040	0.08	0.02	0.08	0.55	99.1
22808	76730	0.075	0.009	0.090	0.003	0.041	0.09	0.02	0.12	0.60	98.9
22809	77600	0.058	0.007	0.082	0.001	0.036	0.07	0.01	0.07	0.27	99.4
22810	74940	0.052	0.008	0.074	0.001	0.037	0.07	0.01	0.07	0.44	99.2
22811	77250	0.044	0.007	0.069	0.002	0.039	0.06	0.02	0.08	0.36	99.3
22812	74650	0.031	0.015	0.065	0.002	0.034	0.06	0.02	0.10	0.45	99.2
∅	78133	0.087	0.014	0.119	0.003	0.039	0.10	0.02	0.08	0.60	98.9

Table 25: Data of materials discharged per heat calculated by mass balances, RIVA

No.	C^{A} [kg]	SI^{B} [kg]	MN^{C} [kg]	CR^{D} [kg]	$O_2{}^{G}$ [m^3(STP)]	$CH_4{}^{H}$ [kg/t]	C^{I} [kg/t]	C^{J} [kg]	$NO_x{}^{K}$ [kg/t]	CO^{L} [kg/t]	$CO_2{}^{L}$ [kg/t]	C^{L} [kg/t]	$O_2{}^{M}$ [kg/t]	$O_2{}^{N}$ [kg/t]
22772	47	6	74	68	2145	1.61	7.27	13	0.0264	34	13	15	35	32
22773	142	46	146	190	2362	2.41	3.97	11	0.0177	33	28	21	39	40
22774	131	18	111	112	2178	2.36	4.45	11	0.0244	32	27	20	36	39
22775	27	6	93	47	2094	2.31	4.21	11	0.0366	32	11	13	34	29
22776	39	6	76	40	2078	2.18	5.24	11	0.0240	31	10	13	34	28
22777	56	5	99	48	2102	2.21	11.09	18	0.0339	34	19	17	34	36
22778	60	5	81	53	2142	2.16	4.11	11	0.0268	34	18	17	35	35
22779	68	5	88	55	1998	2.04	6.25	11	0.0242	28	17	15	33	30
22780	42	7	72	44	1992	2.08	3.48	10	0.0246	31	13	14	33	30
22781	33	12	56	46	2060	2.09	4.84	10	0.0329	37	18	18	34	37
22782	60	9	84	63	2067	2.05	3.13	9	0.0280	34	17	17	34	34
22783	123	20	139	115	2264	2.21	3.09	9	0.0227	38	23	20	37	41
22784	251	27	166	125	2696	2.33	4.34	10	0.0222	41	19	19	45	40
22785	116	27	178	132	2082	2.05	4.23	9	0.0321	33	14	15	34	32
22788	90	23	158	135	2080	2.02	3.84	9	0.0162	34	20	18	34	36
22787	79	21	184	111	2131	2.05	5.34	11	0.0240	32	18	17	35	34
22788	49	20	154	96	2574	2.52	5.56	14	0.0442	35	20	18	43	37
22792	54	9	52	56	1960	2.26	3.72	11	0.0305	32	11	13	36	31
22797	28	10	46	57	2335	2.40	4.90	13	0.0327	36	20	18	32	29
22798	38	6	57	60	1931	2.13	9.37	17	0.0321	35	19	17	38	38
22799	53	5	65	77	2035	2.36	3.42	10	0.0307	33	18	17	32	36
22800	48	8	91	91	1920	2.31	3.71	10	0.0290	31	15	15	33	35
22801	90	6	113	105	1968	2.27	2.01	9	0.0312	32	14	15	32	32
22802	66	4	89	73	1999	2.20	1.84	8	0.0230	31	16	16	32	31
22803	81	4	84	71	1805	2.04	2.80	8	0.0219	32	14	15	33	32
22804	35	5	60	57	1804	2.11	2.36	8	0.0298	29	12	13	30	31
22805	86	3	103	69	2029	2.23	3.81	10	0.0280	35	18	17	29	28
22806	53	6	72	60	2020	2.35	3.13	9	0.0322	34	18	17	33	36
22808	57	7	69	72	2272	2.41	6.03	13	0.0409	38	15	17	33	35
22809	45	5	64	58	2193	2.36	5.46	10	0.0358	32	11	13	37	34
22810	39	6	55	53	2175	2.67	3.67	9	0.0271	36	16	16	36	36
22811	34	6	54	48	2204	2.43	4.49	13	0.0359	32	10	13	35	30
22812	23	11	48	45	2076	2.45	5.76	13	0.0264	34	13	15	36	35
∅	68	11	93	77	2114	2.23	4.57	11	0.0287	33	17	16	35	34

A,H,I,J,L:

$$\left(\sum_{\text{Scrap i}} x_{C,i}\, m_i\right)+\left(\sum_{\text{Basket i}} x_{C,i}\, m_i\right)+\left(x_{C,\text{Carbon}}\, m\right)^{I,J}+\left(x_{C,\text{Nat. gas}}\int \dot{m}\, dt\right)^{H,J}+\left(x_{C,\text{Electrode}}\, m\right)$$

$$=\left(x_{C,\text{Melt}}\, m\right)^{A}+\left(\sum_{i=CO,CO_2,CH_4}\int x_{C,i}\, \dot{m}\, dt\right)^{L}$$

G,M,N:

$$\left(m_{\text{Lance }O_2}\right)^{G,M}+\left(\sum_{\text{Cojet i}} x_{O,i}\, m\right)^{M}+\left(\sum_{\text{EBT i}} x_{O,i}\, m\right)^{M}+\left(\sum_{\text{Scrap i}} x_{O,i}\, m\right)+\left(\int x_{O,\text{Air}}\, \dot{m} dt\right)$$

$$=\left(\sum_{\text{Slag i}} x_{O,i}\, m\right)+\left(\sum_{\text{Dust i}} x_{O,i}\, m\right)+\left(M_O \dot{n}_{\text{off-gas}}\left(x_{CO}+2\,x_{CO_2}+2\,x_{O_2}\right)\right)^{N}$$

K:

$$\left(NO_x{}^{\text{ARC}}+NO_x{}^{\text{PC}}+NO_x{}^{\text{RB}}\right)^{K}=\left(\int\left(x_{NO}+x_{NO_2}\right)\dot{m}_{\text{off-gas}}\, dt\right)^{K}$$

2.3.4.7 Evaluation of exhaust gas results and operational data and correlation of results with steel analysis

This section covers Task 4.7 and 4.8. Within project duration (a) an evaluation of the total NO_x emissions and comparison to further data records and (b) an evaluation of operational data in order to point out whether unnecessary high NO_x emissions have been emitted, has been conducted.

Figure 88 shows the total NO_x content vs. the carbon injected. There is no correlation of high amounts of carbon injected and NO_x emission. This may be because of the already CO rich atmosphere during carbon injection.

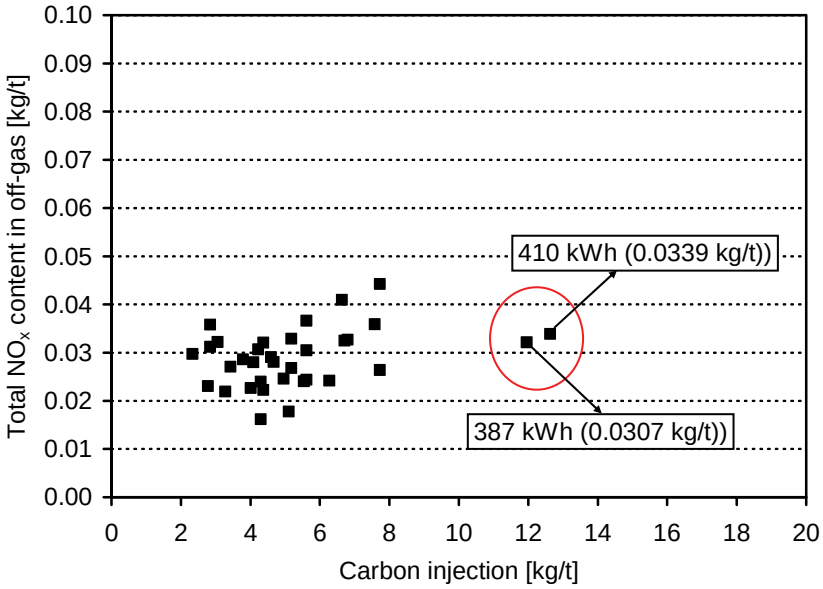

Figure 88: Total NO_x content in the off-gas compared to the carbon injection

Figure 89 presents the total NO_x emissions per charge in the off-gas. There has been a measurement campaign in 2006 at point B. The NO_x was 0.02 kg/t_{Steel} to 0.055 kg/t_{Steel}. At point B the post combustion is completed and there is no further NO_x source to be taken into account. Measurements at point A from 2008 show average NO_x emissions of 0.03 kg/t_{Steel} at average amounts of carbon in the off-gas of 16 kg/t_{Steel}. Therefore for RIVA there seems to be no further NO_x source downstream point A. The NO_x is formed inside the EAF vessel. Main sources are: (a) the arc, (b) the burner/injectors and (c) post combustion reactions in a nitrogen/oxygen rich atmosphere.

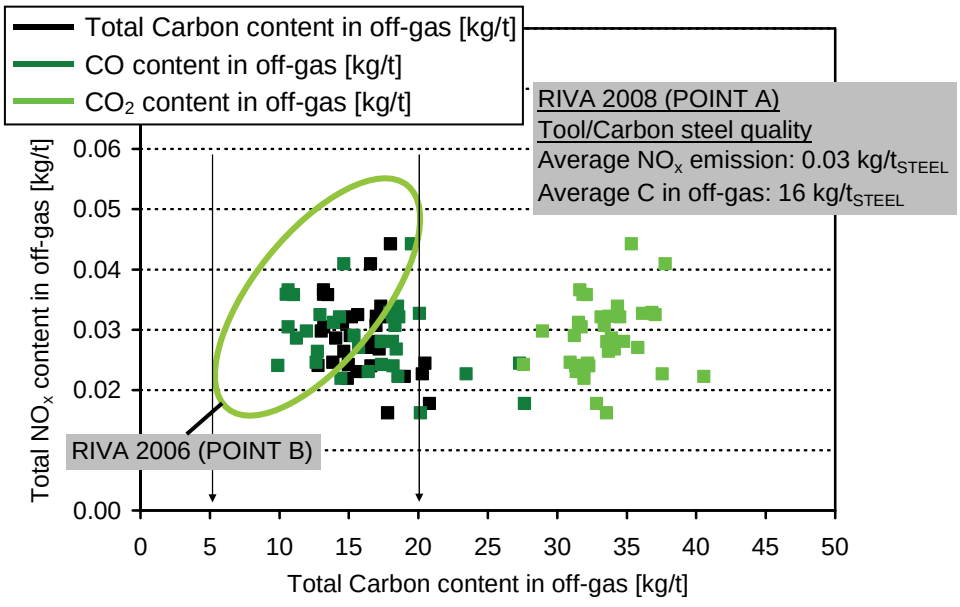

Figure 89: Total NO_x content in the off-gas vs. total carbon content in the off-gas at RIVA

Figure 90 shows the NO_x content at DEWG from 2006. This figure has been presented in the proposal. The range of NO_x is 0.02 kg/t_{Steel} up to 0.06 kg/t_{Steel} at point B. The total carbon content in off-gas is 5 kg/t_{Steel} to 20 kg/t_{Steel} at the RIVA furnace and 10 kg/t_{Steel} to 25 kg/t_{Steel} at the DEWG furnace.

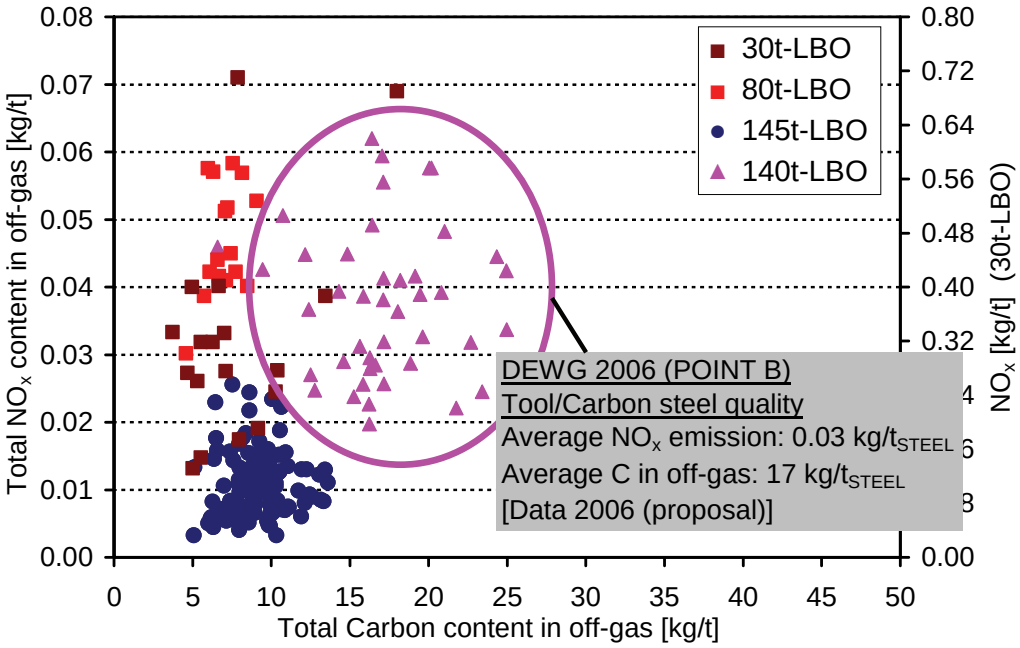

Figure 90: Total NO_x content in off-gas vs. total carbon content in the off-gas at DEWG

Figure 91 presents the correlation of carbon/oxygen and total NO_x content in the off-gas at point A at the RIVA EAF. There is a light correlation of high CO content and low NO_x emission. On the other hand there is also a light correlation of CO_2 and NO_x. This is because of high CO combustion inside the EAF vessel will result in high off-gas temperature and simultaneously high post combustion ratio.

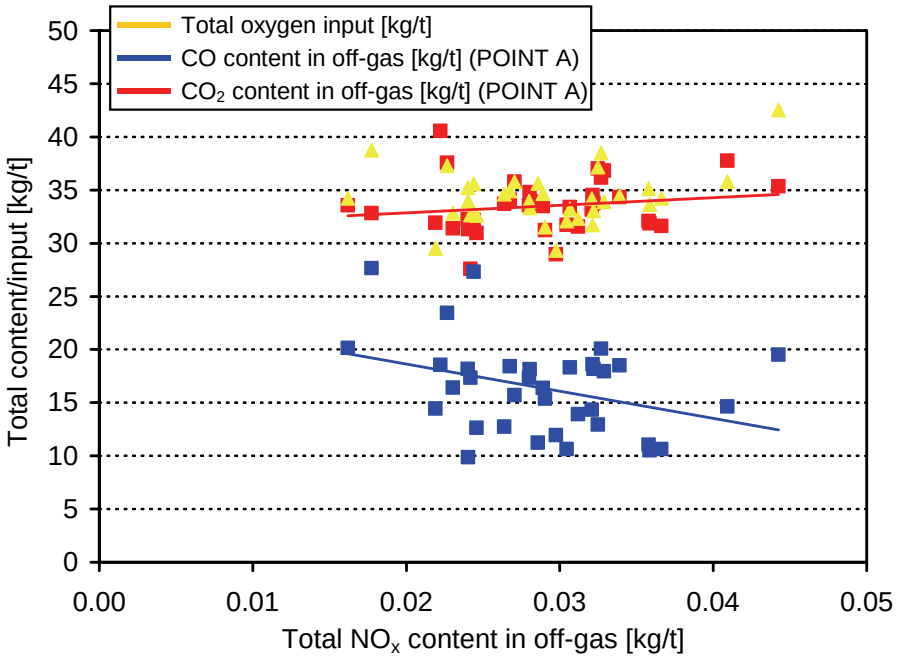

Figure 91: Correlation of carbon & oxygen and total NO_x content in the off-gas

2.3.4.8 Definition of best practices in order to minimise the NO_x generation

During tests RIVA made about changing ratio between oxygen and methane the more relevant result was a strong reduction of NO_x emissions using less oxygen in lance period (and a constant methane flow) to avoid bounding with nitrogen from air (no connection with slag door). **Figure 92** shows how an oxygen/methane ratio of 15 allows a decrease of NO_x emission of about 30% (in our trials).

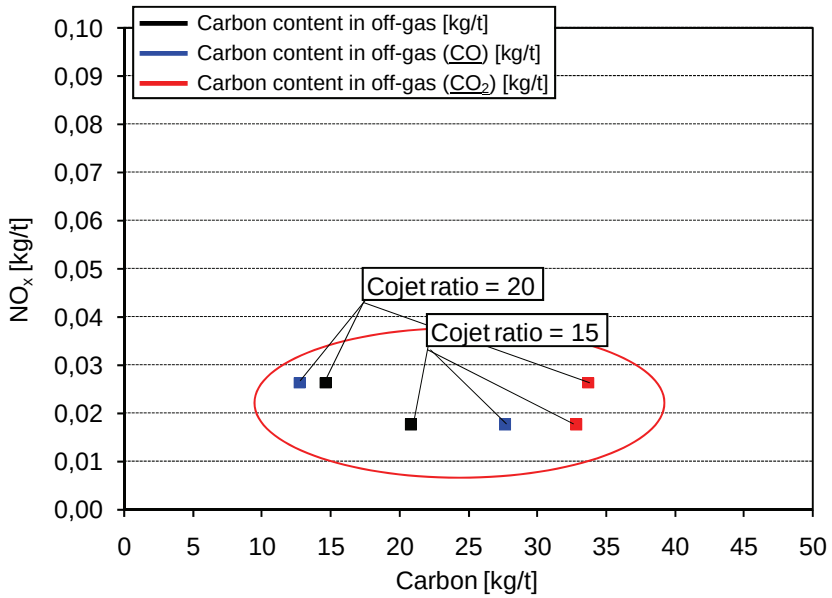

Figure 92: Cutting down in NO_x emissions changing the O_2/CH_4 ratio

During trials with changes in the carbon amount injected at RIVA, no effect on NO_x emissions could be found. The carbon injection primarily investigated at DEW is done to create a foamy slag to shield the electric arc. A side effect of this practice is the generation of a reducing CO rich atmosphere which has a positive effect on NO_x content of the off-gas. Since the slag foaming is standard practice in the production of carbon steel qualities there is no need to change anything for these qualities. Regarding the production of stainless qualities the practice is not used right now because there are no foamable stainless steel slags known at the moment. New developments in foamy slags for stainless steel should be evaluated constantly and put into operational use as soon as available.

2.3.4.9 Characterisation of the process under economical point of view

During the last trial test (2 weeks of measurements) at RIVA with modified oxygen input (200 m^3 (STP) per melt) 2 different series of hits with the best O_2/CH_4 ratio for NO_x emissions (15) and the ratio we normally used in the past (20) were analyzed from an economical point of view.

Table 26 presents series with a ratio of 15 (BEP) compared with series with ratio of 20 (standard).

Table 26: Trials with modified (200 m^3 (STP) per melt) and standard oxygen input

Data	Colata	Durata	PwON	KWh Spec	O2	Data	Colata	Durata	PwON	KWh Spec	O2
		min	min	Spillato	Nm3			min	min	Spillato	Nm3
02/05/2009	26833	76	62	524	2038	25/05/2009	27178	65	47	396	2958
02/05/2009	26834	63	49	449	2285	25/05/2009	27179	61	47	400	2716
02/05/2009	26835	59	49	424	2221	25/05/2009	27180	71	47	411	2643
02/05/2009	26836	62	49	405	2262	25/05/2009	27181	71	48	419	2942
02/05/2009	26837	64	50	420	2216	25/05/2009	27182	71	49	417	2885
02/05/2009	26838	66	49	395	2375	25/05/2009	27183	80	48	428	2833
02/05/2009	26839	64	47	404	2252	25/05/2009	27184	66	48	415	3035
02/05/2009	26840	61	48	397	2379	25/05/2009	27185	74	64	492	2104
02/05/2009	26841	70	53	445	2340	25/05/2009	27186	78	50	398	2790
02/05/2009	26842	72	51	421	2364	25/05/2009	27187	66	51	405	2664
02/05/2009	26843	69	50	445	2584	26/05/2009	27188	67	48	396	3245
02/05/2009	26844	63	50	423	2387	26/05/2009	27189	73	47	411	3032
02/05/2009	26845	69	53	442	2391	26/05/2009	27190	70	47	404	2759
02/05/2009	26846	67	51	446	2237	26/05/2009	27191	65	49	406	3140
03/05/2009	26847	71	54	445	2537	26/05/2009	27192	64	49	417	3043
03/05/2009	26848	68	53	414	2588	26/05/2009	27193	65	48	407	3049
03/05/2009	26849	61	50	412	2365	26/05/2009	27194	66	48	413	3083
03/05/2009	26850	62	49	401	2389	26/05/2009	27195	70	47	398	3014

From **Table 26** it's possible to obtain these average values of reductions:

- m^3 (STP) O_2 → -10%
- Power on → - 2%
- Tap to tap → - 2.5%
- kWh/ton → - 0.5%In short, using best practices it is possible to cut down NO_x emission of about 30%. At the same time using correct O_2/CH_4 ratio RIVA can save oxygen (10% less), production time (2% less power on, 2.5% less tap to tap) and specific electric energy (TLS, 0.5% less).

2.3.5 Impact of scrap preheating (Consteel) on NO_x emission

This WP is devoted to industrial measurements of NO_x emission different plant conditions. These measurements have been necessary because the model is based on physical parameters, and for this reason it is not directly related to plant operations. In order to understand how plant operations modify the physical parameter constituting the model extensive measurement campaigns have been carried out. For example, one key point was to correlate the presence of oxygen and nitrogen inside the EAF atmosphere with EAF working conditions (fumes aspiration, post combustion).

This activity permitted to:

a) to establish correlations among NO_x concentration in the off gas and the main operational parameters, considering also the process step in the pre-heating conveyor,

b) to evaluate the effect of post combustion inside the furnace and inside the conveyor on NO_x formation and emission,

c) to compare the results of the plant measurements with model prediction,

d) to elaborate guidelines for improved practices with reduced emission of NO_x, on the basis of measurements with the aid of model calculations.

2.3.5.1 Off-gas measurements at the Consteel tunnel with variation of process parameters (O_2 lancing, carbon injection, dedusting system operation)

To reach these goals two measurements campaigns have been carried out at ORI Martin Steel plant. The gas analysers were set simultaneously at two sampling points: at the fourth hole of the furnace (where there is an already installed gas analysis probe, EFSOP™) and in the fume duct downstream (see **Figure 93**).

The first campaign has been devoted to establish a better correlation of NO_x with operational parameters.

The second campaign has been carried out to evaluate the contribution of the post-combustion inside the EAF to NO_x formation and to differentiate the amount of NO_x formed in the EAF and in the tunnel.

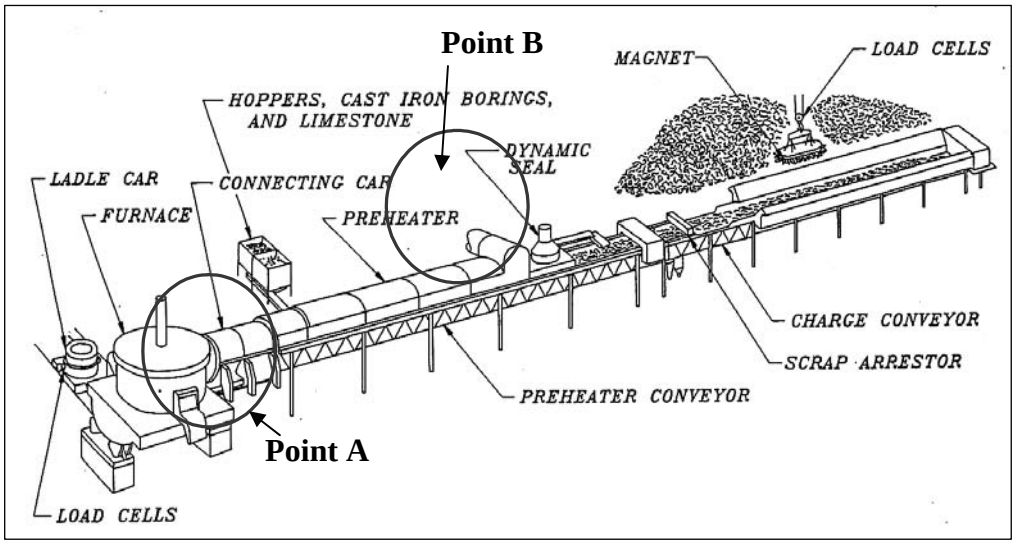

Figure 93: Scheme of the Consteel plant with indicated the two positions to perform gas analysis

First campaign

Table 27 reports the process data of the first campaign; **Table 28** reports the measured gas compositions.

Table 27: Process data of the test heats. Moreover, in two of these five heats basket was also charged in order to take into account the effect of working under batch operations

Heat	Scrap ton	Pig iron ton	Lump coal kg	Injected O_2 m^3 (STP)	Inj. coal kg
AC2081	76.6	3.4	1096	1120	80
AC2082	78.4	1.6	1363	1230	390
*AC2083	77.9	2.1	1000	1470	90
AC2084	72.0	8.0	1171	1690	530
*AC2085	114.1	2.0	1008	1890	740

Table 28: Composition of the gaseous atmosphere measured in points A and B during the five selected test heats (in point B no H_2 is present)

Heat	Point A CO [% vol]	Point A O_2 [% vol]	Point A CO_2 [% vol]	Point A H_2 [% vol]	Point B CO [ppm]	Point B O_2 [% vol]	Point B CO_2 [% vol]
AC2081	19.6	1.0	12.8	13.5	569	20.0	2.8
AC2082	18.1	0.7	19.5	23.0	276	17.7	4.1
*AC2083	13.6	1.7	16.2	16.8	417	18.7	2.5
AC2084	16.2	0.75	23.4	20.1	689	17.1	4.8
*AC2085	10.5	3.5	16.5	10.8	558	19.3	3.2

* basket charge

Figure 94 reports the NO_x concentration at point B for all the five test heats. In the figure the two heats in which an extra basket with scarp has been charged are also indicated. In these two heats two strong peaks can be seen, due to the opening operations of the furnace roof and subsequent large air inlet. **Figure 95** shows the effect of the reducing agents (CO and H_2) on NO_x concentrations. This trend confirmed what already found in the preliminary measurements.

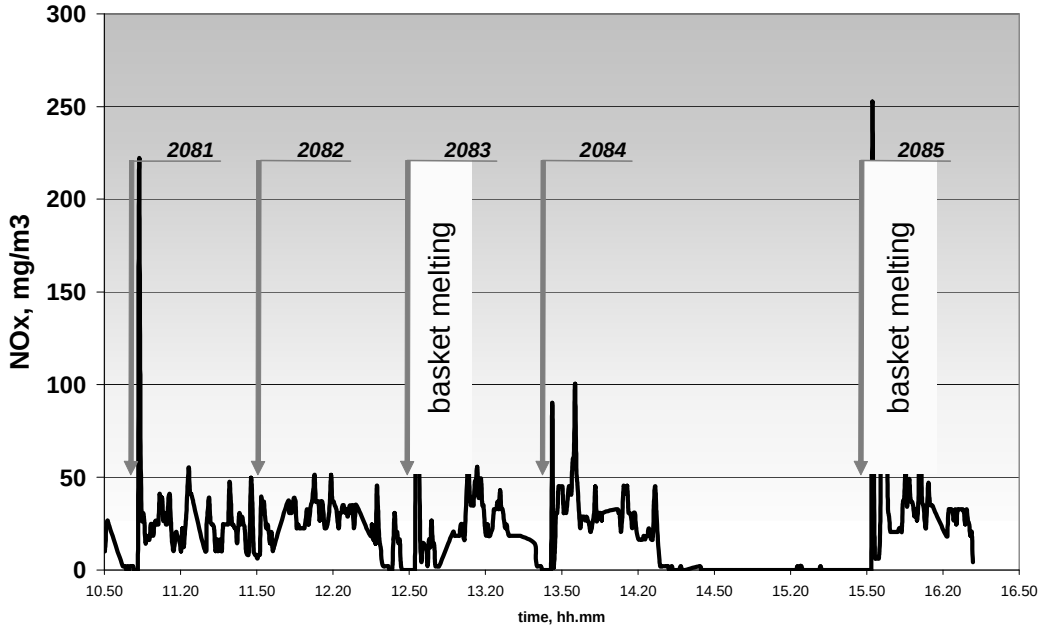

Figure 94: NO_x concentration at point B in the five test heats

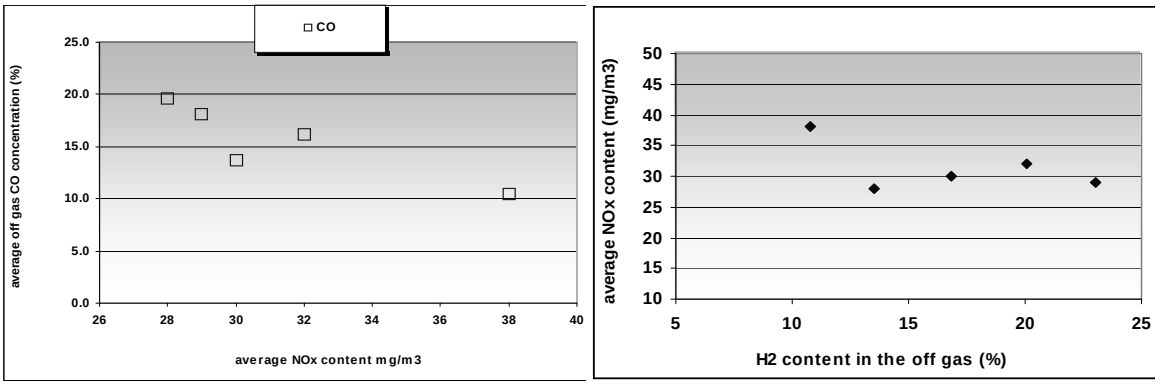

CO H_2

Figure 95: Effect on NO_x concentration of reducing agents CO and H_2

Figure 96 reports the effect of gas temperature. According to the thermal mechanism of formation of NO_x, an increase of temperature would cause an increase of NO_x formation. Reporting the average NO_x content vs the average value of gas temperature at point B, an almost linear correlation has been observed. Only one heat deviates significantly from the general obtained trend. In this particular heat an extra basket was charged into the furnace, causing large air inlet and promoting NO_x formation. Moreover, also the operating conditions were strongly different from the other ones: larger amount of scrap was used (114 tons of scrap instead of average value of 76 tons) and larger amount of oxygen and coal.

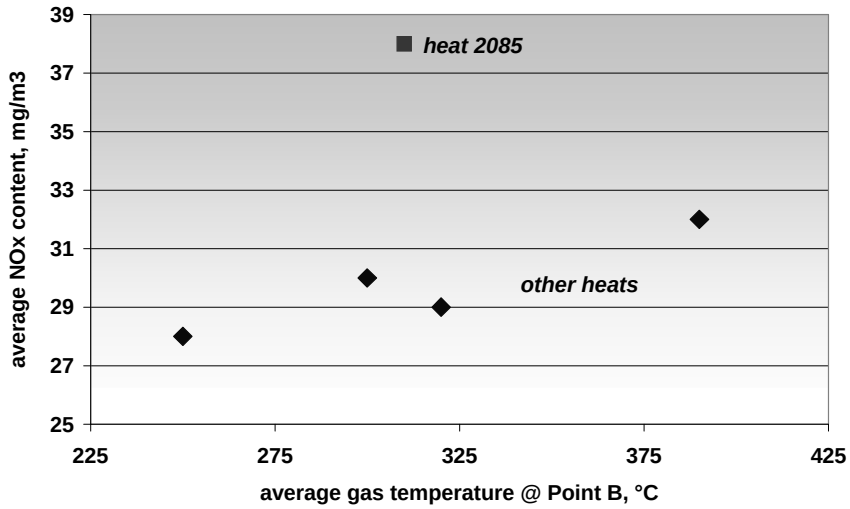

Figure 96: NO_x concentration as a function of off gas temperature

From the performed measurements the following correlations are individuated:

- NO_x concentration is inversely proportional respect to CO and H_2 concentration in the off gas; reducing conditions, which decrease the oxygen concentration in the gas also decrease the NO_x content,
- NO_x concentration increases with temperature; according to the formation mechanisms available in literature, the so called "thermal NO_x" is an important mechanism also in the EAF atmosphere,
- Air entrance produces an increase of NO_x concentration in the gas; this effect is well visible with heat 2085, which in **Figure 96** does not follow the trend of the other heats with temperature showing larger NO_x content than the others. This fact can be explained with the air intake after furnace opening for extra basket charge.

Second campaign

In the Consteel plant post combustion can be managed by modulation of PC ratio inside the electric furnace or in the conveyor.

An opposite measurement campaign has been carried out to evaluate the effect of both types of post combustion form the point of view of NO_x emission.

From the data reported in **Table 29** and considering as order of magnitude 10.000-15.000 m^3 (STP)/h EAF gas flow rate and 80.000-100.000 m^3 (STP)/h downstream gas flow rate, the average mass flow rate of NO_x from EAF is about 1kg/h, while average mass flow rate of NO_x from tunnel is about 2.5 kg/h.

In all the monitored heats the NO_x average concentration is always below 40 mg/m^3 (STP), but at the beginning of the heat, in transient operations, a large peak of NO_x emission is recorded.

Data reported in **Table 30** permitted also to quantify the amount of NO_x formed in the EAF and in the tunnel. The estimated values show that the amount generated after the fourth hole is about five times larger (about 490 g at fourth hole against 2400 g downstream, per heat).

Table 29: Process data of the tests heats. The post combustion ratio (PCR), $CO_2/(CO+CO_2)$ is also reported

heat	Pig iron t	Scrap t	lump coal kg	inj. Coal kg	lance O_2 m^3 (STP)/h	post comb. O_2 m^3 (STP)/h	<PCR> %
924	4.5	90.0	1775	0	3220	80	67
925	4.5	91.0	1236	120	2020	400	72
926	12	72.6	1509	20	2420	80	63
928	32	80.3	1325	140	3610	150	65
929	26.8	69.6	809	100	3340	750	75

Table 30: Values of NO_x concentrations in EAF and downstream. The column 'NO_x formed post EAF' is the difference between the NO_x measured downstream and the total NO_x measured at the EAF

heat	avg NO_x EAF mg/m^3	tot NOx EAF g	avg NO_x downstrem mg/m^3	tot NO_x downstream g	NO_x formed post EAF g
924	55.4	440	45.0	2369	1929
925	56.1	395	68.8	3448	3053
926	61.1	491	55.4	3155	2664
928	26.9	594	52.2	3090	2496
929	63.9	533	35.7	2420	1887

Figure 97 reports an example of NO_x emission, measured at points A and B with and without EAF post-combustion rate.

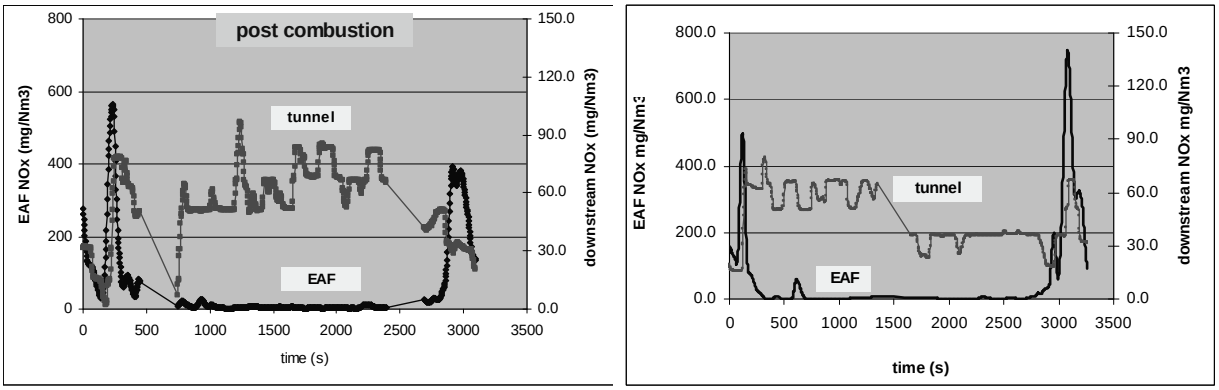

With post combustion *Without post combustion*

Figure 97: Example of NO_x emission, measured at points A and B with and without EAF post-combustion

The EAF post combustion does not alter significantly the path of NO_x emission inside the EAF and in the tunnel.

Figure 98 reports the NO_x emission expressed as g/t (ton refers to tapped steel, which is 75 tons) as a function of post combustion ratio PCR. The higher the PCR the lower the amount of NO_x, if there is enough coal to guarantee CO_x formation in the furnace and decrease the air leakage from the door.

The result in **Figure 98** indicates also that nitrogen from coal gives a negligible contribution to NO_x formation and confirms the model hypothesis.

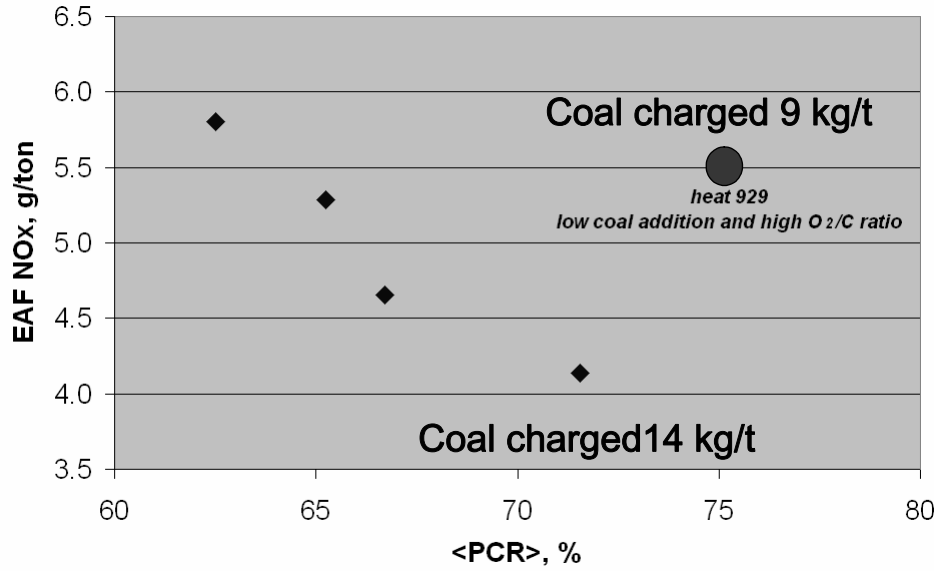

Figure 98: EAF NO_x emission as a function of post combustion ratio PCR, expressed in g/ton

The effect of pressure on NO_x formation has been evaluated indirectly. The EAF-Consteel system is controlled through pressure measurement: pressure inside at the tunnel inlet is a balance between gas flow rate entering the tunnel and suction power from the fans. Gas flow entering the tunnel is the sum of process gas ($CO+CO_2$) and air from outside. Higher process gas means lower air entrance. Higher process gas means higher CO_2 concentration in the gas flowing in the tunnel. The average $\%CO_2$ measured downstream is an index of air entrance (fixed C amount feeding of the furnace): the higher the $\%CO_2$ the lower the air leakage (see **Figure 99**).

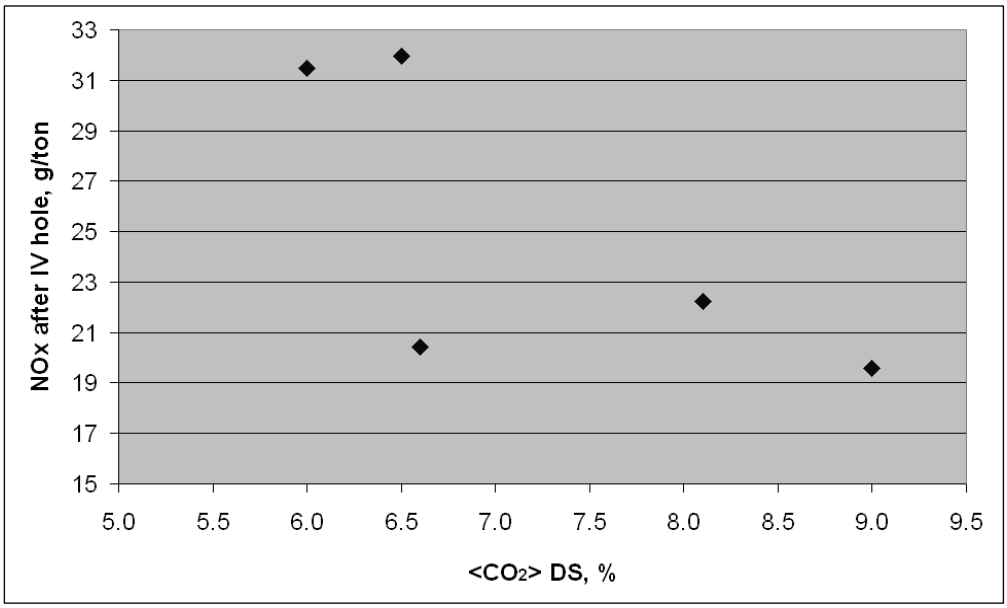

Figure 99: NO_x vs CO_2, measured downstream (DS) after the IV hole

In the Consteel operations the operating parameters (coal flow rate and oxygen flow rates) can be adjusted in order to tune the distribution of the chemical energy between EAF and tunnel. From the point of view of energetic balance, this means to evaluate if the recovery of energy from the CO of the

EAF fumes, is more efficient directly inside the EAF or inside the scrap pre-heating conveyor. This matter has already been treated in other RFCS project [17].

Here the same phenomenon is studied from the point of view of NO_x emissions: the objective is to study the effect of distribution of chemical energy, generated by the post-combustion, between EAF and tunnel, on global NO_x emission.

Figure 100 shows the heat average post combustion ratio (PCR = $CO_2/(CO+CO_2)$, taking the average values of gas concentration during post combustion) as a function of injected oxygen. The good correlation obtained confirms that effectively injected oxygen reacts with CO inside the EAF.

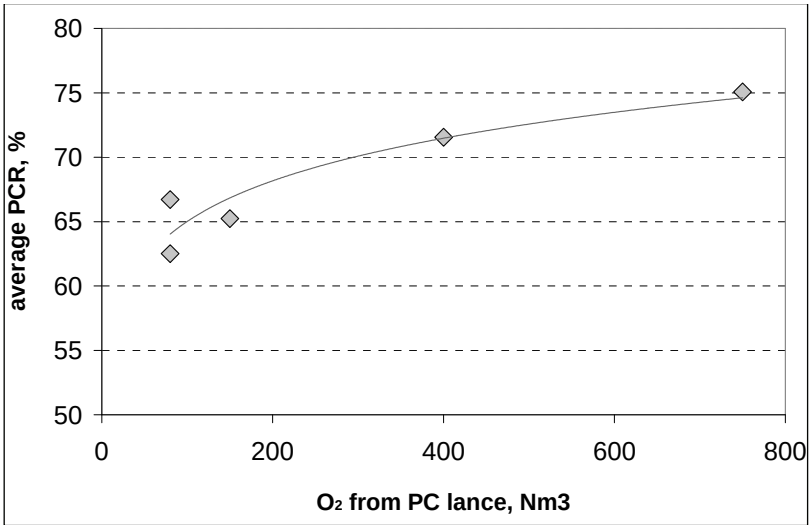

Figure 100: Average post combustion ratio (PCR) measured in the final measuring campaign as a function of post combustion oxygen

Figure 101 reports the variation of NO_x with post combustion oxygen injection in the EAF, measured at points A and B. NO_x emission (expressed as g/t) increased weakly with post combustion oxygen. This means that Post combustion in the furnace contributes to NO_x emission, but the effect is small. The EAF post combustion is not a critical step from the point of view of NO_x emission. For this reason, the opportunity to promote or not the post combustion inside the EAF or in the tunnel must be evaluated only from the energetic and economic point of view.

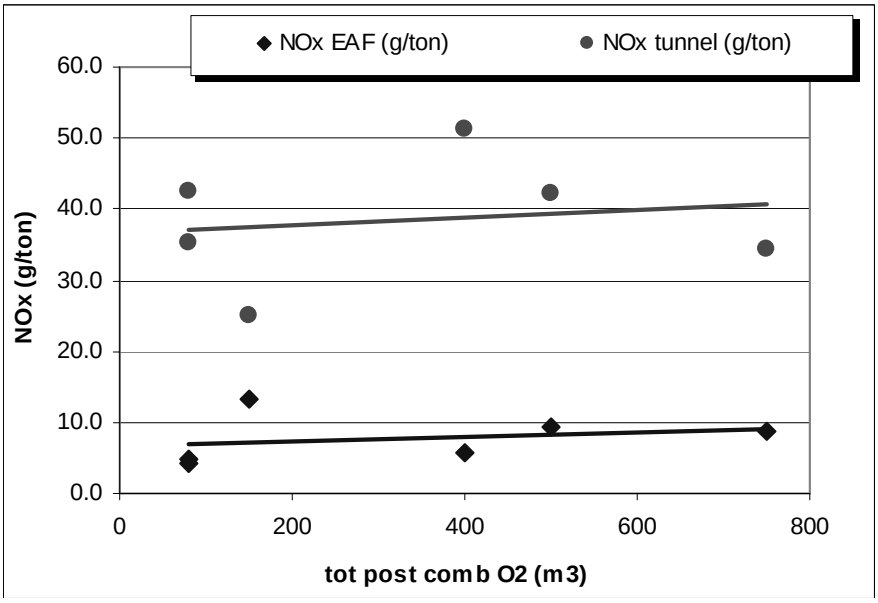

Figure 101: NO_x emission (measured at EAF and downstream) as a function of post combustion oxygen

Most of NO_x emission depends on the condition inside the tunnel, mainly temperature and air flow rate, which in turn depends also on fumes aspiration.

2.3.5.2 Assessment of the measurements with respect to model predictions

According to the performed activities, the following phenomena have been individuated as to have a direct effect on NO_x formation:

a) Leak air flow rate

b) Fumes temperature

c) Post combustion inside the EAF and post combustion inside the tunnel

d) Presence of oxidizing/reducing agents in EAF fumes

e) Batch operations

Leak air flow rate has a direct influence on the amount of formation of NO_x [9]. The model confirms that a reduction of the leak air flow rate reduces NO_x formation drastically.

The effect of temperature has been verified by industrial measurements; also pilot plant tests were performed to consider the effect of temperature and to calibrate the variation of kinetic constants with temperature. Fumes temperature depends in turn on the post combustion amount.

According to the variation of kinetic constants with temperature, and confirmed by experimental measurements, the increase of NO_x emission, in the range of 1500-1600 is almost linear.

According to model simulations (see **Figure 102**), and also by plant measurements, post combustion inside the EAF increases the amount of NO_x formation, but the increase is small. The injection of 1500 m^3/h (STP) of oxygen for EAF post combustion increases the NO_x concentration of the order of magnitude of 7%.

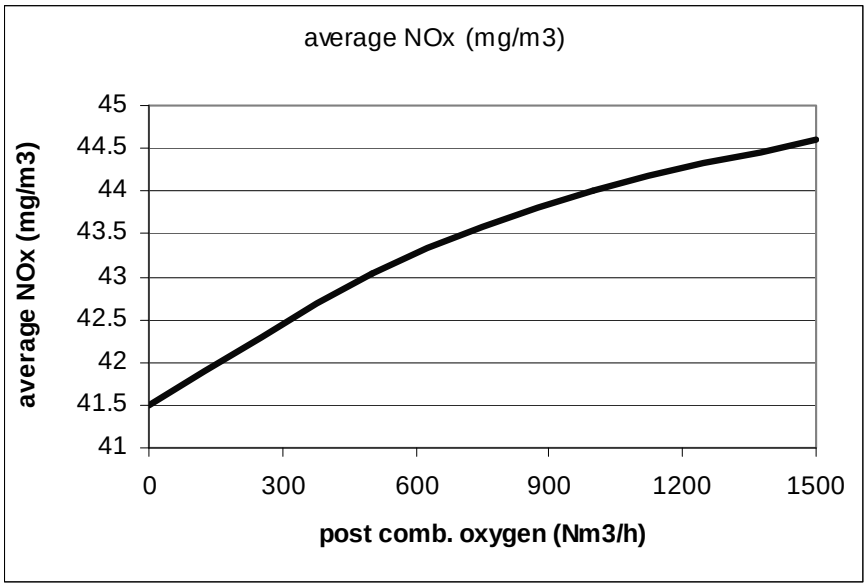

Figure 102: Calculated NO_x emission from EAF as a function of O_2 injection for EAF post combustion

The data with 400 and 750 m^3/h (STP) have been validated by plant tests (see previous paragraph). Considering an average CO content in the EAF atmosphere of 20% with an average value of off-gas flow rate of 10,000 m^3/h (STP), the CO flow rate is of 90 kmol/h. This means that, theoretically, an injection of 1000 m^3/h (STP) of O_2, which corresponds to 45 kmol/h, would be enough to consume all the CO with EAF post combustion, avoiding (or, at least limiting) the NO_x formation downstream in the tunnel. This means that complete, or almost complete, post combustion inside the EAF would not impact in a significant way on global NO_x emission.

On the contrary, the post combustion reactions in the tunnel due to the large amount of air, gives a strong contribution to further NO_x formation in the tunnel.

2.3.5.3 Definition of best practices in order to minimise the NO_x generation at the Consteel EAF

The model has been applied to support the definition of improved guidelines to manage EAF Consteel in order to decrease NO_x emissions.

Model indications have been confirmed by two apposite measurement plant campaigns, in which the effect of Consteel operations, the contribution of NO_x formed in the EAF and in the tunnel and the contribution of EAF post combustion have been investigated.

Available data from static pressure measurement do not give clear relationships about the effect of the de-dusting system operation but an indication of the role of the downstream air leakage is given by the average $\%CO_2$ so an optimal balancing of the effective depression through the heat is required to avoid excess of air leakage at the IVth hole outlet.

Post Combustion inside the EAF (by dedicate lancing) contributes to lower the emission decreasing the air in-leakage even if a suitable amount of coal is required to generate enough (and as long as possible) CO_x (both for filling the freeboard and slag foaming), so the net effect of coal addition is 'positive' and the nitrogen content doesn't appear to play a significant role.

In terms of average g/ton of NO_x formation downstream the amount formed is about 5 times the one generated in the furnace, due to the air dilution and reactions to complete combustion of residual CO and H_2 coming out from EAF.

As final conclusion, the final results have been achieved:

- Peaks of NO_x emission (concentration) appear generally during the transient operation in the furnace; these peaks are difficult to avoid but they do not affect the average emissions strongly,
- During main period of the heats NO_x formation decreases strongly due to the CO_x formation that 'fills' the furnace freeboard and decrease the air in-leakage,
- Post Combustion inside the EAF (by dedicate lancing) contributes to lower the NO_x emission decreasing the air in-leakage even if a suitable amount of coal is required to generate enough (and as long as possible) CO_x (both for filling the freeboard and slag foaming),
- So the net effect of coal addition is 'positive' and the nitrogen content of coal doesn't appear to play a significant role,
- In terms of average g/ton of NO_x formation the amount formed downstream is about 5 times the one generated in the furnace, due to the air dilution and reactions to complete combustion of residual CO and H_2 coming out from EAF; the reduction of CO content with EAF post combustion would play a positive role decreasing the contribution of downstream NO_x formation to total emission; this fact has been also confirmed and quantified by model calculations,
- Available data from static pressure measurement do not give clear relationships about the effect of the de-dusting system operation but an indication of the role of the downstream air leakage is given by the average %CO2 so an optimal balancing of the effective depression through the heat is required to avoid excess of air leakage at the IVth hole outlet.

2.3.6 Impact of adapted dedusting on NO_x emission

2.3.6.1 Oxygen injection by door lance with changing O_2/N_2 ratio

Arc ignitions in oxygen rich atmosphere after charging and post combustion of CO inside and outside the EAF both contribute to total NO_x emissions. Typically the off-gas composition changes rapidly to high content of CO when oxygen is lanced. The injection of oxygen by door lances is used for: (a) decarburization of the melt, (b) homogenization of the melt, (c) superheating of the melt, (d) speedup of the meltdown phase. On the one hand oxygen lancing accelerates the melting down period. On the other hand oxygen lancing seems to increase the total NO_x emission because of additional oxygen inside the EAF vessel. Whereas the contribution from arc ignition seems to be more or less constant, other contributions depend on EAF equipment and operation: Natural gas burners (a); Use of air as carrier medium for carbon or dust (b); Air-tightness of furnace (c); Parameters of off-gas extraction by EAF dedusting system (d).

NO formation is due to the oxidation of atmospheric N_2 (thermal NO at high temperature and prompt NO via the reaction of nitrogen radicals and hydrocarbons (HC), followed by the oxidation of the HCN to NO) or the oxidation of nitrogen compounds bounded in fossil fuels (fuel NO). As fuel gas in steel industry does not contain chemically bound nitrogen, thermal NO formation is the dominant source of NO_x emission from the EAF. Thermal NO is formed when O_2 and N_2 partial pressure, gas temperature and residence time in the reaction zone is high enough. Thermal NO occurs by dissociation of air in post combustion zone of CO/H_2 gas mixture and in the electric arc in accordance with the Zeldovich mechanism. The electric arc spots and the post combustion reactions can be distinguished as primary NO sources at EAF: $NO^{EAF} = NO^{electric\ arc} + NO^{post\ combustion}$. In order to reduce NO_x emission of the EAF process, primary and secondary measures can be taken. Primary measures are due to an optimum process operation to avoid NO_x formation. Secondary measures reduce the concentration of already formed NO_x by introduction of NO_x reducing agents into the off-gas stream to form water (H_2O) and nitrogen (N_2). As secondary measures are very difficult to apply in EAF dedusting systems due to the narrow gas temperature range of efficient reduction (600°C to 1000°C depending on reducing agent), due to high dust load and rapid changes in composition and temperature of the EAF off-gas, we focus on primary measures that are suitable for current EAF steel making processes.

Primary measures that are suitable for NO_x reduction during the start phase comprise: Minimum number of arc ignition processes (a); Rapid change to reducing furnace atmosphere (b); Minimum off-gas volume flow during the starting phase (c); Inert carrier gas in dust and coal injection (d); Maximum air-tightness of EAF (e); Improve foamy slag practice to shield electric arc (f).

Off-gas analysis was performed at the primary dedusting system at the EAF at DEWG. Off-gas measurements have been conducted simultaneously at a measurement point A and point B. In **Table 31** the evaluated charges for the plant trial program performed are shown. Main goal for the plant trial program was to determine the effect of changing the program for oxygen lancing at DEWG. **Figure 103** shows an exemplary off-gas profile for the beginning of a carbon steel heat.

Table 31: Plant trial program at DEWG

Heat No.	Trial	Off-gas analysis at	
		Point A	Point B
201011	X		X
201013	X		X
201015	X		X
201017	X		X
201019	X		X
201021			X
201023			X
201025			X
201027			X
201029			X
201031	X		X
201033	X		X
201035	X		X
201037	X		X
201039	X		X
201041	X		X
201043	X	X	X
201045	X	X	X
201047	X	X	X
201049		X	X
201053		X	X
201055		X	X
201057	X	X	X
201059	X	X	X
201061	X	X	X
201063	X	X	X

When producing carbon steel grades the oxygen lance at DEWG is used like a cutting torch during melt down of the first basket of scrap to speed up the melt down. In the regular programme the oxygen lancing therefore starts shortly after arc ignition as can be seen in **Figure 103**. To operate the oxygen lance it is also necessary for the slag door to be open. Additionally some minutes after starting of the arc, dust is injected into the furnace by compressed air using also a lance. For the exemplary heat given this programme results in maximum NO_x concentrations of 200 ppm (410 mg/m³) at the beginning of the heat.

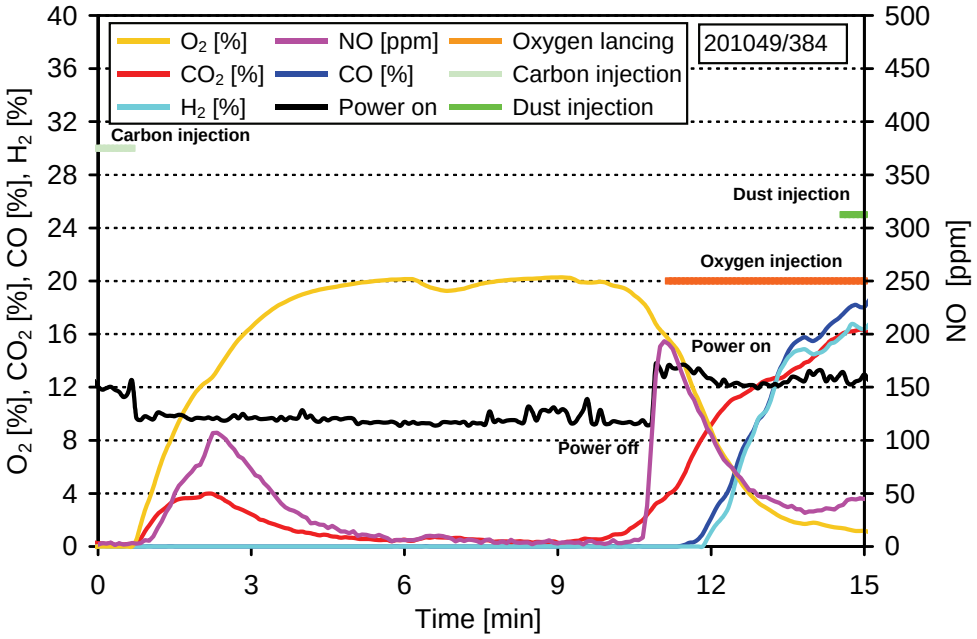

Figure 103: Exemplary carbon steel heat, regular programme

For the trials this regular programme was changed into the trial programme. In the trial programme the slag door stays closed during arc ignition for the first basket and then finally is opened to start the oxygen lancing 5 minutes after arc ignition. There is no dust injection within the trial programme. These measures should as kind of primary DENOX methods reduce the oxygen supply and thereby reduce the NO_x emissions. **Figure 104** shows the beginning of one of the trial heats and the effect of the delayed oxygen lancing. The maximum NO concentration at arc ignition is only at about 70 ppm (144 mg/m³) and therefore reduced by more than half in comparison to the exemplary regular heat.

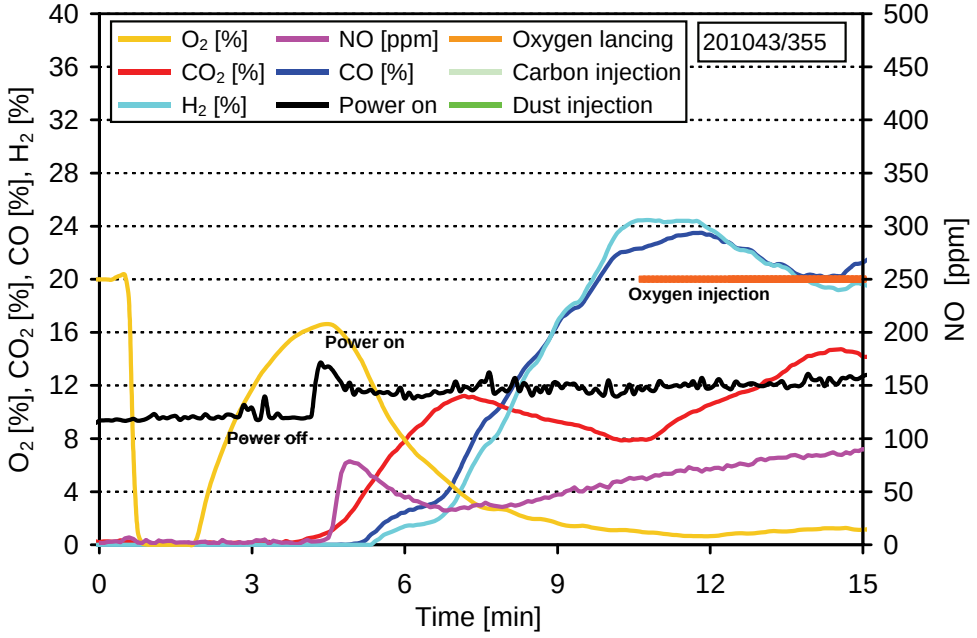

Figure 104: Trial heat with delayed oxygen lancing

The CO_2 and NO_x emissions at measurement point A and point B for some selective heats can be seen in **Table 32**. It becomes clear that the delayed oxygen lancing as a NO_x reducing method is lowering the NO_x emissions during ignition/start of the first melt down period. This effect is due to the reduced oxygen supply in the hot zone of the EAF vessel.

Table 32: NO_x emissions for regular and trial programme

Heat no.	Trial	CO_2 (point A)	CO_2 (point B)	NO_x (point A)	NO_x (point B)
201043/355	X	11.80 %	7.00 %	70 ppm	40 ppm
201047/356	X	11.70 %	8.00 %	30 ppm	33 ppm
201049/384	-	16.00 %	8.00 %	200 ppm	50 ppm
201053/386	-	12.40 %	9.00 %	150 ppm	53 ppm

2.3.6.2 Injection of carbon and dust with nitrogen by door lances

To investigate the influence of the carrier gas for carbon and dust injection on the NO_x emissions at DEWG plant trials were performed in December 2007. At DEWG compressed air is used as standard carrier gas for the injection of carbon and dust through the door lances. The dust injection into the EAF vessel is used for the enrichment of alloying elements level during steelmaking in the entire dust amount.

For the trials the carrier gas has been changed to nitrogen and off-gas measurements have been conducted at measurement point B, which is located at the end of the water-cooled hot gas dedusting system after complete post combustion, before the water spraying unit (**Figure 105**). The NO_x emissions detected at point B could be generated by two sources: (a) electric arcs and (b) post combustion reactions. The measurement results from trial operation are therefore compared with results from normal operation so that the influences of different carrier gases on the off-gas composition or the off-gas temperature can be investigated.

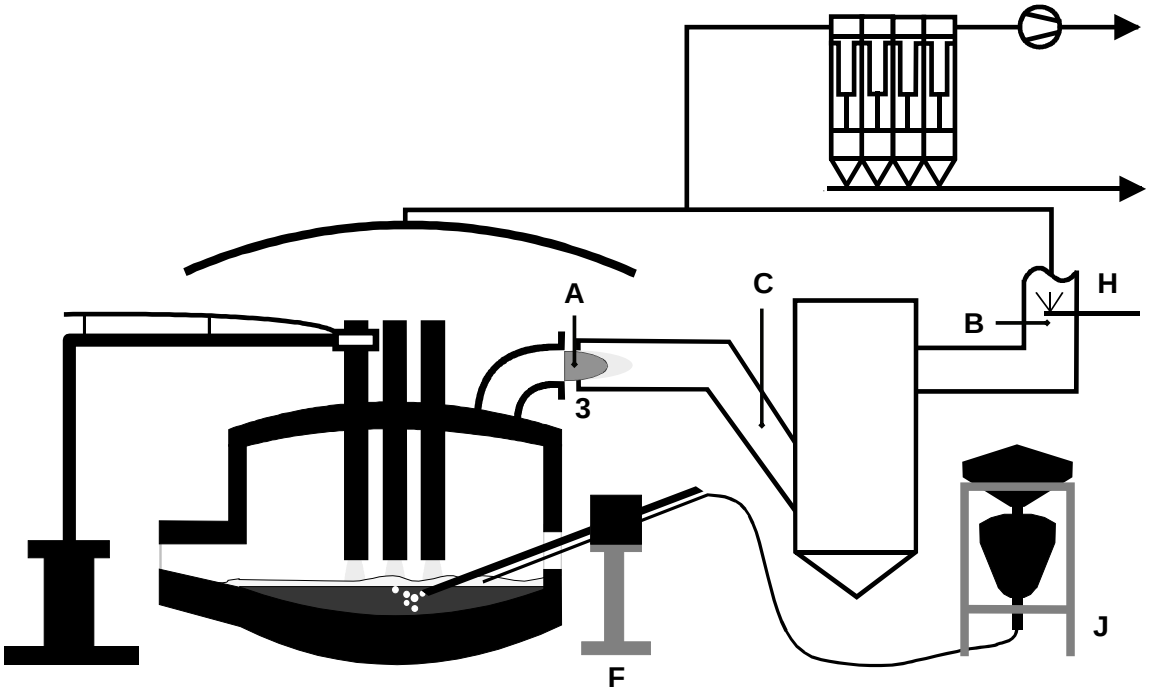

Figure 105: EAF layout at DEWG
A: measurement point A, B: measurement point B, C: temperature measurement, H: water injector, F: oxygen/dust injector, J: dust silo; 3: gap between EAF vessel and primary dedusting system

The injection of dust and coal is usually performed with compressed air (p = 6 bar) (**Figure 106**). At the bay wheel the compressed air pressure is reduced (p = 2 bar). By using a switch the carrier gas can be changed from nitrogen to compressed air for the trials.

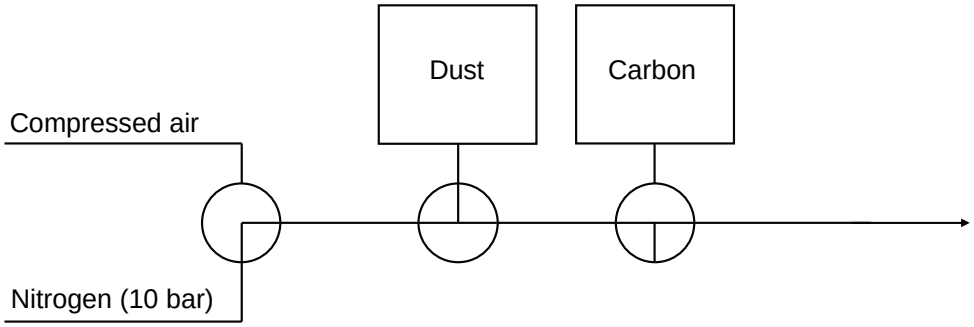

Figure 106: Injection of Dust and Coal

The start of dust injection depends on slag level. In case of a low slag level the dust injection is not performed. In case of a high slag level the injection is performed early. The plant trial was carried out for carbon steel heats only. The total volume flow rate through the primary dedusting system for carbon steel heats is about 100000 m³ (STP)/h. After the feeding of the 1st basket the dust is injected into the EAF. The carbon is usually injected after the feeding of the 2nd basket.

During trials some technical problems occurred. In contrast to the operation with pressurized air the piping of the injection lance irregularly clogged when nitrogen was used as carrier gas. As a consequence to piping of the lance had to be dismantled completely, cleaned and then reinstalled. Therefore additional work on the design of the lance piping will be necessary if one will use nitrogen as standard carrier gas in future.

Figure 107 and **Figure 108** show exemplary results of the trials. **Figure 107** presents the operating data and the off-gas measurement data at point B for a standard heat where the dust was injected with compressed air. A NO_x peak of about 38 ppm can be seen after 1st ignition. The NO_x concentration is then decreasing until the 2nd ignition takes place after charging of the 2nd basket. The represented NO profile shows a similar tendency as the represented temperature profile. The CO content while melting down the 1st basket is below 250 ppm. The O_2 content decreases clearly down to 15 %.

In **Figure 108** the operating data and the off-gas measurement data at point B for a trial heat with nitrogen as carrier gas are shown. The NO_x peak after the 1st arc ignition is only up to 15 ppm. The individual peak value is lower than for normal EAF operation. Simultaneously the CO concentration increases up to 2000 ppm. After the CO increase the NO concentration increases up to 25 ppm. At the end of the 1st ignition period there is a NO maximum and CO minimum values. This may be due to a high post combustion rate in the EAF vessel, in the gap between EAF and primary dedusting system, and in the post combustion chamber. During the 2nd ignition period the O_2 concentration decreases down to 10 %. Simultaneously the CO concentration increases. The NO profile during both ignition periods can be compared. With the decrease of the off-gas temperature and maximum O_2 concentration, a NO maximum concentration was identified.

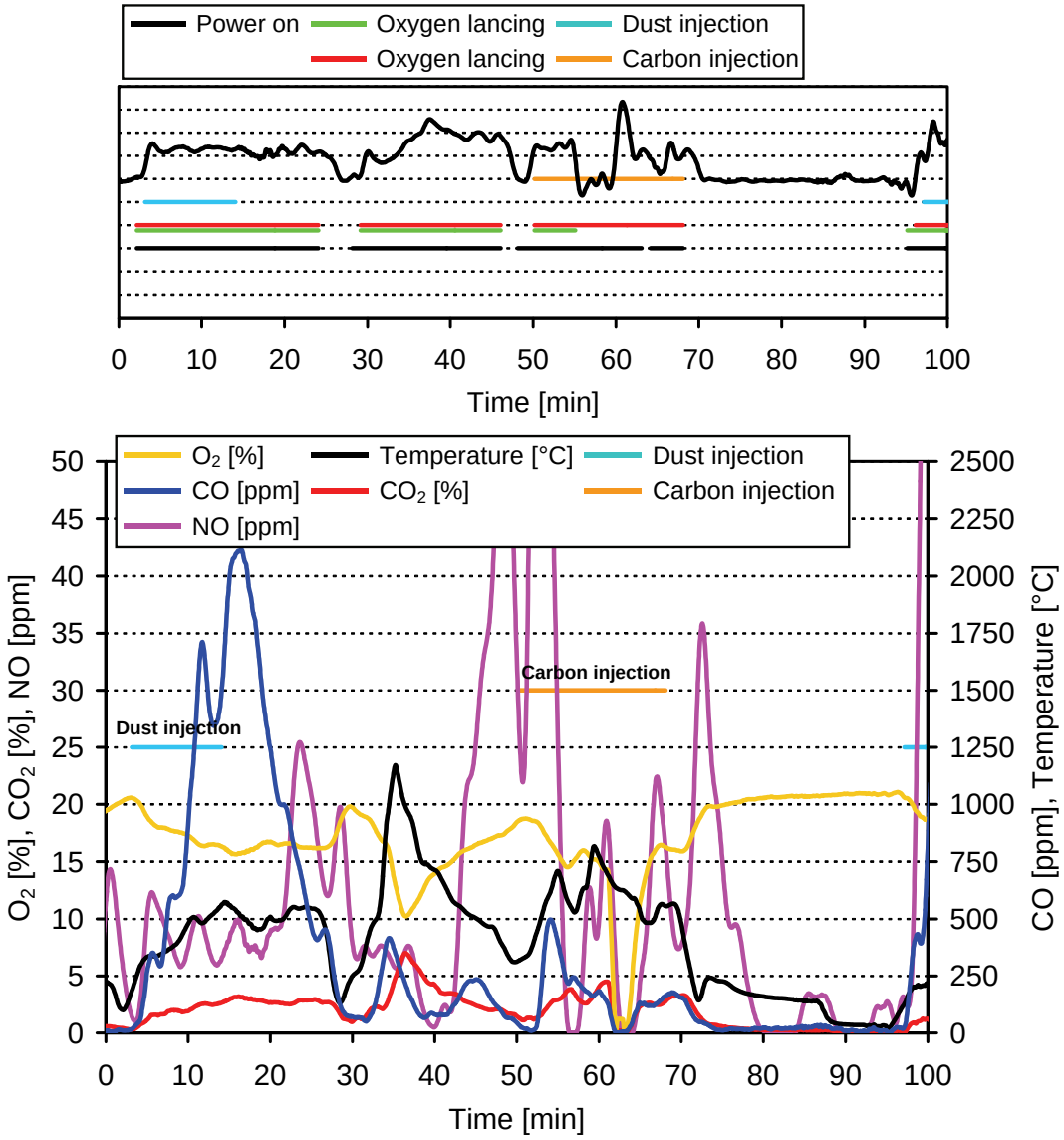

Figure 107: EAF operation data (top) and measured off-gas composition at point B (bottom) for an exemplary heat with dust and coal injection by compressed air

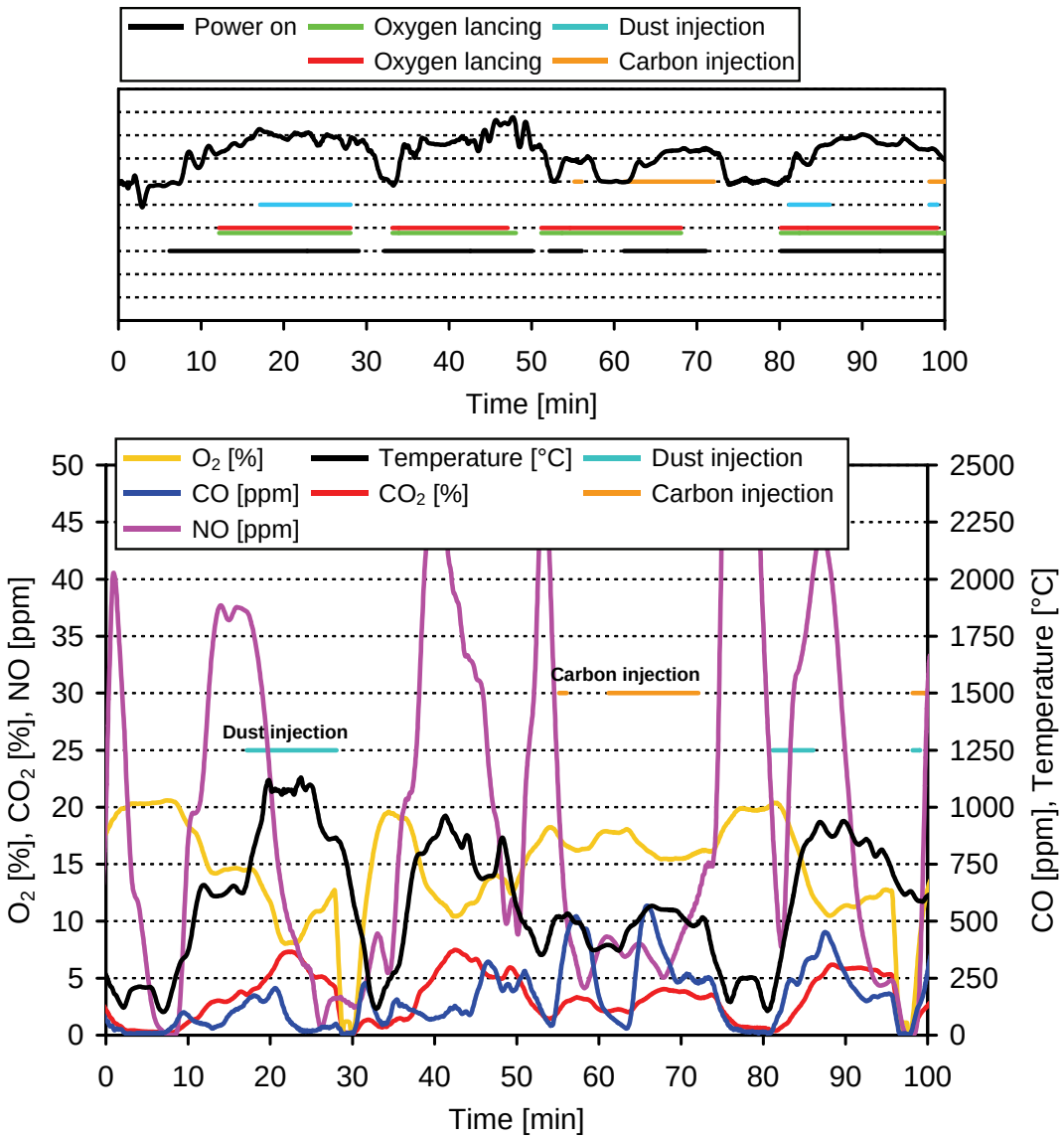

Figure 108: EAF operation data (top) and measured off-gas composition at point B (bottom) for a trial heat with dust and coal injection by nitrogen

The results of the off-gas analysis show that the carrier gas has an influence on the total NO_x emissions at point B. **Figure 109** shows the measured O_2 concentration vs. the measured NO emission. In case compressed air is used as carrier gas for the dust, oxygen concentrations of less than 10 % are reached and NO concentrations up to 38 ppm are measured. Higher NO content correlates with higher oxygen concentrations in the off-gas. When nitrogen is used as carrier gas for the dust injection O_2 concentrations of more than 15 % are reached and NO concentrations of about 10 ppm are measured. The total NO emission during the dust injection with nitrogen is smaller compared to the use of compressed air. The CO content of the off-gas in relation to the NO concentration is shown in **Figure 110**. The measured CO content for use of nitrogen as carrier gas for the dust is with 1800 ppm clearly higher than the 300 ppm of CO measured for the use of compressed air.

Regarding the phases of carbon injection there is no advantage in the use of nitrogen as carrier gas noticeable. On the contrary even higher NO concentrations have been measured when using N_2 instead of air for the carbon injection (**Figure 109** and **Figure 110**) which could be due to a later post combustion and higher post combustion rate.

So nitrogen can be used as carrier gas during dust injection to reduce the NO_x emissions of the EAF, whereas during carbon injection the use of compressed air can be continued.

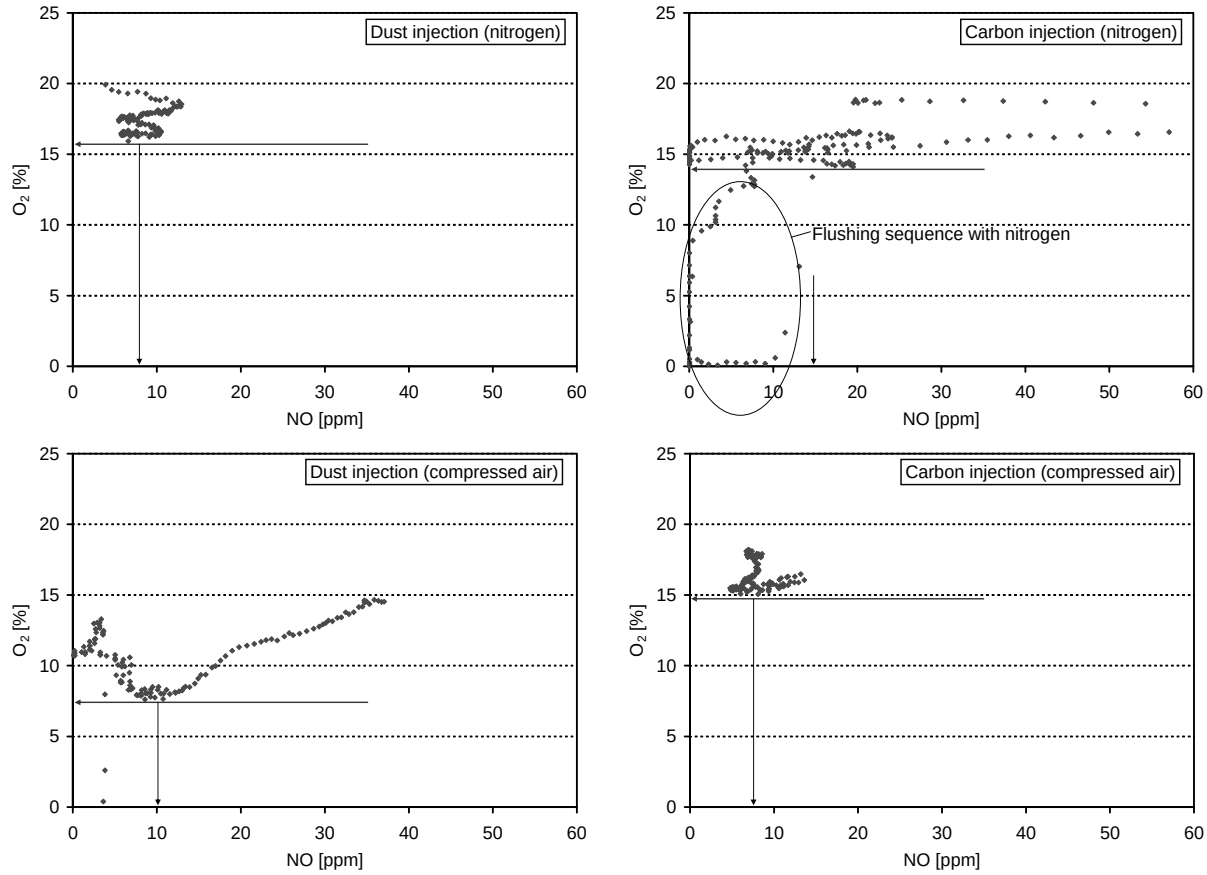

Figure 109: Measured O_2 concentration vs. NO concentration at point B

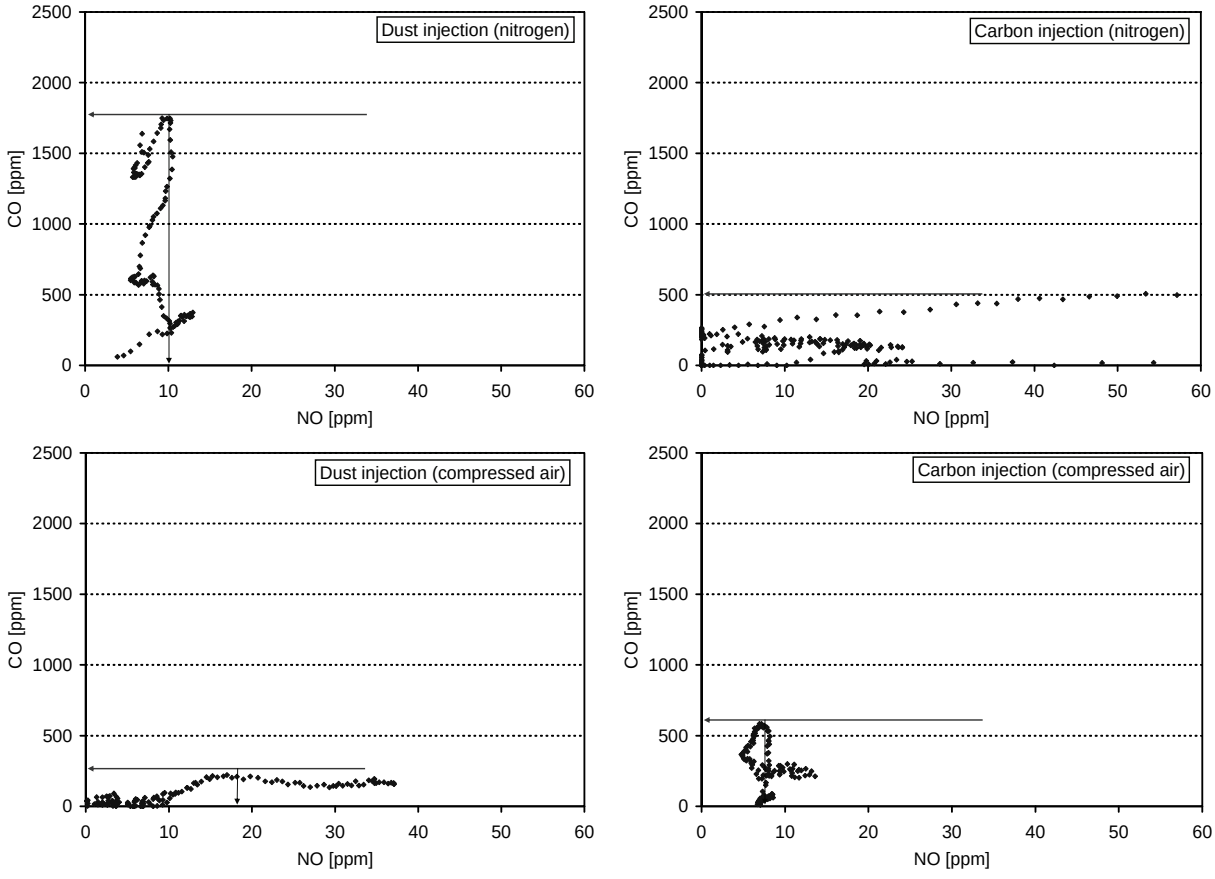

Figure 110: Measured CO concentration vs. NO concentration at point B

2.3.6.3 Influence of dedusting system operation (primary exhaust gas varied by DEC)

Figure 111 shows the NO_x and CO profile for measurement point A and point B. At DEWG there is no sliding muffle installed. With a sliding muffle air intake at the gap between EAF elbow and primary dedusting system could be controlled. At DEWG there is a fixed gap so air intake is to be set fixed/constant. The off-gas volume flow rate is 60000 m^3 (STP)/h (stainless) and 100000 m^3 (STP)/h (tool/carbon). The average NO_x emission at point A is 188 mg/m^3 (STP) and at point B 60 mg/m^3 (STP). This is due to dilution of direct process off-gas with air intake at the gap. The CO content is burned at the gap and partly downstream point A.

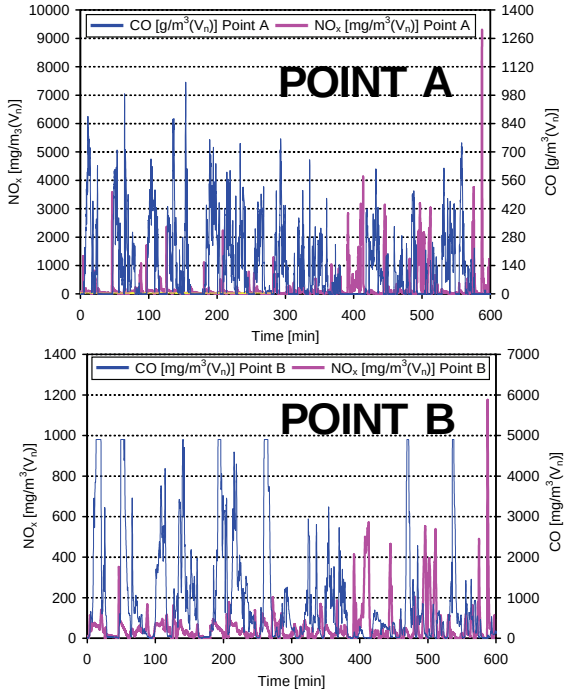

Average NO_x emission at Point A:
NO_x: 188 mg/($m^3(V_n)$) (0.49 g/s)

Average CO_x emission at Point A:
CO: 131 g/($m^3(V_n)$) (209 g/s)
CO_2: 856 g/s

Average NO_x emission at Point B:
NO_x: 60 mg/($m^3(V_n)$) (0.78 g/s)

Average CO_x emission at Point B:
CO: 900 mg/($m^3(V_n)$)
CO_2: 1214 kg/s

Figure 111: NO_x and CO profile measured at point A (top) point B (bottom)

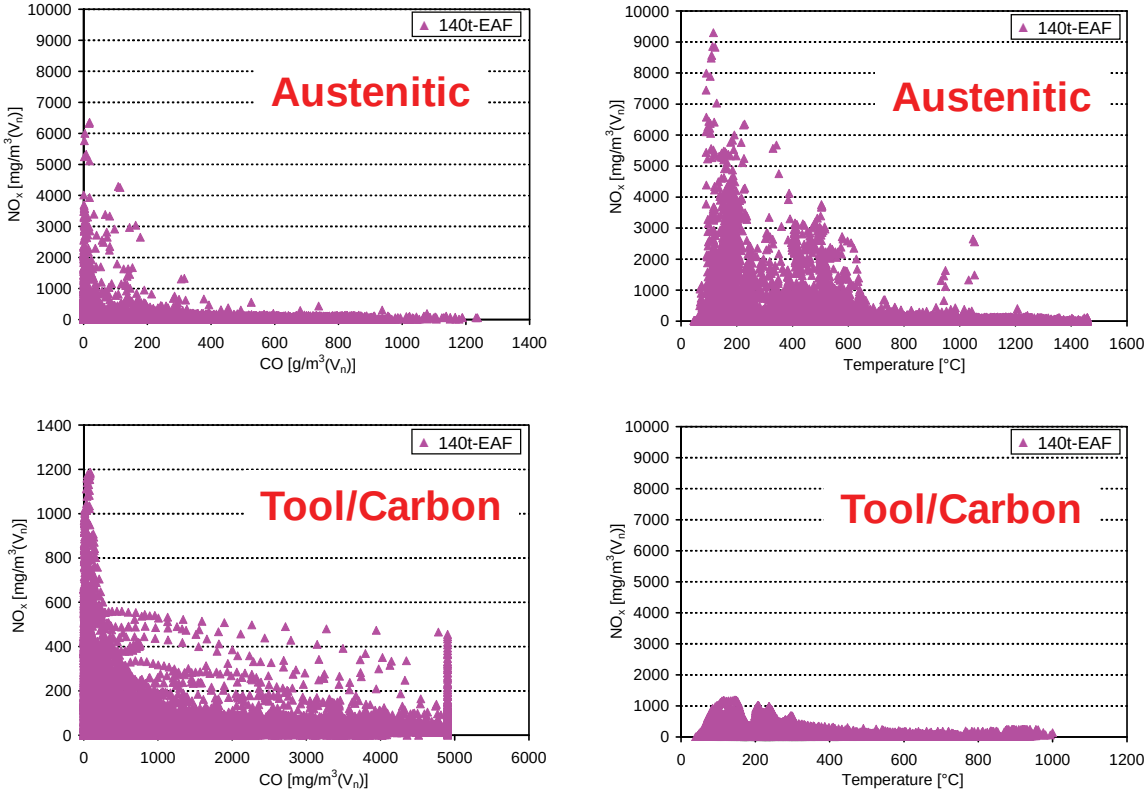

Figure 112: NO_x content vs. CO content (left) and off-gas temperature (right) for stainless and carbon steel qualities

Figure 112 shows the NO_x content of the off-gas vs. the CO content as well as the off-gas temperature for stainless (austenitic) and carbon steel qualities. Stainless qualities are produced with the lower fixed off-gas volume flow rate. In general the amount of NO_x measured as well as the off-gas temperature are higher for stainless and the amount of CO measured in the off-gas is higher for carbon qualities.

2.3.6.4 Evaluation of exhaust gas results and operational data

Figure 113 shows the specific NO_x emissions in the off-gas grouped for stainless and tool/carbon steel qualities. There is a clear distinction between the two groups given by the different operational parameters of the production in the EAF. Whereas the average NO_x emission for stainless steel could be measured with 0.031 kg/t_{steel} for stainless qualities during production of tool/carbon qualities only 0.012 kg/t_{steel} were emitted in average. The main reasons for this difference are presumably the different off-gas volume flow rates and the lack of foamy slag in stainless steel production.

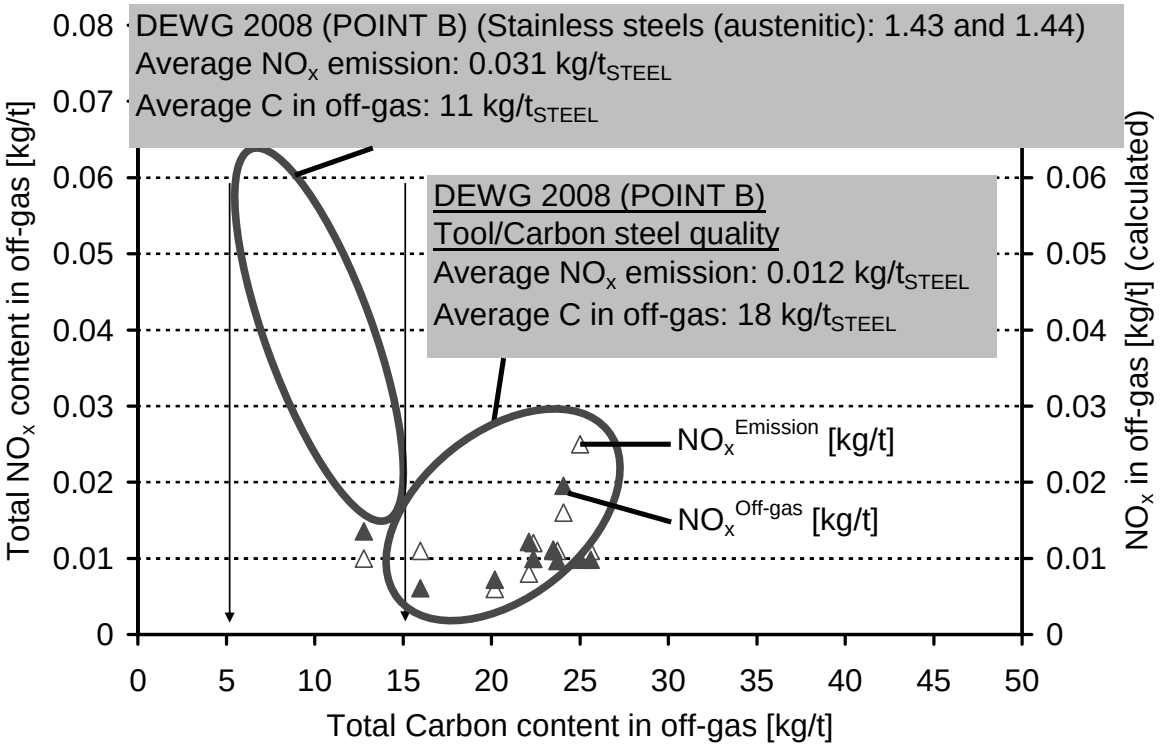

Figure 113: Specific NO_x content in off-gas vs. specific C content in off-gas at point B

2.3.6.5 Definition of the best practices in order to minimise the NO_x generation

Concluding this work package out of the results of the single tasks in order to minimise the NO_x emissions the following best practices could be phrased:

- Delaying of oxygen injection for some time after the arc ignition.
- Use of an inert carrier gas for dust injection into the furnace.
- Maximum air tightness of the EAF (closed slag door if possible).
- Minimized off-gas volume flow (variable DEC).

All these measures could be used to reduce the oxygen content of the furnace atmosphere and increase the residence time of the off-gas within the furnace freeboard. Each single method has been shown to be useful in reducing the NO_x emissions. The delayed oxygen injection after first arc ignition has reduced the NO_x emissions in the beginning of the meltdown phase. The use of nitrogen as inert carrier gas for the dust injection also leads to lower NO_x emissions. However the use of nitrogen instead of compressed air resulted in some technical problems. And last but not least the air intake of the EAF should be minimized and therefore the off-gas flow rate should be as low as possible and the EAF as airtight as possible.

2.3.7 CFD simulations of NO_x formation

2.3.7.1 Calculations of gas flow patterns of EAF off-gasses with defined boundary conditions from off-gas measurements at industrial partners

Discretisation of the geometry of the EAF systems to be investigated

The EAF that is investigated is an electric arc furnace of the steel plant of the Deutsche Edelstahlwerke (DEW) in Siegen, Germany.

EAF Type:	AC-electric-arc-furnace
Tap weight:	140 t for alloyed engineering steel 120 t for stainless, acid-/heat-resistant steel
Tap to tap time:	68 minutes / 100 minutes
Transformer output:	105 MVA/ 600 -1200 V
Vessel diameter:	6900 mm
Volume:	160 m^3
Electrode diameter:	610 mm

The electric arc furnace operating cycle (tap-to-tap cycle) generally consists of the following steps: Furnace charging, melting, refining, de-slagging, tapping and furnace turn-around.

The processes taking place within the EAF vessel during a tap-to-tap cycle are extremely complex and transient. Especially the time period after furnace charging is extremely hard to simulate. The freshly charged scrap is cold, has to be heated and melting takes place locally where the arc has contact with the metal. The scrap heap changes and collapses as the metal melts. Not only does this mean a constantly changing geometry for the numerical model, but also the local melting of the metal, the unknown composition and mass distribution of the scrap heap as well as the constantly changing contact position of the arc with the metal scrap have to be considered. The conditions inside the EAF vessel during this time are highly transient.

The main objective of this project is to investigate the NO_x formation in the EAF, whereby the various sources of NO_x formation are to be identified and the effect of parameter variations is to be estimated. Therefore it was decided to model the refining period at the end of the EAF cycle, during which the molten pool of metal below the slag layer is heated by the electric arc and no scrap remains. During this time period it is possible to estimate the boundary conditions for the off-gas within the vessel and the geometry is fixed.

It is not necessary to model the entire EAF system. The region of interest is the off-gas inside the EAF, starting above the slag layer and at the opening to the slag door and ending downstream from the combustion gap. In order to calculate the gas -flow patterns and NO_x formation inside the EAF, the thermal conditions at all of the surfaces encompassing the flow region must be modelled and the numerical model must include the gaps through which air ingress into the flow region can take place. The geometry of the numerical model of the EAF is shown in **Figure 114**.

The numerical model includes the following:

- Central roof area around electrodes
- Electrode gap (30 mm) around each electrode (∅ 610 mm)
- Top and side roof area
- Exhaust duct (starting from fourth-hole in roof)
- Combustion gap (150 mm)
- Off-gas extraction
- Roof-ring gap (50 mm)
- Upper vessel (∅ 6900 mm)
- Lower vessel above top of slag layer
- Slag layer with a height of 200 mm and top part of pool of molten metal

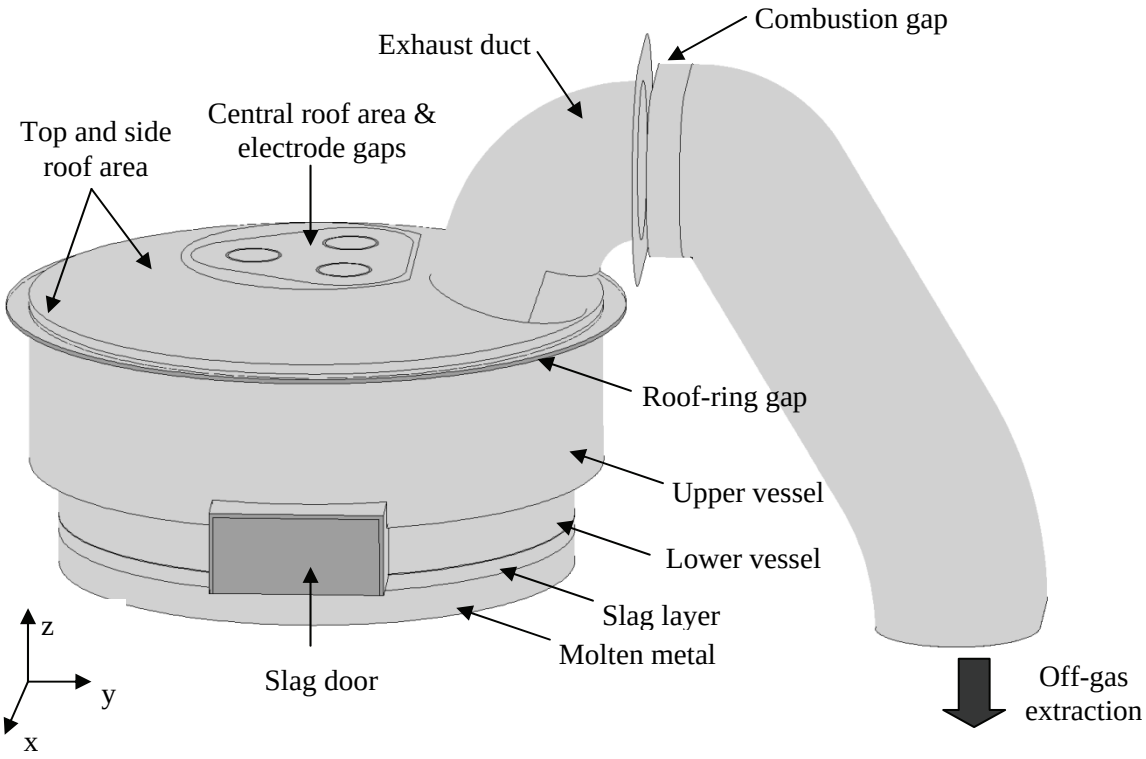

Figure 114: Geometry of the EAF in the numerical simulation model

The electrode gap and roof-ring gap sizes are estimated values, as the true gap sizes are not known. In addition to the features listed above, as shown in **Figure 115** below, the numerical model geometry includes the outer surface of the three electrodes, which have a diameter of 610 mm, as well as three cylindrical electric arc regions. The electric arc regions extend from the tip of each electrode, down to the surface of the metal pool.

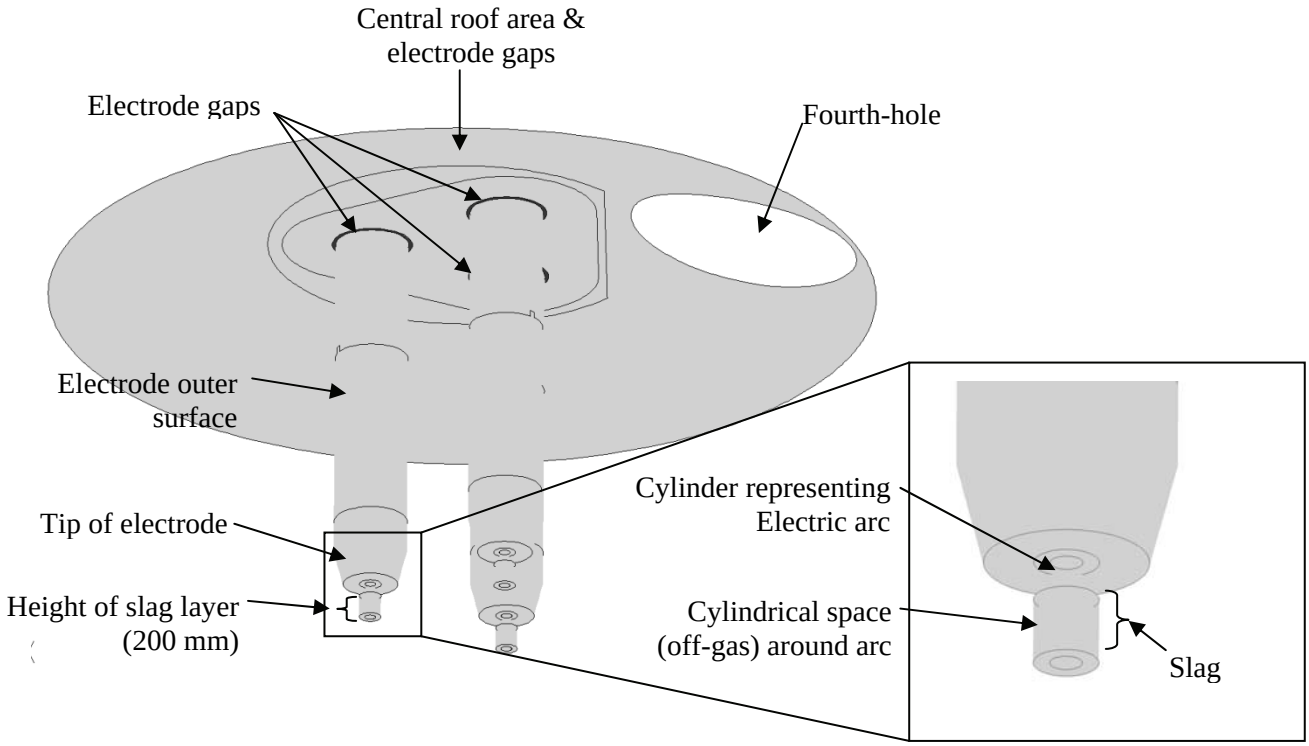

Figure 115: Details of the inner geometry of the numerical simulation model

In the case of this investigation a slag layer of 200 mm is assumed. It is furthermore assumed that during the refining period the voltage drop between cathode (electrode) and anode (metal pool) is 340V. The electric arc current is assumed to be 64 kA.

The electric arc, which in reality jumps from electrode to electrode, is represented by three cylinders extending from each tapered electrode tip to the surface of the molten metal. The diameter (d_{Arc}) and length (l_{Arc}) of the arc region, represented by a cylindrical channel, is calculated using the channel model (Kanalmodel) [18] for an alternating current electric arc.

Estimation of arc length:

$$V_{Arc} = V_{Cathode} + E_{Arc} \cdot l_{Arc} + V_{Anode} \quad (24)$$

$V_{Cathode}$ - Voltage drop of cathode (approximately 3 to 10 V)
V_{Anode} - Voltage drop of anode (approximately 10 to 30 V)
E_{Arc} - Electric arc field strength (approximately 1 V/mm for alternating current electric arcs)
l_{Arc} - Arc length

Equation (24) can be reformulated using the approximate values for an alternating electric arc [18].

$$V_{Arc} = 40\,V + 1\frac{V}{mm} \cdot l_{Arc} \quad (25)$$

With V_{Arc} = 340 V the electric arc length is determined to be l_{Arc} = 300mm.

Calculation of electric arc radius (channel model (Kanalmodel) [18]):

$$j_{Arc,channel\,model} = \frac{I_{Arc}}{A_{Arc}} \quad (26)$$

j - Electric arc current density (approximately 1 kA/cm^2)
I_{Arc} - Electric arc current
A_{Arc} - Electric arc cross-sectional Area, channel model

$$A_{Arc} = \pi \cdot r_{Arc}^2 \quad (27)$$

With I_{Arc} = 64 kA the electric arc radius is determined to be r_{Arc} = 45.14 mm.

In order to keep the calculation time within acceptable limits, the numerical model was split into two separate models, Model 1 and Model 2. The calculated flow field profiles at the outlet of Model 1 are set as the inlet flow field profiles of Model 2 in order to calculate the post-combustion taking place in the combustion gap. The discretised geometry of the numerical model of the EAF is shown in **Figure 116**.

In order to keep the calculation time within acceptable limits, the numerical model was split into two separate models, Model 1 and Model 2, as shown above. The calculated flow field profiles at the outlet of Model 1 are set as the boundary conditions for the inlet of Model 2 in order to calculate the post-combustion taking place in the combustion gap.

Simulation of gas flow patterns inside the EAF vessel for selected boundary conditions

Definition of the boundary conditions of the numerical model

In the case of this investigation, the numerical simulations were carried out with the commercial CFD software FLUENT (Version 12.1.4). The geometry was discretised using the software GAMBIT (Version 2.4.6).

The calculated NO_x formation in the EAF vessel depends to a great extent on the boundary conditions defined for the numerical model. Ideally, the boundary conditions should be as close to the real conditions in the investigated EAF as possible. One of the main challenges of this investigation lies in finding acceptable values for the boundary conditions, as in many cases the true values are unknown (e.g. conditions in the electric arc).

Model 1 & 2 – Material Properties and Numerical Simulation Settings:

The material properties defined for the walls, molten slag and pool of molten metal of the numerical model are summarized in **Table 33**.

Profiles for temperature, mass fraction of individual species and velocity
at outlet of Model 1 -> boundary conditions for inlet of Model 2

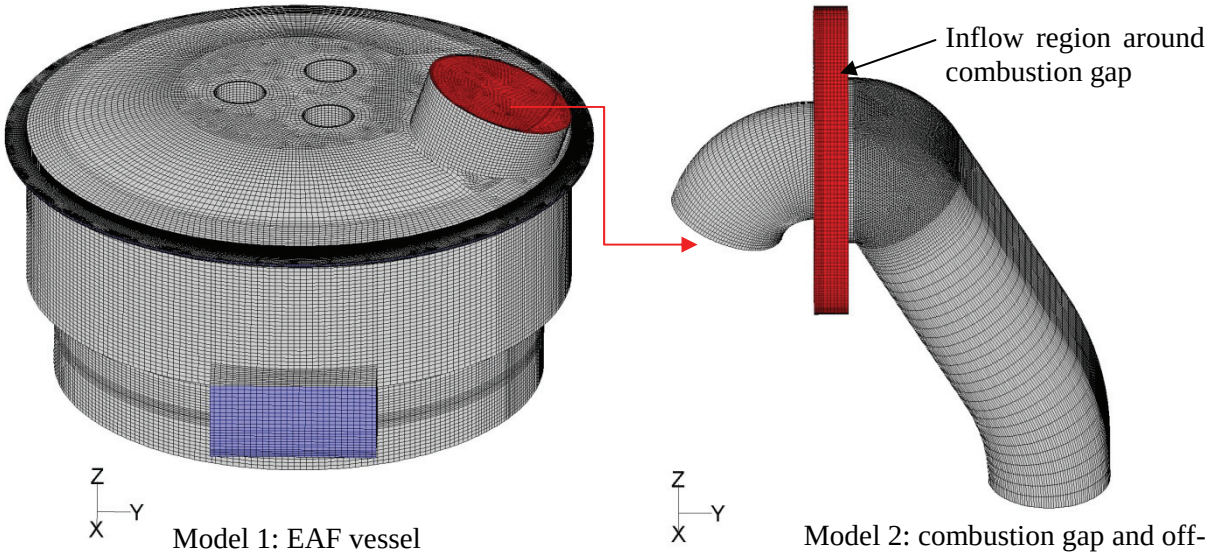

Figure 116: Discretised geometry of the numerical model of the EAF

Table 33: Summary of the material properties used for the numerical model [3],[13],[19],[5],[6],[22]

Material	Application	Estimated temp. range in EAF vessel	Density	Thermal conductivity	Emissivity
			ρ	λ	ε
		[°C]	[kg/m^{3}]	[W/m*K]	[-]
Graphite	electrodes	up to 3327	1700	240	0.85
Refractory material	walls of lower shell and central roof area	1000 - 1700	1760	2.4	0.6
Slag layer (solid)	walls of upper vessel, exhaust duct, top and side roof area	up to 1500 °C ($\approx T_{liquidus}$)	1760	2.2	0.6
Slag (molten)	slag layer (200 mm) on top of molten steel	greater than 1500°C	2900	initially 2.2 (changed to 4.4)	0.6
Steel (molten)	bath of molten steel	1500 - 1700	7590	initially 18.5 (changed to 30)	-

The material properties (e.g. thermal conductivity, viscosity, heat of formation) for the considered species of the off-gas (N_2, O_2, H_2O, CO, CO_2, NO_x) are defined using the FLUENT Material Database (FLUENT Version 12.1).

The following settings are used for the off-gas material properties and flow field calculation:

- Energy equation on
- Heat radiation exchange between all surfaces (slag- , electrodes-, electric arc- and EAF vessel surfaces)
  - Model 1 - Calculated using Discrete Ordinates Radiation Model
  - Model 2 - deactivated
- Realizable k-ε turbulence model used (viscous heating assumed negligible)
- Turbulence intensity of 5% assumed at all flow inlets
- Standard wall functions are used for near wall treatment of turbulence
- Operating pressure and operating temperature are 101325 Pa and 298.15 K respectively

- Density calculated using incompressible ideal gas law
- Gravity (g_z = -9.81 m/s^2) is activated, buoyancy effects are taken into account
- Piecewise-polynomial function for the temperature dependence of the specific heat of the individual species
- Mass-weighted mixing law for the properties of the off-gas mixture

Model 1 & 2 – Chemical Reactions:

In order to take the interaction of the off-gas species CO, CO_2 and O_2 into account in the EAF-vessel, the following volumetric reactions are activated in the numerical simulation model:

$$CO + 0.5\,O_2 \rightarrow CO_2 \tag{28}$$

$$CO_2 \rightarrow CO + 0.5\,O_2 \tag{29}$$

For Reaction (28) and (29) the finite-rate/eddy dissipation option is activated for the turbulence-chemistry interaction. The rate constants for these two reactions supplied in the FLUENT Database for a carbon-monoxide air mixture are used.

The FLUENT NO_x formation Model was activated in order to calculate the NO_x production in the EAF vessel. Three principle formation mechanisms exist for NO_x formation: Thermal, Prompt and Fuel-NO_x. Prompt NO_x is relevant for fuel rich flames and Fuel NO_x concerns the oxidisation of fuel bound nitrogen [9]. As for this investigation the time period within the EAF where only the electric arc is used to heat the molten metal is considered, it is only necessary to activate the Thermal NO_x formation option of the NO_x formation Model.

The Thermal NO_x formation option takes the following highly temperature dependant chemical reactions (extended Zeldovich thermal NO mechanism) into account:

$$O + N_2 \leftrightarrow N + NO \tag{30}$$

$$N + O_2 \leftrightarrow NO + O \tag{31}$$

$$N + OH \leftrightarrow H + NO \tag{32}$$

The reaction rate constants used in the FLUENT NO_x formation Model for these three reactions have been measured in numerous experimental studies and the data obtained from these studies have been critically evaluated [7].

Model 1 & 2 – Boundary conditions defined for EAF upper vessel-, top and side roof area- and exhaust duct walls:

The EAF vessel-, top and side roof area- and exhaust duct walls are defined as smooth walls covered by a layer of slag. In reality the slag layer thickness is not constant at all. The melting temperature of steel slag, depending on its composition, is approximately 1500 °C. This, amongst other things, has an influence on the thickness of the slag layer that is deposited and builds up on the EAF vessel walls during its service life.

For this investigation a slag layer thickness of 0.020 m is assumed. This slag layer thickness corresponds to that assumed by D. Guo et al.[13] in their work concerning the modelling of radiation intensity in an EAF. The material properties used for the slag layer are shown in **Table 33**.

The EAF vessel-, top and side roof area- and exhaust duct walls are cooled extensively in order to prevent damage to the vessel walls due to hot spots caused by the heat radiation from the electric arc. It is known that the temperature of the cooling water in the wall heat exchanger pipes has a maximum temperature of approximately 60 °C. As the amount of heat extracted from the areas modelled is not explicitly known, the cooling of these surfaces was taken into account by setting a constant temperature of 373.15 K (100 °C) at the base of the slag layer. The heat extracted across the thickness of the walls is then a function of the temperature at the surface ($T_{slag,surface}$) as shown in equation (33).

$$\frac{\dot{Q}_{wall}}{A_{wall}} = \lambda_{slag} \cdot b_{slag} \cdot \left(T_{slag,surface} - T_{slag,base} \right) \tag{33}$$

λ_{slag} - thermal conductivity of slag
b_{slag} - slag layer thickness
$T_{slag,base}$ - temperature at the base of the slag layer

Model 1 - Boundary conditions defined for EAF lower vessel- and central roof area walls:

The lower vessel- and central roof area walls are not cooled and consist of refractory material. The material properties used for this material are given in **Table 33** at the beginning of this section.

These surfaces are defined as smooth adiabatic walls, as the amount of heat lost is negligible when compared to the amount of heat drawn out of the EAF vessel through the cooled walls.

Model 1 – Boundary conditions defined for the electrode surfaces:

The electrode surfaces are defined as a smooth wall. The material of this wall is defined to be graphite, whereby typical values for the material properties of graphite electrodes are used (refer to **Table 33**). The surfaces of the electrodes in an EAF have a fairly high temperature distribution, as they are not only heated by heat radiation and convection, but also by the alternating electric current flowing through them when the electric arc is in operation. The conditions at the upper end of the electrodes also influence the temperature profile.

A reasonable value for the maximum electrode surface temperature at the electrode tip is 3600 K[19] (3327 °C). In comparison, the sublimation point of graphite is 3925 K[19]. For this investigation a temperature profile based on measured temperature profiles at the surface of electrodes in an EAF[2] is used for the numerical model.

The characteristics of the work electrodes and EAF for which the measurements where done are as follows[19]:

- Alternating electric current of 64 kA
- Electrode diameter of 0.6 m
- Total electrode length of 7.2 m

The alternating electric current and electrode diameter of the work electrodes and the electrodes of the numerical model correspond. The length of the electrodes of the numerical model is however only 3.1 m. Therefore the measured temperature profiles were adapted for the numerical model based on the following assumptions:

- Hot tip electrode temperature is 3600 K
- Temperature profile close to tip of electrodes correspond
- Temperature gradient between tip and top part of electrode correspond
- Temperature gradient for top part of electrode will be similar

Both the measured and adapted temperature profiles are shown in **Figure 117**. In order to establish the sensitivity of the calculated NO_x formation to the adapted temperature profile, a numerical simulation was also carried out using the alternative adapted temperature profile.

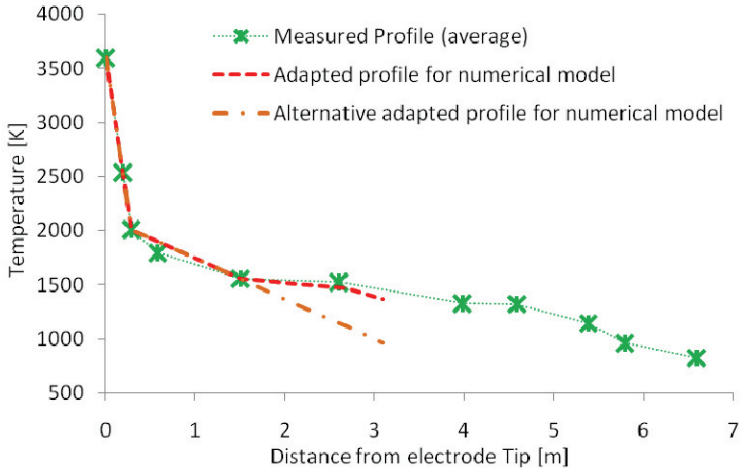

Figure 117: Measured vs. adapted and alternative adapted electrode temperature profiles

Model 1 – Boundary conditions defined for the cylindrical surfaces representing the electric arc:

As described before the channel model (Kanalmodel) was used to define three cylindrical surfaces representing the position of the electric arc between the electrode tips and the molten metal. However, in reality the arc will jump from electrode to electrode. Including this fact in the numerical model would necessitate a transient calculation, which would generate extremely large amounts of data. Such a simulation would perhaps be called for, if possible, if the aim of this investigation were a detailed study of the effect of the electric arc on the flow field characteristics limited to the flow field region around the electric arc. As this investigation is aimed at considering the entire EAF-vessel as well as the combustion gap, a different approach was adopted.

The surfaces defining the three possible electric arc positions according to the channel model are defined as a smooth wall. Results of research done by M. Ramírez-Argáez et al.[20] to investigate direct current electric arcs burning in different atmospheres were used to apply an appropriate temperature profile to the three surfaces.

First a temperature profile was determined, which corresponds approximately to the temperature profile calculated in the research by M. Ramírez- Argáez et al.[20] in the electric arc at the radius of the three channel model cylinders (r_{arc} = 45 mm). In order to achieve this, the arc was partitioned into six zones of equal height as shown in **Figure 118**. The approximate temperature determined by Ramírez- Argáez et al. in each of the six zones at $r \approx r_{arc}$ was used.

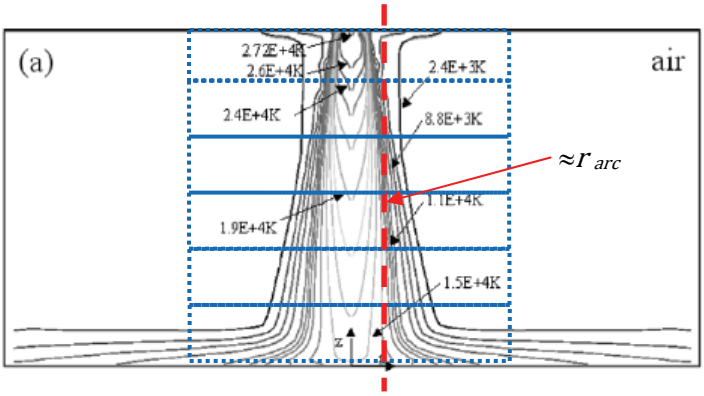

Figure 118: Temperature contours for electric arcs (44 kA DC current, 0.3 m length) with different gas atmospheres by M. Ramírez-Argáez et al. used to define temperature profile for arc representation in numerical model.

As not only one, but three such surfaces are present in the model, the temperature ($T_{i\ zone,arc}$) profile was adapted so that the sum of the heat radiation to a surrounding atmosphere with a temperature (T_{atm}) of 400K above the slag layer and 2000K below the slag layer for all three surfaces ($Q_{radiation,\ 3\ surfaces}$) is equal to the corresponding heat radiation of one surface ($Q_{radiation,\ 1\ surface}$) as calculated using equation (34) to equation (36) below.

$$Q_{radiation,1surface} = \sum_{i=1}^{6} \sigma \cdot \varepsilon \cdot \left(T^4_{i\,zone,arc} - T^4_{atm,i} \right) \tag{34}$$

$$Q_{radiation,3surfaces} = 3 \cdot \sum_{i=1}^{6} \sigma \cdot \varepsilon \cdot \left(T^4_{i\,zone,arc\,num\,model} - T^4_{atm,i} \right) \tag{35}$$

$$Q_{radiation,1surface} = Q_{radiation,3surfaces} \tag{36}$$

ε - Emissivity

σ - Stefan Boltzmann constant $5.67*10^{-8}$ W/(m^2*K^4)

The resulting arc temperature profile used in the numerical model is shown in **Figure 119**.

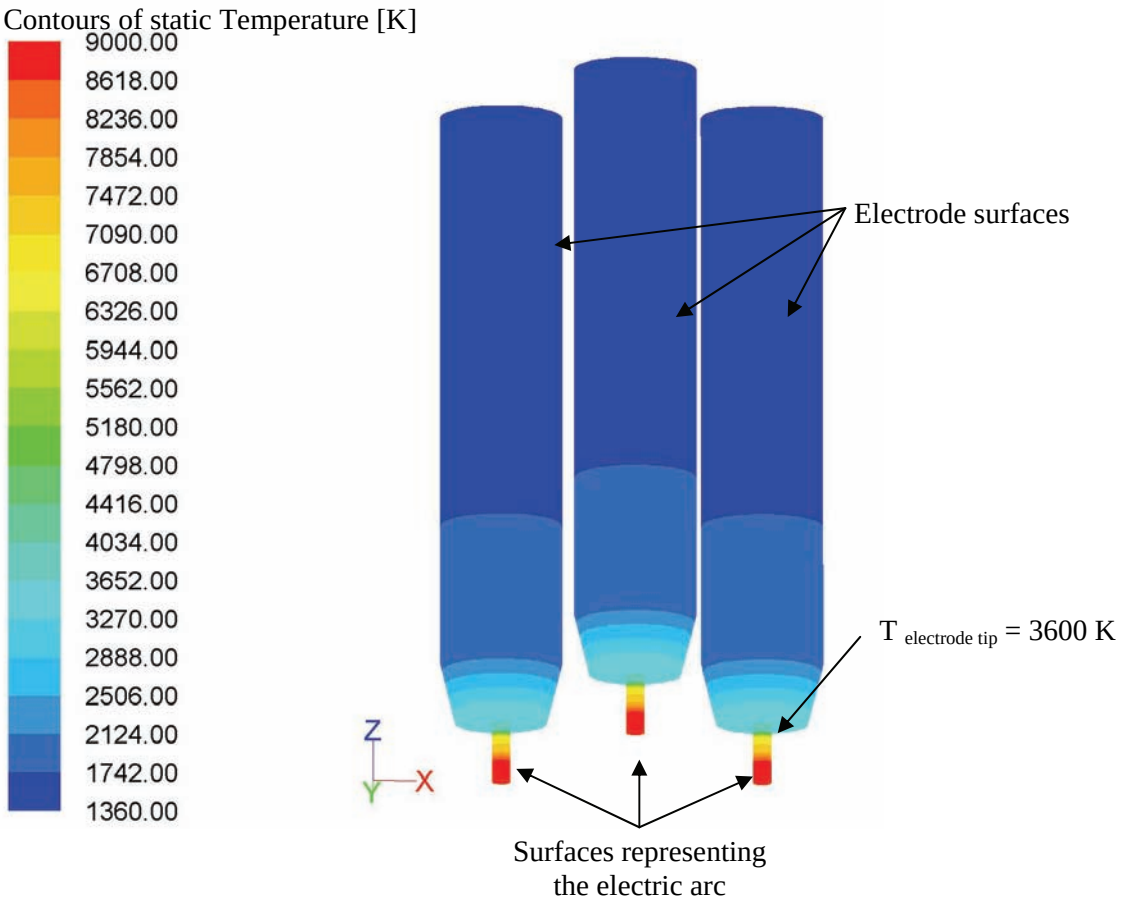

Figure 119: Three-dimensional view of the temperature profiles applied to the electrode- and electric arc surfaces

Model 1 – Boundary conditions defined for the slag layer and molten metal pool:

A slag layer of 200 mm was assumed for this investigation. The form of the molten metal modeled below the slag layer, does not correspond to the real form at the EAF in Siegen. This is due to the fact, that the molten metal in the numerical model is used solely to achieve a temperature distribution on the surface of the slag layer, which results during the numerical simulation. This temperature distribution is not only determined by convection and heat radiation with the EAF vessel walls /electric arc, but also by heat conduction down through the slag layer and molten metal.

The thermal conductivity of the molten metal and slag layer were chosen as shown in **Table 33**, so that the minimum temperature of the slag layer would be equal to or greater than 1773.15 K (1500 °C). The slag layer is known to be fluid and not solid; therefore the temperature at its surface should lie above its liquidus temperature of approximately 1500 °C. The exception to this is the region directly at the slag door, where the relatively cold air with a temperature of 25 °C flows into the vessel. Here it might be possible that a crust of solidified slag is present on the slag layer.

In this investigation the flow field of the slag and molten metal are not considered, as this would greatly increase the complexity and size of the numerical model.

A temperature of 1873.15 K (1600 °C) is set at the base of the molten metal. At the interface between slag and molten metal the two materials are thermally coupled. The side surfaces of the molten metal and slag layer are defined to be adiabatic.

Model 1 – Boundary conditions defined at the in- and outlets:

The in- and outlets of Model 1 are defined as shown in **Figure 120**. The flow out of the exhaust duct is defined as an outflow region, which means that all variables are a result of the flow field calculation within the flow domain.

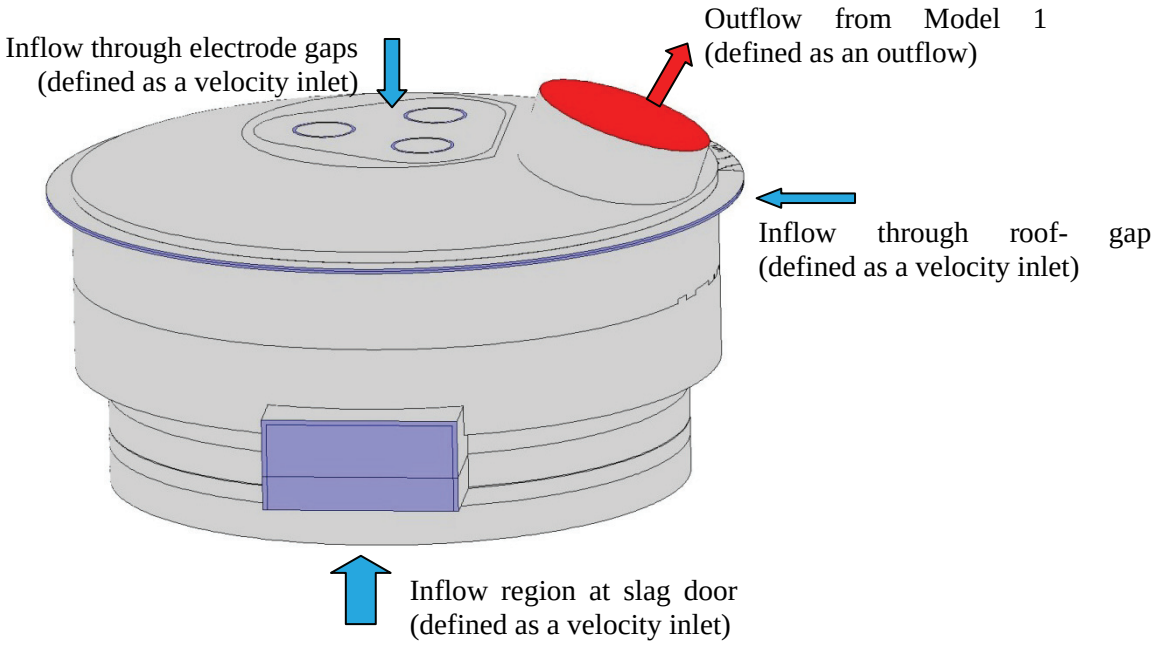

Figure 120: Three-dimensional view of the outer EAF surfaces of Model 1

Due to buoyancy and the hot air rising within the EAF vessel, air is drawn in through the slag door. Therefore this surface is defined as a velocity inlet. In addition, for this investigation it is assumed that no outflow occurs at the roof-gap and electrode gaps, therefore these surfaces can also be defined as velocity inlets. At all velocity inlets an ambient temperature for the inflow of 298.15 K is defined and a turbulence intensity of 5 % is assumed. Furthermore the following mass fraction (ζ_i) for each of the species is given:

- $\zeta_{O2} = 0.234$
- $\zeta_{H2O} = 0.006$
- $\zeta_{N2} = 1 - 0.234 - 0.006$
- $\zeta_{CO} = \zeta_{CO2} = \zeta_{NO} = 0$

These mass fractions correspond to the standard composition of air.

The average velocity and therefore the mass flow rate through the individual inlets at the EAF in Siegen are not known. However the total mass flow rate out of the EAF vessel can be calculated using the measurements done in the centre of the outflow of the combustion gap (measurement point A) and further downstream in the exhaust extraction system (measurement point B).

Measurement Data was collected for many charges at the investigated EAF. As for this investigation the refining period at the end of the EAF cycle is considered, it was decided to use the measurements from the exemplary charge no. 200801. At the end of this charge the electrodes remain in operation after the oxygen injection has ended for a time period of approximately 3 minutes. The measurements from this time interval were used to calculate the average total mass flow rate out of the EAF vessel.

At measurement point A the volumetric fractions (φ_i) are available for the species CO, CO_2, O_2, NO, CH_4 and H_2. At measurement point B the Temperature (T_B), dynamic pressure ($\Delta p_{dynamic}$) and the volumetric fractions (φ_i) are available for the species CO, CO_2, O_2 and NO.

As there are no burners installed at the DEWG EAF, CH_4 is not considered in the numerical simulation. H_2 is considered indirectly within the NO_x model, but is not calculated explicitly within the flow region. The average mass fraction for these two species measured at the EAF during the considered time period is as follows:

- $\varphi_{H2,average} = 0.9$ %
- $\varphi_{CH4,average} = 0.01$ %

Calculation of the average total mass flow rate at measurement point B:

First the total mass flow rate at measurement point B is calculated using the following equations:

$$M_{off-gas} = \sum_{i=1}^{n} \varphi_i \cdot M_i \tag{37}$$

φ_i - Volumetric fraction of species

M - Molecular mass

$$\zeta_i = \varphi_i \cdot \frac{M_i}{M_{off-gas}} \tag{38}$$

ζ_i - Mass fraction of species

$$\rho_{off-gas,B} = \frac{p_{atm}}{\left(\frac{R}{M_{off-gas}}\right) \cdot T_B} \quad \text{(incompressible ideal gas)} \tag{39}$$

$\rho_{off\text{-}gas,\,B}$ - Density of off-gas at point B

R - Universal gas constant 8.314472 J/(K*mol)

$$\overline{v}_{off-gas,B} = \sqrt{2 \cdot \frac{\Delta p_{dynamic,B}}{\rho_{off-gas,B}}} \tag{40}$$

$$\dot{m}_{off-gas,B} = \rho_{off-gas} \cdot \dot{v}_{off-gas} \cdot A_B \tag{41}$$

A value of 13.643 kg/s was calculated for the total mass flow at measurement point B using the measurement data from the exemplary charge no. 200801 as shown in Equations (37) to (41) above.

Calculation of the carbon mass flow rate out of the EAF vessel:

Once the total mass flow rate at point B has been determined, the corresponding mass flow rate of carbon (in the form of CO and CO_2) can be calculated as follows:

$$\dot{m}_{C,B} = M_C \cdot \dot{n}_C = M_C \left(\frac{\zeta_{CO_2,B} \cdot \dot{m}_{off-gas,B}}{M_{CO_2}} \right) + M_C \left(\frac{\zeta_{CO,B} \cdot \dot{m}_{off-gas,B}}{M_{CO}} \right) \tag{42}$$

An average value of 0.317 kg/s (for average mass fractions of $\zeta_{CO2,B}$ = 8.487 % , $\zeta_{CO,B}$ =0.011 %) was calculated for the total mass flow at measurement point B using the measurement data from the exemplary charge no. 200801 as shown in Equation (42) above.

Calculation of the average total mass flow rate out of the EAF vessel:

Using the assumption, that no leakage of either CO or CO_2 takes place between measurement points A and B the following applies:

$$\dot{m}_{C,B} = \dot{m}_{C,A} \tag{43}$$

Based on this assumption, the total mass flow rate out of the EAF vessel based on the species mass fractions measured at A can be calculated as follows:

$$\frac{\dot{m}_{C,A}}{\dot{m}_{off-gas,A}} = M_C \left(\frac{\zeta_{CO_2,A}}{M_{CO_2}} \right) + M_C \left(\frac{\zeta_{CO,A}}{M_{CO}} \right) \tag{44}$$

$$\dot{m}_{off-gas,A} = \frac{\dot{m}_{C,A}}{\left(\frac{\dot{m}_{C,A}}{\dot{m}_{off-gas,A}} \right)} \tag{45}$$

A value of 3.837 kg/s (for average mass fractions of $\zeta_{CO2,A}$ = 22.478 % , $\zeta_{CO,A}$ = 8.487 %) was calculated for the total mass flow rate out of the EAF vessel using the measurement data from the exemplary charge no. 200801 as shown in Equations (43) to (45) above.

Determination of the carbon sources within the flow domain:

Oxidation takes place at the surface of the graphite electrodes. The rate of oxidation (electrode consumption) depends on the material composition of the electrodes, the temperature within the vessel, at the electrode surface and also on the partial pressure of the off-gas species at the electrode surfaces.

For this investigation it was assumed that the mass flow rate of carbon (in the form of CO and CO_2) determined using Equation (42) is caused only by the graphite oxidation at the electrode surfaces, as no oxygen injection is taking place, no burners are in operation and the time interval being considered is at the end of the process, when most of the unwanted carbon has already been removed from the molten metal.

A value of 0.317 kg/s was calculated for the carbon mass flow rate using the measurement data from the exemplary charge no. 200801 as shown in Equations (37) to (42) above. In comparison, M. Grant et al. [12] use a value of 6 lbs/ton of steel (2.72 kg/ton) for the electrode consumption in an EAF. For 140 tons of steel and a tap to tap time of 68 minutes this would correspond to a carbon mass flow rate into the off-gas of 0.093 kg/s.

Considering that the conditions inside the EAF are highly intransient and that the electric arc is not always in operation, the value of 0.317 determined using the measurement data can be considered to be at least within the range expected for the investigated time period, as the value 0.093 kg/s is an estimated average value for the entire tap-to-tap time. The sensitivity of the simulated NO_x formation to the magnitude of the electrode consumption was however also investigated by carrying out a numerical simulation for an electrode consumption corresponding to one third (0.106 kg/s) of the calculated value.

The electrode consumption is included in the numerical model by defining a source of carbon monoxide (CO) and a corresponding sink of oxygen (O_2) within the flow region at the electrode surfaces. The necessary mass sink and source are calculated based on the stoichiometric coefficients of the reaction of C with O_2 to form CO as follows:

$$CO + 0.5\,O_2 \rightarrow CO_2 \tag{46}$$

$$\dot{n}_C = \frac{\dot{m}_C}{M_{CO}} \tag{47}$$

$$\dot{n}_{CO} = \dot{n}_C \tag{48}$$

$$\dot{n}_{O_2} = 0.5 \cdot \dot{n}_{CO} \tag{49}$$

$$\dot{m}_{CO,elec.cons.} = \dot{n}_{CO} \cdot M_{CO} \tag{50}$$

$$\dot{m}_{O_2,elec.cons.} = \dot{n}_{O_2} \cdot M_{O_2} \tag{51}$$

A mass source of 0.739 kg/s for CO and a mass sink of 0.422 kg/s for O2 corresponding to the carbon mass flow rate of 0.317 kg/s was calculated using the equations above.

Calculation of the average mass flow rate of air into the EAF vessel:

In order to ensure that the simulated (Model 1) total mass flow rate out of the EAF vessel is equal to the value of 3.837 kg/s determined with the measurements as shown above, the sum of the mass flow rates at the inlets of Model 1 and of the source and sink within the flow domain must equal the calculated total mass flow rate. The mass flow rate of air into the EAF vessel is calculated as follows:

$$\dot{m}_{air,in} = \dot{m}_{off-gas,A} + \dot{m}_{O_2,elec.cons.} - \dot{m}_{CO,elec.cons.} \tag{52}$$

An air mass flow rate into the EAF vessel of 3.520 kg/s was calculated using the equation above.

As the amount of air flowing in through each individual opening is unknown, four different simulations were carried out with the velocities at the inlets defined as shown in **Table 34** below. The respective mass flow rates for each numerical simulation were determined on the following basis:

- V1 Mass flow rate distributed according to the cross-sectional area of the slag door/ electrode gaps/ roof-gap (same velocity set at all inlets)
- V2 No air flow in through electrode gaps, mass flow through roof gap and slag door set, so that estimated pressure loss due to inflow (according to extended Bernoulli equation) is approximately equal for slag door and roof gap
- V3 No air flow in through roof gap, mass flow through electrode gaps and slag door set, so that estimated pressure loss through inflow (according to extended Bernoulli equation) is approximately equal for slag door and electrode gaps
- V4 Based on V2, with approximately 2% of the air flowing in through the electrode gaps

Table 34: Variation of velocity inlet settings and corresponding distribution of mass flow rates for Model 1

Simulation No.	Velocities set at inlets [m/s]		
	Slag door	Roof-gap	Electrode gaps
V1	0.873	0.873	0.873
V2	0.960	0.854	0.000
V3	1.347	0.000	1.079
V4 (same inlet settings: V5 - V7)	0.944	0.838	0.291
Simulation No.	Corresponding air mass flow rate at inlets [kg/s]		
	Slag door	Roof-gap	Electrode gaps
V1	2.134	1.201	0.186
V2	2.346	1.174	0.000
V3	3.291	0.000	0.229
V4 (same inlet settings: V5 - V7)	2.305	1.153	0.062
Simulation No.	Ratio air mass flow rate at inlet vs. total air mass flow rate [%]		
	Slag door	Roof-gap	Electrode gaps
V1	60.6	34.1	5.3
V2	66.7	33.3	0.0
V3	93.5	0.0	6.5
V4 (same inlet settings: V5 - V7)	65.5	32.8	1.8

Model 2 – Boundary conditions defined at the in- and outlets:

The in- and outlets of Model 2 are defined as shown in **Figure 121** below. As already mentioned before, the calculated flow field profiles at the outlet of Model 1 (velocity components, static temperature, mass fraction of species, kinetic turbulence energy and turbulence dissipation) are set as profiles at the inlet of Model 2. These profiles or are obtained from the outlet of Model 1 once the simulation of the flow field in Model 1 is complete.

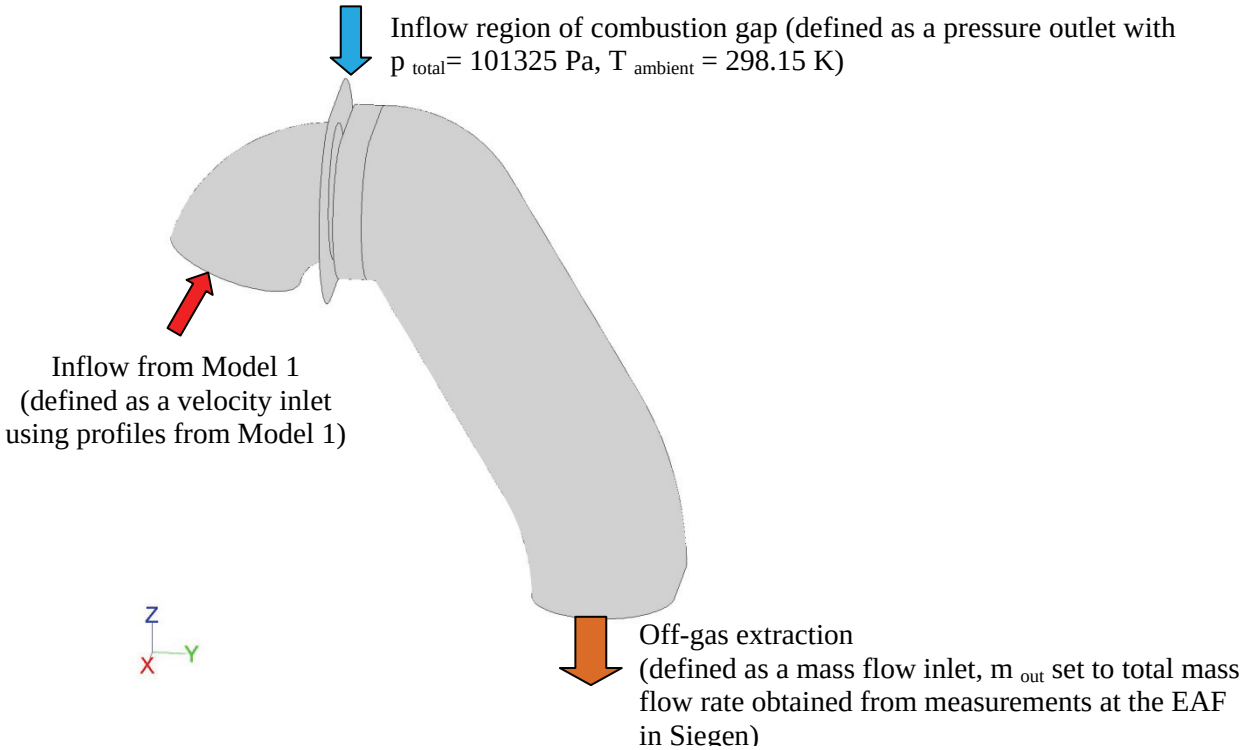

Figure 121: Three-dimensional view of the outer EAF surfaces of Model 2

The outlet of Model 2 is defined as a mass flow inlet, with the mass flow rate set to a negative value (outflow) which corresponds to that determined from measurements done at point B in the off-gas extraction system at the investigated EAF.

This makes it possible to influence the amount of air flowing into the combustion gap, so that it corresponds to that determined by the measurements. At the same time the static temperature and mass fraction distribution of the species at the outlet is solely a result of the simulation, as the flow is directed out of the flow region and the values for these parameters defined at the mass flow inlet are therefore ignored by FLUENT.

Simulated gas flow patterns inside the EAF vessel for the reference boundary conditions

For this investigation the numerical simulation V4 (refer to **Table 34**) is used as the reference simulation with which the results of other simulations with different boundary conditions are compared. The reference boundary conditions of V4 are summarised in **Table 35**.

The simulated gas flow patterns and surface temperature distributions inside the EAF vessel for the boundary conditions of simulation V4 are shown in **Figure 122** to **Figure 130**.

The streamlines from the slag door, roof-gap and electrode gaps to the outflow (in **Figure 122** to **Figure 123**) show the complexity of the flow field in the EAF vessel. The air from the slag door flows into the vessel, divides into three streams flowing between the electrodes and then it heats up and rises to the top of the vessel and out through the exhaust duct. The inflow through the slag door draws the air flowing in through the electrode gaps down and to the front of the EAF vessel before it too flows out through the exhaust duct. The flow from the roof-gap is drawn into the swirls of flow from the slag door all around the circumference of the vessel.

Table 35: Reference boundary conditions of numerical simulation V4 (Model 1 & 2)

Distribution of air inflow into EAF vessel	65.5% slag door, 32.8 % roof-gap, 1.8 % electrode gaps
Carbon mass flow rate (in the form of CO and CO_2)	0.317 kg/s
Temperature profile of electrode surfaces	adapted temperature profile (T_{min} = 1364 K, T_{max} = 3600 K)
Cooling of EAF upper vessel and roof walls	373.15 K at the base of the slag layer
All other boundary conditions	As described before, remain the same for all numerical simulations

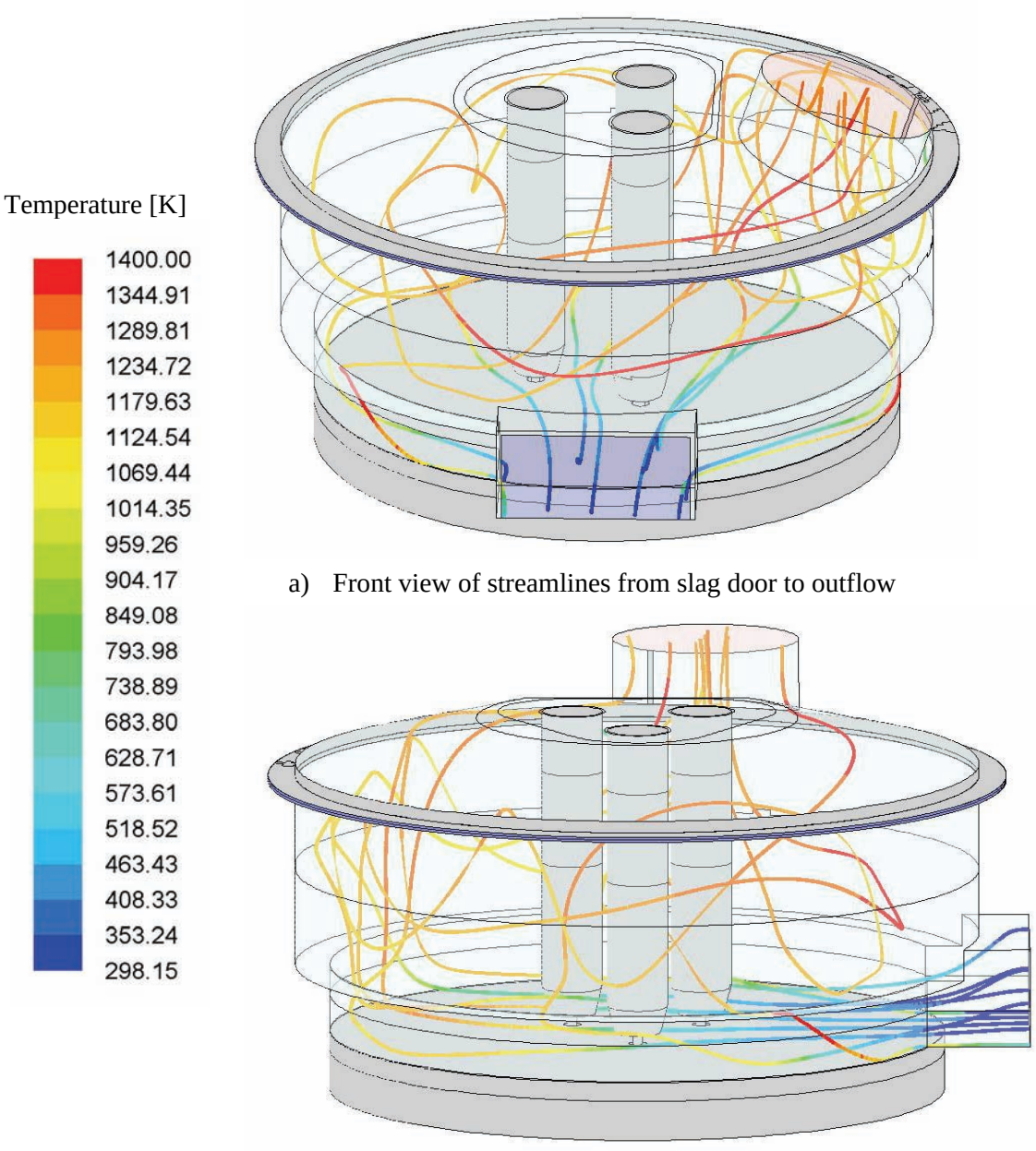

a) Front view of streamlines from slag door to outflow

b) Side view of streamlines from slag door to outflow

Figure 122: Streamlines from slag door to outflow of Model 1 (V4)

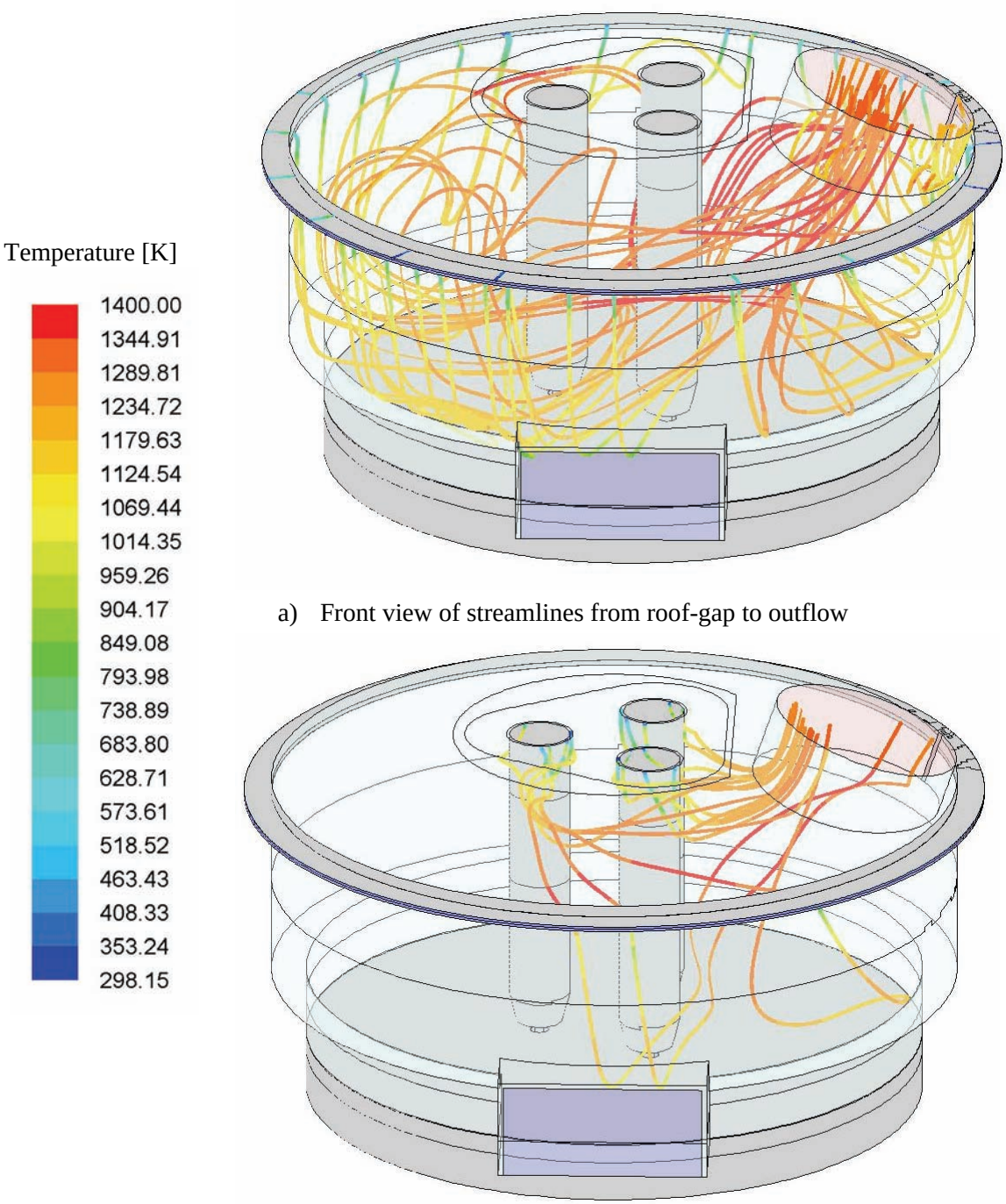

a) Front view of streamlines from roof-gap to outflow

b) Front view of streamlines from electrode gaps to outflow

Figure 123: Streamlines from roof-gap and electrode gaps to outflow of Model 1 (V4)

In **Figure 124.a** the temperature profiles defined on the electrode surfaces and surfaces representing the electric arc position are shown. In addition the temperature distribution on the slag surface is shown. It is a result not only of the convection with the off-gas and heat radiation with the inner EAF surfaces, but also of the thermal conductivity defined for the slag and molten metal and the temperature of 1873 K defined at the bottom of the molten metal. The minimum temperature on the slag surface is less than the approximate slag liquidus temperature of 1773 K. In **Figure 124.b** the temperature distribution within the molten metal and slag is shown. An increase in the thermal conductivity of slag and molten metal would increase the minimum slag surface temperature to above the slag liquidus temperature. It would however also increase the radius of the "hot-spot" zone around the electric arc positions.

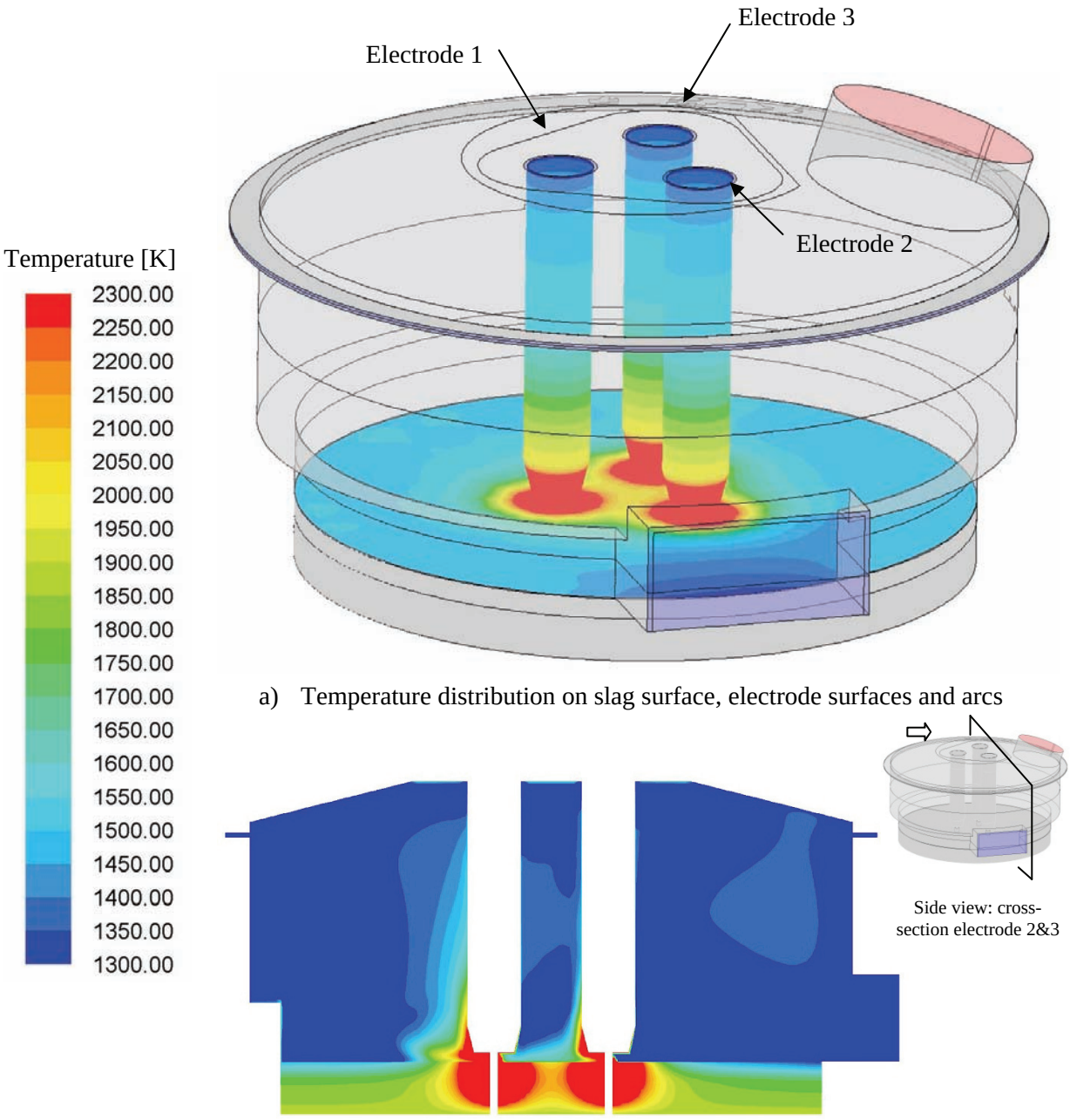

a) Temperature distribution on slag surface, electrode surfaces and arcs

b) Temperature distribution on cross-sectional plane through centre of electrodes 2 and 3

Figure 124: Temperature distribution on the slag surface, electrodes, arcs and in the cross sectional plane through the centre of electrodes 2 and 3 of Model 1 (V4)

In **Figure 125** the temperature distribution on the lower EAF vessel and upper wall is shown. It can be seen that the temperature is not only dependant on the heat radiation from the electric arc positions, which causes hot spots around the circumference of the vessel, but also on the temperature distribution and velocity of the off-gas flowing past the inner surface. The maximum temperature on the surface of the upper vessel lies below the approximate slag liquidus temperature of 1773 K. Therefore the temperature defined at the base of the slag layer of 373.15 K (100 °C) to simulate the cooling of the upper vessel wall is low enough.

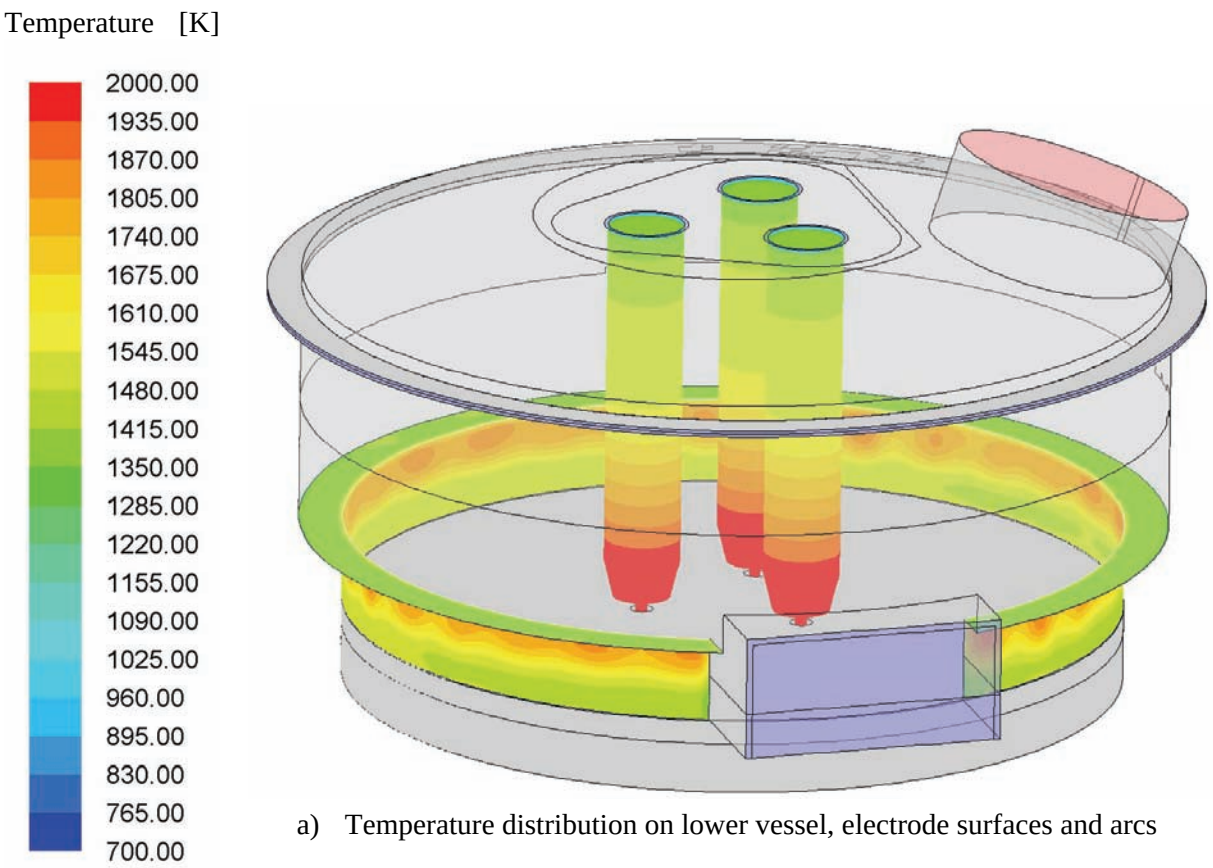

a) Temperature distribution on lower vessel, electrode surfaces and arcs

b) Temperature distribution on upper vessel, electrode surfaces and arcs

Figure 125: Temperature distribution on the electrodes, arcs and the upper vessel of Model 1 (V4)

In **Figure 126** the temperature distribution of the roof of the EAF vessel is shown. The difference in temperature between the cooled and un-cooled roof surfaces is clear. The temperature distribution of the roof surfaces is mainly a result of the heat radiation exchange with the slag layer and convection with the off-gas. The maximum temperature on the surface of the roof lies below the approximate slag liquidus temperature of 1773 K.

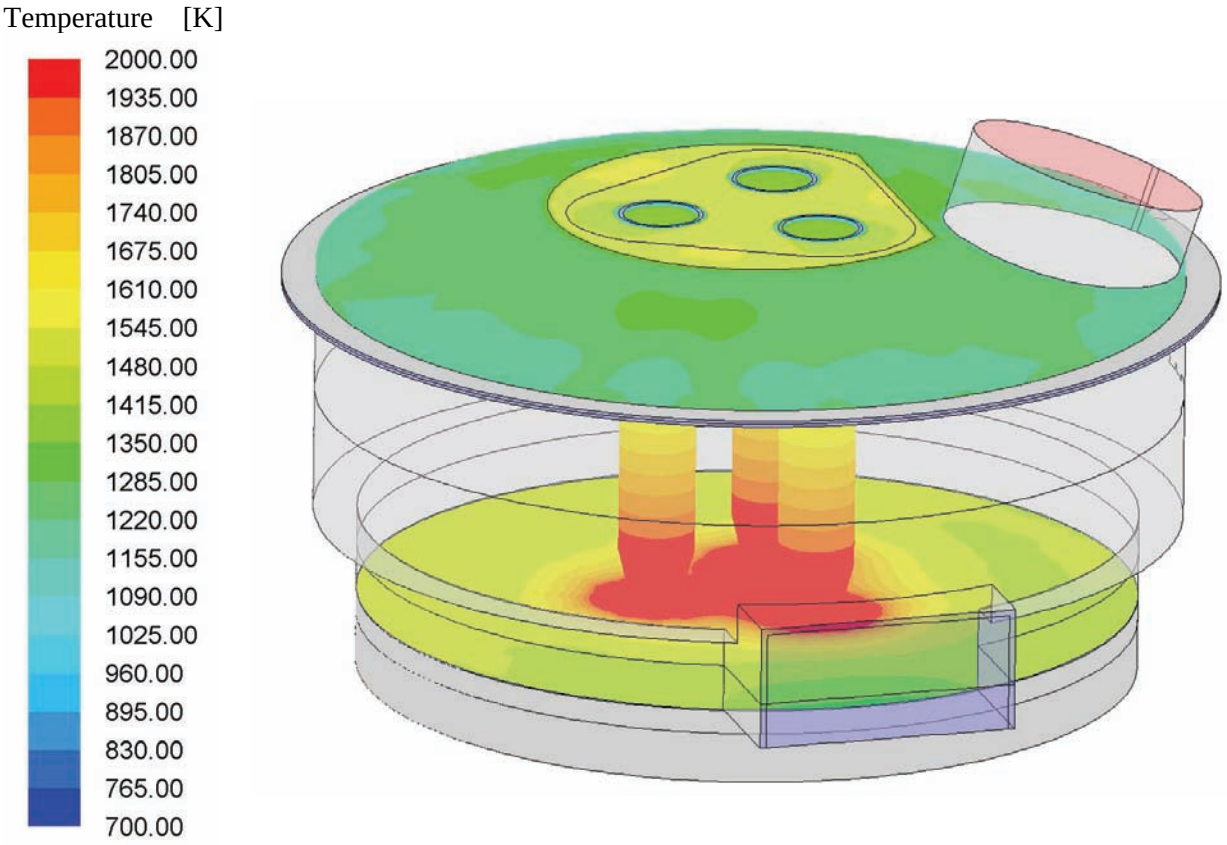

Figure 126: Temperature distribution on the slag surface, electrodes, arcs and roof surfaces of Model 1 (V4)

Figure 127 and **Figure 128** show the dependency of the NO-and CO- distribution in the EAF vessel on the temperature and flow within the EAF vessel. As expected, thermal NO is formed mainly around the location of the electric arc and at the surface of the electrodes where the temperatures are highest. It is transported to the back of the vessel, away from the slag door and then up and out of the vessel. A part of the NO formed is also drawn from the back of the vessel, to the front and then around the electrodes and out (compare NO-contours in **Figure 127** and **Figure 128** to streamlines in **Figure 122**). The effect of the CO-source around the electrode surfaces can also clearly be seen. For the mass flow inlet conditions defined for simulation V4 the CO seems to be displaced to the top part of the vessel.

This corresponds to the O_2- and CO_2- distributions shown in **Figure 129** and **Figure 130**, where low mass fractions for O_2 are shown in the top part of the vessel, with the exception of the area directly at the electrode gap inlets. The mass fraction for CO_2 is higher in those regions, where the temperatures are lower, e.g. at the cooled walls, and where the cool oxygen-rich air mixes with the off-gas.

In **Figure 131** and **Figure 132** the static temperature and mass fraction (NO, CO, O_2, CO_2) distributions are shown for simulation V4 (Model 2). The NO_x formed in the EAF vessel is diluted/reacts with the inflowing air, so that at the outflow of Model 2 the amount left is negligible. The CO reacts with the incoming air, causing an increase in temperature in the off-gas circulating around and down below the main flow coming from the combustion gap, into the off-gas extraction duct.

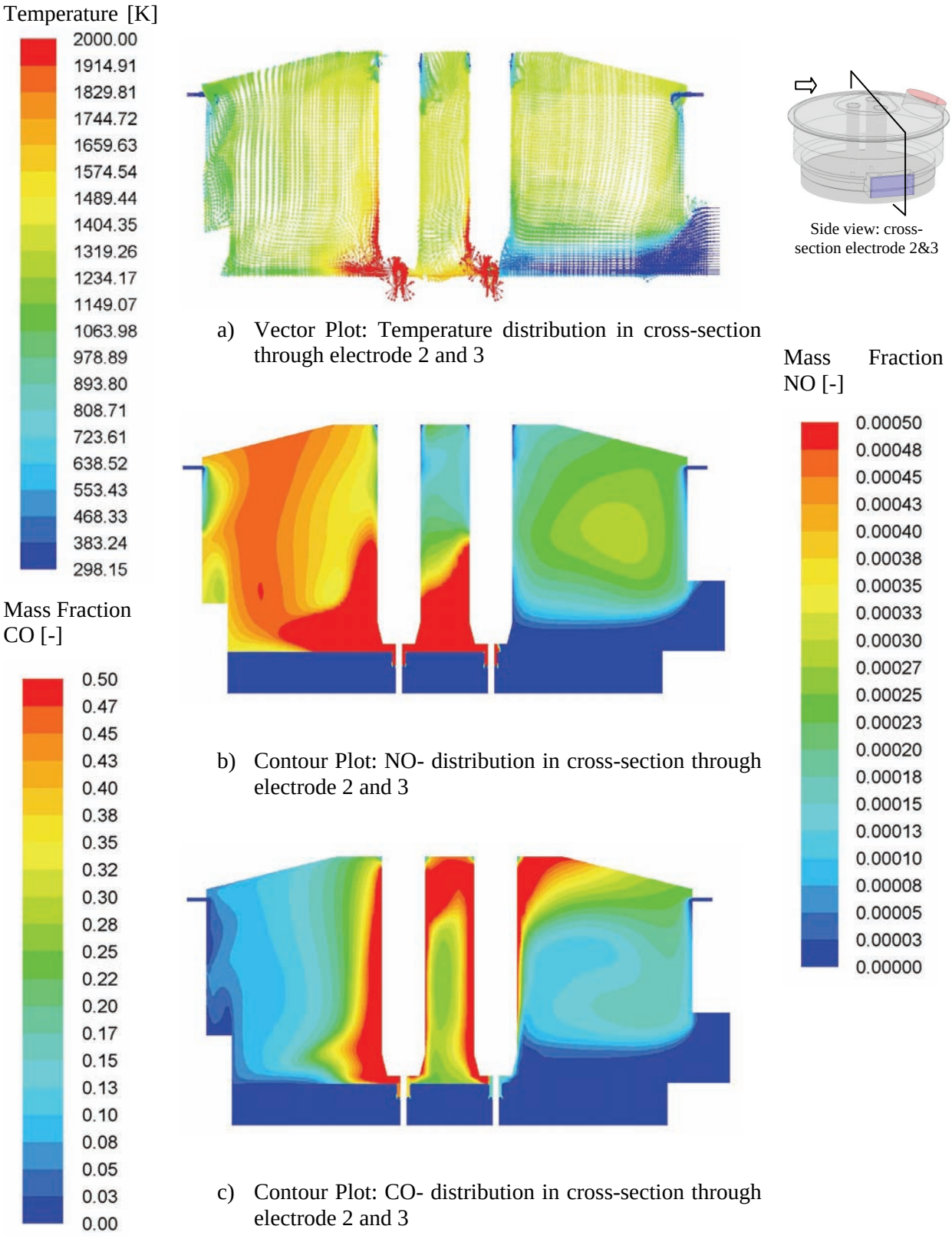

a) Vector Plot: Temperature distribution in cross-section through electrode 2 and 3

b) Contour Plot: NO- distribution in cross-section through electrode 2 and 3

c) Contour Plot: CO- distribution in cross-section through electrode 2 and 3

Figure 127: Static temperature, NO- and CO- distribution in cross-section through electrode 2 and 3 calculated with simulation V4 (Model 1)

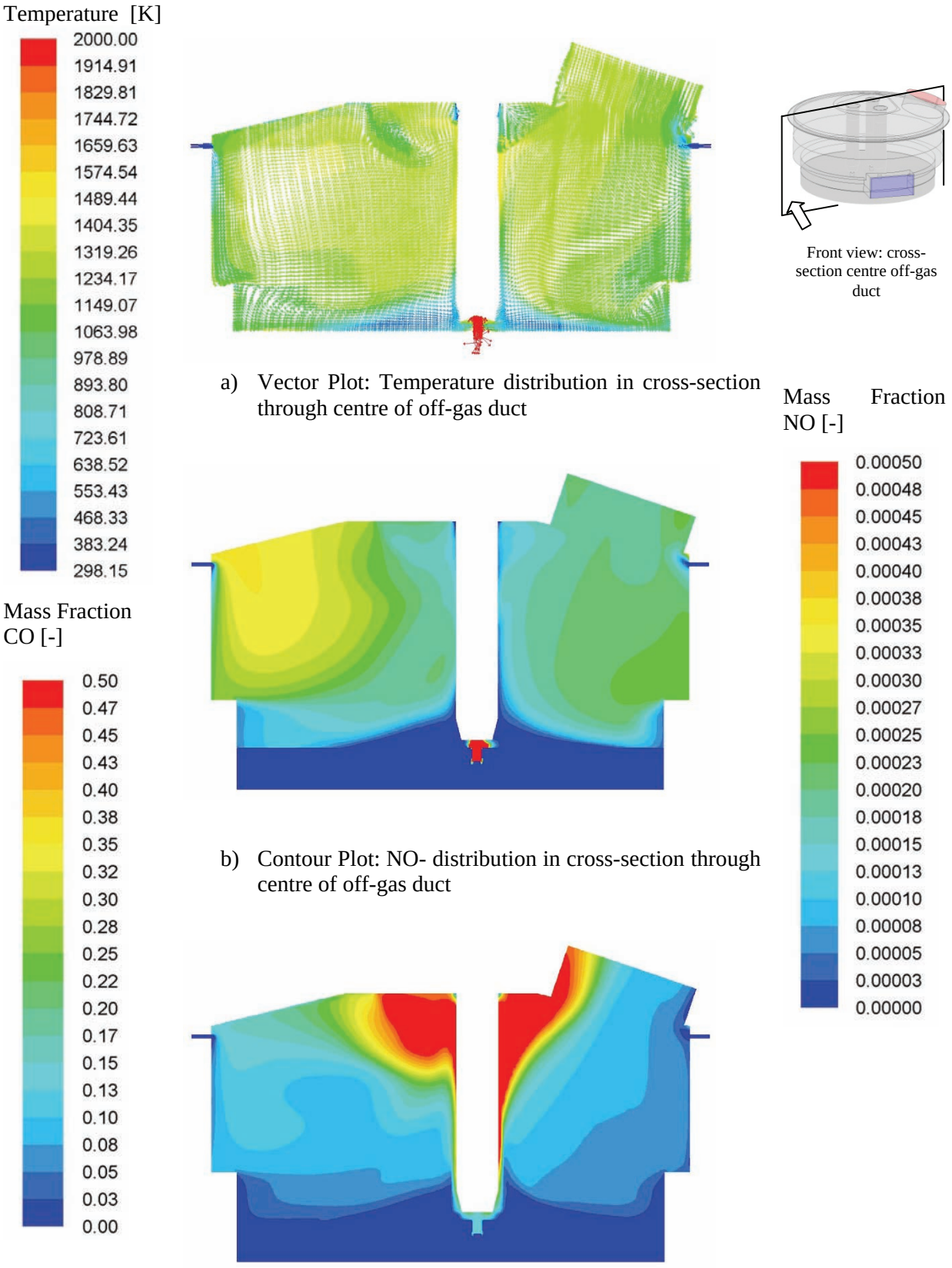

a) Vector Plot: Temperature distribution in cross-section through centre of off-gas duct

b) Contour Plot: NO- distribution in cross-section through centre of off-gas duct

c) Contour Plot: CO distribution in cross-section through centre of off-gas duct

Figure 128: Static temperature, NO- and CO- distribution in cross-section through centre of off-gas duct calculated with simulation V4 (Model 1)

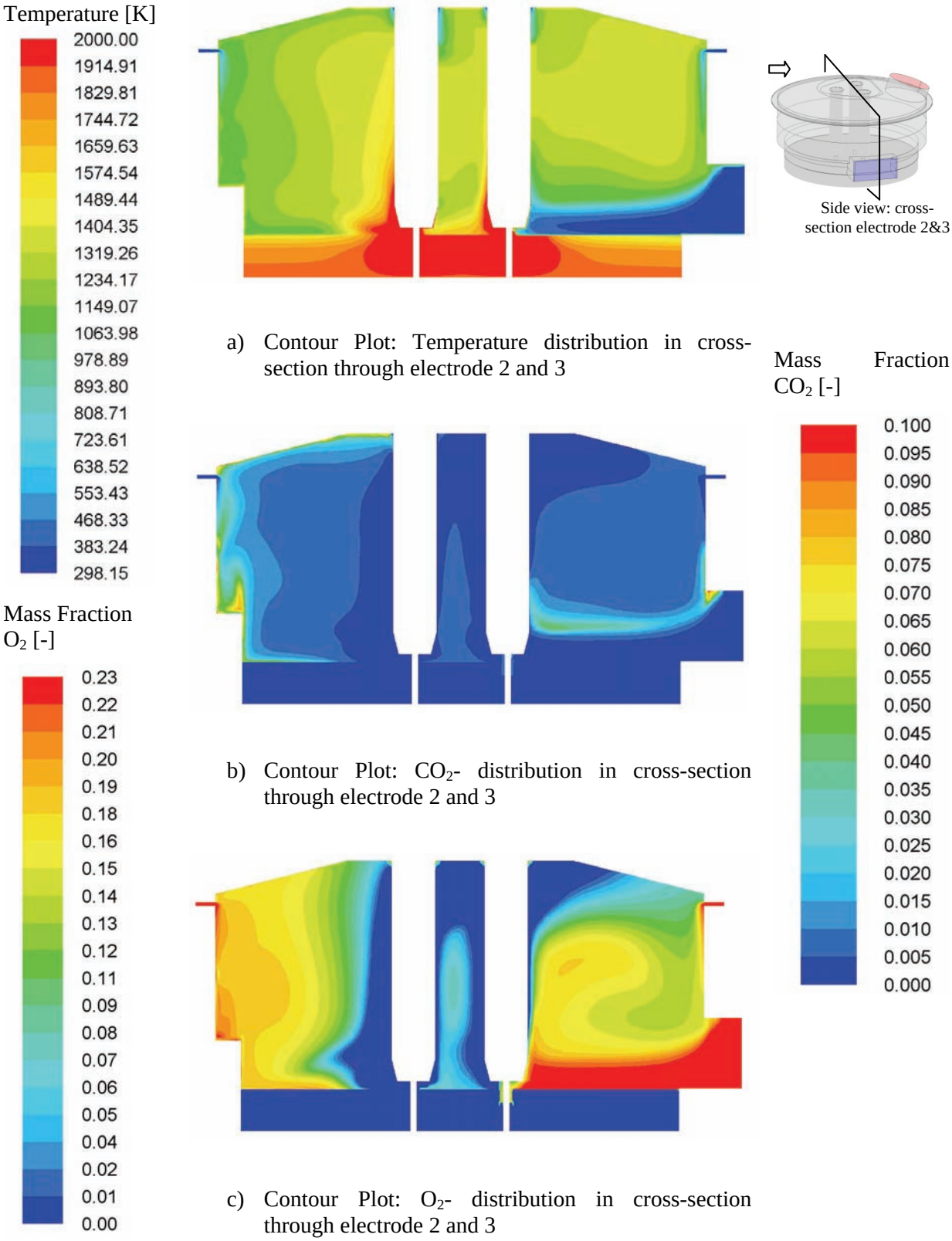

a) Contour Plot: Temperature distribution in cross-section through electrode 2 and 3

b) Contour Plot: CO_2- distribution in cross-section through electrode 2 and 3

c) Contour Plot: O_2- distribution in cross-section through electrode 2 and 3

Figure 129: Static temperature, CO_2- and O_2- distribution in cross-section through electrode 2 and 3 calculated with simulation V4 (Model 1)

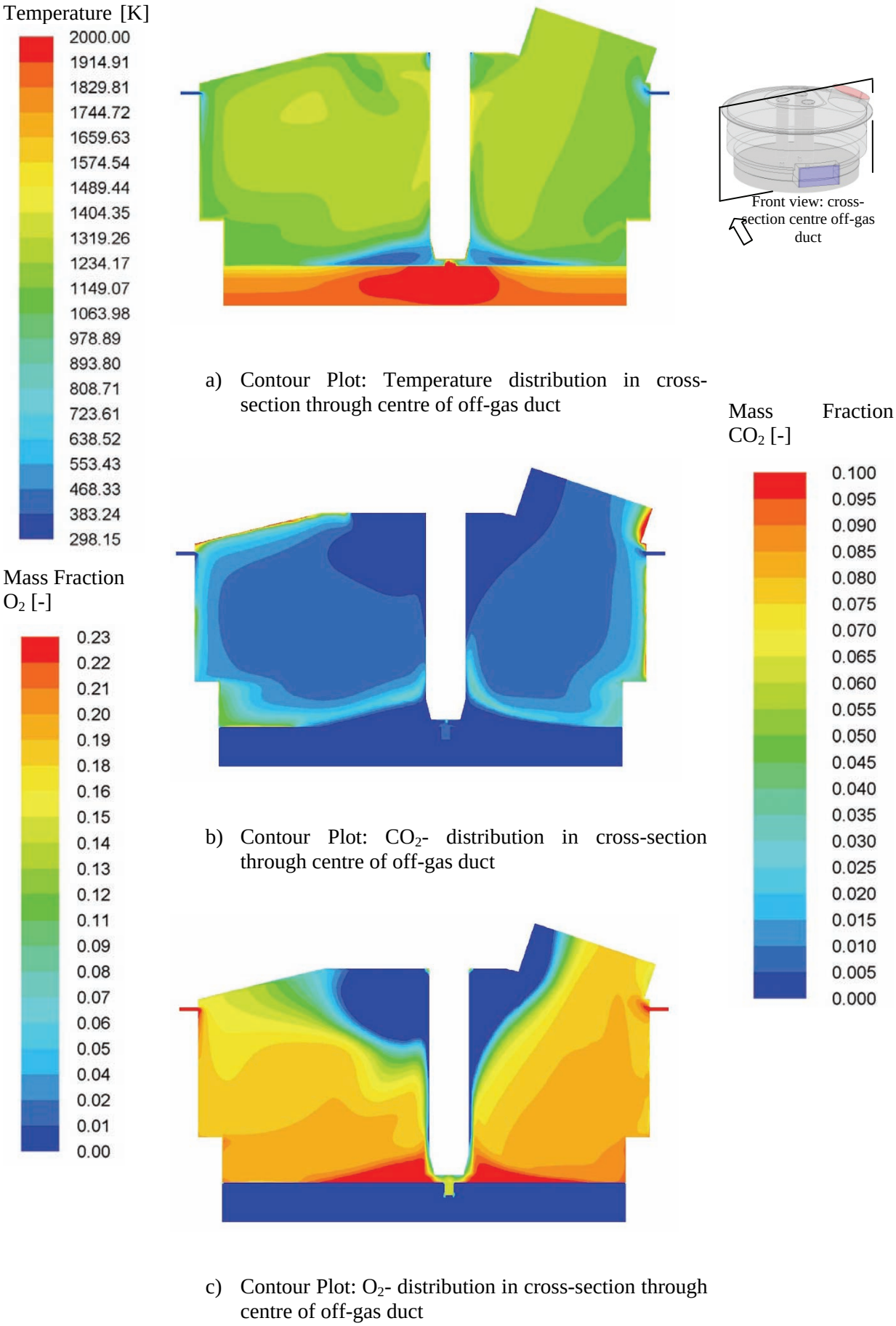

a) Contour Plot: Temperature distribution in cross-section through centre of off-gas duct

b) Contour Plot: CO_2- distribution in cross-section through centre of off-gas duct

c) Contour Plot: O_2- distribution in cross-section through centre of off-gas duct

Figure 130: Static temperature, CO_2- and O_2- distribution in cross-section through centre of off-gas duct calculated with simulation V4 (Model 1)

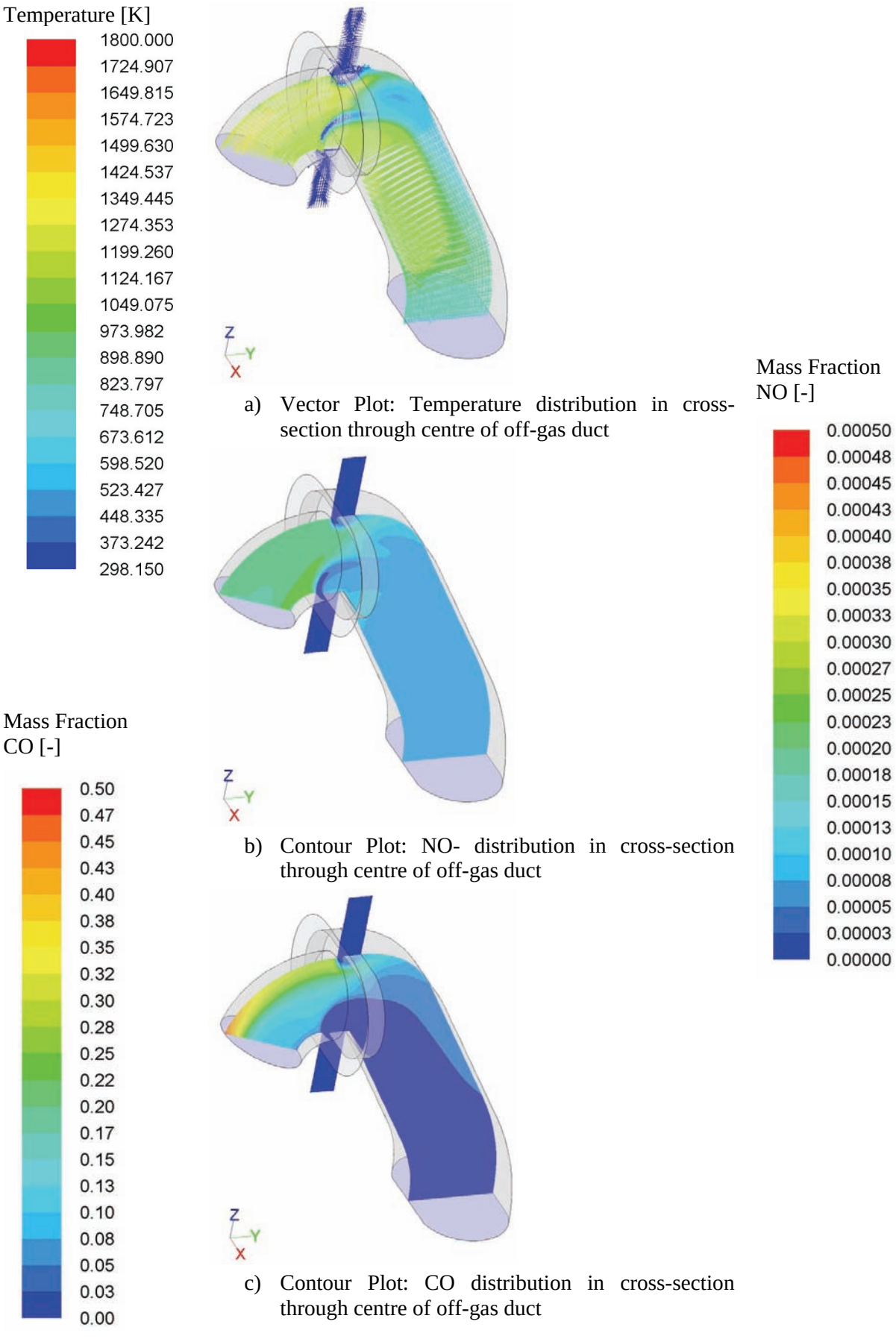

a) Vector Plot: Temperature distribution in cross-section through centre of off-gas duct

b) Contour Plot: NO- distribution in cross-section through centre of off-gas duct

c) Contour Plot: CO distribution in cross-section through centre of off-gas duct

Figure 131: Static temperature, NO- and CO- distribution in cross-section through centre of off-gas duct calculated with simulation V4 (Model 2)

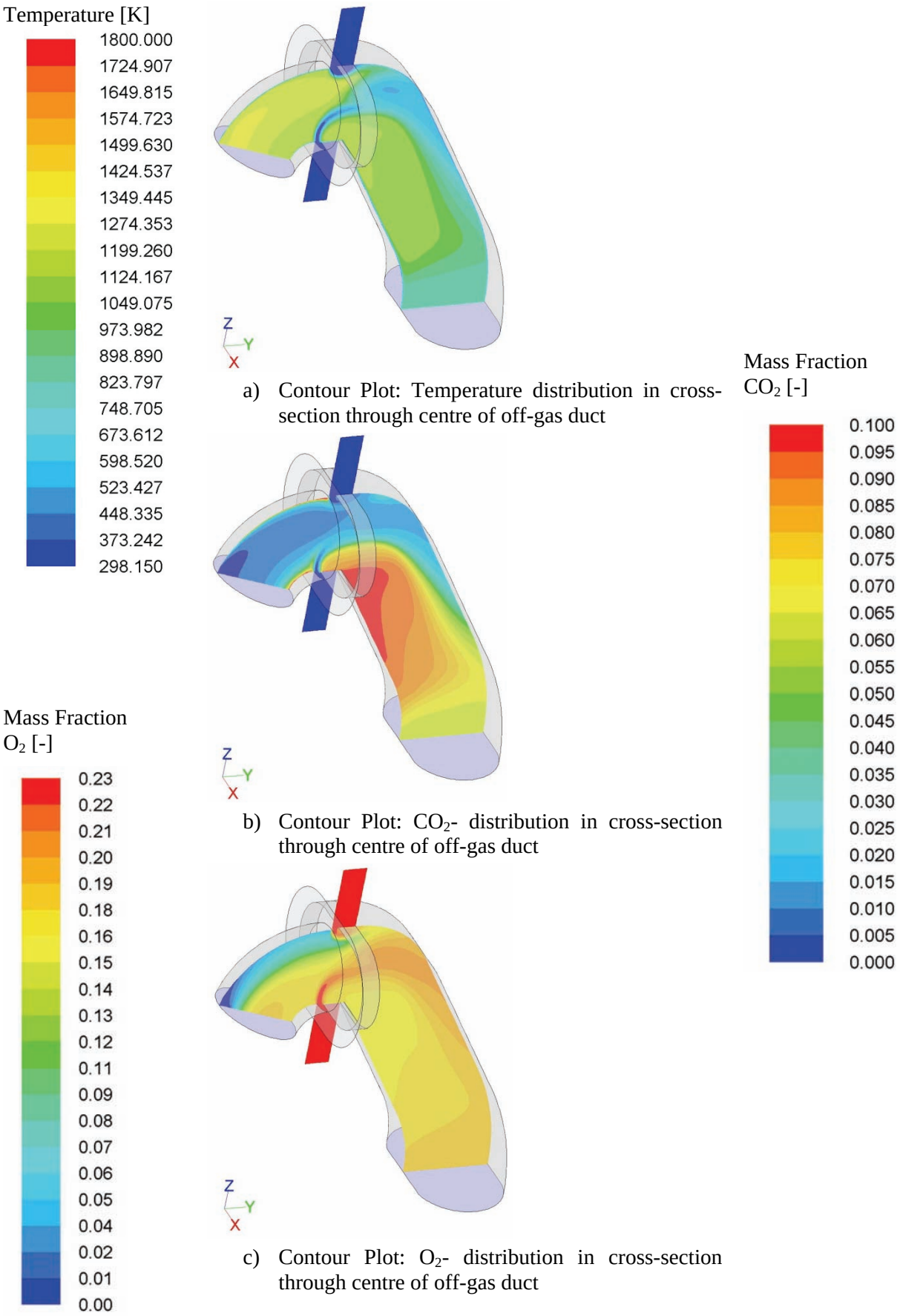

a) Contour Plot: Temperature distribution in cross-section through centre of off-gas duct

b) Contour Plot: CO_2- distribution in cross-section through centre of off-gas duct

c) Contour Plot: O_2- distribution in cross-section through centre of off-gas duct

Figure 132: Static temperature, CO_2- and O_2- distribution in cross-section through centre of off-gas duct calculated with simulation V4 (Model 2)

2.3.7.2 Validation of the models used and variation of boundary conditions to test influence on NO_x formation and species mass fraction distributions

This section covers the tasks 7.2 "Validation and adaption of the reaction models used" and 7.3 "Tests of various reaction kinetic models for NO_x formation".

Comparison of Numerical simulation results to measurement data

The results of the simulation V4 are a first estimate of the NO_x formation due to chemical reactions and gas temperature within the investigated EAF vessel. The next step is to validate the numerical simulation model by comparing the results to the measurements from the exemplary charge no. 200801.

First, the influence of the different distribution of the air inflow into the EAF between slag-door, roof-gap and electrode gaps of simulations V1 to V4 is considered. **Table 36** shows the average mass flow rate of each species at the outflow of Model 1 for simulation V1 to V4.

Table 36: Ratio of average mass flow rate of each species to total mass flow rate at the outflow of Model 1 for simulation V1 to V4

Version	$\dot{m}_{NO}/\dot{m}_{total}$ [%]	$\dot{m}_{CO}/\dot{m}_{total}$ [%]	$\dot{m}_{CO_2}/\dot{m}_{total}$ [%]	$\dot{m}_{O_2}/\dot{m}_{total}$ [%]
V1 (same velocity at all inlets)	0.018	18.9	1.54	11.3
V2 ($\dot{m}_{elec,gaps} = 0$)	0.022	19.0	1.31	11.5
V3 ($\dot{m}_{roofgap} = 0$)	0.024	18.7	1.53	15.3
V4	0.024	19.0	1.36	11.4

The difference in distribution of the air inflow into the EAF between slag-door, roof-gap and electrode gaps has only a minor effect on the average species mass flow rates at the outflow of Model 1, as the total air inflow into the EAF for all four simulations is the same. It does slightly change the structure of the flow field within the EAF and the mass fraction distribution at the outlet. This can be seen by considering the values in **Table 37**.

Table 37: Simulated maximum mass fraction and mass fractions approximately in the centre of cross-section of the combustion gap for simulations V1 to V4

Simulation	$\varsigma_{NO,max}$	$\varsigma_{CO,max}$	$\varsigma_{CO2,max}$	$\varsigma_{O2,max}$	$\varsigma_{NO,centre}$	$\varsigma_{CO,centre}$	$\varsigma_{CO2,centre}$	$\varsigma_{O2,centre}$	$T_{stat,centre}$
	[%]								[K]
V1	0.021	25.8	6.29	23.4	0.017	14.7	1.0	14.7	1183
V2	0.027	28.5	5.46	23.4	0.021	13.0	0.90	15.0	1238
V3	0.031	25.0	5.97	23.4	0.020	17.0	1.0	17.0	1270
V4	0.029	26.8	5.10	23.4	0.022	11.8	1.1	16.3	1210

Based on the fact, that in reality the roof-gap is not closed (as in V3) and a certain amount of air ingress at the electrodes might take place, it was decided to use V4 (air inflow distribution: 65.5% slag door, 32.8 % roof-gap, 1.8 % electrode gaps) as the reference simulation to carry out the validation of the simulations and further investigate the effect of parameter variations on the flow field.

The average measured mass fractions and mass flow rates determined using the measurements for the time interval considered are summarised in **Table 38**.

When comparing the values above with the simulation results, it must be remembered that these values are average values for the time considered at the specific measurement point, either A or B, in the fluid flow. They are not average values for the cross-sectional area at the position of point A or B in the off-gas duct. This point is important to remember, as the results show that the mass fractions, especially at the exit of the EAF vessel and the cross-section in the centre of the combustion gap, are not evenly

distributed. This is evident when viewing the static temperature distributions from simulation V4 (Model 2) shown in **Figure 133**.

Table 38: Average measured mass fractions and mass flow rates determined using measurements from exemplary charge no. 200801

Mass flow rates [kg/s]			
total mass flow rate at point B	carbon mass flow rate at point B	corresponding total mass flow rate at point A	corresponding mass flow rate of air into EAF
13,64	0.32	3.84	3.52
Time average mass fractions at point B [%]			
ς_{NO}	ς_{CO}	ς_{CO2}	ς_{O2}
-	0.011	8.49	17.10
Time average static temperature at point B [K]			
680			
Time average mass fractions at point A (combustion gap) [%]			
ς_{NO}	ς_{CO}	ς_{CO2}	ς_{O2}
0,0049	4.95	22.48	5.65

The measurement data that can best be compared to the simulation results is that at point A, as point B lies much further downstream in the off-gas extraction system than the outlet of Model 2.

In **Table 39** the maximum mass fractions and mass fractions approximately in the centre of the cross-section (where the measurement points are located) of V4 at the centre of the combustion gap are compared to the measurement data.

Table 39: Comparison of results of V4 at the cross-section in the middle of the combustion gap with the measurement data at point A

Simulation	$\varsigma_{NO,max}$	$\varsigma_{CO,max}$	$\varsigma_{CO2,max}$	$\varsigma_{O2,max}$	$\varsigma_{NO,centre}$	$\varsigma_{CO,centre}$	$\varsigma_{CO2,centre}$	$\varsigma_{O2,centre}$	$T_{stat,centre}$
	[%]								[K]
V4	0.029	26.8	5.10	23.4	0.022	11.8	1.1	16.3	1210
Measurement Data (point A)	-	-	-	-	0.0049	4.95	22.48	5.65	Not available

The values in the table above show that the simulated mass fractions at the centre of the cross-section of V4 do not correspond to the measurement data. The simulated mass fraction of CO is more than double of the measured value and the simulated mass fraction for CO_2 is much lower than that measured. This would indicate that either the simulated static temperature in the combustion gap is too high, or that other perhaps local effects might cause the mass fraction distribution during the measurements to have been different from that simulated.

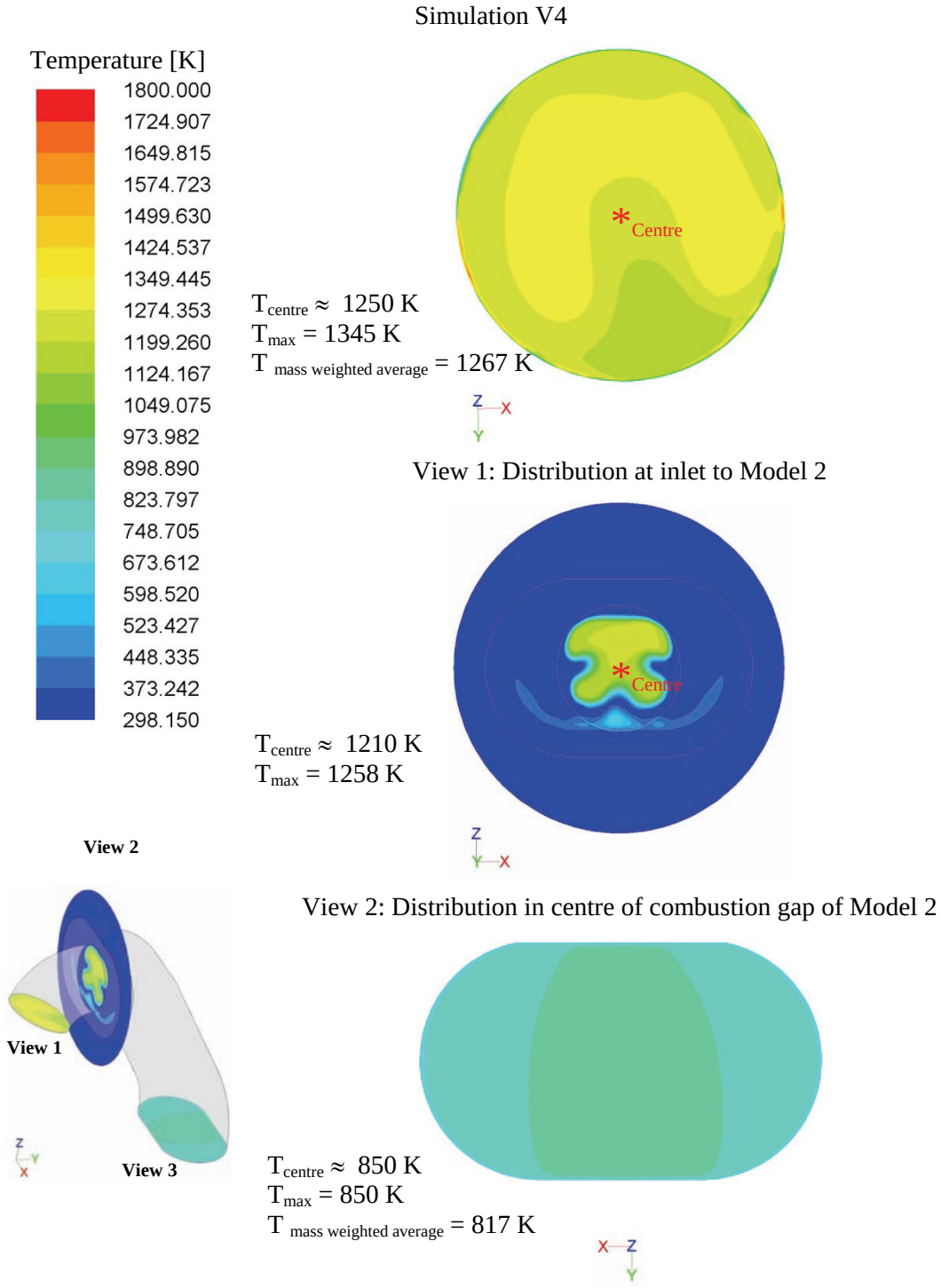

Figure 133: Simulated static temperature distribution in cross-sectional area at inlet, in centre of combustion gap and at outlet of simulation V4 (Model 2)

Three further simulations, based on V4, were therefore carried out in order to investigate the effect of parameter variations in general and to attempt a better correlation between measurement data and results. For each of these simulations only one of the boundary conditions of V4 was changed as shown in **Table 40**.

A comparison of the results of V4 to V7 at the cross-section in the middle of the combustion gap with the measurement data at point A is shown in **Table 41**. The values in this table show that the simulated mass fractions at the centre of the cross-section of V4 to V7 do not correspond to the measurement data.

The simulated CO mass fraction of V5 best fits the measurement data, but this is due to the carbon-monoxide source within the flow region having been set down by one third. The corresponding CO_2

mass fraction of V5 is therefore far too low when compared to the measured value, as the total mass flow of carbon (in the form of CO and CO_2) is only a third of that corresponding to the measured values at point A.

Table 40: Reference boundary conditions of numerical simulation V4 (Model 1 & 2)

Simulation Version	Boundary condition	Values defined
V4	Distribution of air inflow into EAF vessel	65.5% slag door, 32.8 % roof-gap, 1.8 % electrode gaps
	Carbon mass flow rate (in the form of CO and CO_2)	0.317 kg/s
	Temperature profile of electrode surfaces	adapted temperature profile (T_{min} = 1364 K, T_{max} = 3600 K)
	Cooling of EAF upper vessel and roof walls	373.15 K (100 °C) at the base of the slag layer
V5	Carbon mass flow rate (in the form of CO and CO_2)	Set down to (0.317 kg/s)/3
V6	Temperature profile of electrode surfaces	adapted temperature profile (T_{min} = 965 K, T_{max} = 3600 K)
V7	Cooling of EAF upper vessel and roof walls	333.15 K (60 °C) at the base of the slag layer

Table 41: Comparison of results of V4 to V7 at the cross-section in the middle of the combustion gap with the measurement data at point A

Simulation	$\varsigma_{NO,centre}$	$\varsigma_{CO,centre}$	$\varsigma_{CO2,centre}$	$\varsigma_{O2,centre}$	$T_{stat,centre}$
	[%]				[K]
V4	0.022	11.8	1.1	16.3	1210
V5	0.026	4.70	0.8	21.1	1207
V6	0.018	14.4	1.4	18.8	1140
V7	0.019	15.5	1.2	18.7	1166
Measurement Data (point A)	0.0049	4.95	22.48	5.65	Not available

Conclusions of Validation

One possible reason for the difference between simulated values and measurements is the uneven distribution of the flow field variables in the combustion gap, meaning that the measured mass fractions at A differ too much from those of the main flow out of the EAF vessel.

Another possibility is that the measurements at point A did not take place exactly in the centre of the combustion gap or that the gap size used for the numerical simulation of 150 mm (obtained from technical drawings) is too small.

The third possibility, which would best explain the difference in the values, is that the flow within the gap of the investigated EAF is more turbulent, with the flow into the gap from the environment not taking place as evenly as the inflow simulated (see **Figure 134**). This would certainly lead to an increased rate of mixing and therefore a greater oxidation of CO to CO_2.

One would have to include the region around and outside the EAF vessel to properly take the influence of the conditions around the vessel into account. This would however result in a marked increase in the size of the numerical model and therefore also greatly increase the calculation time.

Such a numerical model would necessitate that the geometry of the gaps (slag-door, roof-gap and electrode gaps) be considered in much more detail, as for such a simulation the mass flow being drawn into the EAF would be a function of the inflow areas and the pressure losses at the inlets. Even blockages in front of the inlets, such as a reduced inflow area in front of the slag door due to apparatus being positioned in front of the EAF would have to be considered, as their influence is not necessarily negligible.

Nevertheless, the results of the numerical simulation lead to many revelations concerning the structure of the flow field within the EAF and the factors influencing the mass fraction distribution of the species in the off-gas.

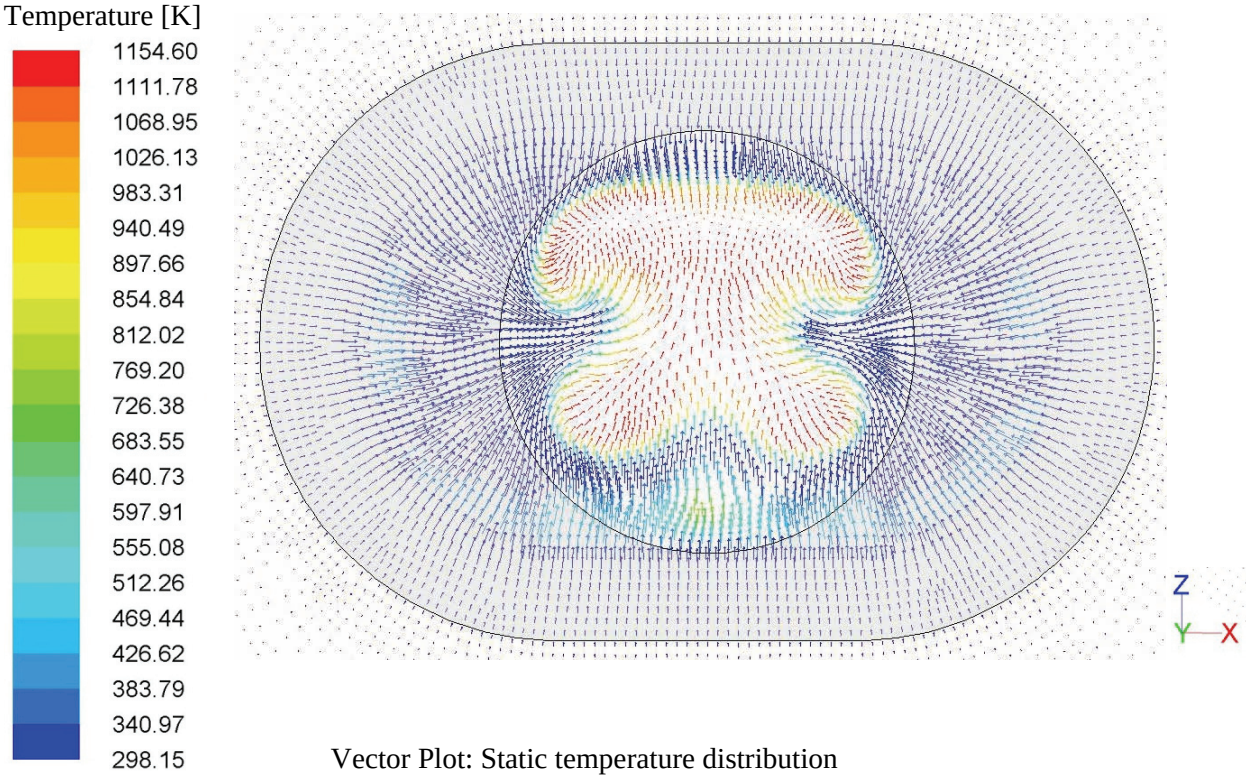

Figure 134: Simulated static temperature distribution in the cross-sectional area of the combustion-gap of simulation V6 (Model 2)

2.3.7.3 Implementation of plasma reaction kinetic models into CFD code and extension of CFD simulation to plasma conditions

In the numerical model used in this investigation the electrode arc is modelled using the channel model (Kanalmodel) to define three cylindrical surfaces representing the position of the electric arc between each electrode tip and the molten metal surface. However in reality the arc will jump from electrode to electrode. Thereby the off-gas drawn into the plasma region at each flash of the arc at a specific electrode will be not only heated to a temperature in the range of 10 000 K, obtain momentum downward towards the molten metal surface, but will also change its composition as the species of the off-gas react at the high temperature in the arc.

How can these effects be included in a numerical model of the entire EAF vessel, whilst still keeping the calculation time and the amount of data within an acceptable limit?

One way to try to extend the CFD simulations to include the chemical reactions taking place inside the plasma region would be to consider the plasma region and the region surrounding it separately and in more detail, than would ever be possible in a numerical model encompassing the entire EAF vessel. The results from such an investigation could then be used to define a sink in the upper region of the arc, drawing off-gas into the plasma region, with a corresponding mass flow source at the base of the arc reintegrating the altered hot off-gas back into the flow region of the vessel.

2.3.7.4 Investigation of varying process parameters on computed NO_x formation and interpretation of results

In section 2.3.7.2 the variation of the boundary conditions of the numerical simulation model (simulations V1 to V7) and the effect on the mass fraction distributions at the cross-sectional area in the centre of the combustion gap are discussed.

In this section the influence of the process parameter variations on the NO_x formation within the EAF vessel is considered and the various sources of NO_x formation within the EAF vessel are identified. The **Figure 135** to **Figure 137** show the effect of the variation in boundary conditions on the mass fraction distribution in the EAF vessel.

The most notable change in NO_x formation is caused by the reduction of the CO-source around the surfaces of the electrodes in simulation V5 (see **Figure 136.b**). This causes an increased availability of oxygen at the hot electrode surfaces, which leads to an increase in the NO_x formation, especially in the hot tip area of the electrodes.

In order to estimate what quantitative difference a reduced oxidation of the electrodes would have in reality, the mechanisms of the carbon oxidation at the electrode surface would have to be considered in more detail. The extent to which the electrode oxidation will influence the NO-formation depends on how far the boundary layer, as far as the increased partial pressure of CO is concerned, extends away from the surface of the electrodes. This will influence not only how much N_2 from the air can penetrate to the electrode surface where the temperature is high, but also how much O_2 will then be available there.

As expected the decrease in the temperature of the electrode surfaces in simulation V6 leads to a reduction in the NO_x formation (see **Figure 136.c**). The increase in the cooling of the walls in simulation V7 has a similar effect to that of decreasing the electrode temperature profiles.

The main sources of NO_x-formation that are identified by these results are: The hot zone around the electric arc, the hot surface of the electrode surfaces, especially the electrode tip and hot EAF wall surface temperatures.

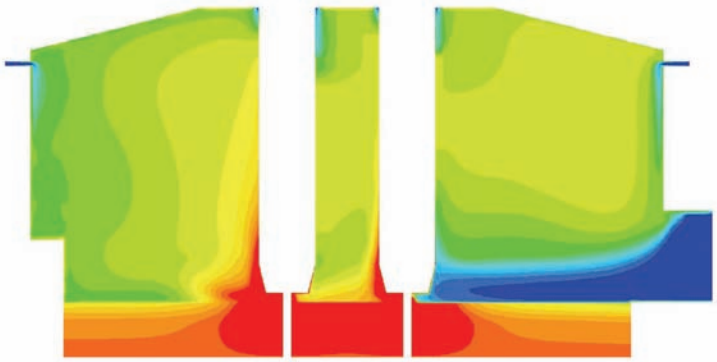

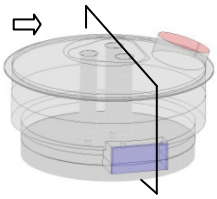

Side view: cross-section electrode 2&3

a) Simulation V4: Reference boundary conditions

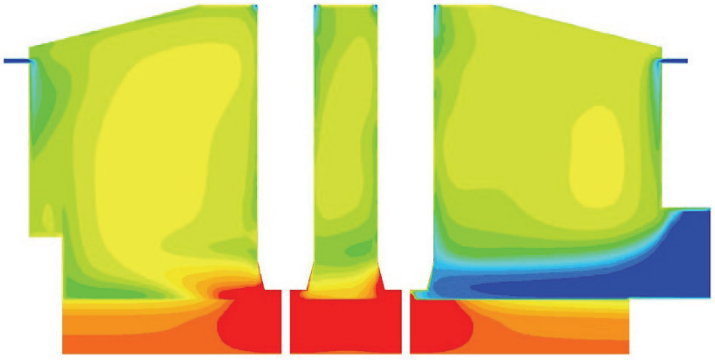

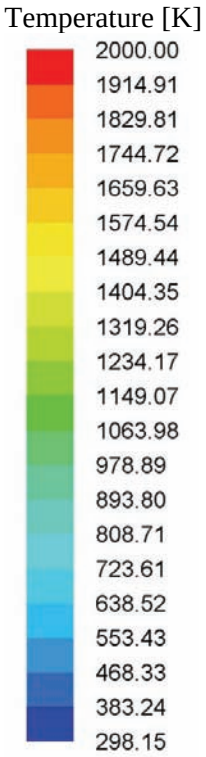

b) Simulation V5: CO-source only a third of that in V4

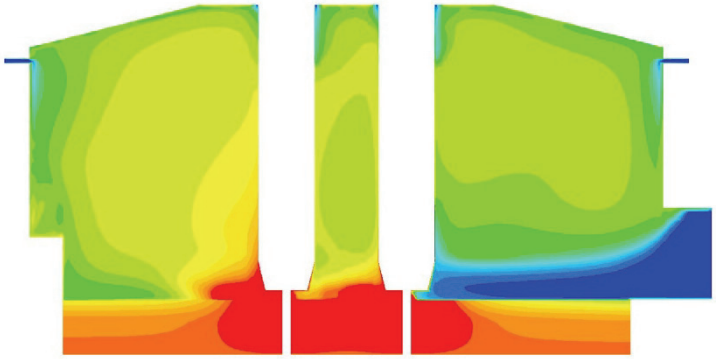

c) Simulation V6: different temperature profile at electr. surfaces ($T_{min,V6}$ = 965.K vs. $T_{min,V4}$ = 1364.K)

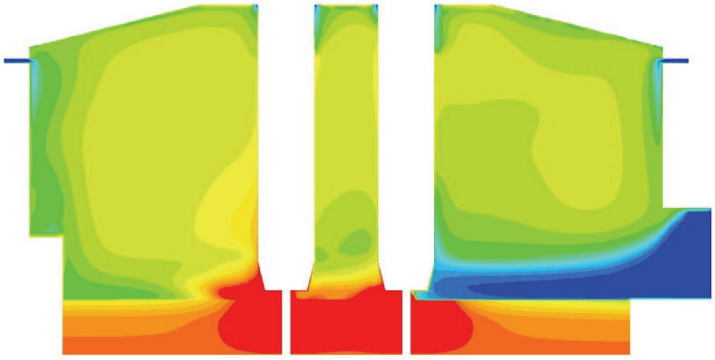

d) Simulation V7: Increased cooling of EAF upper vessel and roof walls

Figure 135: Comparison of static temperature distribution in cross-section through electrode 2 and 3 calculated with simulation V4 to V7

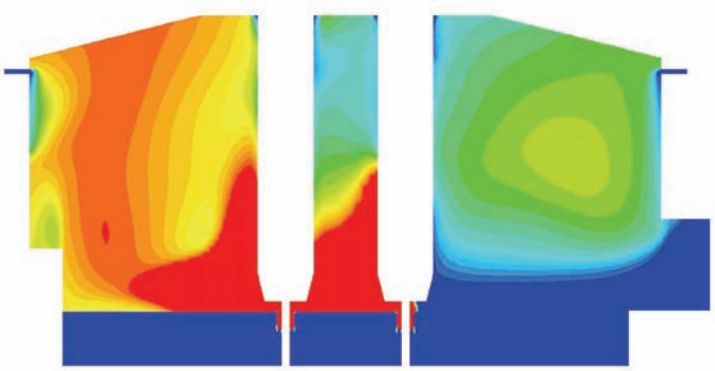

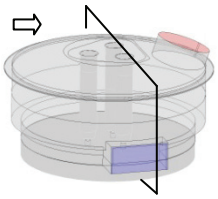

Side view: cross-section electrode 2&3

a) Simulation V4: Reference boundary conditions

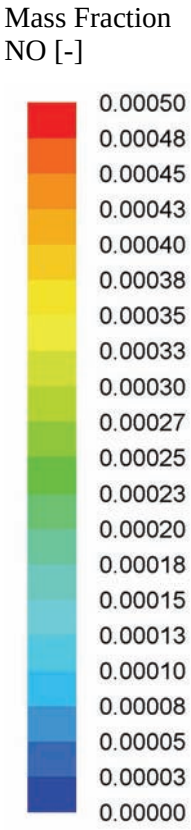

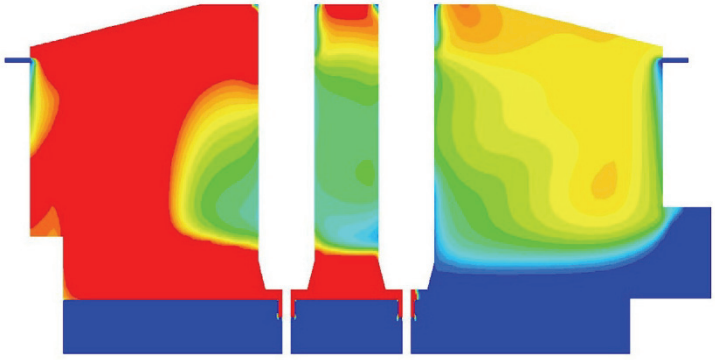

b) Simulation V5: CO-source only a third of that in V4

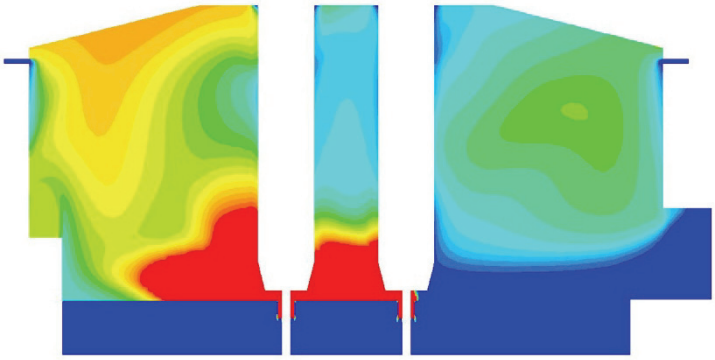

c) Simulation V6: different temperature profile at electr. surfaces ($T_{min,V6}$ = 965 K vs. $T_{min,V4}$ = 1364 K)

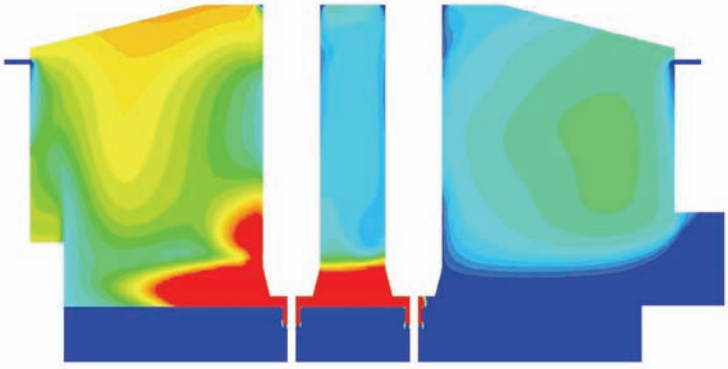

d) Simulation V7: Increased cooling of EAF upper vessel and roof walls

Figure 136: Comparison of NO- distribution in cross-section through electrode 2 and 3 calculated with simulation V4 to V7

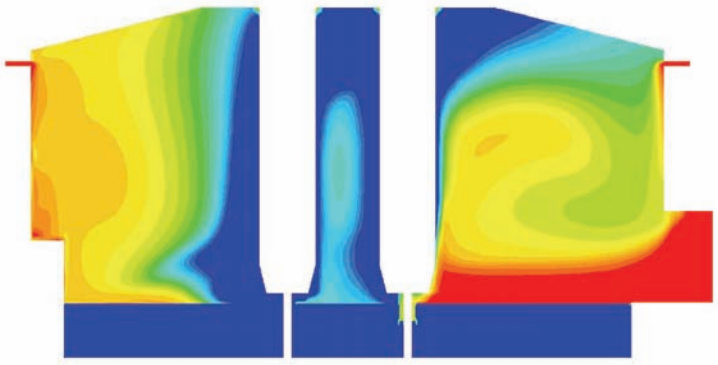

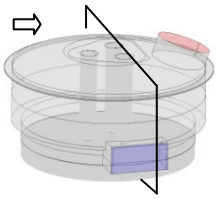

Side view: cross-section electrode 2&3

a) Simulation V4: Reference boundary conditions

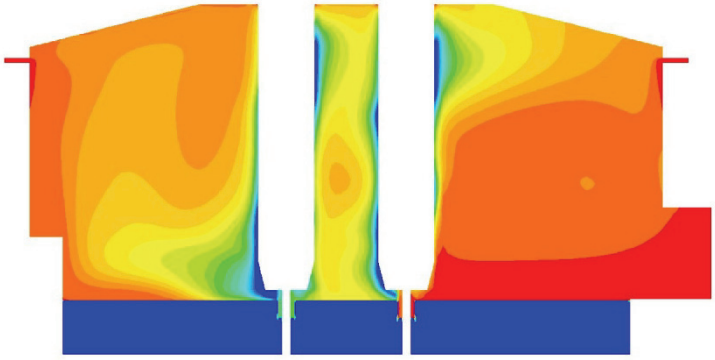

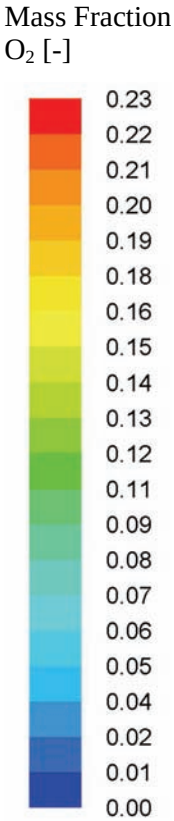

b) Simulation V5: CO-source only a third of that in V4

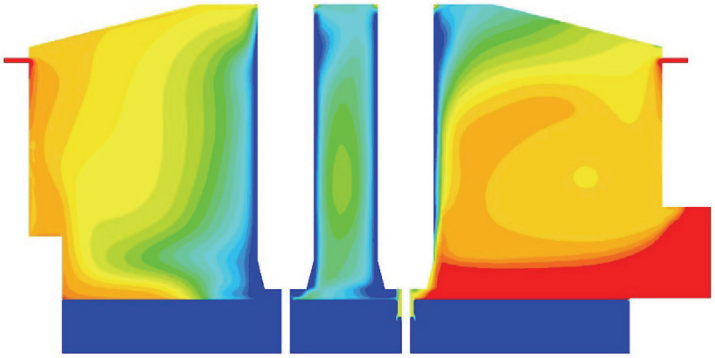

c) Simulation V6: different temperature profile at electr. surfaces ($T_{min,V6}$ = 965 K vs. $T_{min,V4}$ = 1364 K)

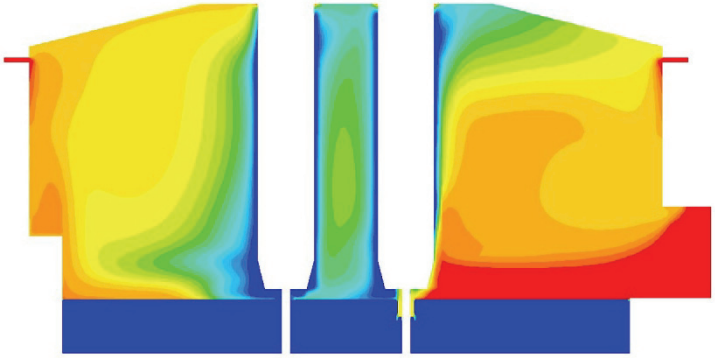

d) Simulation V7: Increased cooling of EAF upper vessel and roof walls

Figure 137: Comparison of static temperature distribution in cross-section through electrode 2 and 3 calculated with simulation V4 to V7

2.4 Conclusions, Exploitation and impact of the research results

Within the scope of this research project the NO_x emissions from the electric steelmaking process in the EAF in general and, as a special case, the Consteel process have been investigated. By means of model calculations and pilot plant as well as industrial trials guidelines to reduce NO_x emissions have been derived for the EAF steel making process.

On the basis of a reference data set of NO_x emissions established by initial measurements at the industrial partner's plants the NO_x generation in the EAF has been studied by combined pilot plant trials and thermodynamic calculations. Additionally a semi-empirical model of the NO_x emissions of the Consteel process has been developed. Main conclusions from these studies in view of the control of NO_x emissions are:

- For the trials conducted the amount of NO_x produced by the electric arc is to be seen as constant and not influenced by electric parameters of the arc (arc current, arc length) within the range of parameter variations technical available and tested.
- The NO_x emission of the pilot plant EAF as well as industrial EAFs is strongly correlated with the composition of the furnace atmosphere the arc is ignited and burning in. The highest amounts of NO_x are produced in O_2 rich atmospheres. Atmospheres like this occur in the EAF e. g. after the scrap charging. To lower NO_x generation in the furnace therefore the amount of leak air increasing the O_2 content of the furnace off-gas has to be as low as possible.
- EAF off-gas is usually not in equilibrium. The kinetics of the gas reactions in the furnace and the post combustion zone are determining the NO_x content of the off-gas. Differences between real off-gas data and equilibrium calculations would be smaller with a longer residence time of the off-gas in the hot zones and higher temperatures respectively. To achieve this objective the off-gas flow rate has to be controlled as low as possible still ensuring sufficient exhaust of any furnace emissions.
- Reducing agents like CO and H_2 are significantly lowering the NO_x concentration in the off-gas and reduce NO_x formed by the electric arc. Because of this, operational practices like slag foaming with the increased generation of CO, which are already in use to lower energy losses in the EAF, have an additional positive effect on the NO_x emissions of EAFs.

To investigate the NO_x formation in the EAF further and to test the conclusions from the theoretical and experimental trials at industrial level, additional industrial trials where conducted. Regarding the impact of oxygen injection and CoJets the following important factors influencing the NO_x emission have been identified:

- There is no correlation between the amount of carbon blown and the total NO_x emissions when carbon is blown at all.
- The correlation between the CO and NO_x content in the furnace off-gas predicted in the modelling stage of WP 3 could be confirmed.
- Trials regarding the ratio of injected oxygen to methane in the CoJet burners led to a reduction of NO_x emissions of up to 30 % by reducing the oxygen amount available inside the furnace. This is also in agreement with the predictions derived from the modelling in WP 3.

Deduced from these results the following best practices have been formulated:

- Continuation of the carbon blowing (slag foaming) standard practice because of the positive influence of the resulting CO-rich atmosphere on the NO_x emissions for carbon steel grades.
- Evaluation of new developments in foamy slags for stainless steel grades and application when available for standard operational use.
- Reduction of the CoJet ratio to reduce the oxygen supply to the furnace and to prevent an oxygen rich atmosphere in the EAF.

Investigations examining the influence of oxygen injection by door lance, of the use of different carrier gases for carbon and dust injection and of airtightness and the dedusting system operation on the NO_x emissions have led to the following main results:

- Delayed oxygen injection during/after arc ignition is lowering the NO_x emissions due to a reduced oxygen supply in the EAF vessel.

- The use of an inert carrier gas instead of air for the injection of carbon and dust is only for the dust injection beneficial in regard to NO_x emissions. When used for the carbon injection it leads to even higher NO_x concentrations in the off-gas.

According to these results the following best practices have been established to reduce the oxygen supply in the EAF:

- Delay of the oxygen injection after arc ignition.
- Use of inert carrier gas for the dust injection into the furnace.
- Keeping the slag door closed if possible to maximise the airtightness of the EAF.
- Variable control of the off-gas volume flow rate to minimise the amount of leak air in the furnace.

The main issues to be pointed out on the basis of the investigations regarding specifically the Consteel process including the impact of the scrap preheating on NO_x emission are:

- Peaks of NO_x emission (concentration) appear generally during the transient operation into the furnace, difficult to avoid but that do not affect strongly the average emission; during main period of the heats NO_x formation decreases strongly, due to the CO/CO_2 formation that 'fills' the furnace freeboard and decreases the air in-leakage.
- Post Combustion inside EAF (by dedicate lancing) contributes to lower the NO_x emission decreasing the air in-leakage even if a suitable amount of coal is required to generate enough (and as longer as possible) CO_x (related to the slag foaming management); the net effect of coal addition is therefore 'positive' being the nitrogen content of this material not playing a significant role in oxides formation.
- The amount (in terms mass flow rate, derived by off gas mass flow rates determination at the furnace exit and downstream) generated in the pre-heater tunnel is about five times higher than the furnace, due to the air dilution and reactions to complete combustion of residual CO and H_2 coming out from EAF.
- Available data show that an optimal balancing of the effective depression throughout the running is required to avoid excess of air leakage at the connecting car stage (i.e. the air that mixes with EAF off gases) by proper setting of the de-dusting system.

The CFD simulations of one of the investigated industrial EAFs were carried out to model the gas flow and air intake inside the EAF vessel and in the post combustion zone of the primary dedusting system. The interaction between gas chemistry, gas flow patterns and NO_x formation due to the electric arc and in post combustion zones has been investigated as well. Various EAF operating conditions like dedusting system operation, origin of leak air, furnace temperatures etc. have been varied and simulated. Main issues to be pointed out on the basis of these CFD simulations are:

- CFD simulations visualized the flow pattern and mass fraction distribution in the EAF and post combustion zone and gave new information regarding the position of off-gas measurement probes.
- As a result of the simulations the off-gas measured at point A is not in thermo-chemical equilibrium but is composed of unburned CO and O_2 simultaneously.
- The amounts of CO and O_2, respectively, available in the furnace have a great influence on NO_x emissions.

On the basis of the developed guidelines for NO_x reduction Consteel Furnace and standard EAF optimisation can be carried out finding the best compromise among energy efficiency and NO_x reduction. The best practise formulated regarding the CoJet application for example besides the potential to reduce NO_x emissions by up to 30 % even proved to be also economically beneficial for RIVA.

The obtained results will be used for publications to be published or presented to specialised congress.

3 List of Figures

4 List of Tables

5 References

[1] Cantera, An object-oriented software toolkit for chemical kinetics, thermodynamics, and transport processes, http://code.google.com/p/cantera/

[2] EAF technology – State of the Art & Future Trends, International Iron and Steel Institute, Brussels, 2000

[3] Elevated temperature physical properties of stainless steels, British Stainless Steel Association, http://www.bssa.org.uk

[4] Alternative control techniques document – NO_x emissions from iron and steel mills, U.S. Environmental Protection Agency, Emission Standard Division, Report EPA-453/R-94-065, 1994

[5] Product Groups, Graphite and Carbon Electrodes, Typical Properties of Graphite Electrodes, SGL Group, http://www.sglgroup.com

[6] Steel Slag Material Description, US Department of Transportation, Federal Highway Administration, http://www.tfhrc.gov/hnr20/recycle/waste/ssa1.htm

[7] Theory Guide – Thermal NO_x Formation, ANSYS FLUENT 12.0/12.1 Documentation, Section 13.1.3, ANSYS

[8] Agarwal, J.C.; Jessiman, N.S.: Nitrogen oxide emission in the steel industry, Iron and Steelmaker, August 1992

[9] Chan, E.; Riley, M.; Thomson, M. J.; Evenson, E. J.: Nitrogen Oxides (NO_x) Formation and Control in an Electric Arc Furnace (EAF): Analysis with Measurements and Computational Fluid Dynamics (CFD) Modelling, ISIJ International, Vol. 44 (2004), No. 2, pp. 429–438

[10] Englund, K.: Quantification of the Discharge of Nitrous Fumes from the Steelplant of AB Sandvik Steel, Department of Chemical and Metallurgical Engineering, Lulea University, Lulea, 2002

[11] Goodwin, D. G.: An Open-Source, Extensible Software Suite for CVD Process Simulation, in: Allendorf, M.; Maury, F.; Teyssandier, F. (Ed.): Chemical Vapor Deposition XVI and EUROCVD 14, ECS Proceedings Volume 2003-08 The Electrochemical Society, 2003, pp. 155-162

[12] Grant, M. G.: Principles and Strategy of EAF Post-Combustion, 58th Electric Furnace Conference, Orlando (USA), November 2000

[13] Guo, D.; Irons, G.: Radiation Modeling in an EAF, AISTech 2004 Proceedings, Vol. 1, pp. 991-999

[14] Jörß, W.; Handke, V.: Bericht der BRD über Emissionen von SO_2, NO_x, NH_3 und NMVOC sowie die Maßnahmen zur Erhaltung der NEC's, Emissionen 2000 und Referenzprognose 2010 (außer Landwirtschaft), Studie im Auftrag des BMU, Institut für Zukunftsstudien und Technologiebewertung, Berlin, 2003

[15] Kirschen, M.; Voj, L.; Pfeifer, H.: NO_x Emission from the Electric Arc Furnace - Measurements and Modelling. AISTech 2005, Association for Iron and Steel Technology, AIST Conf. Proceedings (2005) pp. 585-595

[16] Malikov, G. K.; Lisienko, V. G.; Malikov, K. Y.; Viskanta, R.: Mathematical Modelling and Validation Study of NO_x Emissions in Metal Processing Systems, ISIJ International, Vol. 42 (2002), No. 10, pp. 1175–1181

[17] Martini, U. et al: Development of operating conditions to improve chemical energy yield and performance of dedusting in airtight EAF, RFCS project contract number 7210-PR/328

[18] Pfeifer, H.: Lichtbogenofentechnik, Kap. 2, Gasentladungen und Lichtbögen, lecture script, RWTH Aachen University, pp 2.2 – 2.6

[19] Rafiei, R.; Kermanpur, A.; Ashrafizadeh, F.: Numerical thermal simulation of graphite electrode in EAF during normal operation, Ironmaking and Steelmaking, Vol. 35 (2008), Nr. 6, pp. 465 - 472

[20] Ramírez-Argáez, M. A.; González-Rivera, C.; Trápaga, G.: Mathematical Modeling of High Intensity Electric Arcs Burning in Different Atmospheres, ISIJ International, Vol. 49 (2009), No. 6, pp.796-803

[21] Smith, G. P.; Golden, D. M.; Frenklach, M.; Moriarty, N. W.; Eiteneer, B.; Goldenberg, M.; Bowman, C. T.; Hanson, R. K.; Song, S.; Gardiner, Jr., W. C.; Lissianski, V. V.; Qin, Z.: http://www.me.berkeley.edu/gri_mech/

[22] Verein Deutscher Eisenhüttenleute (VDEh): Slag Atlas, 2nd Edition, Verlag Stahleisen GmbH, Düsseldorf, 1995

6 Abbreviations

AC / DC	Alternating Current / Direct Current
CFD	Computational Fluid Dynamics
CLD	Chemiluminescence detector
CSM	Centro Sviluppo Materiali
EAF	Electric Arc Furnace
EBT	Eccentric Bottom Tapping
DEC	Direct Exhaust Control
DEWG	Deutsche Edelstahlwerke
IR	Infrared
RIVA	Riva Acciaio Spa
RWTH	Rheinisch Westfälische Technische Hochschule
ORI	ORI Martin – Acciaieria E Ferreira di Brescia
WP	Work Package

European Commission

EUR 25078 — Control of nitrogen oxide emission at the electric arc furnace — CONOX

H. Pfeifer, T. Echterhof, L. Voj, J. Gruber, H.-P. Jung, S. Lenz, C. Beiler, F. Cirilli, U. De Miranda, N. Veneri, E. Bressan

Luxembourg: Publications Office of the European Union

2012 — 134 pp. — 21 × 29.7 cm

Research Fund for Coal and Steel series

ISBN 978-92-79-22227-6

doi:10.2777/25616

ISSN 1831-9424

HOW TO OBTAIN EU PUBLICATIONS

Free publications:

- via EU Bookshop (http://bookshop.europa.eu);
- at the European Union's representations or delegations. You can obtain their contact details on the Internet (http://ec.europa.eu) or by sending a fax to +352 2929-42758.

Priced publications:

- via EU Bookshop (http://bookshop.europa.eu).

Priced subscriptions (e.g. annual series of the *Official Journal of the European Union* and reports of cases before the Court of Justice of the European Union):

- via one of the sales agents of the Publications Office of the European Union (http://publications.europa.eu/others/agents/index_en.htm).

The CONOX project has been focused on investigating the electric steelmaking process in the EAF and, as a special case, the Consteel EAF with regards to NOx emissions. The investigations were carried out by a consortium of research institutes (RWTH, CSM) and three electric steelmaking plants (DEWG, ORI Martin, RIVA Verona) with a wide range of produced steel grades and EAF technologies (oxygen, dust, and coal injectors, gas burners, CoJets, scrap preheating, slag foaming).

The project was based on the combination of experimental investigations of the NOx formation in EAFs at industrial plants as well as pilot plant EAFs at well defined conditions and modelling of the NOx formation in the EAF. The general objective was to elaborate guidelines to reduce NOx emissions from the Consteel process (CSM, ORI) as well as standard EAFs employing various EAF technologies (RWTH, DEWG, RIVA).

The activities of CSM and ORI have been focused on the investigation of the Consteel process. A semi empirical model of NOx emissions has been developed based on literature data, pilot furnace tests and industrial measurements. Plant measurements carried out permitted to quantify the amount of NOx generated in the EAF and downstream in the tunnel and provided data for model refining and application. The model has been applied to support the definition of improved guidelines to decrease NOx emissions.

The activities of RWTH, DEWG and RIVA have been focused on the experimental investigation and modelling of different process conditions and a deduction of predictions regarding NOx formation. These predictions have been further investigated and validated by industrial plant measurement. Eventually best practices to reduce NOx emissions have been derived from the combined results of modelling and industrial measurements.

KI-NA-25078-EN-N

Publications Office